UNIVERSITEIT VAN PRETORIA
UNIVERSITY OF PRETORIA
YUNIBESITHI YA PRETORIA

UNIVERSITEIT VAN PRETORIA
UNIVERSITY OF PRETORIA
YUNIBESITHI YA PRETORIA

Aerodynamic Loss Reduction In A Vane Cascade with Leading-Edge Fillet and Upstream Endwall Film-cooling

Submitted in partial fulfilment of the requirements for the degree of

Master of Engineering

In

The department of mechanical and aeronautical engineering

University of Pretoria

by

keenesh arnachellan

June 2017

supervisor: Dr G.I. Mahmood

Co-supervisor: Prof J.P. Meyer

I. ABSTRACT

Title: Aerodynamic loss reduction in a vane cascade with leading-edge fillet and upstream endwall film-cooling.

Supervisor: Dr G.I. Mahmood
Co-supervisor: Prof J.P. Meyer

Department: Mechanical and Aeronautical Engineering

Secondary flow structures account for nearly 50% of aerodynamic losses experienced in the turbine blade passages. The adverse effects of these vortex structures transport the hot mainstream fluid towards the endwall blade surfaces, which enhances thermal stresses and leads to blade failure. The effects of leading-edge fillets and film-cooling with flush slots located upstream near the leading-edge region were investigated experimentally in the study in a large-scale linear vane cascade in which the aerodynamic flow field was considered. The introduction of slot film flow and fillet aimed to reduce the effects of the secondary flow structures from the leading edge through the passage towards the exit in an effort to decrease the pressure losses, improve film-cooling coverage and flow field uniformity for the next blade row. The two-dimensional vane profile was obtained from the hub-side airfoil of the GE-E^3 engine nozzle guide vane. The slots were configured for two experimental cases to evaluate the influence of coolant flow rate and momentum; first, the effects of slot film injection from all four slots were observed and then compared with the second case injecting coolant only through the two central slots. Further effects were investigated by combining slot film-cooling with the leading-edge fillets employed on the endwall blade junction. The flow field measurements were quantified with spatial distributions of axial vorticity, total pressure loss, endwall static pressure and flow angle deviations taken across the cascade passage. The measurements were obtained at a Reynolds number of 2.0E+05 based on the cascade inlet velocity and vane chord length. Film-cooling inlet blowing ratios between 1.1 and 2.3 were investigated with the supply of coolant provided by a secondary channel. Film-cooling results were compared with the baseline case without slot film flow and fillet. The results indicated substantial improvement in the passage and exit planes with high inlet blowing ratios. The introduction of high momentum coolant flow from the central slots was seen to create laterally reversed axial vorticity, thereby counteracting the cross-flow tendency in the passage. The effects at the passage exit showed suppressed vortex structures with slot film injection from the two central slots only, with further improvements in the flow angle deviations. The leading-edge slots were seen to contribute positive axial vorticity, which enhanced the passage vortex that was pushed away from the endwall at the exit. When the fillet was introduced, it had favourable effects in reducing the pitchwise pressure gradients along the endwall. Filleted film-cooling then resulted in a faint passage vortex system (50-80% size and 20-50% strength reduction) with a restored endwall boundary layer at high film flow rates. The leading-edge fillet was highly effective at the inlet of the blade passage because it weakened the horseshoe vortex formation. Thus, upstream slot film-cooling has great potential to decrease the aerodynamic losses and is further compounded with the leading-edge fillet.

II. ACKNOWLEDGEMENTS

I would like to acknowledge the following people for their help and support in this study:

- Dr G.I. Mahmood, for his role as supervisor and sharing his expertise on the subject;
- Mr A.S. Shote, for his support and assistance as a fellow researcher on the project;
- Mr C. Govinder and Mr D. Keetse, for their ongoing assistance in the wind tunnel laboratory at UP;
- the institutions which provided support and funding:
  - CSIR
  - Armscor
  - University of Pretoria (UP);
- my parents, for their continuous support and guidance throughout my academic career.

III. CONFERENCE PAPER

The following conference paper was produced as part of the study:

- Shote, A.S., Arnachellan, K., Mahmood, G.I., Meyer, J.P.; Total pressure losses and endwall region temperature field in a linear vane cascade with slot filmcooling flow, International Aerospace Symposium of South Africa 2016 (IASSA 2016), CSIR ICC Pretoria, 20-21 October 2016.

IV. DECLARATION

I, the undersigned, hereby declare that:

- I understand what plagiarism is and I am aware of the University's policy in this regard;
- the work contained in this dissertation is my own original work;
- I did not refer to work of current or previous students, lecture notes, handbooks or any other study material without proper referencing;
- where other people's work has been used, this has been properly acknowledged and referenced;
- I have not allowed anyone to copy any part of my dissertation;
- I have not previously in its entirety or in part submitted this dissertation at any university for a degree.

Signature of student: _____

Name of student: Keenesh Arnachellan

Student number: 10316842

Date: _____

TABLE OF CONTENTS

V. LIST OF FIGURES

VI. LIST OF TABLES

VII. NOMENCLATURE

Symbol	Description	Unit
a	Best-fit intercept	
b	Bias Best-fit slope	
C	Actual chord of blade airfoil	
C_{ax}	Axial chord of blade airfoil	
C_D	Discharge coefficient	
C_{Ps}	Coefficient of static pressure	
$C_{Pt,Loss}$	Coefficient of total pressure loss	
D	Diameter	M
g	Gravity	m/s^2
L	Delivery length of film-cooling slot	M
m	Gradient	
$\dot{m}$	Mass flow rate	kg/s
M	Sampling rate	Samples per second
M_{in}	Film-cooling inlet blow ratio	
n	Number of variables Number of data points	
p	Precision	
P	Pressure	Pa
ΔP	Pressure drop	Pa
R	Result Specific gas constant	$J.kg^{-1}.K^{-1}$
Re	Reynolds number	
S_{xx}	Sum of the squares of x	
S_{xy}	Sum of the squares of x and y	
S_{yx}	Standard error of best fit	
S_{yy}	Sum of the squares of y	
S.D.	Standard deviation	
t	Student's t-statistic	
T	Temperature	Kelvin [K]
U	Streamwise velocity	m/s
u, v, w	Local x-velocity	m/s
V	Voltage	V
W	Width of film-cooling slot	m
X_G, Y_G, Z_G	Global coordinates	
x, y, z	Local coordinates	

Greek Symbol	Description	Unit
β	Orifice plate diameter ratio	
δ	Uncertainty boundary layer thickness	Mm
δ_1	Displacement thickness	Mm
δ_2	Momentum thickness	Mm
∂	Partial derivative	
ρ	Density	kg/m^3
π	Mathematical constant	

Subscripts	Description
0	Free-stream quantity
atm	Atmospheric condition
C_i	Calculated value
H_2O	Water
Hg	Mercury
I	Index
Dyn	Dynamic
s	Static
t	Total
ref	Reference
Local	Measured value

Superscripts	Description
-	Average quantity

Abbreviations	Description
MFR	Mass flow ratio (Film-cooling)
PS	Pressure side
SS	Suction side
TE	Trailing edge

CHAPTER 1: INTRODUCTION

1.1 Background

The invention and development of the gas turbine have led to major improvements in the world we live in today. Although the gas turbine in its early days was not very efficient, its usage grew and with it the need to improve design and performance. The applications of turbomachinery have increased so greatly that the designer cannot simply accept working principles alone, but must continuously look to the future by ensuring sustainability and improvement. The use of turbomachinery in power generation forms an integral part of transportation (aircraft propulsion, ship engines) and industrial power uses.

The gas turbine was born by combining two fields of technology, the steam turbine and the combustion engine. Ideally, a gas turbine is simply an external combustion engine, which is capable of burning a variety of fuels, one of its greatest traits.

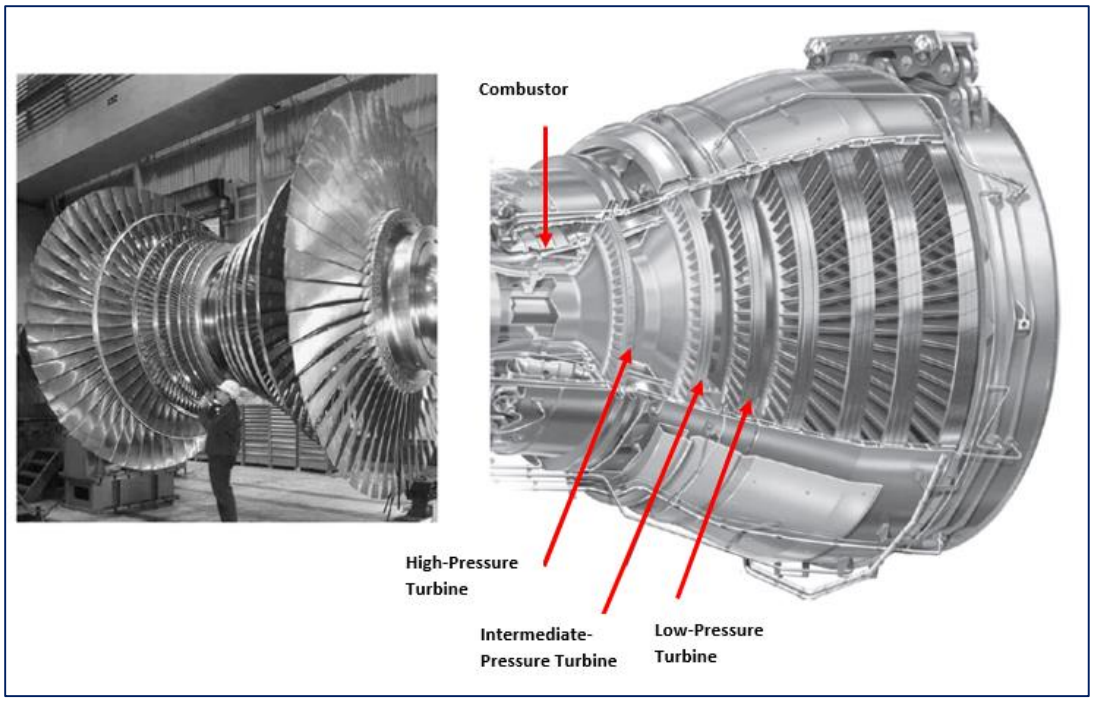

FIGURE 1.1 LARGE LOW-PRESSURE STEAM TURBINE (LEFT) AND TURBINE SECTION OF MODERN TURBOFAN JET ENGINE (RIGHT) (S. L. DIXON, 2010).

In the modern world, gas turbines and other turbomachinery provide critical applications such as power plant use in aircraft, large shipping vessels, helicopters as well as basic power generation when electricity is needed. The need to improve and increase the efficiency of the gas turbine is of great importance due to the wide range of application it offers. By increasing the efficiency of the gas turbine, more energy can be saved by spending less energy to operate. This, in turn, will have a domino effect on the cost of living as a whole because all products and services are delivered via transportation, whether by air or sea, and these savings in energy can relieve financial bounds in these areas. On the other hand, the operation of such gas turbines can become less harmful to the environment by minimising the amount of fuel required to burn and therefore reduce carbon emissions significantly.

However, the matter at hand begins with where and how to effectively increase the aerodynamic performance of the gas turbine. To do this the gas turbine must be reduced into a collection of parts or processes which perform key functions. These can be summarised best into three basic functions: the compression, combustion and expansion processes. Furthermore, these processes can be reduced to their basic form in thermodynamic principles.

The compressor and turbine can be seen as similar devices as they are designed on similar principles, compression and expansion, but perform opposing functions. Hence their performance can be compared and evaluated in much the same manner. Compressors and turbines consist of a central shaft on which there is a series of stator and rotor rows. These rows contain airfoil-shaped blades, which extend in a radial pattern around the circular base, which is attached to the shaft. When fluid flows through the blade passages in a compressor, lift force is generated and thus provides the force for which the fluid is driven through the system. In the turbine stage, the fluid flow is caught by the blades, which then rotate (rotor) and result in the energy transfer.

The combination of these processes results in a three-dimensional flow system in which the fluid spins about the axis of rotation as it travels from compressor to turbine and thus through the engine. Three-dimensional flows are extremely difficult to model and therefore to measure with clear understanding. A two-dimensional linear cascade is one of the most common methods used to model compressor and turbine blade-passage aerodynamics. The cascade consists of multiple airfoils placed one over the other, which create a model section of a rotor or stator section if the blade rows were to be unwrapped by the circumference and placed in a straight line. Usually, the airfoil-shaped blades are much smaller in size and therefore the cascade allows the scale to be increased for experimental measurements. The configuration of the cascade creates a periodic flow structure due to the blades being spaced at a constant pitch distance. This results in a comparable two-dimensional flow model to obtain measurements in terms of aerodynamics and other physical properties which exist in the blade passages.

The largest aerodynamic losses which impact turbine performance pertain to the three-dimensional flow structures which exist within the vane-blade passages, particularly at the turbine inlet where the guide vanes are located. These losses are commonly known as secondary flows, which occur due to the formation and propagation of vortex structures in the near-wall region of the blade passages. The vortex structures are further strengthened by the pitchwise pressure gradients, which exist in the passage along the endwall and therefore drive these secondary flows. The result of the vortical structures entrain the endwall boundary layer fluid as they progress towards the passage exit and thereby disrupt the uniformity of the flow field considerably. As a consequence, the high energy (temperature) fluid is then convected from the mainstream to the near-wall region due to the circulation by these vortices and increases thermal loading on the blade-endwall surfaces, which reduces the life of turbine parts and decreases thermal efficiency. The aerodynamic efficiency is ultimately reduced by the vortex structures and has a continued influence as the resultant flow field progresses downstream in the turbine through the rotor-stator stages. Overall, power output losses of nearly 50% are suffered due to the aerodynamic losses. The aerodynamic losses also render film-cooling flows ineffective as they rely on the attached boundary layer to provide relief to targeted surfaces.

1.2 Problem statement

Energy losses are of main concern inside the turbine, as the turbine produces expendable power. Mechanical losses in gas turbine engines are minimal due to the continuous flow in the system, because the fluid flow is never stopped at any stage. The efficiency therefore is most dependent upon the energy losses associated with the three-dimensional flow structures inside the blade passages, and these are known as aerodynamic losses. The turbine section consists of rows of stator and rotor discs. The rotor discs rotate under the forces applied by the expanding fluid as it passes through each stage. Thus the moving fluid imparts rotational energy to the rotor as it acts on the blades, while the stator rows aim to direct the moving fluid between successive rotor-blade rows with minimal pressure losses. The pressure losses which commonly occur in turbine blade passages are known as secondary flows. The secondary flows occur predominantly at the blade-endwall junction where it is common to observe the creation and evolution of vortex flow structures. These vortices create regions of circulation in the flow, thereby reducing the total energy of the fluid. As a result, a deficiency in rotation of the blades is seen, which leads to less power produced. The secondary flows are depicted in Figure 1.2.

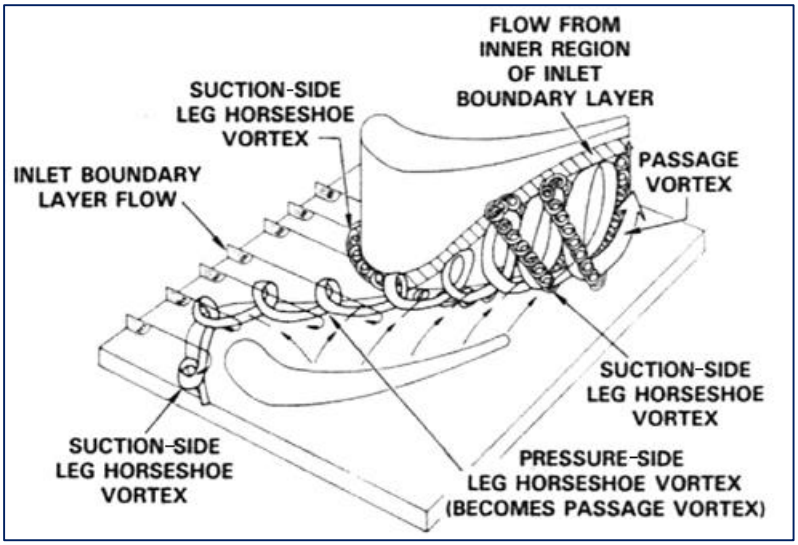

FIGURE 1.2 SECONDARY FLOW STRUCTURES IN BLADE PASSAGE (SCHNEIDER ET AL., 2013).

The maximum power output produced by the Brayton cycle is dependent on the combustion process. If maximum temperatures can be achieved at the turbine inlet, maximum power output will be reached. However, excessive inlet temperatures at the turbine must be limited due to the thermal loading experienced by the turbine blades and supporting parts during operation. This is due to limitations on operating temperatures of the turbine component materials, because the combustion process can achieve temperatures far beyond the maximum operating temperature of the turbine blades themselves. Secondary flows further aggravate the problem because the vortex structures bring the high energy and high-temperature fluid from the passage centre closer to the blade-endwall junction where thermal loading is undesirable. By law of conservation of energy, a thermal gradient is present between the endwall surface and the passage centre. Excessive thermal loads create creep and result in failure in the turbine blade-endwall region and this significantly decreases the lifetime of the turbine as well as its efficiency. Turbine components such as the hub, shaft and discs (rotor and stator) are designed for a specific operating lifetime, after which the parts must be replaced completely. These costs can become significantly high if the turnover rate of turbine parts increases, which is directly a root cause of the secondary flow structures apart from operational wear and degradation. The highest of these costs are associated with the airfoils (blade and guide vanes) due to manufacturing and can reach between $400 000 and $700 000 for a complete set of high pressure turbine blades (Ackert, 2011).

One critical aerodynamic problem which occurs is the resultant non-uniform flow field at the exit of each stage. Due to secondary flows, the resultant flow field at the exit of a blade stage follows into successive blade stages, thereby decreasing each blade stage efficiency downstream in the turbine. Hence if the secondary flows can be weakened or eradicated completely at the inlet, the overall efficiency of the gas turbine will increase dramatically.

It is also clear that secondary flows affect the heat transfer issue presented by the inlet temperatures to the turbine. If heat transfer incurred from the fluid to the blade-endwall regions is enhanced, then the turbine efficiency reduces based on thermodynamic principles of the Brayton cycle. Film-cooling has been developed and integrated inside the turbine blade passages to reduce significant heat transfer to these components but the secondary flow structures remain dominant and pose challenges for the coolant coverage to target affected areas within the blade passages near the blade-endwall region. Thus, it is also desirable to eliminate secondary flows as much as possible to improve cooling mechanisms within the turbine blade passages and therefore maintain higher film-cooling effectiveness. Alternatively, increased demand for film-cooling supply requires more energy from the turbine engine, which compromises performance output. The need for increased energy thereby leads to larger compressor-turbine sizes, which are not cost-effective because the secondary flows still contribute to the high aerodynamic and thermal efficiency losses within the turbine.

1.3 Justification

It is evident that there exists a great need to improve the aerodynamic flow field within the turbine blade passages because this holds the key to improving performance and efficiency. Hence the primary aim of this research is to weaken and if possible eradicate the presence of secondary flows at the inlet stage of the turbine, the guide vanes. Two potential methods have been identified to improve the aerodynamic behaviour within the turbine blade passages. These methods include the use of leading-edge fillets and upstream slot film-cooling. Additional investigations will include the combination of both methods to determine their overall effect on the system. The above-mentioned methods have been investigated by other researchers in the past but the design of the leading-edge fillet as well as upstream slot film-cooling is unique to this study to improve upon past research. Previous researchers and designers in the turbomachinery field have implemented many methods in their cascade research to counter the effects of three-dimensional endwall flows including film-cooling and leading-edge fillet. There also exist other techniques such as contoured endwall (two-dimensional and three-dimensional), blade thickening at the leading edge and active flow control with film-cooling holes and upstream slots. It is important to note that this investigation is primarily focused on the aerodynamic flow structures involved but which are also directly related to the heat transfer problems that occur. However, heat transfer investigations will not be conducted experimentally for this study.

1.4 Aim of the study

The aim of the study is to successfully identify and document the secondary flow structures that exist in the linear vane cascade passages of a two-dimensional vane profile, for which experimental

investigations will be done. Thereafter, leading-edge modifications in the form of leading-edge fillets and upstream slot film-cooling will be conducted and evaluated experimentally to determine the potential aerodynamic performance and improvements thereof. Further documentation will be conducted of the endwall flow field with the inclusion of the above modifications. The results of the investigations will help gas turbine designers to implement simple geometric modifications in the blade/vane passages to improve aerodynamic and thermal performances of the gas turbine engine.

1.5 Methodology

The methods implemented to materialise the research goals of the study are both theoretical and experimental and are described as follows:

a) Design and construct an experimental set-up to model the flow field inside the stator vane rows of a gas turbine based on the GE-E^3 vane airfoil. The test section should model the periodic flow field by employing a linear vane cascade with instrumentation for the flow field measurements for validation of endwall modifications. The endwall modifications pertain to employing fillets at the vane-endwall junction on the top wall and the capability of upstream slot film-cooling on the bottom wall. Furthermore, flow field measurements along the vane cascade include the endwall static-pressure distributions, total pressure distributions, local flow orientations, velocity vector and vorticity distributions. The design and construction of an open-circuit wind tunnel to provide airflow through the test section under suction are then supplemented with provisions upstream of the test section for calibration procedures and boundary layer characterisation. The design of the fillet is supported by Mr A.S. Shote, a doctoral student on the same project, where CFD studies are conducted to validate the fillet chosen for experimental studies.

b) Design and construct a secondary open-circuit film-cooling supply channel to provide coolant flow when upstream slot film-cooling is employed in the flow field measurements.

c) The theoretical investigations involve a comprehensive literature study, which will complement the validation of the experimental methods and set-up. Thereafter, the quantification of flow field measurements for the baseline case and comparisons with the endwall modifications will be reported in a concise format.

d) Present the experimental results with supporting discussion in the form of a journal publication to expose the research that has been done.

1.6 Scope of work

This research study is the outcome of a master's degree of which the duration is limited to a year due to funding support provided. Thus, a major part of this project is dedicated to the design and construction of the wind tunnel and housing the test section with additional calibration and boundary layer characterisation procedures which are vital to the experimental phase. Before the project began, only the linear vane cascade existed but was unsuccessful in prior studies in which a blow-type wind tunnel was used. Therefore, the project required redesign and completely new build of a suction-type wind tunnel to achieve quality flow results that can be compared with realistic gas turbines. The experimental build was completed with Mr A.S. Shote with supporting assistance from Mr C. Govinder and Mr D. Keetse, who designated the required floor space in the wind tunnel laboratory at the University of Pretoria as well as aided in the construction process when needed. The construction and commissioning of the linear vane cascade facility took approximately 10 months and this left the remaining months for experimental investigations and dissertation writing thereafter. Thus the experimental scope was limited to this time duration as well as financial constraints imposed by the sponsors of the project. The entire investigation consisted of the experimental measurements of the flow field in the cascade facility with a five-hole total pressure probe and wall static pressure taps. A constant temperature hot-wire anemometer was only used to characterise the reference properties of the cascade flow.

1.7 Outcomes

The outcomes of this research are related to identifying and understanding the aerodynamic flow field that exists inside the blade passages of a gas turbine. The improvement of the aerodynamic performance is then considered by designing and implementing the leading-edge modifications, fillet and film-cooling flow from upstream slots, and evaluating the measured flow field with scientific relations and conclusions. The overall outcome is to reduce the aerodynamic losses associated with the secondary flow structures and also to increase the endwall film flow coverage inside the vane passages with leading-edge modifications described earlier.

1.8 Overview of dissertation

The dissertation consists of the following chapters, covering the following material:

a) Chapter 2 presents a detailed literature review to gain more insight into secondary flows, film-cooling and leading-edge fillet research.
b) Chapter 3 contains the design and description of the experimental set-up with supporting equipment, experimental methods and procedures.
c) Chapter 4 provides uncertainty estimates of all measured data and results for validation and confidence in the study.

d) Chapter 5 presents the experimental results for all test cases and compares the aerodynamic performance of the baseline case with the leading-edge modifications.
e) Chapter 6 concludes with summaries and recommendations of the study.
f) Appendix A – Pressure transducer calibration
g) Appendix B – Five-hole probe calibration
h) Appendix C – Uncertainty analysis
i) Appendix D – Endwall static pressure port coordinates for top and bottom walls.
j) Appendix E – Complete Experimental Results

CHAPTER 2: LITERATURE REVIEW

Gas turbine efficiency can be improved by resolving the aerodynamic losses which arise within the turbine blade passages of both the guide vane row, and stator-rotor blade rows downstream. The aerodynamic losses occur primarily due to the secondary flows, which are caused by the horseshoe vortex at the leading edge of the blade-endwall junction, boundary layer separation at the endwall and pitchwise pressure gradient in the blade passage. Thus it is a critical area for improvement in the overall performance of the gas turbine. The secondary flows also enhance heat transfer in the turbine blade-endwall region. Film-cooling flow at the endwall and modifications of the endwall itself have been explored and validated by different configurations with substantial flow field improvement inside the gas turbine. Not only does film-cooling provide heat transfer relief but under special circumstances, it can be used to weaken and reduce secondary flows. This will be an important experimental objective as well.

Before an experimental method can be developed, it is important to understand the secondary flow structures which occur inside the turbine blade passages. It is also necessary to review relevant research which has been conducted regarding the use of leading-edge fillets as well as the vast research that has been done on film-cooling with aerodynamic interest in gas turbine passages.

2.1 Secondary flows

Secondary flows develop in the turbine vane passages as a consequence of the geometrical design of the blade-endwall junction. The sharp transition between the blade and hub wall causes the incoming flow to turn along the passage and deviate from the mean flow direction due to the boundary layer at the endwall as it travels through the vane passage. The result of the deviations from the mainstream flow direction as well as the aerodynamic pressure gradients and boundary layer interactions which exist in the passage is the formation of a series of vortex structures, which develops and propagates through the passage, becoming larger in magnitude and size. The aerodynamic losses caused by secondary flows contribute to the efficiency losses experienced by the modern gas turbine engine. The secondary flow structures have been investigated thoroughly and identified as they develop through the blade passages.

A thorough explanation regarding the formation of the horseshoe vortex was documented by Zess and Thole (2002) as well as Kubendran et al. (1988), Eckerle and Langston (1987), Pierce and Shin (1992) and Praisner et al. (1997). When an incoming boundary layer approaches the turbine blade along the endwall, a pressure gradient arises along the span direction at the leading edge as a result of the decrease in velocity near the endwall region. Because of the positive pressure gradient from the endwall to midspan region along the leading edge, this spanwise pressure

gradient causes the boundary layer flow to be directed towards the endwall where it rolls into a vortex structure as it turns back upstream to maintain continuity. The result is the formation of the leading-edge horseshoe vortex. Consequently, the total pressure decreases significantly in the vortex formation region along the passage.

The horseshoe vortex forms around the leading edge and disperses into two legs on either side of the blade. The suction-side leg moves towards the suction surface and the pressure-side leg moves towards the pressure surface, each with opposing rotation, as indicated by Wang et al. (1995). Thereafter, the pressure-side leg moves rapidly towards the suction side of the adjacent blade due to the pitchwise pressure gradient between the pressure and the suction side. The passage vortex forms as the pressure- and suction-side leg vortex meet due to the cross-flow pressure gradient between the adjacent blade surfaces in the passage. The passage vortex then increases in strength and moves along the suction-side endwall region where it is enhanced by the cross-flow and boundary layer separation on the endwall. The passage vortex then lifts up from the endwall region and proceeds along the suction-side blade towards the trailing edge as it continues to grow in size and magnitude due to the entrainment of the boundary layer fluids.

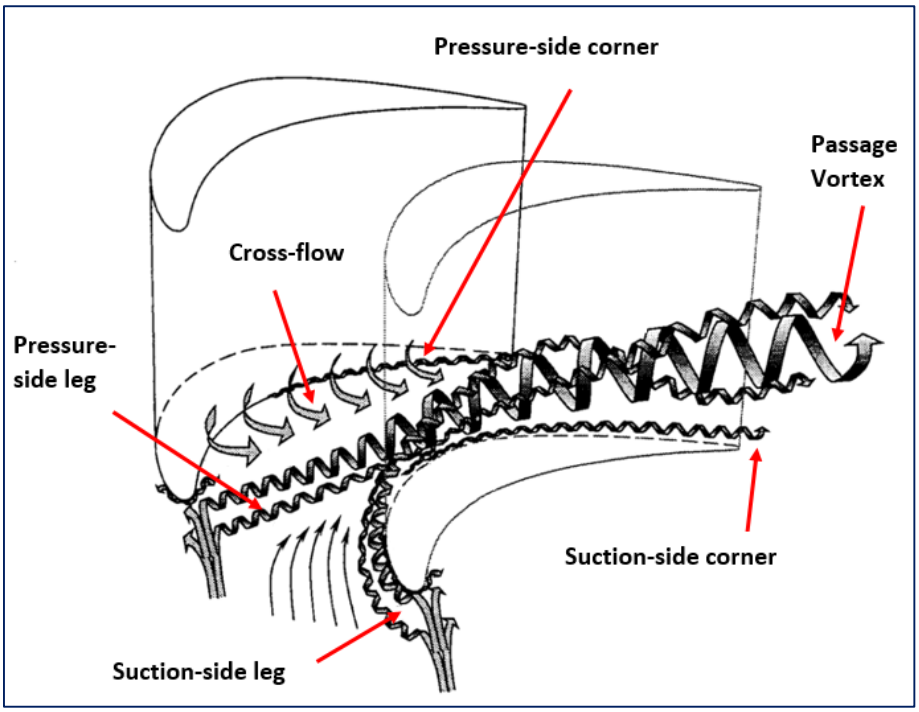

FIGURE 2.1 VORTEX FLOW STRUCTURES IN THE TURBINE BLADE PASSAGE (WANG ET AL. (1995).

Figure 2.1 depicts the findings made by Wang et al. (1995) where smoke-wire visualisation techniques along with mass transfer measurements were used to obtain images of the vortex structures within the turbine blade passages. As can be seen, they were able to track the propagation of the vortex structures from the leading edge all the way through to the exit plane

where the vortex structure developed into the passage vortex. Due to the size of the corner vortices being significantly smaller, the visualisation study was not able to pick up these areas with smoke but did not discredit their existence. Comparative results were also found by Mahmood et al. (2005) using smoke-wire visualisation techniques and they found the vortex structures to be periodically unsteady based on turbulence intensity measured near the endwall region.

The corner vortices were better investigated by Goldstein et al. (1995) as they carried out a naphthalene sublimation technique to simulate the convective heat transfer over a turbine blade. They used a naphthalene-coated turbine blade to measure the amount of mass transferred from the blade when exposed to airflow, because the mass is picked up by the near-wall flow convection. At the near-wall locations of vortex structures, the mass transfer from the naphthalene layer is higher than for the other regions of naphthalene layer, thereby indicating the location, size and strength of the secondary vortex flows.

Because the turbine receives high-energy fluid from the combustor, it is also important to consider the turbulent effects which follow. Radomsky and Thole (1999) investigated the effects of high turbulence on the convective surface heat transfer on the turbine vanes for boundary layer prediction and calculations. Combustor turbulence levels were simulated by placing an active turbulence generator grid upstream of the blades while flow field measurements of all three velocity components were obtained with a two-component Laser Doppler Velocimetry (LDV) system. The results showed that near the endwall regions increased fluctuations in spanwise velocity components were seen, indicative of the secondary flow structures on the blade-endwall region. Furthermore, by increasing the turbulence intensity, the boundary layer transition on the suction side occurred earlier along the blade surface as well as increased turbulent kinetic energy near the stagnation region of the blade. The velocity components measured also confirmed the presence of cross-flow, as the fluid progressed from pressure side to suction side of the passage.

Kang et al. (1999) conducted both computational and experimental investigations into secondary flow structures and heat transfer along the endwall of a stator vane passage to determine a correlation between the aerodynamic behaviour and the resultant heat transfer effects. Two Reynolds numbers (Re), based on boundary layer thickness, were investigated inside a large vane cascade to match the Re with the real blade passage Re. Flow field measurements were resolved with a two-component LDV system and revealed the secondary flow effects clearly. The effects of the Reynolds numbers showed great influence on the leading-edge horseshoe vortex formation. The lower Re resulted in a more complete leading-edge vortex, which was larger and stronger. These were verified by the higher turbulent kinetic energy levels present in the vortex core than for the higher case. The streak line visualisation also showed that the higher case led to the passage vortex being lifted off the wall and impinged on the suction-side surface as the endwall pressure was lowered in this region. This indicated the strong pressure gradients which existed

between the pressure side and suction side and which drove the cross-flow. Hence the higher Re effects were seen further downstream whereas the lower Re effects were seen upstream at the leading-edge endwall stagnation region. It is clear that the endwall flows play a significant role in the secondary flow formation and evolution downstream of the leading edge. Also evident is that heat transfer is greatly influenced by secondary flows, which are detrimental to the turbine performance and lifespan.

The effect of inlet conditions was investigated by Hermanson and Thole (2000) using CFD as well as experimental studies to validate the secondary flow structures inside a commercial first-stage stator vane passage. The CFD studies aimed to determine the overall effects of the inlet boundary layer in both temperature and velocity on secondary flow formation and evolution inside the vane passage. The flow field measurements were quantified by simple LDV measurements, which validated predictions near the leading-edge endwall region. The simulations were done with different inlet boundary layer thickness and temperature gradients to determine their influence on the secondary flow structure near the endwall. As seen previously by Kang et al. (1999), the effects of a thinner boundary layer resulted in more intense secondary flow with a larger passage vortex occupying the endwall. An inlet profile with constant Mach number provided the most beneficial results in that the total pressure loss for this case was the least compared with that of the other inlet profiles. The reason for this remarkable improvement was based on the stagnation flow region where the total pressure gradient near the leading-edge endwall region was constant for this case. The flow field visualisation showed no indication of leading-edge or passage vortices when the Mach number was constant thereby deducing that the secondary flow was driven by the total pressure gradients near the leading-edge stagnation region.

Mahmood et al. (2008) conducted both computational and experimental investigations in a linear vane cascade with compressible flow to identify the secondary flow structures as they developed inside the blade passage and influenced the endwall heat transfer. The computational model consisted of the hub side of a GE-E^3 first-stage vane (Timko, 1990) scaled up to 4.7 times the actual geometry. The numerical predictions showed the critical development of the leading-edge horseshoe vortex as it migrated and split into the suction-side leg and pressure-side leg, which were identified by the normalised axial vorticity field. The pressure-side leg vortex was seen to increase in size and strength as it formed the passage vortex and continued to move along the endwall towards the suction side where it entrained the suction-side leg horseshoe vortex. The suction-side leg horseshoe vortex was identified by negative values of axial vorticity with the passage vortex having positive values, thereby indicating the opposing sense of rotation of the vortex pairs. The streamlines predicted by the numerical solution also showed the origin and evolution of the secondary flow patterns along the endwall where the three-dimensional boundary layer separation and reattachment lines occurred. Along these lines, much of the endwall boundary layer fluid was entrained by the vortices as they travelled through the passage.

These flow patterns therefore resulted in increased heat transfer along the endwall, particularly near the pressure side as the separation lines dominated the boundary layer fluid movement. From a film-cooling perspective, this was undesirable because the introduction of upstream film-cooling flow would inevitably be lifted up along these separation lines within the vortex flow. The predicted Nusselt number distribution successfully showed this occurrence.

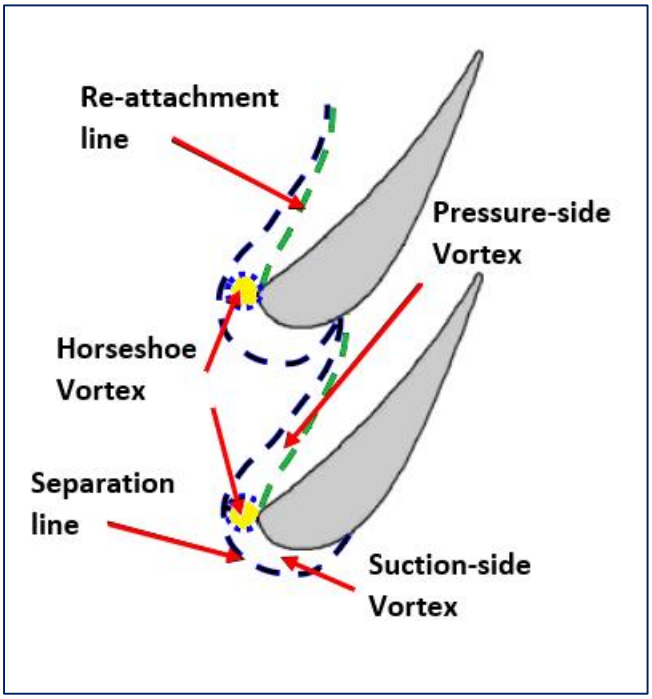

FIGURE 2.2 SECONDARY FLOW PATTERNS ALONG ENDWALL (MAHMOOD ET AL., 2008).

The above investigations have provided more clarity regarding secondary flows as well as how they are created and develop within the turbine blade passages. The key areas of interest are the regions near or at the leading-edge endwall junction where the secondary flows are born and propagate downstream. The weakening and reduction of the horseshoe vortex will reduce the aerodynamic losses near the leading edge and thereby counteract the development of the passage vortex overall. Further downstream, the strong pressure gradient which exists between the pressure side and suction side near the endwall results in cross-flow, which drives the pressure-side leg horseshoe vortex towards the suction side, thereby inducing the creation of the passage vortex. If the pitchwise gradient can be reduced, then the cross-flow will be weakened and therefore the passage vortex will reduce in strength and size. This will also be advantageous for film-cooling as the intended coolant flow will be able to provide heat transfer relief in the endwall blade regions that are needed most. Lastly, the resultant flow field will be improved in terms of uniformity for the next blade row leading to improved performance in each successive stage.

2.2 Leading-edge fillet

The first area of concern lies in reducing the leading-edge horseshoe vortex formation. Several methods of blade-endwall modification have been investigated, most notably the implementation of leading-edge fillets. The leading-edge endwall region has been shown to experience the highest heat transfer coefficients due to the secondary flow structures which arise at these locations (Kang et al., 1999). Increased thermal loading on the blade-endwall surfaces is experienced due to the vortical flows which convect the high temperature fluid from the mainstream to the endwall regions. Therefore, the leading-edge endwall region is the primary area of consideration in reducing and eliminating the development of the horseshoe vortex structure.

The leading-edge fillet is used as a geometrical modification to the blade-endwall junction where the secondary flow structures begin to develop. The critical factors which determine the effectiveness of the fillet, to reduce the horseshoe vortex, rely upon the design parameters of the fillet geometry. Many researchers have studied the use of leading-edge fillets by varying the size and shapes and have found a correlation between the boundary layer characteristics and the fillet geometry. Most researchers have found best results in leading-edge fillets where the length (streamwise) of the fillet exceeds the height (spanwise) (Sung and Lin, 1988).

It is beneficial to simulate the influence of the fillet on the blade-endwall passage through computational fluid dynamics (CFD) in order to conduct feasibility studies. A computational and experimental study was conducted by Zess and Thole (2002) in which several variations of leading-edge fillets were simulated for use in a large-scale turbine vane cascade with experimental methods similar to those of Radomsky and Thole (1999). It is vitally important that the influence of the leading-edge fillets does not render the blade loading as this will reduce the energy produced by the turbine significantly. Hence the static pressure profile around the unfilleted blade surface in the midspan region was measured and shown to agree well when the fillet was introduced.

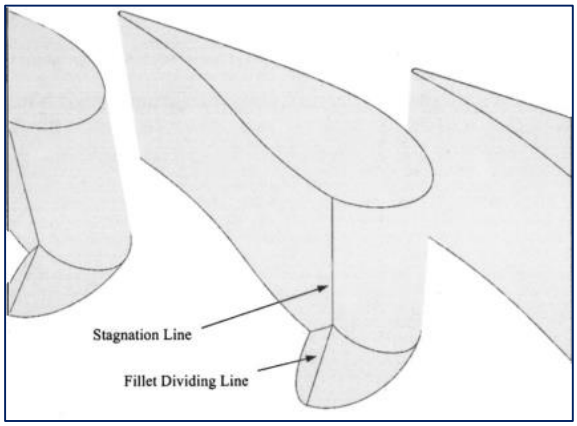

FIGURE 2.3 LEADING-EDGE FILLET PROFILE INVESTIGATED BY ZESS AND THOLE (2002).

The CFD predictions in Zess and Thole (2002) indicated that the most effective fillet, based on reduction of the horseshoe vortex, resulted in an asymmetric profile (on suction-side) fillet with an elliptical-shaped geometry where the fillet height varied linearly from the vane surface to the endwall, shown in Figure 2.3. The experimental results agreed well with computational data in the leading-edge region where the horseshoe vortex was eliminated successfully but did not effectively eliminate the passage vortex further downstream because cross-flow was still present. However, the turbulent kinetic energy levels in those regions were reduced significantly and further validated the effectiveness of this particular fillet. Gregory-Smith and Biesinger (1992) showed that turbulent kinetic energy played a major role in aerodynamic losses, indicative of highly unsteady vortex structures within the turbine blade passages (Radomsky and Thole, 2000). The success of this asymmetric elliptical-shaped fillet in reducing the horseshoe vortex formation near the leading edge may be attributed to its well-defined geometry because the length and height of the fillet extend well into the passage region where the vortex core is located. Thus it is crucial for the leading edge or any modification to target the vortex core in order to reduce the secondary flow structures completely.

Earlier studies by Sauer et al. (2001) investigated both numerically and experimentally a series of leading-edge bulbs inside a low-speed cascade wind tunnel. The total pressure losses experienced at the exit of the cascade were measured with pitot probes as well as five-hole probes to determine the exit flow angles. The leading-edge bulbs increased the thickness around the leading-edge endwall region, where more attention was given to the suction side. This was believed to intensify the suction-side leg horseshoe vortex, which would be used to counteract the formation of the passage vortex due to the opposite sense of rotation in the passage. The most effective leading-edge bulb design resulted in a more pronounced suction side because it was able to reduce the endwall losses by approximately 50%, with numerical results in good agreement. The experimental data showed that the intensified suction-side horseshoe vortex was able to move the passage vortex away from the endwall as well as reduce its strength and size significantly. The resultant exit flow angles were also shown to improve in uniformity with the addition of the leading-edge bulb.

The leading-edge fillet design was explored further by Mahmood et al. (2005) with key objectives in reduction of secondary flow structures as well as heat transfer along the endwall of the blade passage. Experimental details of the flow structure through smoke-wire visualisation techniques as well as quantitative measurements with a five-hole probe provided insight into the evaluation of four different leading-edge fillets, shown in Figure 2.4, along with endwall heat transfer. The design of the fillets followed an asymmetrical elliptical leading-edge profile with a larger length on the suction side, similar to that investigated by others. The key differences were the manner in which the fillet profile was blended into the endwall and blade surfaces. The underlying effects of the fillets proved successful in reducing the leading-edge horseshoe vortex, where streamwise

vorticity and velocity fluctuations were reduced significantly. The fillets were only effective between the leading edge and throat region because further downstream the effects of the passage vortex system were still present due to the cross-flow and pitchwise pressure gradients. These results were confirmed near the endwall downstream of the throat by increased turbulence intensity. The total pressure loss coefficients measured downstream of the trailing edge showed no significant changes with the addition of the fillets, indicating that their effects were not felt throughout the blade passage. Overall, the most effective fillet could not be identified because all designs gave similar outcomes but the fillets with smoother profile transitioning into the endwall and blade simultaneously showed best improvements in reducing the secondary flow structures. Hence the design of an effective fillet should follow smooth transition towards the endwall and blade surfaces. Furthermore, an important factor in the successful reduction in secondary flow structures with leading-edge modification will be to improve the fillet design along the pressure side to resolve the cross-flow and pitchwise pressure gradient. Mahmood and Acharya (2007) continued experimental investigations with two leading-edge fillets by documenting the resultant secondary flow structure throughout the turbine vane passage. Both fillets were able to reduce the size and strength of the leading-edge horseshoe vortex with reduced total pressure loss coefficients and the flow angle deviations throughout the passage. The passage vortex also was reduced in size and strength with the addition of the fillets.

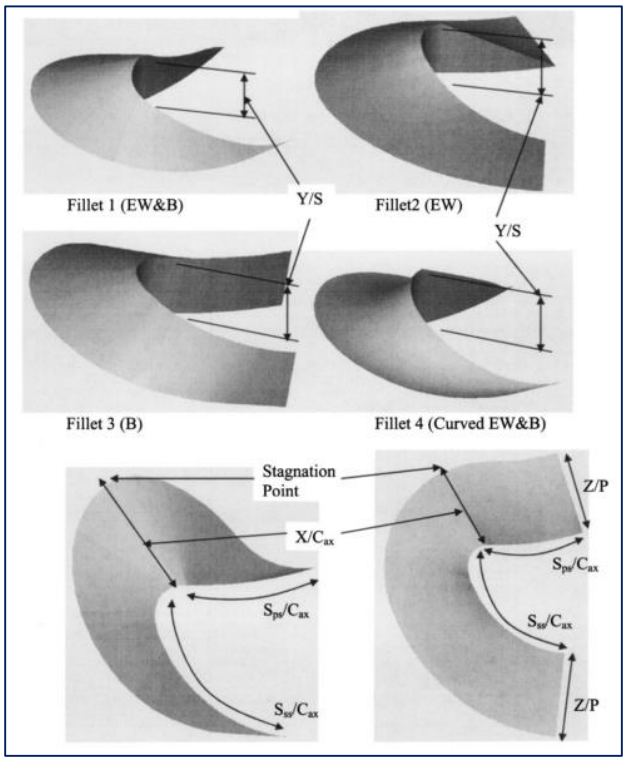

FIGURE 2.4 LEADING-EDGE FILLET PROFILES INVESTIGATED BY MAHMOOD ET AL. (2005) AND MAHMOOD AND ACHARYA (2007)

Lethander et al. (2003) conducted a CFD optimisation study to minimise the size and shape of the fillet, which would result in overall reduction in the adiabatic temperatures of the endwall, vane and fillet surfaces. The result of the converged solution led to an increased fillet size, which was larger in height and extended all around the vane on both suction and pressure sides. The optimised fillet was successful in eliminating the horseshoe vortex at the leading edge as well as delaying the formation of the passage vortex in the throat region. However, the cross-passage flow still remained as the optimised fillet resulted in a net increase of 1.6% in total pressure losses; but the overall heat transfer effects were seen to outweigh these aerodynamic losses as the reduction of surface temperatures on the pressure-side fillet increased by 10.5% and maximum reduction on the endwall and fillet was more than 7.5%. The optimised fillet eliminated the horseshoe vortex at the leading edge and therefore increased film-cooling effectiveness inside the turbine blade passage. Hence the impact of leading modification not only has potential to decrease aerodynamic losses but can be beneficial to a film-cooling configuration as well.

Shih and Lin (2003) conducted a CFD study where secondary flows could be harnessed to decrease the aerodynamic losses and surface heat transfer inside the nozzle guide vane of a turbine. Simulations were done with two different leading-edge fillets both of round shape and with the effects of inlet swirl. The two leading-edge fillets differed in that one fillet was designed to blend smoothly into the airfoil while the other faded into the endwall in a similar manner. The results obtained from the introduction of the fillets showed that the change in total stagnation pressure across the stage was reduced by as much as 44% with minimal increase in mass flow rate in the passage. The surface heat transfer was also improved with reductions of up to 37% on both the airfoil and endwall surfaces. Therefore, they concluded that the overall aerodynamic losses and heat transfer rates suffered in the turbine passage are not dominated by secondary flows alone. The improved effects were believed to be a direct result of the increased stagnation region at the leading-edge endwall region where the turbulence intensity was reduced because the flow speeds were lower here.

The use of the leading-edge fillet within the turbine vane/blade passage has shown to improve the aerodynamic performance in certain areas of the blade passage, most notably at the leading edge. The design and geometry of the leading-edge fillet was mainly based on the leading-edge region geometry and inlet conditions of the vane passage. Further into the passage, the resultant pitchwise pressure gradient which drives the cross-flow is also another major design point of the fillet shape as there exists potential for the leading-edge modification to extend further along the vane endwall to resolve these areas, particularly on the pressure side. These aspects will form part of the experimental investigation directed towards the leading-edge fillet design.

It is important to note that the development of the leading-edge fillet can be applied to all regions of turbine stages (stator or rotor stage), research efforts have also been directed towards the

possibility of endwall contouring inside the passage to improve aerodynamic losses along the endwall. Although endwall contouring will not be investigated experimentally in this study, it is important to review its contributions in the improvement of turbine aerodynamic performance. These aspects will be discussed in the section under film-cooling.

2.3 Film-cooling

Gas turbine efficiency is highly dependent on the combustion process to increase the fluid temperature to its maximum for entry into the turbine stage. However, with increased temperatures comes the issue of heat transfer and thermal stresses placed on the surfaces of the turbine passages as the hot gas passes through, the materials of the turbine blade and endwall are limited to temperatures which are well exceeded by the combustion gases that enter and therefore require adequate heat management in the form of cooling.

Film-cooling has been introduced by supplying coolant through the endwall and vane surfaces to provide a layer of protection between the hot gases in the mainstream flow and the relevant surfaces. Coolant is supplied through the discrete holes or slot configurations. Film-cooling can be sourced from the compressor stage without adversely impacting on the turbine design. However, design considerations must be made to limit the compressor supply in order to maintain turbine performance while improving the effectiveness of the film-cooling configuration. The film-cooling effectiveness is also impacted by secondary flows whereby the injected coolant may become entrained by the vortex flows and therefore do not provide sufficient cooling in certain areas. Hence it is highly desirable to design the film-cooling configuration where it will provide most effectiveness with minimal coolant supply. Furthermore, film-cooling studies have also aimed to deal with secondary flows with the injection of coolant in strategic locations and momentum.

The film-cooling effectiveness inside a low-speed linear turbine cascade was assessed by Friedrichs et al. (1995) using an ammonia and diazo technique to quantify measurements. The coolant air was ejected from a plenum chamber through 43 holes on the endwall configured by four pitchwise rows along the passage. The first row was located upstream of the leading edge while the next two rows were found between the throat region and the last row was placed near the trailing edge. It was found that film-cooling coverage was ineffective near the separation point of the endwall boundary layer where the secondary flow is forming into the horseshoe vortex. The film coverage improved when coolant was ejected away from the separation point, which moved slightly downstream and the cross-flow was seen to enhance the lateral coverage on the pressure side at the endwall. The effect of the film-cooling row located near the trailing edge was seen to reduce the cross-flow because the pressure gradient was overcome by the addition of coolant flow towards the pressure side. Hence it could be seen that the film-cooling resolved both heat transfer and secondary flows in special cases.

The aerodynamic losses were resolved further by Friedrichs et al. (1997) on the same film-cooling configuration. The flow field measurements were resolved using a five-hole probe and pitot probe at a location downstream of the trailing edge where the total pressure contours and secondary flow vectors were measured. The losses were divided into three categories based on entropy generation: the losses generated within the coolant hole, the losses generated due to mixing of coolant with mainstream flow and the losses generated due to the flow within the passage as it was affected by coolant injection (secondary flow). Overall, the losses increased with the coolant flow rate but when the streamwise components of the coolant flow and free-stream flow were equalled, they resulted in an optimum coolant supply pressure, which minimised losses in the passage. When the coolant flow rate was increased, large losses appeared and were attributed to the flow characteristics near the hole as the coolant lifted off the surface and therefore did not mix with the endwall boundary layer effectively. The greatest source of loss was associated with the coolant holes and it was seen that coolant ejection into regions of low static pressure resulted in increased loss per unit coolant mass flow. By ejecting coolant further upstream from the leading edge, it was seen that the three-dimensional separation lines were delayed resulting in reduced secondary formation in the passage. This caused the leading-edge vortex core to remain closer to the endwall and thereby a more uniform flow field left the blade passage. Therefore, both negative and positive effects arose from increasing coolant mass flow into the passage.

Friedrichs et al. (1999) further attempted to improve the endwall film-cooling configuration by improving the coolant coverage in regions downstream of the three-dimensional separation lines. It was seen previously (1995, 1997) that the coolant ejection upstream of the three-dimensional separation lines proved ineffective because the secondary flow structures caused the coolant to be entrained in the lift-off lines of the passage vortex. Hence they proposed a new configuration on the endwall of the same test facility used previously, shown in Figure 2.5. The improved design was accomplished through CFD predictions of the endwall surface pressure field, without film-cooling, which determined the strategic locations of film-cooling hole placement. The idea was to employ coolant coverage based on the streamline trajectories along the endwall and the influence of coolant momentum into the passage flow field. The endwall was divided into several regions for individual coolant hole placement based on the static pressure field to achieve local cooling in specific areas. The first region was identified as the area between the leading edge and the lift-off lines of the passage vortex, i.e. separation lines. The second region was between the blade pressure side and halfway towards the separation line in the passage, where the main passage vortex migrated and the surface flow followed the inviscid streamlines in this region. The third region was between the separation line and the remaining area towards the second region. Here, the streamlines tended to turn towards the blade suction side due to strong cross-flow. Lastly, the blade suction-side endwall corner was also identified but the film-cooling effectiveness was rather low due to the presence of a corner vortex.

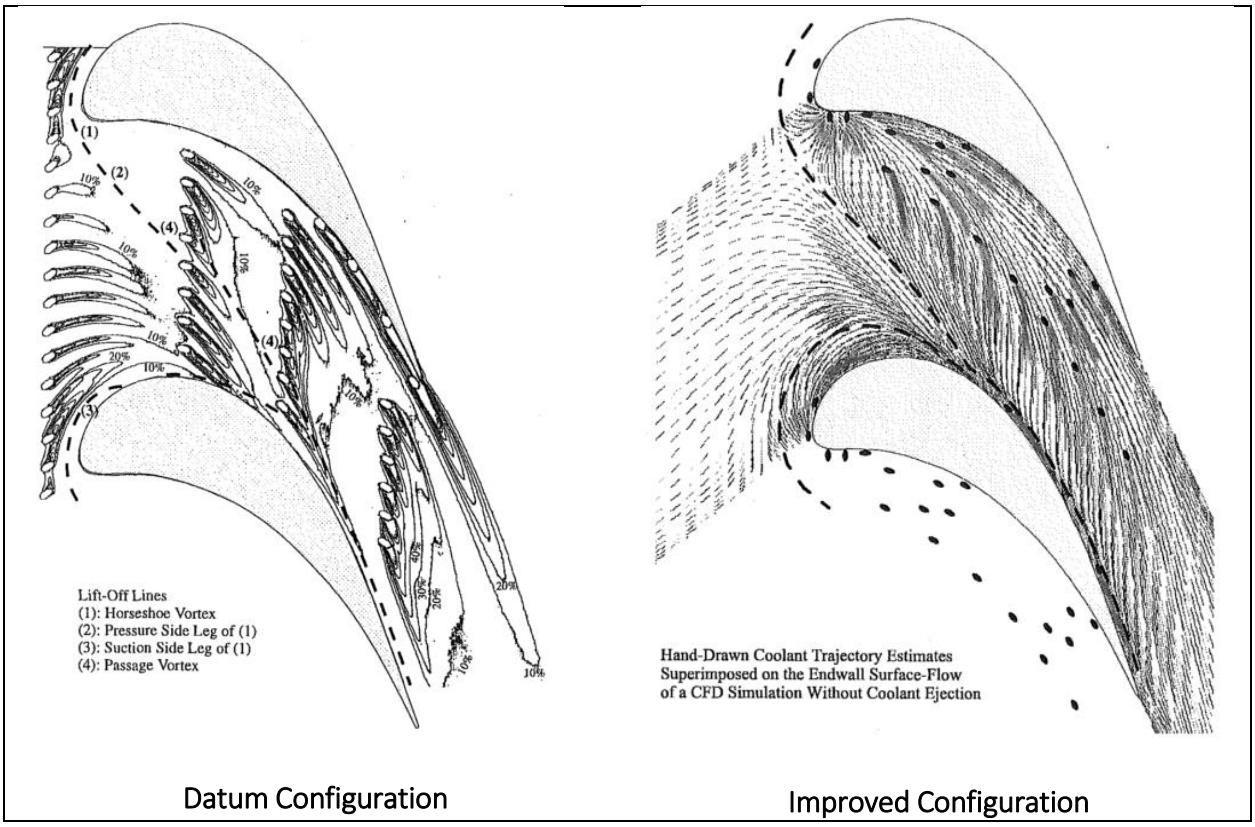

FIGURE 2.5 FILM-COOLING CONFIGURATIONS INVESTIGATED BY FRIEDRICHS ET AL. (1999).

Overall, the film-cooling effectiveness was increased because more coverage was obtained with the improved configuration when compared with the original configuration of holes located downstream of the separation lines. It was seen that the case of the lower inlet blowing ratio increased the film-cooling effectiveness by over 50% with the improved configuration. The aerodynamic losses incurred were also less than for the old configuration while the coolant consumption was maintained as desired. It was also noted that the secondary flow structures were unaffected by the improved cooling configuration as the total pressure contours showed no differences when compared. Therefore, it was concluded that the film-cooling configuration of the endwall region could be improved.

Most film-cooling investigations have been based on the injection of coolant in the same direction as the mainstream flow, the streamwise direction. However, a few studies have turned their focus on the effect of varying this injection. Lateral injection of film-cooling was investigated by Kaszeta et al. (1998), in which the film-cooling holes injected coolant perpendicular to the streamwise flow direction (pressure-side to suction-side orientation). They conducted experimental investigations at high turbulence, with two injection plates for streamwise and lateral coolant ejection. The streamwise injection plate consisted of a column of 12 equally spaced holes whereas the lateral injection plate had eight equally spaced holes oriented perpendicular to the streamwise. The lateral injection case was seen to increase coverage of coolant in comparison with the streamwise

injection. The streamwise injection showed the typical formation of “kidney” vortices which appear between the holes but the lateral injection shows major improvement in coolant coverage, with a smaller single vortex forming away from each hole. Another important aspect was that coolant blow-off did not occur with lateral injection but was more susceptible with streamwise injection.

Discharge coefficients are a measure of the flow losses through the film-cooling configuration and system as a whole. Many factors influence the discharge coefficients of film-cooling configurations such as the geometrical aspects of the holes, size and length of delivery, the size of the supply plenum as well as the direction at which the coolant enters the holes and turbine passage. These factors were investigated in detail by Burd and Simon (1999) in a high-turbulence wind tunnel that simulated combustor exit turbulence profiles of actual turbines as described by Kaszeta et al. (1998). The discharge coefficient was defined as the fraction of the ideal mass flow rate, which was delivered through the film-cooling holes.

The results of the measurements obtained by Burd and Simon (1999) showed that higher discharge coefficients were achieved with lower length-to-diameter (L/D) ratios. When coolant was supplied in the same direction as the free stream, the discharge coefficients increased and the loss coefficients increased. Lateral injection was also shown to improve losses when higher blowing ratios were investigated. The results of the investigation concluded that film-cooling configurations with shorter delivery lengths provided more coolant mass flow into the free stream thus directly influencing the film-cooling effectiveness and the aerodynamic mixing losses inside the turbine passage.

Gritsch et al. (2001) conducted experimental investigations on the influence of internal and external cross-flows on cylindrical film-cooling holes with varying inclination and orientation angles on the discharge coefficients. The results of the calculated discharge coefficients indicated that there existed a strong dependence on the flow conditions, both external and internal. The effect of hole inclination and orientation angles had a more significant impact as the discharge coefficients were reduced when these parameters were increased due to the losses experienced at the hole entrance. However, in some cases where large inclination and orientation angles were employed, the discharge coefficient was enhanced due to suction of the flow from the hole exit. Hence the film-cooling hole discharge coefficients plays an important role in the design of an effective and efficient film-cooling system. Furthermore, film-cooling hole performance is highly dependent on geometry in combination with the main flow conditions.

In addition to traditional film-cooling, some turbine designs have incorporated leakage flow of coolant between the combustor-turbine interface through an upstream slot, originally to prevent ingestion of hot fluid into these assembly regions. The slot is located further upstream and provides additional coolant flow into the passage to compound the film-cooling areas within the

passage. Knost and Thole (2005) and Thole and Knost (2005) compared two different film-cooling patterns in combination with leakage slot flow on the effects of endwall heat transfer in a linear vane cascade, shown in Figure 2.6. A flush slot was placed a third chord length upstream at an injection angle of 45° relative to the surface, while the holes were injected at 30°. The two film-cooling patterns were designed based on the isovelocity contours on the endwall. The first pattern placed holes along these contours as they would ensure uniform blowing rates and momentum flux ratios across each contour line in the aid of preventing coolant jet lift-off. The second pattern made use of less holes to incorporate a gutter for coolant flow between the joining sections of adjacent blade airfoils. Additionally, holes were also located along isovelocity contours but placed in axially directed lines rather than following the contours. CFD predictions were obtained to estimate coolant trajectories along the endwall based on the local static pressure distribution and streamlines.

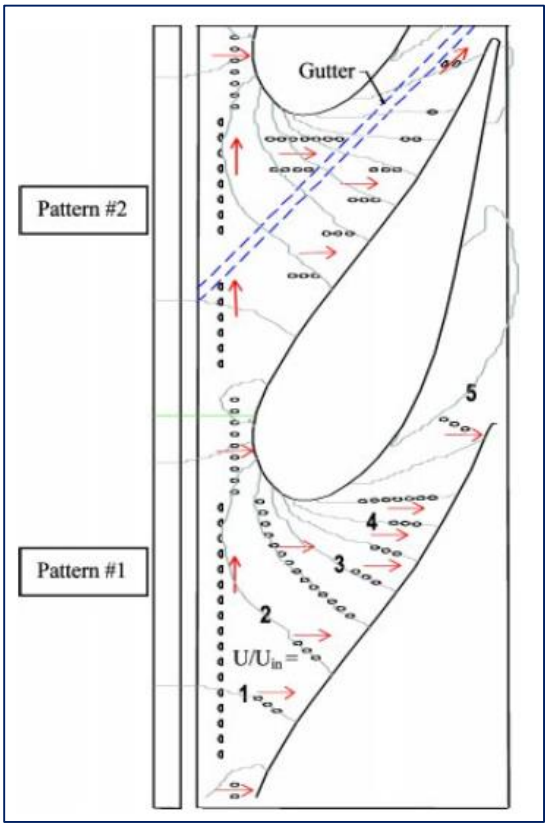

FIGURE 2.6 TWO FILM-COOLING PATTERNS WITH UPSTREAM SLOT SIMULATED BY KNOST AND THOLE (2005) AND THOLE AND KNOST (2005).

The results of the film-cooling patterns without slot flow showed that the first pattern, iso-velocity contours, provided a more uniform coverage at the lower blowing rate while coolant lift-off occurred when the film flow rate was increased, thereby reducing the adiabatic effectiveness. The second pattern showed better film coverage at higher momentum flux ratios at the leading edge

as well as on the pressure side. The high blowing rates near the leading edge resulted in coolant lift-off, which collided with the blade surface and washed back onto the endwall. The higher momentum flux on the pressure side for pattern 2 was able to penetrate further downstream than in the upstream region where lift-off occurred. When both slot film-cooling and hole film-cooling were employed together, it was seen that a large hot streak appeared in the centre of the passage for pattern 2 due to the provision of a gutter and hence less film-cooling holes. Additionally, there was also a large region at the beginning of the passage that was overcooled due to the combined cooling of holes with the slot, and therefore these holes were seen to be ineffective in those locations and could be relocated for better coverage in other areas. Overall, the low slot flow rates resulted in a more uniform exit flow of the passage while the high slot flows enhanced cross-flow along the endwall. The importance of the variation of the streamlines between the endwall region and midspan region must therefore be considered in the design of an effective film-cooling pattern.

Gustafson et al. (2007) investigated the influence of three-dimensional endwall contouring with film-cooling inside a linear blade cascade passage in a pioneering effort to reduce the inherent cross-flows which drive the secondary flow structures in the blade passages. A total of 71 film-cooling holes were strategically placed along the contoured endwall and oriented at 30° relative to the local slope. The orientation and arrangement of the coolant holes were chosen to reduce the pressure losses in the holes while enhancing the coolant coverage from pressure side to suction side. Also, hole locations downstream of the three-dimensional separation lines ensured coolant jets were not swept away from the endwall surface by the passage vortex.

The results obtained by Gustafson et al. (2007) showed key improvements with the introduction of film-cooling flow because the suction-side vortex reduced in strength and at high inlet blowing ratios, the vortex was eliminated successfully. However, the introduction of high momentum coolant jets contributed positive axial vorticity along the endwall and thus enhanced the pressure-side vortex and passage vortex significantly as the endwall boundary layer was energised by the increased kinetic energy of the coolant jets and this was also seen to improve the uniformity of the flow angles near the passage exit. The total pressure losses were seen to increase in the vortex flow regions but reduce near the endwall region due to the high momentum coolant jets. The overall performance of the asymmetrically contoured endwall showed great improvement in the cascade flow field as the passage vortex was reduced and the film-cooling coverage maintained along the endwall thus improving cooling effectiveness.

The experimental investigation by Mahmood et al. (2008) was conducted in a high-speed linear vane cascade with an actual-scale vane geometry. An upstream film-cooling configuration consisted of two rows of cylindrical coolant holes. The first row of holes injected coolant parallel to the vane axial location while the second row injected coolant perpendicular to this direction,

with all holes oriented 30° relative to the endwall surface. The results of the film-cooling effectiveness showed best improvement with high inlet blowing ratios as the high momentum coolant jets penetrated the separation lines and provided coolant coverage near the pressure side, which previously remained uncooled. However, at high coolant momentum, the endwall boundary layer was energised and turned less towards the suction side thus reducing the film-cooling coverage. Overall, the film-cooling effectiveness improved with increased inlet blowing ratios and coolant momentum.

Lynch and Thole (2011) further investigated the effect of the combustor-turbine upstream slot with the midpassage gap presented by the mating of adjacent blade airfoils in the turbine disc assembly. The location of the upstream slot was varied relative to the vane leading edge. The introduction of the midpassage gap showed higher heat transfer rates around the vane endwall as the gap ingested flow near the endwall at the upstream side and ejected the flow downstream near the vane throat region. The computational study further validated the flow behaviour by the gap indicating that a small vortex formed as flow ejected near the throat region and thereby increased heat transfer near the suction side as was observed by the measured endwall. Overall, the increasing of leakage flow rates of both features did not improve the heat transfer along the endwall because the upstream region of the passage would still remain cool by the slot flow while the throat region would experience excessive heat transfer due to the low cooling effectiveness in those regions provided by the gap flow. These were also attributed to the effects of the secondary flow structures because the upstream slot provided effective coverage while the midpassage gap was adversely affected by the secondary flow, which caused the ingestion of flow.

Furthermore, Lynch et al. (2011) conducted computational and experimental investigations into the heat transfer and film-cooling over a non-axisymmetric contoured endwall. Coolant was ejected through five cylindrical holes along the endwall near the pressure side. The choice of this location was based on the high heat transfer rates experienced near the pressure-side endwall region and thus it was expected that the effect of the cross-flows would distribute the coolant over the endwall. The contoured endwall improved the total pressure loss measured in the exit plane of the cascade, which was attributed to the reduction in pitchwise cross-flow in the passage. As a result, the film-cooling coverage suffered because the coolant was not entrained by the reduced cross-flow and so high heat transfer regions were seen on the endwall near the stagnation region and reduced heat transfer at the downstream pressure side, opposite to the case for the flat endwall. The film-cooling effectiveness showed better performance at lower inlet blowing ratio because the higher ratio resulted in coolant jet lift-off. Overall, the contoured endwall reduced the film-cooling effectiveness on the endwall but had significant improvement in reducing the secondary flow structures by weakening the passage cross-flow.

Li et al. (2015) and Li et al. (2016) conducted both numerical and experimental investigations with multiple rows of laterally spaced cylindrical film-cooling holes along a flat vane endwall in a linear vane cascade, shown in Figure 2.7. The results of Li et al. (2015) showed that the first row of film-cooling holes were seen to blow off the surface for all blowing ratios due to the high static pressure located in that region of the endwall. The film flow was then able to reattach to the endwall surface further downstream because the favourable pressure gradient in the passage entrained the coolant and improved the coverage. Increasing blowing ratio increased coverage distance as the effectiveness levels were augmented further into the passage. On the other hand, increasing the blowing ratio resulted in coolant jet structures with a lateral flow direction, which counteracted the cross-flow near the pressure side and thereby increased the film coverage because the passage vortex development was reduced significantly in that area as it was swept from pressure side to suction side by the cross-flow, at low blowing ratio. Overall, the endwall film-cooling was strongly influenced by the secondary flow structures at the near-wall region. It was also evident that the film-cooling flows themselves had a significant impact on the development and formation of the secondary flows, particularly at high coolant momentum at the upstream portion of the passage.

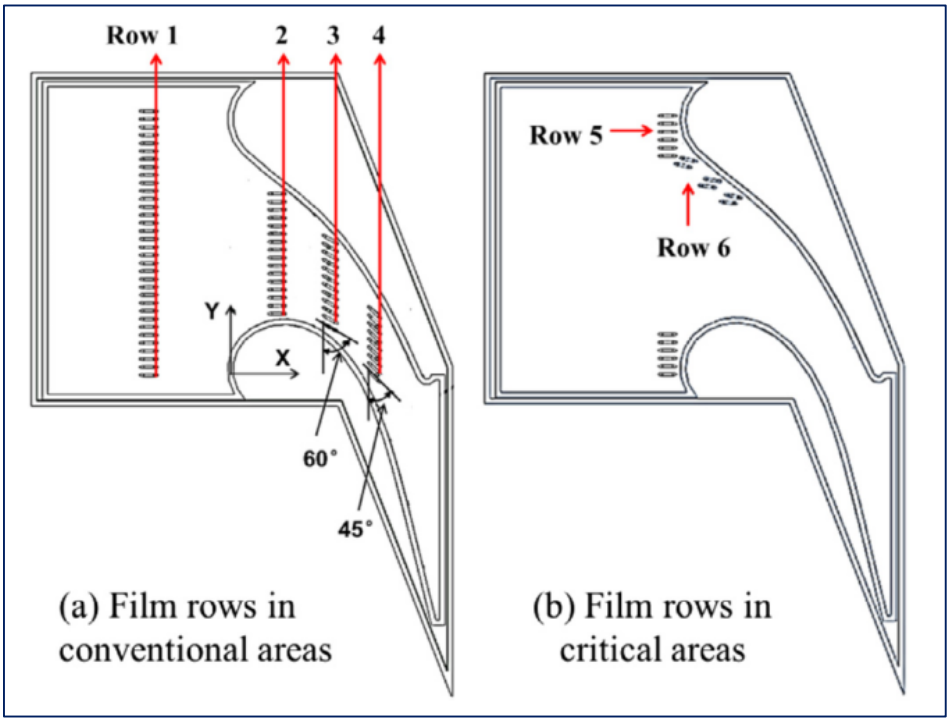

FIGURE 2.7 FILM-COOLING CONFIGURATIONS INVESTIGATED BY LI ET AL. (2015) AND LI ET AL. (2016).

Li et al. (2016) then conducted further investigations with multiple-row film-cooling flows as in the study of 2015 but with interest in the effects of film-cooling row combinations and full-coverage film flow on the vane endwall. Their approach tended to overpredict film-cooling effectiveness in

areas near the film-cooling rows while underprediction occurred further downstream. This was due to the assumption of the superposition method whereby the effects of each film-cooling row did not influence each other and thus the resultant flow field from the upstream rows did not impact on the film-cooling injections from rows which followed downstream.

The research space which has been explored in film-cooling is vast and ever growing with increased numerical investigations being employed to validate performance of different configurations and objectives. The advantages of film-cooling are seen to be two-fold, with the main objective being to improve coolant coverage characteristics along the vane endwall. The second has the potential to improve the flow field inside the vane passage with strong influence on the secondary flow structures in order to reduce aerodynamic losses. Improvement of the flow field will further enhance film-cooling effectiveness, a mutual benefit, as has been concluded by various researchers in this field. Thus, the desire to improve upon past film-cooling configurations is beneficial for all outcomes in the turbine blade passage.

2.4 Summary

A comprehensive review of the literature applicable to this study has been provided to obtain further knowledge of the flow field behaviour within the linear vane cascade passages. The identification and investigation of secondary flow structures with in the blade passage have been documented thoroughly with numerous researchers proposing different models; however, there is strong correlation with the main characteristics of the secondary flow patterns along the vane endwall. These common patterns include the origin and evolution of the leading-edge horseshoe vortex, which splits into the suction-side leg and pressure-side leg vortices as the vortex migrates through the passage. The strong pitchwise pressure gradient then drives the cross-flow in the passage from pressure side to suction side, which is a major driving force of the larger passage vortex forming along the pressure-side endwall. The cross-flow then carries the passage vortex towards the suction side where it entrains the suction-side horseshoe vortex in its migration. The adverse effects of these vortical structures result in increased aerodynamic losses because the inlet boundary layer is entrained by these structures which results in an exit flow field that is far less uniform. Therefore, the consecutive blade rows which follow continue to receive distorted fluid flow, which further reduces performance throughout the turbine stages. The secondary flows thus reduce the total energy of the fluid, which would otherwise contribute to the power production from the turbine stator-rotor rows.

Various researchers have proposed and developed methods to overcome the secondary flow effects either by endwall modification or through aerodynamic control through film-cooling. Endwall modification methods employ leading-edge modifications through fillets and endwall contouring with the aim of reducing the leading-edge horseshoe vortex as well as eliminating the cross-flow in the passage to counteract the passage vortex formation. These methods have been

shown through various research efforts to affect the passage flow field and improve the aerodynamic losses in some areas.

The application of endwall film-cooling is vast because the performance and impact is highly dependent upon the design and configuration of the injection locations. Past research have shown how to impact the secondary flow field through aerodynamic control with film-cooling injection at high momentum as well as decrease the heat transfer along the endwall with strategic placement of the coolant jets. The design and configuration of an effective and efficient film-cooling configuration are greatly influenced by the flow field near the endwall, shown by researchers in this field. Some designs have incorporated full-coverage film-cooling throughout the entire passage with promising results in the film-cooling effectiveness improvements as well as the resultant improvement in aerodynamic losses due to vortical flows. Most investigations have shown that the aerodynamic flow patterns can be improved with high momentum coolant injection, which counteracts the secondary flow structures, but consideration must be given to limiting the coolant supply, which is extracted from the compressor stage.

Film-cooling through an upstream slot of the combustor-turbine interface has been shown to increase the film-cooling effectiveness based on the distance from the leading edge as well as in combination with traditional film-cooling holes. The aerodynamic flow field behaviour which arises with high momentum flow through this slot is yet to be fully examined and forms an integral part of this research study along with a modified slot configuration and geometry.

CHAPTER 3: EXPERIMENTAL DESIGN

A representative model of the turbine blade passages of an actual turbine is required to simulate the characteristic flow conditions and obtain detailed measurements. Furthermore, the influence of the instruments used to obtain experimental data must be kept to a minimum within the flow regions to achieve valid results. The flow conditions of real gas turbine engines are highly three-dimensional (3-D) and complex with high-speed flows, which can be difficult to match in an experimental model. Thus a two-dimensional approach is taken to represent the turbine blade passages in a large-scale linear vane cascade.

The cascade runs under the incompressible flow conditions, but the scaled-up model of the cascade simulates the Reynolds number conditions of the actual turbine blade passage. Past studies have shown that the linear vane-blade cascades have the same three-dimensional flow features as the actual turbine blade passages, i.e. pitchwise pressure gradient, passage vortex, boundary layer separation and reattachment and unsteadiness in the secondary flows (S. L. Dixon, 2010). Because of the effects from the compressibility and radial pressure gradient, the location, size and strength of the secondary flows are different in the actual blade passages from those in the two-dimensional cascade passage. Details of the experimental test facility, supporting equipment, instrumentation and experimental procedures will be provided further on in this chapter.

3.1 Linear vane cascade and wind tunnel

A linear vane cascade is a two-dimensional (2-D) representation of the first-stage stator vane (guide vane) row in an actual turbine. Actual blade airfoils are three-dimensional but for this experimental study only a two-dimensional profile is considered to investigate the flow conditions at the blade-endwall junction. The model assumes periodic flow conditions, which are accomplished by placing several blades in a linear pattern to create the successive passages.

The linear pattern can be seen as a scaled-up section of the stator disc if it were to be placed in a straight line about the circumference. A schematic of the experimental test facility is shown in Figure 3.1. The atmospheric wind tunnel houses the linear vane cascade test section consisting of seven scaled-up 2-D vane airfoil geometries created by extruding the hub-side vane profile of the GE-E^3 first-stage nozzle guide vane (Timko, 1990). The vane profile and other cascade parameters such as the blade span and pitch of the hub side of the actual nozzle guide vane are scaled up six times in the experimental cascade. The geometric parameters for the linear cascade test section are provided in Table 3.1. The test and flow conditions in the cascade are provided in the next chapter.

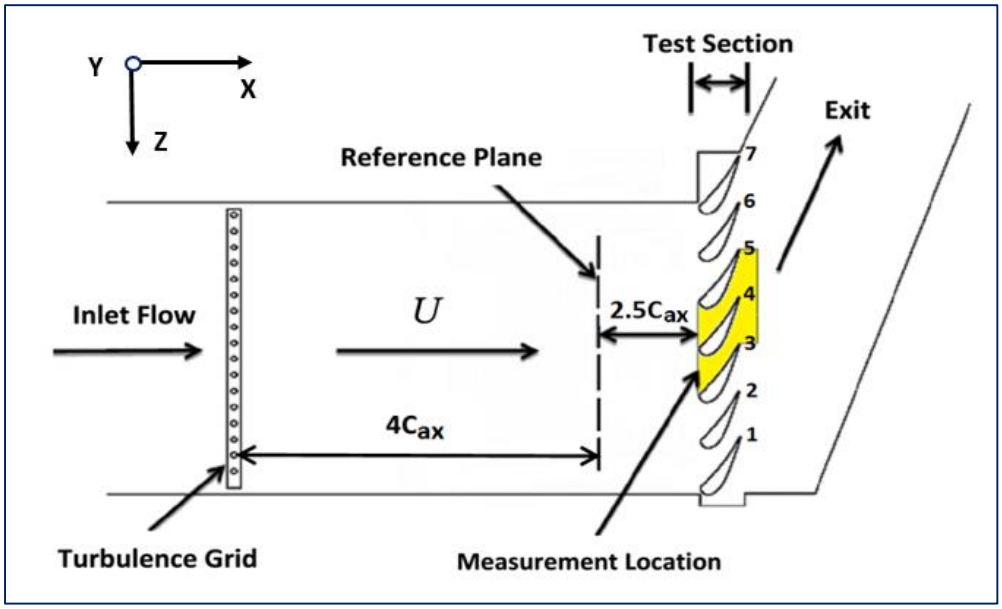

FIGURE 3.1 SCHEMATIC OF LINEAR VANE CASCADE AND WIND TUNNEL.

TABLE 3.1 GEOMETRIC PARAMETERS OF LINEAR VANE CASCADE.

Geometric Parameter	Symbol	Value
Actual chord length [mm]	C	354.5
Axial chord length [mm]	C_{ax}	202.6
Aspect ratio (True chord length to blade span)	C/S	1.479
Solidity ratio (True chord length to blade pitch)	C/P	1.328
Scale factor		6
Flow inlet angle [°]		0
Flow exit angle [°]		74

The cascade test section and the wind tunnel have a rectangular cross-section. The open-circuit wind tunnel is operated under suction of two axial duct fans (7.5 kW and 15 kW) placed in series downstream of the exit. Ambient air is drawn into the wind tunnel through a smooth two-dimensional contraction, which accelerates the flow as it is conditioned through a honeycomb screen at the inlet. A schematic 2-D representation of the wind tunnel upstream of the cascade test section is shown in Figure 3.2. The flow proceeds through the rectangular cross-section and passes through a passive turbulence grid, which generates free-stream turbulence into the cascade inlet flow. The passive turbulence grid consists of 6mm cylindrical metal rods, which span the channel height at $6.5C_{ax}$ upstream of the cascade inlet, spaced 20mm apart over the entire channel. The length of the wind tunnel upstream of the turbulence grid and upstream of the test section (Figure 3.1 and Figure 3.2) provides a smooth and uniform turbulent inlet velocity profile into the cascade inlet. A measuring slot on the top endwall is placed $2.5C_{ax}$ upstream of the cascade

inlet to obtain the reference flow properties with the pitot-static pressure probe, five-hole pressure probe and single wire hot-wire probe.

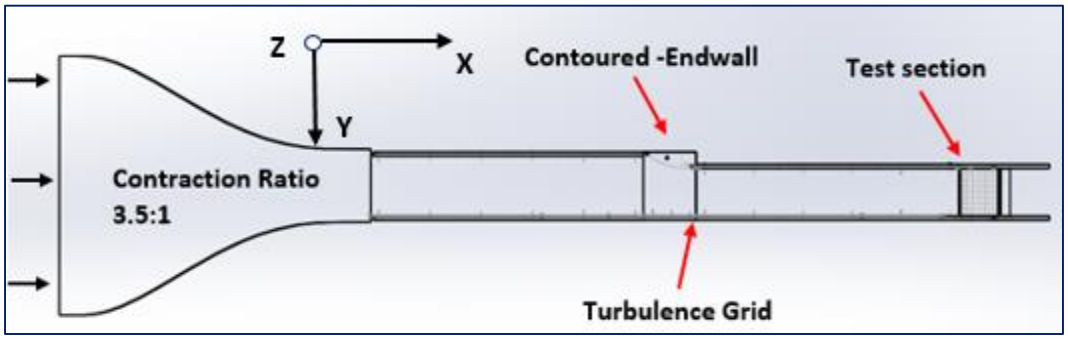

FIGURE 3.2 X-Y PLANE VIEW OF WIND TUNNEL FACILITY.

The contour shapes of the contraction section are cut in two plywood sheets and then are fitted with flexible galvanised sheet metal to form the contraction tunnel of the rectangular cross-section seen in Figure 3.2.The downstream rectangular walls are constructed of 18 mm thick high-density wood supported by wooden ribs on all sides to maintain the inner-channel geometry. The walls of the vane cascade test section are fabricated from 20mm thick high-density clear cast acrylic to provide visibility inside the test section. The main channel, the section just upstream of the cascade test section, has an aspect ratio of 5.2:1, with the channel height taken as the blade span. Downstream of the contraction lies a contoured wall which is designed for endwall contouring measurements as it can be fitted at the leading edge of the cascade on the top endwall. The location of the contoured-endwall is found where the step is seen in Figure 3.2, and is placed here until it is required for experimentation. The vane airfoil geometries are manufactured with polycarbonate material for strength and coated with polyurethane to provide smooth surface finish.

The top endwall of the test section has a removable window instrumented with static pressure taps and with cut-out slots to allow for probe insertion inside the blade passages. The location of the removable window section in the top endwall is shown by the yellow region in Figure 3.1. The bottom endwall allows for film-cooling to be introduced to the cascade test section at the leading edge in the form of a plate that can be interchanged for different film-cooling configurations and geometry. A schematic of the locations of the measurement planes and film-cooling geometry is superimposed in Figure 3.3. The flow field measurements are obtained in the pitchwise normal planes 1-3 with a five-hole pressure probe between blades 3 and 4 for all cases to maintain consistency in the measurements. The global (X_G, Y_G, Z_G) and local (x, y, z) coordinate systems are also defined for the measurement passage in Figure 3.3. The axial locations (X_G/C_{ax}) of the measurement planes also dictate the traversal directions of the probes used for measurement in

the passage. The axial locations in Figure 3.3 are taken from the leading edge stagnation as the origin.

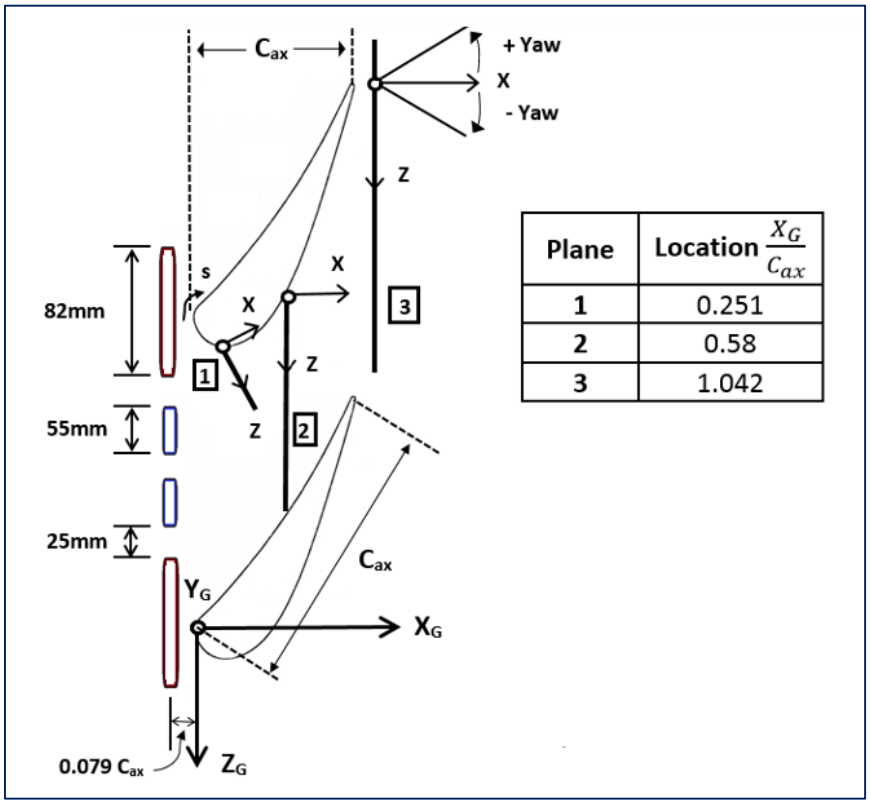

Plane	Location $\frac{X_G}{C_{ax}}$
1	0.251
2	0.58
3	1.042

FIGURE 3.3 COORDINATE SYSTEM AND MEASUREMENT LOCATIONS.

The global coordinate system (X_G, Y_G, Z_G) originates at the stagnation location of the leading edge of blade 3 in Figure 3.3. The local coordinate z at each measurement plane is taken to be aligned with the slot direction in the z-direction. Measurement plane-1 is aligned normal to the suction-side surface at that axial location. The second and third measurement planes (plane-2 and plane-3) are aligned parallel to the global Z-coordinate. Plane-2 extends over the complete pitch distance from pressure to suction side for this axial location, which also falls partly inside the passage throat region. Plane-3 is located just aft of the trailing edge, which covers the pressure and suction sides completely and slightly more than one full pitch distance at the exit of the passage. The measured local velocity components (u, v, w) are then parallel to the local coordinates.

3.2 Instrumentation

3.2.1 Vane static pressure

The three blades (blade 3, 4 and 5 as shown in Figure 3.1) within the test section, where measurements are taken, are fabricated with 21 pressure taps to obtain the pressure distributions

on the blade profiles as indicated in Figure 3.4. The pressure tap holes are 0.3 mm in diameter and located along the midspan location (Y_G/S= 0.5), placed over the blade surface from the suction-side trailing edge to pressure-side trailing edge. The holes are drilled normal to the surface into the hollow core of the blade where they are connected to the flexible plastic tubing and routed through the top endwall to a multiport scanner. The multiport scanner houses three sets of holes on three diametrical positions, as shown in Figure 3.4, which receive the pressure tubes, one set of holes per blade. The scanner then has three output ports on a rotary section connected on its other side that connects to an individual pressure transducer for each blade. Circular movement of the rotary part of the scanner then allows each pressure tap location to be measured. One pressure tap from each blade thus can be scanned at the same time as the rotary part is rotated on the pressure tap connections on the scanner. The blade profile pressure measurements indicate the periodicity of flow through these passages as they match each other and are thus taken first when different test cases are conducted.

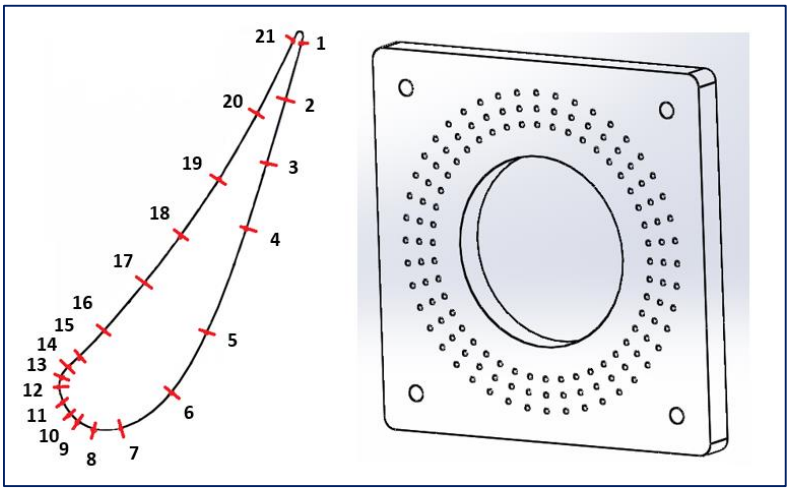

FIGURE 3.4 BLADE PRESSURE TAPS AND MULTIPORT SCANNER HOUSING.

3.2.2 Endwall static pressure

The endwall static pressure is measured on both the top and bottom endwall to provide quantitative results on the surface pressure distributions. Theoretically, both of these endwalls should display identical surface pressure distributions due to the symmetric blade passage about the midspan. Therefore, each endwall is used to measure different test cases for simplicity. The top endwall is employed for high resolution static pressure measurement for the baseline and filleted endwall cases. The bottom endwall is reserved for film-cooling test cases due to the film-cooling supply being located on this side of the cascade. The film-cooling test case is measured with a lower resolution of pressure distribution for comparison purposes. For both of these endwalls, a multiport scanner is designed and fabricated specifically based on the required number of pressure ports needed and is similar to that shown in Figure 3.4. Both of these endwalls,

including the instrumentation window for probe insertion, are manufactured from 10 mm high-density clear cast acrylic with a CNC laser cutter using the CAD drawings.

3.2.2.1 Top endwall

The replaceable section in the top endwall is replaced by a similar shaped static pressure window. This window consists of various window panels that are interchangeable so that their location can be varied. The locations and geometry of the window panels are marked as A.1-A.4, C.1-C.5 and B.1 for three different shapes in Figure 3.5. The panels marked as "A" are interchangeable as are the "C" panels based on their shapes. This is chosen to employ a single panel fabricated with the pressure tap holes of 1.5 mm diameter and 10 mm spacing in x-z directions, which can be swapped around with the other window panels of similar geometry to simplify measurements and cost. The blank panels aid to seal the passage while measurements are taken only at the panel with the pressure taps. Thus the entire region of the top endwall between blade 3 and blade 4 is covered for pressure distribution measurements. The design of the window is shown in Figure 3.5 with the assigned panels. Figure 3.5 also shows the dimensions of the window panels with the locations of the pressure taps.

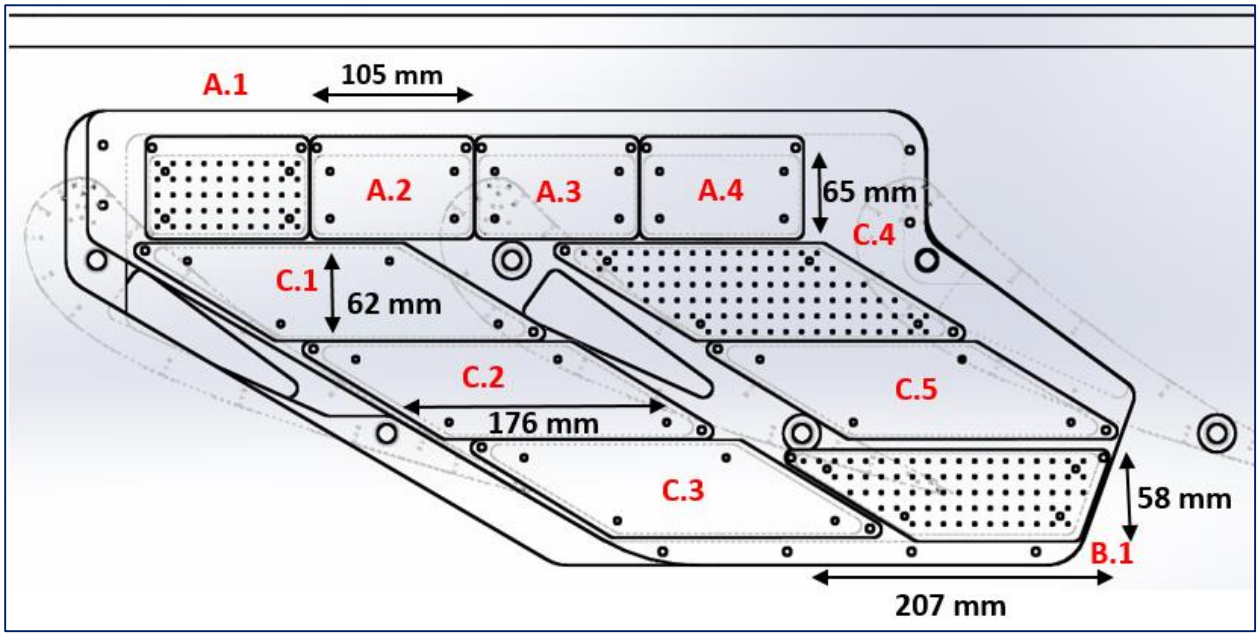

FIGURE 3.5 TOP ENDWALL STATIC PRESSURE WINDOW.

Each of the three panels in Figure 3.5 with the pressure tap holes, are connected to a three-channel multiport scanner with flexible PVC tubing and then to three pressure transducers as described earlier. The panels near the leading edge are rectangular with 50 pressure tap holes, which measure the surfaces denoted by A.1 – A.4. The single panel B.1 is unique because of the shape of the window in that area and houses 76 pressure tap holes for measurement in the trailing-edge region on both sides of blade 4. The parallelogram panels (C.1 – C.5) cover most of

the regions in between the blade 3 and 4 passage, and the "C" panel houses 97 pressure tap holes. Details of the pressure tap coordinates are provided in Appendix D.

3.2.2.2 Bottom endwall

The bottom endwall is manufactured with less pressure tap holes to measure the induced effects of the film-cooling on the endwall pressure distributions. The locations of the bottom endwall pressure taps are shown in Figure 3.6. The bottom endwall is modified to accommodate the instrumented section by splitting the original wall into three sections. The middle section forms part of the test section where the pressure tap holes are located. There are 48 pressure tap holes of 1.6 mm diameter spread across the passage endwall between blades 3 and 4 with non-uniform spacing. The pressure taps are connected by the flexible plastic tubing to the multiport scanner and then to a pressure transducer. The tubes from the endwall are then routed through the hollow blade cores to the other side where the multiport scanner and pressure transducers are located. The details of the pressure tap coordinates of this endwall are also provided in Appendix D.

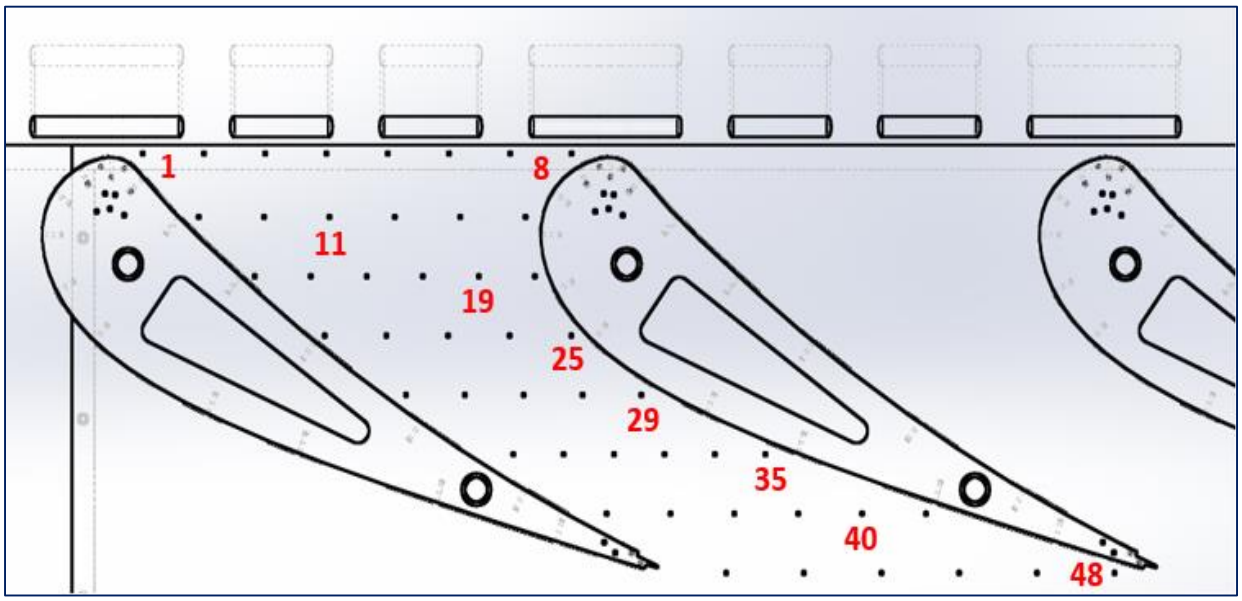

FIGURE 3.6 BOTTOM ENDWALL STATIC PRESSURE PORTS.

The endwall static pressure, as well as blade surface pressure, are evaluated and compared by normalising this pressure with the reference pressure measured upstream of the test section. The coefficient of static pressure provides a measure of the change in pressure on the endwall and indicates the change in fluid speed as it progresses through the blade passages and surfaces. The coefficient of static pressure is defined below:

Coefficient of static pressure:
$$C_{P,s} = \frac{P_{s,local} - P_{s,ref}}{\frac{1}{2}\rho {U_{ref}}^2} = \frac{P_{s,local} - P_{s,ref}}{P_{t,ref} - P_{s,ref}} \quad (3.1)$$

3.2.3 Reference plane

The reference plane is located $2.5C_{ax}$ upstream of the cascade inlet shown in Figure 3.1. This measurement plane is used to obtain properties such as the inlet pressure conditions (static and total), temperature and turbulence intensity with the relevant probes mentioned earlier. The inlet boundary layer is measured at this location with the five-hole pressure probe as well to determine the inlet velocity conditions for the cascade. These measurements are important as they are used to evaluate the experimental results in order to normalise the measured data and results for comparability with published literature. The reference properties will also indicate whether the test conditions of the cascade can be matched to the Reynolds number of actual turbine flow conditions. The reference properties are provided in the next chapter.

3.2.4 Five-hole probe

A miniature five-hole pressure probe is used to measure the velocity field and pressure field inside the blade passage at the indicated measurement planes described previously. The five-hole probe is able to determine the three components of velocity (u, v, w) and the total andstatic pressures in a spatial field based on the methods and procedures described by Ligrani et al. (1989a) and Ligrani et al. (1989b). The local velocity components are determined by the calibrated pitch and yaw angles of the measured flow field. A cobra-head five-hole pressure probe manufactured by Aeroprobe™ is used to obtain the flow field measurements with the aid of a motorised two-axis traverse system. The geometry and arrangement of the five-hole probe are shown Figure 3.7.

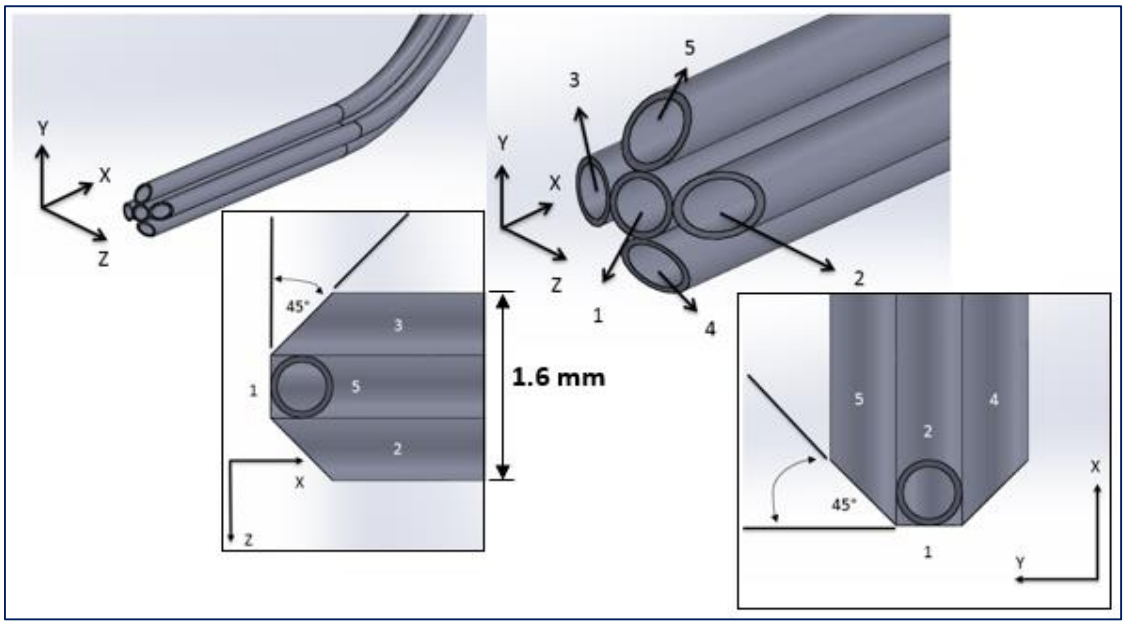

FIGURE 3.7 FIVE-HOLE PROBE GEOMETRY AND ARRANGEMENT.

The probe consists of five identical stainless steel tubes of 0.5 mm inside diameter and a total tip diameter of 1.6 mm. The probe tip is arranged with the central tube opening normal to the tube axis denoted as port 1. The central tube is surrounded by four tubes at 90 degree angular pitch. Two of these tubes (port 4 and port 5) are arranged in the vertical plane (pitch plane), as shown in Figure 3.7. The other two tubes (port 2 and port 3) are then arranged in the horizontal plane (yaw plane). These side tubes are trimmed at 45° at the tip relative to the central tube (port 1) axis. The cobra-head allows the probe to read five pressures without the influence of the probe arm near the tip and has an arm length of 35 cm, which is capable of measuring the full span of the passage if necessary. The individual steel tubes extrude at the end of the probe arm, which can then be connected to five pressure transducers via flexible plastic tubing to obtain measurement from separate pressure transducers.

The five-hole probe is calibrated in the same wind tunnel housing the cascade using a cut-out slot in the top wall of the tunnel upstream of the passive turbulence grid with the use of a calibrator rig. The calibration slot is aligned parallel to the streamwise direction as opposed to the reference measurement plane, which is perpendicular. This alignment allows the calibrator rig to rotate the five-hole probe about its tip in the x-y plane for pitch angle calibration and in the z-x plane for yaw angle calibration, as indicated in Figure 3.8. The chosen calibration range for both pitch and yaw angle is -25° to +25° at a streamwise x-velocity of 10 m/s and is provided in Appendix B. This provides a total of 121 calibration points with 11 pitch and 11 yaw angles.

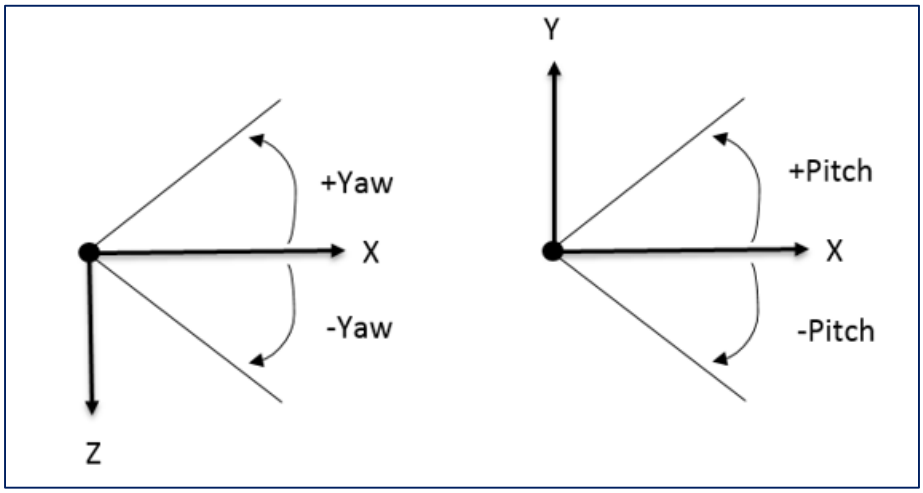

FIGURE 3.8 PITCH AND YAW ANGLE NOTATION.

The calibration rig, shown in Figure 3.9, provides the two-axis rotation with the calibrated angle increments provided on the instrument. During calibration, the probe is manually fixed at a known yaw angle and then rotated through the pitch range. The reference total and static pressures are also measured at the calibration location simultaneously with a pitot-static pressure probe to

determine the pressure coefficients. The pressure coefficients are described according to Ligrani et al. (1989a).

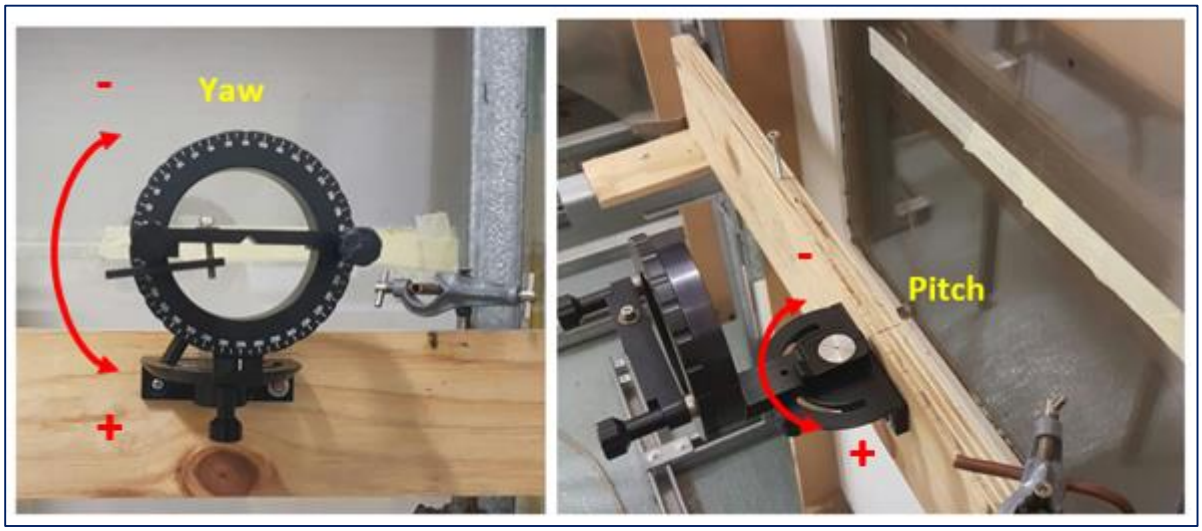

FIGURE 3.9 FIVE-HOLE PROBE CALIBRATION RIG.

Yaw coefficient:
$$C_{py} = \frac{P_2 - P_3}{P_1 - \bar{P}} \quad (3.2)$$

Pitch coefficient
$$C_{pp} = \frac{P_4 - P_5}{P_1 - \bar{P}} \quad (3.3)$$

Total pressure coefficient:
$$C_{pt} = \frac{P_{t,ref} - \bar{P}}{P_1 - \bar{P}} \quad (3.4)$$

Total-static pressure coefficient
$$C_{pts} = \frac{P_{t,ref} - P_{s,ref}}{P_1 - \bar{P}} \quad (3.5)$$

Average pressure:
$$\bar{P} = \frac{P_2 + P_3 + P_4 + P_5}{4} \quad (3.6)$$

The numbered subscripts indicate which tube is measured as well as the reference values used for the total and static pressures. The voltage signals from the pressure transducers connected to the tubes are digitised in a National Instrument data acquisition system and recorded on a computer. The voltages are then converted to the pressure unit employing the pre-calibrations of the transducers. Details of the data acquisitions are provided later. When the probe is employed for measurements in the cascade test section, it uses the same pressure transducer and connection arrangements as the calibration run. During the measurements, a single in-house Labview™ program acquires the data from the pressure transducers and traverses the probe in the

measurement plane. After data acquisition is completed for a given measurement plane and test case, post-processing is done. The first step performs a pressure correction to account for the spatial differences between each hole on the probe, because they are close together. The pitch and yaw angles are then determined as described above by employing the calibration data to interpolate between the measured coefficients and calibration coefficients. Thereafter, the pressures and velocities can be determined similarly via interpolation from the calibration data. Lastly, a downwash velocity correction is performed to account for the streamline curvature near the probe tip due to its finite dimensions and flow blockage. The one-dimensional downwash corrections are applied based on the procedure described in Ligrani et al. (1989b). Thereafter, the deduced total pressure at a measurement location is used to determine the total pressure loss coefficient:

Total pressure loss coefficient:

$$C_{Pt,Loss} = \frac{P_{t,ref} - P_{t,local}}{\frac{1}{2}\rho {U_{ref}}^2} = \frac{P_{t,ref} - P_{t,local}}{P_{t,ref} - P_{s,ref}} \tag{3.7}$$

The total pressure loss coefficient provides a measure of the aerodynamic loss caused by the secondary flow structures, which influence the passage flow field. During data acquisition, the probe tip is maintained at a constant distance from the endwall to obtain suitable measurements, because the probe tip provides blockage and may influence the flow field in the near-wall region. Because the probe tip is 1.6 mm in diameter, a spacing of 2 mm from the endwall is adhered to for all five-hole probe measurements to achieve quality spatial resolution near the endwall region. To further ensure experimental accuracy, the probe tip is oriented in the mean streamwise direction at each measurement plane to reduce the flow yaw angle corrections.

The local velocity components (u, v, w) computed from the five-hole probe pressures are then used to determine the vorticity distribution perpendicular to the measurement plane. The vorticity is defined below:

Vorticity vector field:

$$\hat{\omega} = \hat{\imath}\left(\frac{\partial w}{\partial y} - \frac{\partial v}{\partial z}\right) \tag{3.8}$$

Because the spatial measurements are taken in the y-z plane, the partial derivatives of the velocity components (v, w) can be obtained to compute only the ω_x component (normal to the plane) of the vorticity vector.

Axial vorticity magnitude:

$$\omega_x = \frac{\partial w}{\partial y} - \frac{\partial v}{\partial z} \tag{3.9}$$

To compute the derivative $\frac{\partial w}{\partial y}$ at a given location (y, z), a spline curve is fitted through all the w-velocity vectors at the constant z-location and then the slope of the spline is determined at the (y,

z) location. Similarly, the derivative $\frac{\partial v}{\partial z}$ at a given (y, z) location is computed fitting another spline through the v vectors at the constant y-location.

The unit of vorticity is 1/s and therefore the normalisation of this quantity is determined from the blade chord length (true) and free-stream velocity:

Normalised axial vorticity: $$\frac{\omega_x C}{U_{ref}} \quad (3.10)$$

The normalised axial vorticity provides a measure of the rotation in the velocity field due to the secondary flow structures.

3.2.5 Hot-wire anemometry

A constant temperature hot-wire anemometry (CTA) system manufactured by Dantec Dynamics™ is used to determine the inlet turbulence conditions to the cascade passages. The CTA principle is based on convective heat transfer from a heated sensor to the surrounding fluid, which is directly related to the fluid velocity (Jorgensen, 2004). The sensor wires are fine enough to measure velocity fluctuations and frequencies in the fluid flow, with high temporal resolution. The CTA measurements are obtained in the reference plane to quantify the homogeneity and increase in the turbulence intensity due to the presence of the turbulence rods upstream. No other measurements are obtained in the cascade passage with the CTA system.

The CTA system is used with a two-wire probe along with the manufacturer software to measure the streamwise velocity fluctuations and boundary layer thickness at the reference location upstream of the cascade inlet. The probe is mounted on the same two-axis traverse used for five-hole probe measurements, to scan a 2-D section in the reference plane. The CTA software allows a traversal measurement process to be controlled with data acquisition accordingly.

The probe is chosen based on the application and fluid medium (air) as well as the measurement requirements. Because the turbulence intensity is measured upstream of the cascade inlet, the velocity fluctuations in that plane must be determined as well as the directional velocities in the axial direction and perpendicular to the probe. A dual sensor X-probe is chosen to measure the two velocity components and is calibrated with a dedicated probe calibrator, which is supplied with compressed air. The calibrator and calibration software are also part of the Dantec Dynamics™ system. The calibration procedure is used to quantify the velocity range and direction (pitch and yaw angle) to be expected during measurement. Thus, the reference plane is fairly uniform in flow angle and the free-stream velocity is constant and as such the calibration is simplified to these requirements.

During data acquisition, 36 spatial coordinates are measured in a rectangular grid in the inviscid region at the reference location (Y-Z plane). Each point is recorded with a frequency of 20 kHz and 40 000 samples for both channels (u- and v-velocity). The CTA software is automated to record each measurement location specified by an input file with these coordinates. A separate file for each measured point is then written in which the time and velocity components are recorded. Temperature is monitored during data acquisition because the CTA is only applicable at constant temperature, at the same location plane as the measurements. During post-processing, each coordinate file is then analysed by spectral analysis to determine the necessary filtering for noise reduction. The CTA signal conditioner provides some filtering but further steps are taken to reduce the noise.

The improved signal is shown with the original data set for u-velocity in Figure 3.10. The u-velocity now falls in the measured range confirmed by the pitot-static probe.

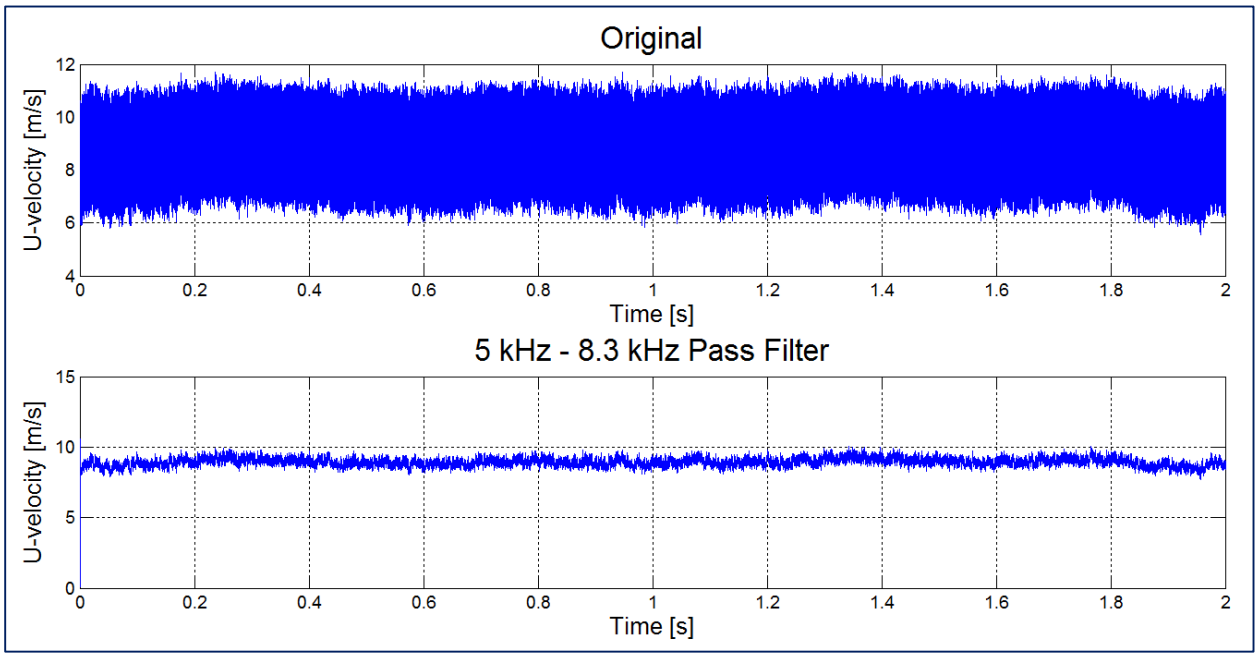

FIGURE 3.10 FILTERED CTA SIGNAL FOR A GIVEN MEASUREMENT POINT.

The CTA signal is then analysed in the amplitude domain to determine the mean u-velocity, standard deviation of u-velocity and turbulence intensity.

Mean velocity: $$\overline{U} = \frac{1}{N}\sum_{N}^{i} u_i \qquad (3.11)$$

Standard deviation:
$$U_{rms} = \left(\frac{1}{N-1} \sum_{N}^{i} (u_i - \bar{U})^2 \right)^{1/2} \quad (3.12)$$

Turbulence intensity:
$$TI\ \% = \frac{U_{rms}}{\bar{U}} \times 100 \quad (3.13)$$

3.3 Fillet design

The modification of the leading-edge endwall junction to reduce the secondary flow structures has been investigated by many researchers with varying fillet designs, all of which are highly dependent on the inlet flow conditions. The same approach is undertaken in the design of the present fillet employed as those presented by Lethander et al. (2003), Mahmood et al. (2005), Sauer et al. (2001), Shih and Lin (2003) and Zess and Thole (2002). The most effective leading-edge fillets were seen to extend at least two boundary layer thicknesses upstream of the blade stagnation point and one boundary layer thickness in height along the span of the blade leading edge. The axial distance to which the fillet extends along the passage is arbitrary and is therefore chosen for this investigation. Only one fillet design is considered for the present study and is given in Figure 3.11 along with defining geometric parameters. Some computational studies in the commercial CFD code Star CCM+ were conducted to determine the final design of the fillet that shows some promise in affecting the secondary flows.

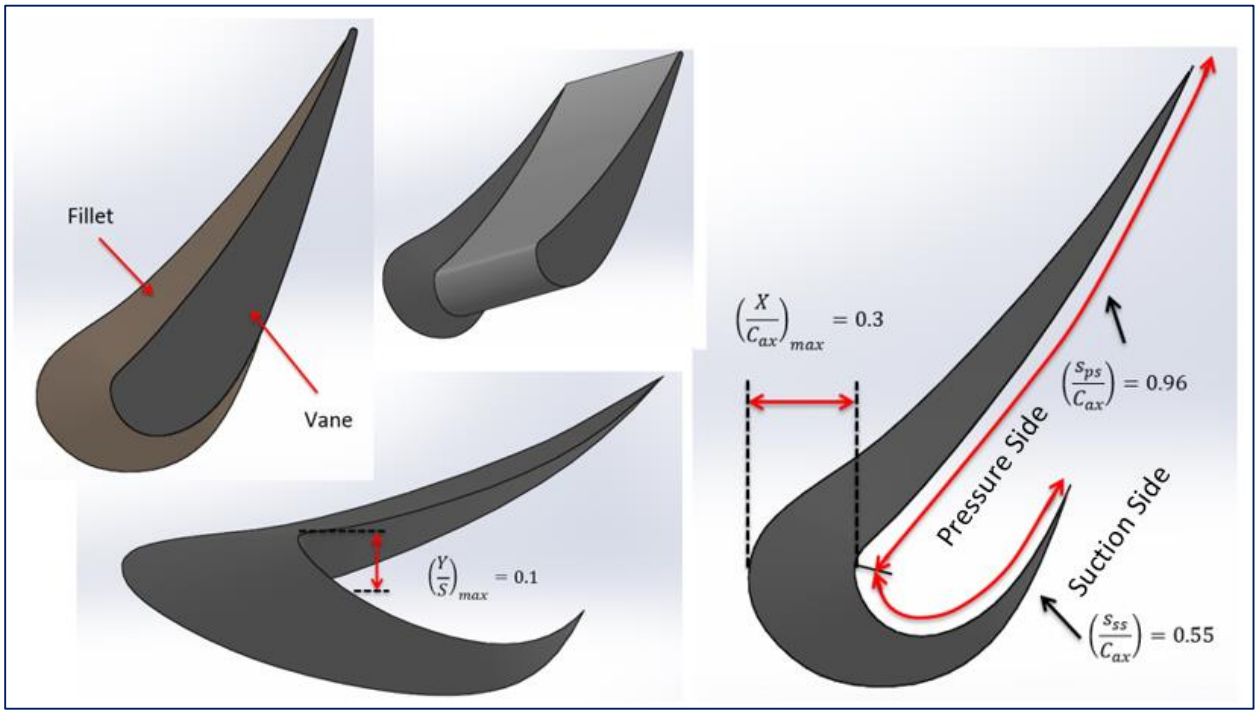

FIGURE 3.11 FILLET DESIGN AND GEOMETRY.

The profile of the fillet on the endwall follows the curvature of the vane profile. The height of the fillet from the vane wall to endwall varies linearly perpendicular to the vane surface. The fillet height is the maximum at the leading edge of the vane and decreases linearly from the leading edge towards the trailing edge on both the pressure side and suction side. The fillet then blends smoothly and simultaneously into the endwall and vane surface as it extends into the passage on both the pressure and suction side where the fillet ends, as shown in Figure 3.11. It can be seen that the fillet only extends to roughly halfway into the passage (throat region) on the suction side, whereas the pressure side reaches near the trailing edge. The throat region on the pressure side is located near the trailing edge. Thus, the throat area of the vane passage is not affected by employing the fillet. The pressure-side curvature of the fillet is chosen to resolve the cross-flow in the passage as seen similarly with endwall contouring where the pressure-side endwall region is elevated to reduce the pressure in this region. The leading edge of the fillet is the maximum to reduce the size of the horseshoe vortex by accelerating the flow in the boundary layer as it approaches the leading edge, thereby reducing the total pressure gradient at the stagnation location.

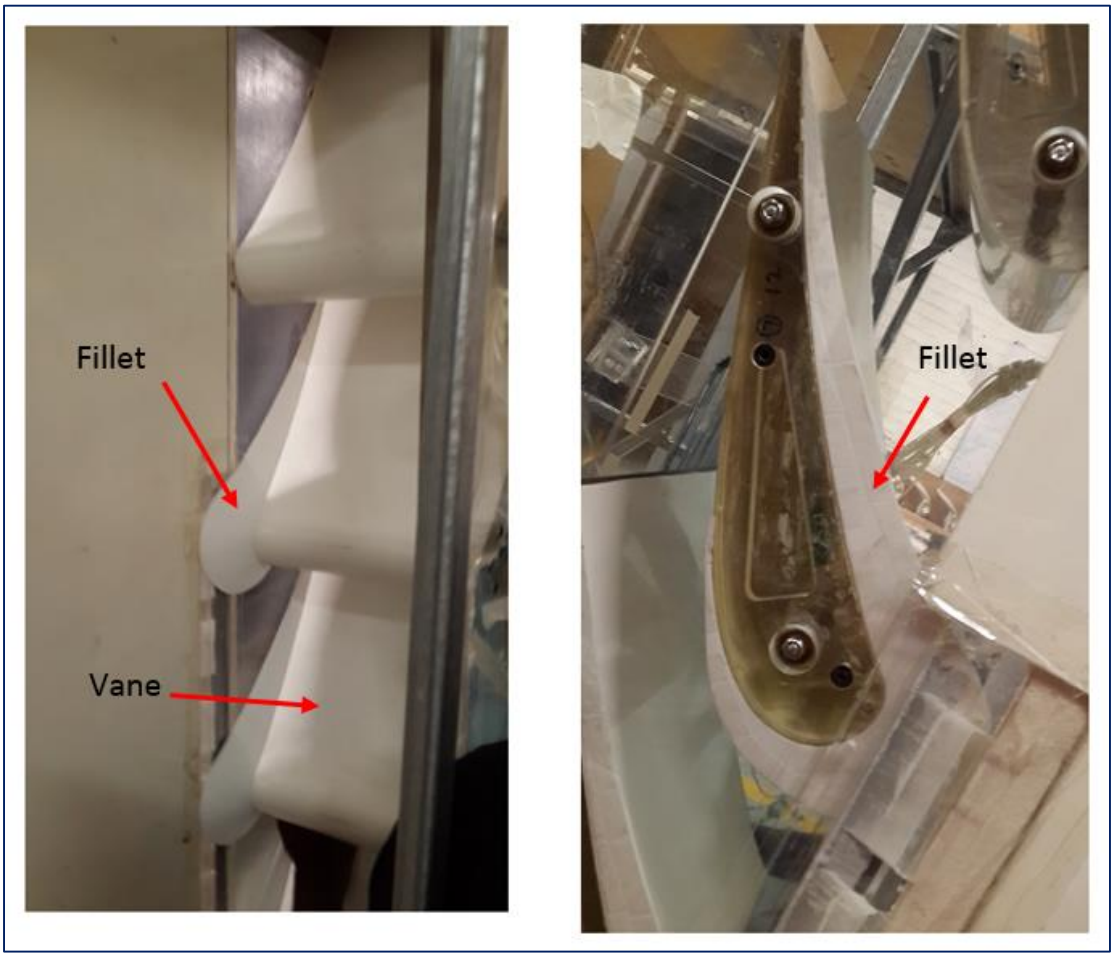

FIGURE 3.12 INSTALLATION OF FILLET INSIDE THE VANE CASCADE.

The design of the fillet is conceptualised through CAD with the use of Solidworks™ and then fabricated with 3-D printing using the ABS material. The profile is printed with high-density filling for thermal insulation for heat transfer investigations. To achieve a smooth surface finish, the fillet profile is also chemically treated and painted to reduce surface roughness effects. A total of five fillet profiles are made for the bottom endwall to facilitate five-hole probe experiments, and three fillet profiles made for the top endwall for surface static pressure measurements. The fillets are placed inside the test section and secured with thin double-sided tape on the flat endwall surface. Thereafter, the edges between the blade endwall and fillets are filled with mouldable white non-permanent adhesive to cover the small gaps that can affect the local flows. The adhesive further secures the fillets onto each blade. Visuals of the fillet installation are shown in Figure 3.12.

3.4 Film-cooling design

Past researchers have shown that the flow field and heat transfer in a turbine blade passage are affected through upstream slot film-cooling where the combustor-turbine interface is located. The upstream slot was formerly employed to prevent ingestion of the hot gases expelled from the combustor into these internal pathways created by the assembly between the turbine-combustor interfaces. Traditionally, a single continuous upstream slot which extended over the entire pitch of a blade passage was employed for film-cooling studies (Lynch and Thole (2011), Knost and Thole (2005)), where it was noted that the upstream location influenced the flow field near the leading edge. Thus, the present study aims to investigate further the influence of upstream slot film-cooling on the passage flow field in an effort to reduce the secondary flow structures at the leading edge and possibly inside the passage and thereby reduce the aerodynamic losses experienced. The design and configuration of the upstream film-cooling slot are described in this section.

3.4.1 Film-cooling loop

The film-cooling loop provides the coolant supply to the test section where measurements are made. The wind tunnel facility allows film-cooling implementation along the bottom endwall in the form of a plate, which is placed just upstream of the vane leading edge of the linear cascade. The film-cooling flow is supplied through the machined slots in the plate. The plate is interchangeable, thereby allowing different configurations and geometries to be investigated, as shown in Figure 3.13. The film-cooling supply loop provides air to a plenum box, which is placed just beneath the coolant supply slots. The plenum cross-section and opening to the slot inlet are large enough to minimise the velocity and turbulence of the coolant flow into the slots.

The film-cooling supply line consists of a squirrel cage blower (1 kW), metered pipe section with orifice plate, a refrigerant chiller unit (not used for measurements in this study) including an axial fan and heat exchanger (evaporator) encased in a duct, and plenum box, as shown in Figure 3.13. Inlet air enters the squirrel cage blower (1kW), draws in the laboratory air and blows it through

the orifice plate. The axial fan (800W) located downstream of the orifice plate provides additional power to the air flow, which then passes through the evaporator of the chiller unit to be cooled. The air flow then enters the large plenum box where the flow velocity slows down and the total pressure in the plenum increases. The plenum box, as indicated earlier, provides the coolant supply pressure to deliver air into the test section through the upstream slots. A baffle board is placed in the plenum box to guide the airflow smoothly and without turbulence to the inlet of the film-cooling slots. The baffle also provides coolant flow in the same direction as the streamwise flow inside the wind tunnel. This has been seen to minimise the pressure losses from the slots (Burd and Simon, 1999).

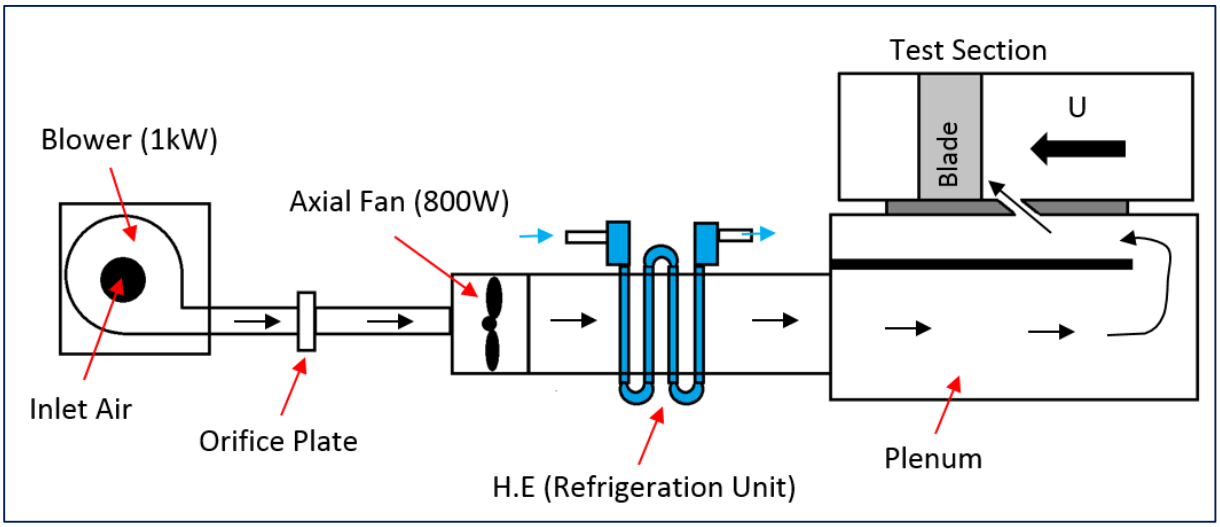

FIGURE 3.13 A SCHEMATIC OF THE FILM-COOLING LOOP.

The film-cooling experiments are conducted for different coolant mass flow rates and are identified by the blowing ratios. An inlet blowing is defined as follows by Friedrichs et al. (1997) (Eq. 3.14) for the present study:

Inlet blowing ratio:
$$M_{in} = \sqrt{\frac{P_{0,Plenum} - P_{t,ref}}{P_{t,ref} - P_{s,ref}}} \qquad (3.14)$$

$P_{0,Plenum}$, refers to the stagnation or total pressure of coolant in the plenum box. The mass flow rate of coolant is determined by measuring the pressure drop across the orifice plate:

Film-cooling flow rate:
$$\dot{m}_{Film} = \rho C_D \left(\frac{\pi}{4} {D_{Orifice}}^2\right) \sqrt{\frac{2\Delta P_{Orifice}}{\rho(1-\beta)}} \qquad (3.15)$$

A value of 0.60 is used for the discharge coefficient, C_d in Eq. 3.15. The pressure drop across the orifice plate is measured by pressure tap holes located upstream (1.0D) and downstream (0.5D)

of the orifice hole, as prescribed in the ASME standards (Standard, 1984). The pressure tap holes are connected to a single differential pressure transducer that is pre-calibrated. The coolant stagnation pressure is assumed to be equal to the static pressure inside the plenum box because the film-cooling flow speed inside the plenum is very low and incompressible. Therefore, the average coolant static pressure of the plenum box is measured by placing pressure tap holes on surrounding plenum walls at locations between the slot and baffle board. The pressure tap holes are then joined to a single pressure transducer to determine the average coolant stagnation pressure for the inlet blowing ratio. The pictures of the actual film-cooling loop and orifice plate assembly are shown in Figure 3.14.

FIGURE 3.14 FILM-COOLING LOOP (LEFT) AND ORIFICE PLATE ASSEMBLY (RIGHT).

The orifice plate-pipe assembly can be changed for different "beta" ratios to achieve the experimental inlet blowing ratios between 1.0 and 2.3. This is achieved by using two different sizes of orifice plate bore diameter and pipe diameter. A 2” pipe (50.8 mm diameter with an orifice bore diameter of 36 mm) allows inlet blowing ratios of 1.0 and 1.4 to be achieved, by using either the axial fan or both fan and blower simultaneously. Similarly, inlet blowing ratios of 1.8 and 2.3 are obtained with a 4” pipe (101.6 mm diameter with an orifice bore diameter of 72 mm), by using either the axial fan or the fan and blower simultaneously. Both orifice plates and pipe assembly provide the beta (β) ratio of 0.7 and are connected with the PVC pipes and PVC flanges. The beta ratio is defined as the ratio of the orifice diameter to the pipe diameter shown in Eq. 3.16.

Beta Ratio (β) :

$$\beta = \frac{D_{Orifice}}{D_{Pipe}} \tag{3.16}$$

The PVC pipes are then connected on either side of the flange openings and have prescribed lengths based on the ASME standards. The pressure tap holes of 1 mm diameter are drilled (normal) into the pipe upstream of the orifice and into the flange at the downstream. A 2 mm diameter hole is then drilled as a countersink to house a brass tube connector for the flexible plastic tubes which link to the pressure transducer. Similar static pressure tap holes are made on the plenum box, which is constructed from 18 mm thick high-density wood. The mass flow of coolant supply is evaluated in terms of the mass flow ratio (MFR) (Eq.3.17) of the coolant mass flow-to-passage mass flow for each film-cooling case. The passage flow rate is computed from the free-stream velocity and pitchwise inlet area of the blade passage, using the blade pitch and span dimensions.

Mass flow ratio: $$MFR = \frac{\dot{m}_{Film}}{\dot{m}_{Passage}} \quad (3.17)$$

All the ducts and plenum box of the coolant flow supply line are insulated. The entire coolant supply line is supported by a steel frame, which houses the refrigeration equipment below the duct.

3.4.2 Film-cooling configuration

The chosen configuration for the upstream slot is shown in Figure 3.15. The configuration shows a different approach to the traditional slot in that four separate slots are placed along the blade pitch of the measurement passages just upstream of the leading edge. The slots near the leading edges are elongated to cover the entire leading-edge region while the two central slots are smaller in length. With this arrangement, it is possible to choose which slots are employed and investigate their influence on the passage flow field. Thus, for this study, two experimental film-cooling cases are investigated by blocking and opening the slots at the leading edge. The film-cooling cases and the internal slot geometry are depicted in Figure 3.15 as well as the internal slot geometry.

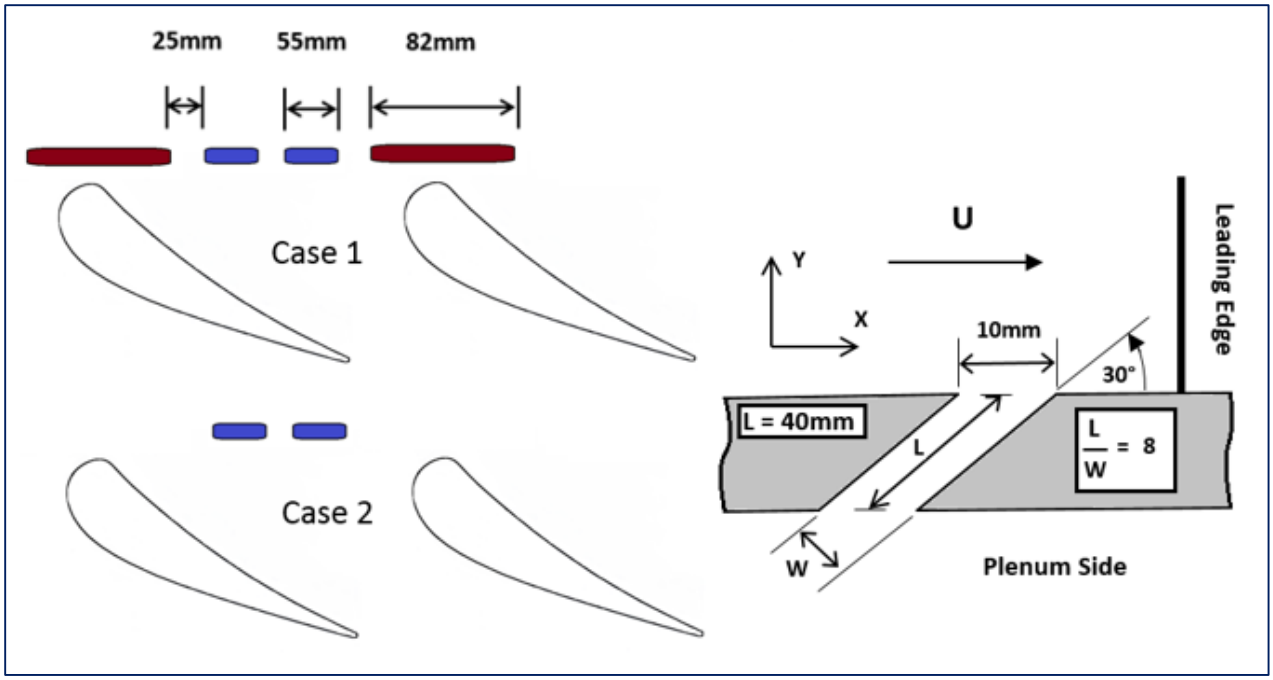

FIGURE 3.15 FILM-COOLING EXPERIMENTAL CASES AND INTERNAL SLOT GEOMETRY.

Film-cooling case-1 is investigated with all slots fully open. All the slots have identical delivery length-to-width ratios of eight and inject coolant at an angle of 30° relative to the endwall surface. The orientation of the slots is normal to the streamwise direction. The slots are located $0.079C_{ax}$ upstream of the leading edge. The red slots, which are located in front of the leading edges of the measurement passage, extend over 82 mm in length in the pitchwise direction. The blue slots in the centre of the passage are smaller in length in the pitchwise direction with 55 mm. Each slot is equally spaced apart by 25 mm. Film-cooling case-2 is investigated by blocking the slots located in front of the leading edges and thereby leaving the two central slots open. This is done by placing thin tape over the red slots. The case-2 configuration in Figure 3.15 is chosen when the fillet is employed in the film-cooling investigations, the fillet profile almost completely suppresses the elongated slots. The film-cooling cases also provide a comparison of the effects of the slot placement and flow rate variation. The resultant momentum flux of coolant is expected to increase with the second film-cooling case, when the same MFR is employed for the two cases, because there are fewer slots to inject the same amount of coolant. Therefore, more coolant flow per slot will be achieved when the red slots are blocked off. The influence of coolant momentum can then be evaluated accordingly, as was done by past studies.

The angled slots in the film-cooling plate are machined using the CNC milling machine. The film-cooling plate is made of clear acrylic plastic. The same film-cooling plate also contains similar slots that are sealed off with tape during the measurements in the passage between blade 3 and blade 4.

3.5 Data acquisition and control equipment

The measurements are controlled and recorded with a data acquisition system and desktop computer. The data acquisition system consists of a National Instruments™ NI-USB 6001 Data Acquisition (DAQ) card, which provides eight single-ended analogue input channels or four differential channels that digitise the voltage signals from the pressure transducers. The output connections of all the pressure transducers are connected to this DAQ card, which interfaces with the desktop computer through an in-house built Labview™ program. The pressure transducers require an excitation voltage to obtain measurements, which are provided with standard 30V-10A DC power supply benches. Pressure transducers with similar input excitations are then connected together and others are powered individually. The DAQ system and top wall side of the actual test section are shown in Figure 3.16. Figure 3.17 shows the traverse system and main axial duct fans of the linear cascade test facility.

A custom in-house Labview™ program is used to traverse, measure and record the five-hole probe data and endwall/blade static pressure data. The pressure transducers provide output data in the form of voltage signals, which vary linearly according to the pressure experienced. Each pressure transducer has a specific measuring range and voltage output range identically. Therefore, all the pressure transducers are calibrated to obtain analytical equations for conversion from voltage to Pascal. Details of the pressure transducer calibration curves are provided in Appendix A.

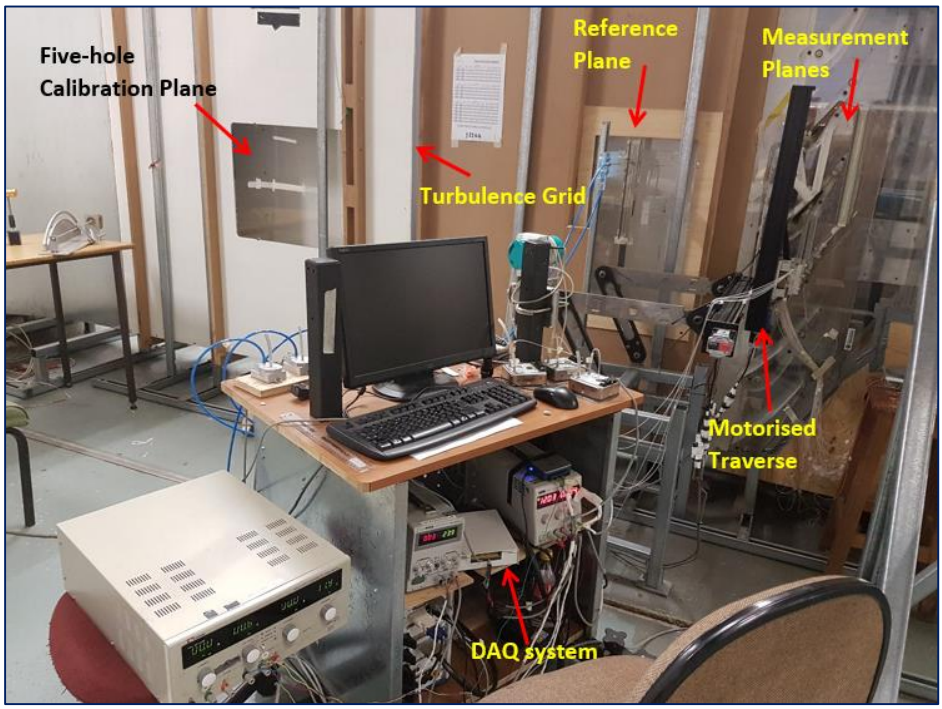

FIGURE 3.16 DAQ SYSTEM AND TOP WALL SIDE OF LINEAR VANE CASCADE.

The same Labview™ program that acquires voltage signals from the five-hole probe is used to control the motorised two-axis traverse, which scans the measurement plane along the pitch direction in the passage or upstream of the passage. Thus, the data acquisition and probe movement are synchronised without time lag or slip of measurement location. Figure 3.17 shows a picture of the actual two-axis traverse system. At each measurement plane, an input location file is specified with coordinates which indicate where the probe needs to move and measure within the Y-Z space. This is particularly important when the fillet measurements are taken as the probe must navigate the contour of the fillet surface in the passage at each measurement plane. The program controls the traverse through a Velmex™ motor controller, which sends out commands to the stepper motors of the traverse slides accordingly. The spatial resolutions of the data location employed are 2 mm to 4 mm near the endwall or vane wall and 5 mm in the free-stream region.

The pitchwise distance of the measurement slots dictates the time required to complete the scan, as well as the waiting time required for data to be recorded successfully. For five-hole probe measurements, five pressures as well as two reference pressures ($P_{t,ref}$, $P_{s,ref}$) are recorded at each probe scan location. Therefore, a sufficient waiting time of two seconds per transducer and five-second waiting time for the probe to move to each location is specified in the Labview™ computer program. This allows steady measurements to be obtained with greater accuracy. The system measures the voltage signals at a frequency of 100 Hz for two seconds from each transducer. The voltage signals are then time-averaged in the Labview™ program to account for time-based unsteadiness. Post-processing with transducer calibrations and five-hole probe calibration are conducted in a separate in-house built FORTRAN program, as mentioned earlier in this chapter, to deduce the local velocity components and pressures.

FIGURE 3.17 FIVE-HOLE PROBE TWO-AXIS TRAVERSE (LEFT) AND AXIAL DUCT FANS (RIGHT).

For all measurements taken with the five-hole probe, the coordinates are set to measure just over the half-span location. Before starting any experiments, a sample of five to 10 readings of the offset-voltage for each pressure transducer is recorded with no flow conditions to eliminate the bias errors in the pressure signals. Thereafter, the fans are powered and air is drawn through the test section. Steady-state flow conditions are achieved within 15-20 minutes, in which the reference pressures are observed to change not more than 1% to 2% over time. On average, measurement plane-1 requires six hours, plane-2 requires nine hours and plane-3 requires 17 hours to complete the spatial scan. Endwall static pressure measurements require five to seven hours to cover an entire passage on the top wall. When film-cooling is employed, static pressure measurements on the bottom wall require an hour for each inlet blowing ratio. The reference temperature is recorded upstream with a thermocouple and linked to the data acquisition system accordingly. Ambient conditions are also recorded for all measurements taken inside the passage.

3.6 Summary

The experimental set-up is described along with the measurement techniques and equipment used to obtain data. Design and calibration of measurement probes were provided with reference to the appendices. The coordinate system adopted for measurements were outlined with chosen notations and directions specified. The experimental process during tests were also described with details of the post-processing tasks.

To avoid confusion, it is stated here that time-averaged results will be discussed only with those measurements associated with the five-hole probe. The hot-wire anemometry is only used to obtain reference turbulence quantities upstream of the cascade. The current hot-wire system is not suitable for 3-D measurements within the cascade and is thus not associated with any of these results presented in Chapter 5.

CHAPTER 4: UNCERTAINTY

An uncertainty analysis is conducted on the measurements and results presented in the next section. The degree of accuracy which can be placed upon measured data and calculated results is vitally important in establishing the validity of the experimental investigation. The uncertainty analysis is determined by methods described by Moffat (1988) and Dunn (2014). The total uncertainty is taken as the magnitude of the bias and precision errors of which a 95% confidence level is assumed for the probability that the actual error does not exceed the estimate. Details of the uncertainty estimation, methods and procedure are given in Appendix C.

4.1 Pressure transducers

The uncertainty in the pressure transducers is determined by linear regression analysis to obtain the precision error component. The bias error component is taken as the accuracy of the pressure calibrator unit and transducers manufacturer's quoted accuracy. The overall uncertainty for each pressure transducer is summarised in Table 4.1.

TABLE 4.1 UNCERTAINTY OF PRESSURE TRANSDUCERS FOR AVERAGE CALIBRATED PRESSURES.

Pressure Transducer	Manufacturer	Measurement	Bias Component (Manufacturer's Accuracy) [Pa]	Max. Precision Component [Pa]	Max. Overall Uncertainty Calibrated [Pa]	Max. Overall Uncertainty % -Calibrated [Pa]
1	Siemens SITRANS P	Five-hole probe Port 1	1.0	2.67	3.18	1.83
2	Omega PX653	Five-hole probe Port 2	3.105	1.08	3.58	0.78
3	Omega PX653	Five-hole probe Port 3	3.105	1.69	3.812	0.83
4	Omega PX653	Five-hole probe Port 4	3.105	0.867	3.523	0.79
5	Omega PX653	Five-hole probe Port 5	3.105	0.66	3.47	0.76
6	Omega PX2650	Pitot-static probe Total Pressure	0.31	1.279	1.936	4.23
7	Omega PX2650	Pitot-static probe Static Pressure	1.24	0.506	1.953	1.05
8	Omega PX2650	Plenum Total Pressure	3.1	2.57	3.93	0.75
9	Omega PX164	Orifice Pressure Drop	3.0	4.77	5.81	1.04

4.2 Five-hole probe measurements with film-cooling

The uncertainty in the five-hole probe results is determined by the method of sequential perturbation described by Moffat (1988) for computerised uncertainty analysis. This method uses the data processing program to compute the uncertainties of calculated results by sequentially perturbing each independent variable (inputs to calculate result) by its associated uncertainty interval. Therefore, the five-hole probe analysis program is used to determine the uncertainties in calculated results produced by the program such as the velocity components, total pressure, static pressure, pitch angle and yaw angle. The resultant total pressure calculated by the program is then used to determine the coefficient of total pressure loss and its uncertainty as well. Furthermore, the velocity components are then used to determine the axial vorticity for the associated measurement plane, which then provides a method to determine the uncertainties in the axial vorticity results. This method is adopted because the uncertainties in the five-hole results require operations that are difficult to differentiate analytically (table look-ups and numerical approximations/interpolations).

For the uncertainty procedure, a sample of four measurements is taken at three distinct regions in measurement plane-2 with film-cooling case-1 at M_{in} = 2.3. A region near the suction-side endwall, inviscid mid-pitch and pressure-side endwall is measured spatially to provide qualitative data for the uncertainty analysis. It can be seen that due to the secondary flow patterns near the suction side (film-cooling), the uncertainty in the calculated results as well as measured pressures is significantly affected and is shown to be relatively high due to the unsteadiness of the secondary flows. Table 4.2 provides a summary of the overall uncertainties in measured pressures using the five-hole probe.

TABLE 4.2 OVERALL UNCERTAINTIES IN MEASURED PRESSURES AS PERCENTAGE.

Measurement	% Uncertainty – Pressure side	% Uncertainty – Inviscid region	% Uncertainty – Suction side
P1	1.64 – 11.57	1.46 – 9.56	0.75 – 18.99
P2	1.19 – 7.85	2.72 – 9.35	2.05– 15.84
P3	1.1 – 7.86	1.65 – 9.24	4.21 – 14.76
P4	1.07 – 9.37	1.95 – 9.35	2.65 – 12.01
P5	1.28 – 6.22	2.45 – 9.61	2.3 – 9.62

The uncertainties in the reference pressures measured upstream of the test section are shown to be 14.76% and 3.6% in the total and static pressure respectively, measured by the pitot-static probe. The uncertainty in the free-stream velocity is then determined to be $\delta U_0 = 3.34\%$. The uncertainties in the plenum pressure and pressure drop across the orifice plate are shown to be

2.33% and 3.42% respectively, for M_{in} = 2.3. The corresponding uncertainty in the film-cooling inlet blow ratio is $\delta M_{in} = 3.31\%$ and film-cooling flow rate is $\delta \dot{m}_{Film} = 1.69\%$.

Table 4.3 summarises the overall uncertainties in the five-hole probe results as well as axial vorticity.

TABLE 4.3 UNCERTAINTY IN FIVE-HOLE PROBE RESULTS AS PERCENTAGE.

Calculated Result	% Uncertainty – Pressure side	% Uncertainty – Inviscid region	% Uncertainty – Suction side
u	2.4 – 6.56	1.2 – 5.82	1.1 – 7.67
v	1.09 – 15.2	1.5 – 8.4	2.24 – 16.6
w	2.7 – 14.6	1.12 – 9.7	1.56 – 19.8
$P_{Total\_five\text{-}hole}$	2.3 – 15.08	1.8 – 10.4	2.34 – 18.3
$P_{Static\_five\text{-}hole}$	1.8 – 6.29	1.34 – 6.3	1.05 – 9.4
Pitch angle	1.4 – 15.3	1.21 – 11.9	1.3 – 17.1
Yaw angle	2.36 – 13.4	1.34 – 10.13	1.5 – 17.6
$C_{Pt,Loss}$	4.38 – 12.31	1.53 – 11.6	2.8 – 19.32
$\omega_x C/U$	3.5 – 12.7	1.43 – 14.8	2.4 – 17.67

The uncertainty estimates in the five-hole probe pressures and calculated results are shown to be relatively high when compared with the estimates given for the reference pressures and free-stream velocity. This comes as a consequence of the five-hole ports, which are significantly small (0.5 mm diameter) with increased tube length for traversal (30 – 60 cm), thereby increasing the time response of the probe which contributes the most in the uncertainty approximations. It is also evident that the uncertainty estimation near the secondary flow regions of the suction and pressure side is greatly influenced by the unsteadiness of the vortex formation as well as film-cooling flows. This is seen in the increased uncertainty in pitch-yaw angles for the regions near the blade surfaces. The estimation of the flow angles is more likely to be affected by the calibration curves for the five-hole probe as these quantities are interpolated and their actual values may lie beyond the calibration range in some areas where there is a higher degree of turning, especially near the suction-side where the yaw angles reach extremes and in the near-wall region and the boundary layer effects are felt. The uncertainties are higher in the suction-side and pressure-side endwall regions. Furthermore, the introduction of film-cooling may induce further uncertainty with the contribution of external fluid flow, which interacts directly with the mainstream flow.

4.3 Endwall static pressure measurements with film-cooling

An uncertainty analysis is conducted on the endwall static pressure measurements with film-cooling case-2 at M_{in} = 1.4. A sample of six measurements is taken at nine locations along the endwall film-cooling side to determine the uncertainty in the measured and calculated values. The

pressure tap locations are measured with pressure transducer 2 with the use of a fabricated multiport scanner. Details of the endwall static pressure port coordinates can be found in Appendix D.

The uncertainties in the reference pressures measured upstream of the test section are shown to be 8.7% and 2.33% in the total and static pressure respectively, measured by the pitot-static probe. The uncertainty in the free-stream velocity is then determined to be $\delta U_0 = 2.22\%$. The uncertainties in the plenum pressure and pressure drop across the orifice plate are shown to be 14.6% and 4.37% respectively, for M_{in} = 1.4. The corresponding uncertainty in the film-cooling inlet blow ratio is $\delta M_{in} = 2.46\%$ and film-cooling flow rate is $\delta \dot{m}_{Film} = 2.78\%$.

The overall uncertainty in the endwall static pressure measurements is summarised in Table 4.4.

TABLE 4.4 UNCERTAINTIES IN ENDWALL STATIC PRESSURE COEFFICIENT AS PERCENTAGE.

Port No.	% Uncertainty – $\delta P_{Endwall}$	% Uncertainty – $\delta C_{Ps,Endwall}$
1	11.14	7.58
8	3.12	14.68
20	0.86	5.39
27	1.53	5.57
30	1.43	5.26
33	1.88	5.83
40	1.17	5.78
43	1.5	5.29
48	1.93	5.73

It can be seen from the uncertainty estimates provided that there exist extremities which arise due to the unsteadiness of the secondary flow patterns within the passage. The unsteadiness of the secondary flows is due to the periodic nature as the vortex formation evolves and progresses through the passage near the endwall. The highest uncertainty in the static pressure coefficient occur at the leading-edge stagnation region and upstream of the throat on the pressure side. This is a critical region where secondary flows develop and begin to travel across the passage towards the suction side.

4.4 Blade profile measurements

The uncertainties in the blade surface static pressure and static pressure coefficient are computed for measurements taken with three instrumented blades within the test section. Because each blade is fabricated with 21 surface pressure taps located at midspan Y_G/S = 0.5, a sample of nine measurements are taken at all 21 pressure taps in the uncertainty estimation.

TABLE 4.5 UNCERTAINTY IN BLADE PROFILE PRESSURE AS PERCENTAGE.

Port No.	s/C	$\% \delta P_{Blade\ 1}$	$\% \delta P_{Blade\ 2}$	$\% \delta P_{Blade\ 3}$
1	-1.22	1.82	0.79	1.08
2	-1.09	1.24	0.73	1.12
3	-0.90	1.62	0.79	1.39
4	-0.68	1.95	1.26	1.16
5	-0.53	1.50	1.15	1.53
6	-0.43	1.37	0.97	1.48
7	-0.34	1.62	1.29	1.83
8	-0.25	2.15	0.80	1.81
9	-0.16	1.52	1.76	2.23
10	-0.10	2.22	1.28	1.88
11	-0.05	3.55	3.49	2.99
12	-0.02	10.06	9.57	7.32
13	0.00	16.54	16.84	12.52
14	0.02	18.00	20.31	17.07
15	0.06	10.95	11.63	11.87
16	0.13	8.65	7.77	8.59
17	0.26	5.59	4.73	5.54
18	0.40	3.84	2.29	3.37
19	0.60	2.69	3.31	2.25
20	0.78	1.86	1.61	1.24
21	0.96	1.96	1.83	1.94

The overall uncertainty in the blade profile pressure for all three blades is given in Table 4.5. The maximum uncertainty arises near the leading-edge stagnation region (s/C = 0) towards the pressure side(s/C > 0). The static pressure coefficient is then calculated similarly as in the endwall static pressure coefficient and the maximum uncertainty in this result is seen to be $\delta C_{Ps,Blade\ 1} = 9.83\ \%, \delta C_{Ps,Blade\ 2} = 9.35\ \%$ and $\delta C_{Ps,Blade\ 3} = 9.52\ \%$.

4.5 Hot-wire measurements

The overall uncertainty in the hot-wire velocity measurements is 0.8 % and turbulence intensity is 4.74 % of the nominal measured value. (See Appendix C.)

CHAPTER 5: RESULTS AND DISCUSSIONS

This chapter presents the experimental results and complementing discussions thereof for all cases studied. The experimental investigations are conducted for the baseline, fillet and slot film-cooling cases as well as the fillet with slot film-cooling. Flow field measurements, endwall and vane surface static pressure measurements are presented and discussed in a logical manner from the inlet to the exit of the passage. The reference conditions are measured upstream of the cascade inlet along with the blade profile measurements to ensure test conditions are met in order to obtain valid results. All the measurements are obtained for the periodic flow conditions in the cascade passage, adiabatic wall boundary and isothermal flow conditions, and laboratory atmospheric conditions. Because the reference flow speed is much lower than the Mach number of 0.1 and has almost the same density as the laboratory air, the flow in the cascade is treated as incompressible.

5.1 Boundary layer measurements

Before flow field measurements are obtained, the inlet conditions to the cascade are verified in the reference location upstream ($2.5C_{ax}$ upstream of cascade inlet). Boundary layer characteristics are determined with the five-hole probe by measuring the properties in the Y-Z plane (pitchwise normal) of the reference location. The reference pressures and velocity are measured with the pitot-static probe. It should be noted that because the wind tunnel operates under suction, these pressures are below atmospheric pressure conditions. For simplicity, the values are given without negative signs (due to suction) but the negative gauge pressures are considered in the calculations concerned. The boundary layer and reference conditions are given in Table 5.1.

TABLE 5.1 BOUNDARY LAYER AND REFERENCE CONDITIONS ($2.5C_{AX}$ UPSTREAM OF CASCADE INLET).

Boundary Layer Quantities	Symbol	
Average free-stream reference velocity [m/s]	U_{ref}	9.6
Average reference static pressure (Below atmospheric) [Pa, gauge]	$P_{s,ref}$	60
Average reference total pressure (Below atmospheric) [Pa, gauge]	$P_{t,ref}$	18
Average reference stagnation temperature [K]	T_o	300
Air density [kg/m^3]	ρ	1.02
Inlet Reynolds number (Based on true chord)	Re_C	200 000
Streamwise turbulence intensity [%]	TI	3.3
Boundary layer thickness [mm]	δ	30
Displacement thickness [mm]	δ_1	2.27
Momentum thickness [mm]	δ_2	1.96
Density Ratio	$\frac{\rho_c}{\rho_\infty}$	1

The reference properties are used to normalise the results provided for comparisons between the different experimental cases. The boundary layer properties are determined by numerical integration of the measured velocity data from the five-hole probe. The turbulence properties of the inflow are measured with the two-wire hot-wire anemometer probe. The coolant temperature injected via the film cooling slots in relation to that of the main flow through the cascade is regarded as being the same since the refrigeration unit is not used for this study. Thus the density ratio is unity for all test conditions.

5.2 Blade pressure profile and channel balancing

The blade pressure profiles of three vanes (blade 3, 4 and 5), which form the measurement passages, are compared to ensure equal vane loading and channel balancing in the test section. This ensures that the aerodynamic behaviour is periodic in the cascade passages and equal mass flow exists through each passage. The blade static pressure coefficient ($C_{P,Blade}$) is compared for the baseline, fillet and film-cooling cases at the midspan location ($Y_G/S = 0.5$) in Figure 5.1, Figure 5.2 and Figure 5.3 respectively. In each case, the free stream velocity was not consistent to present all data in a single view and is thereby presented as shown to indicated periodicity for the different experimental cases. The coefficient, $C_{P,Blade}$, is computed from the measured pressure along the vane surface using Eq.(3.1) given in Chapter 3.

The pressure coefficients, $C_{P,Blade}$, shown in the figures below are presented over the blade surface in terms of curvature distance (s) where s/C = 0.0 corresponds to the leading-edge stagnation location and increases towards the pressure side (PS). $C_{P,Blade}$ is the highest at the stagnation point and decreases along both the pressure (PS) and suction (SS) sides of the vane profile as the flow accelerates into the passage. The surface pressure on the suction side decreases further as the $C_{P,Blade}$ reaches a global minimum at s/C = -0.33 where the passage throat region is located. The $C_{P,Blade}$ then increases as the flow decelerates downstream of this point as it approaches the passage exit. The passages are periodic or balanced because the $C_{P,Blade}$ distributions on PS of the three vanes are about equal. The same can be seen for the $C_{P,Blade}$ distributions on SS of the three vanes. The $C_{P,Blade}$ distributions also match well in Figure 5.2 and Figure 5.3, which compare the baseline with the fillet cases and film-cooling cases, indicating that the fillet and film-cooling effects do not extend far into the inviscid region and are mainly focused near the endwall. This is desirable as the effects of the fillets are intended for the near-wall region as is the case for film-cooling. The pressure distributions along the vane midspan thus also provide an indication of the periodicity of the flow when the fillet and film-cooling are employed. However, they do not represent the full blade loading conditions because the near-wall effects are not considered in the $C_{P,Blade}$ measurements.

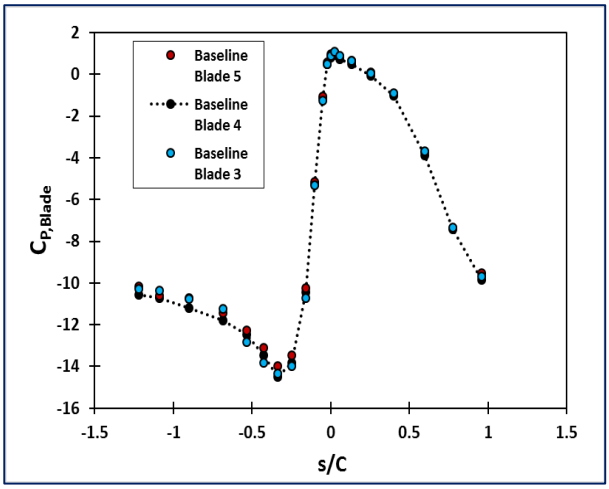

FIGURE 5.1 BLADE SURFACE STATIC PRESSURE COEFFICIENT, $C_{P,BLADE}$ AT $Y_G/S = 0.5$ - BASELINE CASE.

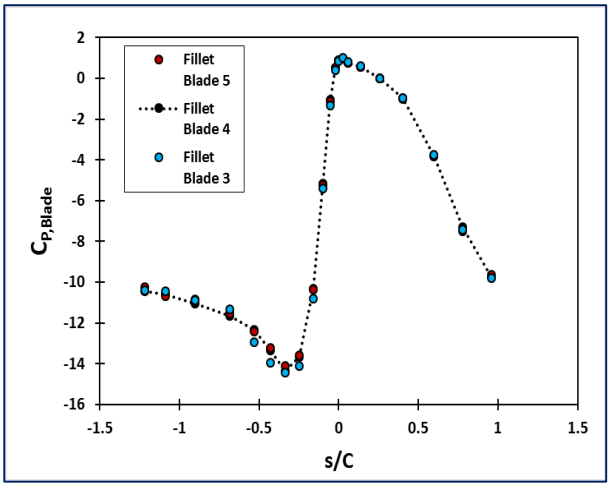

FIGURE 5.2 BLADE SURFACE STATIC PRESSURE COEFFICIENT, $C_{P,BLADE}$ AT $Y_G/S = 0.5$ - FILLET CASE.

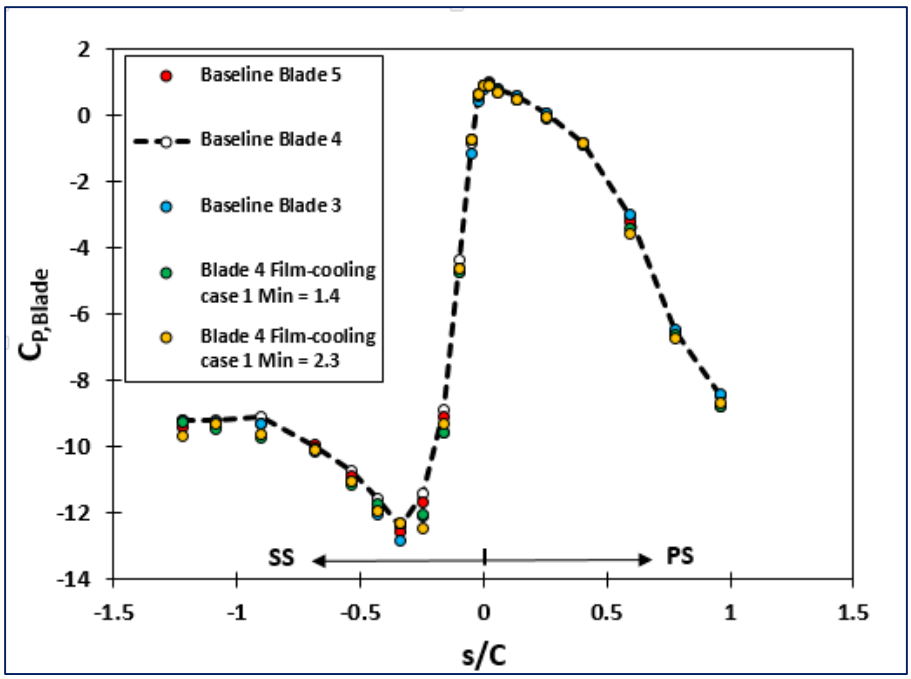

FIGURE 5.3 BLADE SURFACE STATIC PRESSURE COEFFICIENT, $C_{P,BLADE}$ AT $Y_G/S = 0.5$ - FILM-COOLING CASE-1.

5.3 Fillet case (no film-cooling)

The endwall static pressure distribution with the fillets employed is measured along the top endwall and presented as the static pressure coefficient, $C_{Ps,endwall}$, which is determined using the Eq.(3.1). Pressure $P_{s,local}$ in the equation is the measured local pressure on the endwall. The measurements of $P_{s,local}$ on the top endwall are obtained when the fillets are present on both bottom and top endwall. The baseline and fillet endwall static pressure coefficient contours are given in Figure 5.4.

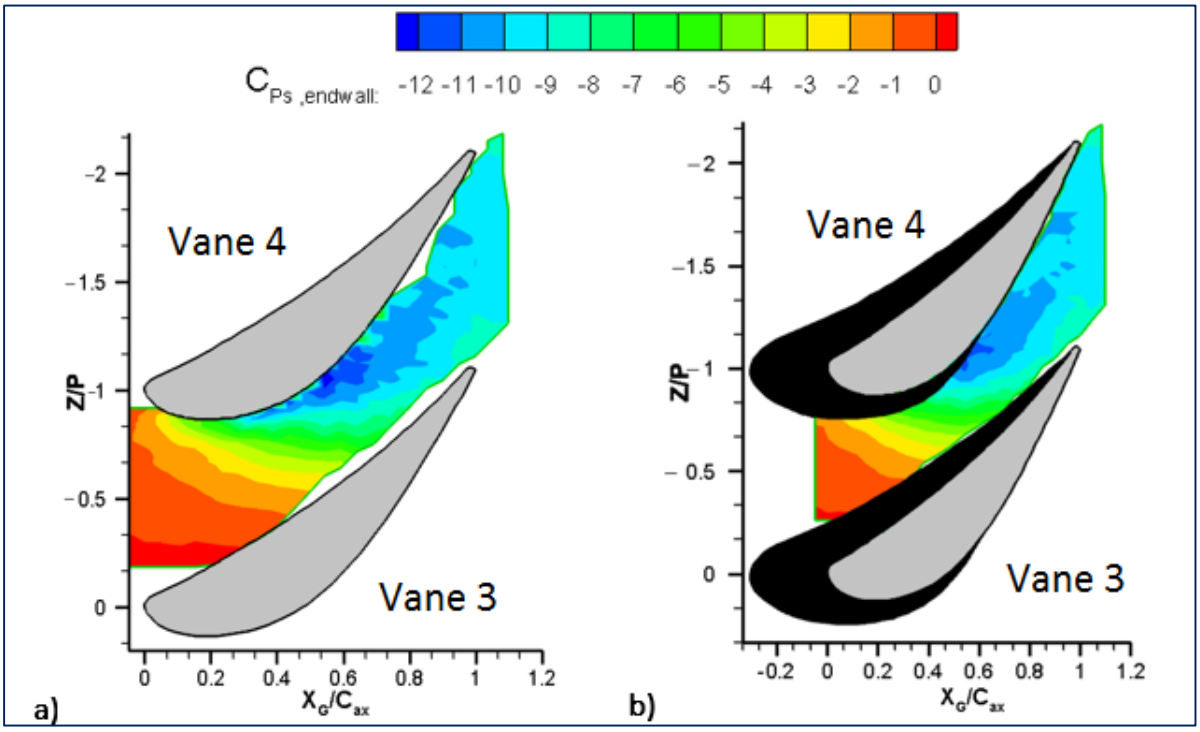

FIGURE 5.4 ENDWALL STATIC PRESSURE COEFFICIENT FOR (A) BASELINE AND (B) FILLET.

The endwall pressure distributions are superimposed with the blade airfoil geometry (grey region) and fillet profile (black region). The $C_{Ps,endwall}$ distributions show the local surface static pressure on the endwall, indicative of how the flow accelerates along the endwall through the passage. Because the wind tunnel operates under suction, the ($P_{s,Local}$ - $P_{s,ref}$) provides the negative values for the $C_{Ps,endwall}$ in Figure 5.4 where no pressure measurements are obtained on the fillet profiles. The contour values of $C_{Ps,endwall}$ in Figure 5.4, in general, decrease along the passage both in the axial direction and from the pressure side of Vane 3 to the suction side of Vane 4. Due to the area reduction and approach of the throat region, the flow accelerations in the axial direction cause the $C_{Ps,endwall}$ to decrease. Also, it is this pressure gradient which exists between the pressure and suction side that drives the cross-flow in the passage and enhances the passage vortex which migrates along the endwall. Comparison of the fillet case in Figure 5.4 b) shows slight increase of the $C_{Ps,endwall}$ at $X_G/C_{ax} > 0.35$ at the suction-side region of the passage. Overall, it is difficult to estimate the effects of the fillet from these static pressure coefficient contours.

A clearer indication is given in Figure 5.5 and Figure 5.6 where the maximum pressure difference and pitchwise-averaged $C_{Ps,endwall}$ between the pressure and suction sides are presented over the axial distance of the passage endwall for baseline and fillet cases respectively. The pressure difference is computed by taking the arithmetic difference between the closest endwall pressure measurement on the endwall at PS and SS locations, respectively.

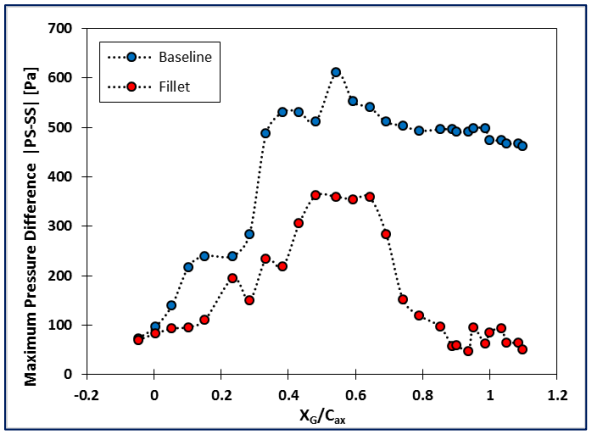

FIGURE 5.5 ENDWALL STATIC PRESSURE DIFFERENCE (MAXIMUM) BETWEEN PRESSURE AND SUCTION SIDES.

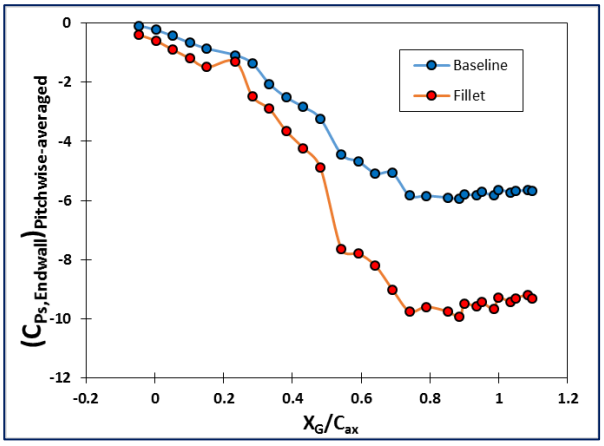

FIGURE 5.6 PITCHWISE-AVERAGED ENDWALL STATIC PRESSURE COEFFICIENT BETWEEN PRESSURE AND SUCTION SIDES.

The fillet case shows visible reduction in the overall pressure differences throughout the passage in Figure 5.5, particularly from the throat region ($X_G/C_{ax} > 0.5$), which then follows similarly in the average static pressure coefficient in Figure 5.6. The effects extend further downstream because there is even larger ($P_{PS} - P_{SS}$) reduction at the passage exit compared with the baseline case. The extension of the fillet profile on the pressure side, covering nearly the full axial chord, thus reduces the pressure in this region, thereby reducing the endwall pitchwise pressure gradient. Hence the fillet successfully resolves the passage cross-flow with major reductions in the pitchwise direction. The effects on the secondary flow formation and development will be discussed next by analysing the flow field results.

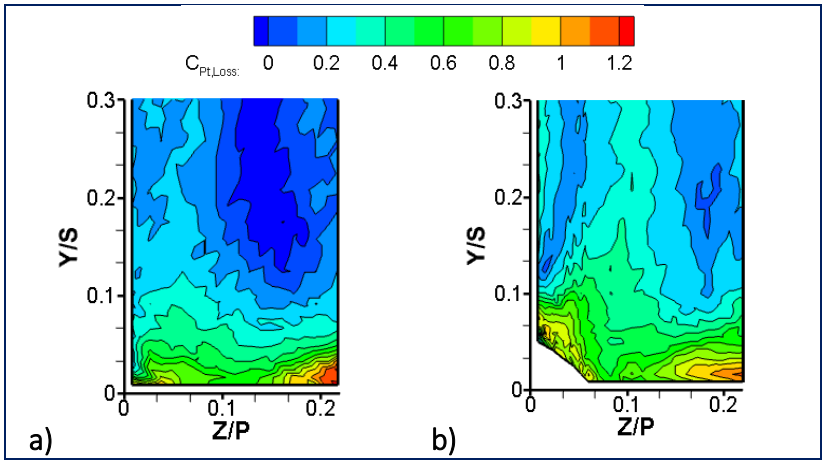

FIGURE 5.7 CONTOURS OF $C_{PT,LOSS}$ AT PLANE-1 (X_G/C_{AX} = 0.251) FOR (A) BASELINE AND (B) FILLET.

The total pressure loss coefficient ($C_{Pt,Loss}$) indicates the total pressure loss distributions in the secondary flow regions along the passage as well as the strength and size of the secondary flow structures. The $C_{Pt,Loss}$ is evaluated from the total pressure measurements, $P_{t,local}$ of the flow at different pitchwise normal planes using the Eq.(3.7). Because of the additional losses in turbulence

and vortical motions of the passage vortex, $C_{Pt,Loss}$ will be higher in the secondary flow regions. The higher the values of $C_{Pt,Loss}$, the higher the size and strength of the passage vortex. The pitchwise plane-1 contours of $C_{Pt,Loss}$ in Figure 5.7 is perpendicular to the suction side of Vane 4 and located near the leading edge. In the figure, where the blade suction side is located at Z/P =0.0, the baseline case shows higher intensity secondary flows near the endwall at Y/S<0.1 in Figure 5.7(a) where $C_{Pt,Loss}$ contour values are high. This location corresponds to the migration path of the pressure-side leg and suction-side leg of the passage vortex, evidently the pressure-side leg vortex located on the lower right corner of Figure 5.7(a) is stronger than the suction-side leg vortex located near the blade suction side (Z/P < 0.1). The filleted case shows improvement as the strength of the pressure-side vortex is reduced in $C_{Pt,Loss}$ magnitude, while the suction-side vortex is minimised near the endwall (Y/S < 0.1) in Figure 5.7(b). The normalised pitchwise velocity (z-velocity, pressure to suction side) and pitch angle (turning about y-axis) contours at measurement plane-1 are given in Figure 5.8 and Figure 5.9. The pitchwise velocity contours in Figure 5.8(a) indicate the changes in w-velocity, which develop across the plane and the pitch angle contours in Figure 5.9(a) indicate the induced turning towards the endwall for the baseline case, which are provided with black arrows showing rotational tendency of the flow at those locations. The velocity values and pitch angles are conventionally taken from positive (high) to negative (low) to derive the flow rotation sense where positive pitch angle notation indicates a direction towards the endwall shown in Figure 3.8. The suction-side leg horseshoe vortex rotates counter-clockwise (CCW) while the pressure-side leg horseshoe vortex does the opposite (CW).

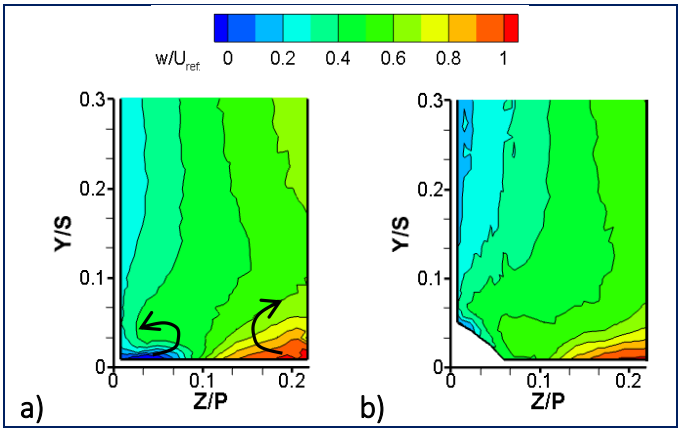

FIGURE 5.8 CONTOURS OF NORMALISED PITCHWISE VELOCITY (W/U_{REF}) AT PLANE-1 (X_G/C_{AX} = 0.251) FOR (A) BASELINE AND (B) FILLET.

Flow turning reduces because the pressure gradient between the pressure side and suction side is reduced with the fillet. This eventually impedes the development of the passage vortex. In Figure 5.9(b), the pitch angles also indicate a smaller pressure-side vortex with significantly lower turning near the blade-endwall junction because the fillet reduces the pressure gradient at this location. Thus the fillet has significant influence near the blade-endwall junction at the early stages of the

passage. The passage throat region and exit plane will be assessed to further evaluate fillet performance on the passage flow field.

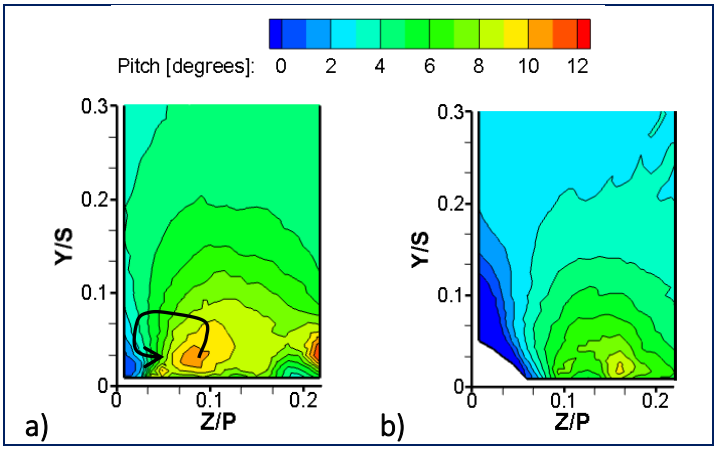

FIGURE 5.9 CONTOURS OF PITCH ANGLE (TURNING ABOUT Y-AXIS) AT PLANE-1 (X_G/C_{AX} = 0.251) FOR (A) BASELINE AND (B) FILLET.

The contours of $C_{Pt,Loss}$ at plane-2 are provided in Figure 5.10, located just aft of the passage throat. The suction-side blade is located at Z/P = 0.0 and the pressure side of the blade is located on the extreme right of this axis. In the baseline contour in Figure 5.10(a), the highest total pressure losses occur at the suction-side blade-endwall junction at Z/P < 0.25, representing the passage vortex system, which has formed near the suction side, as the suction-side leg vortex and pressure side-leg vortex merge. The size of the vortex system occupies a significant region along the endwall (0 < Z/P < 0.3). The development of a smaller corner vortex at the suction-side blade-endwall junction is not clearly visible at this point in the result in Figure 5.10(a).

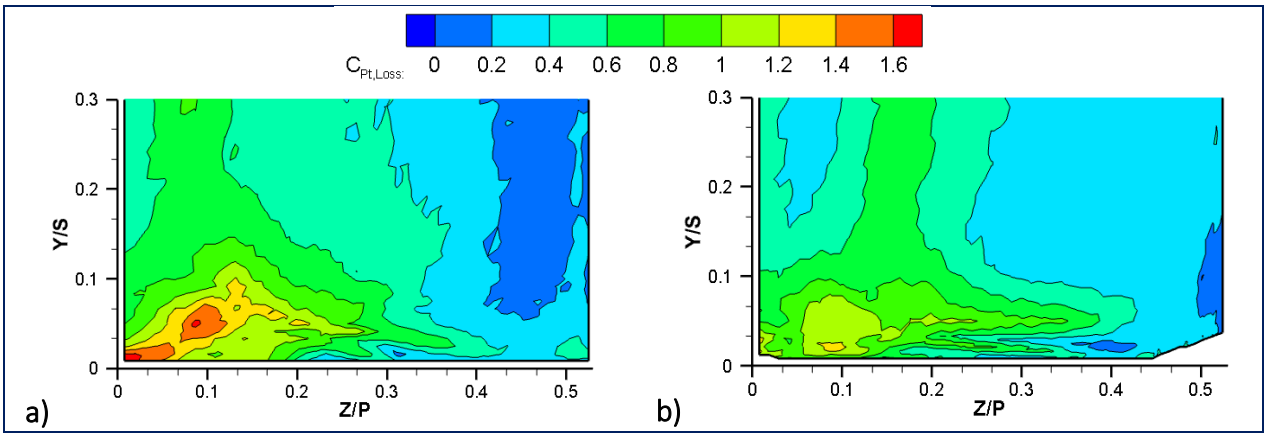

FIGURE 5.10 CONTOURS OF $C_{PT,LOSS}$ AT PLANE-2 (X_G/C_{AX} = 0.58) FOR (A) BASELINE AND (B) FILLET.

Comparing the baseline data in plane-2 with the data in Figure 5.10 b), where the fillet case is shown, the total pressure loss magnitude is reduced remarkably. This result ties in with the reduction in the passage cross-flow, which is the major driving force of the passage vortex system. The strength of the vortex structure is thus reduced considerably with the fillet.

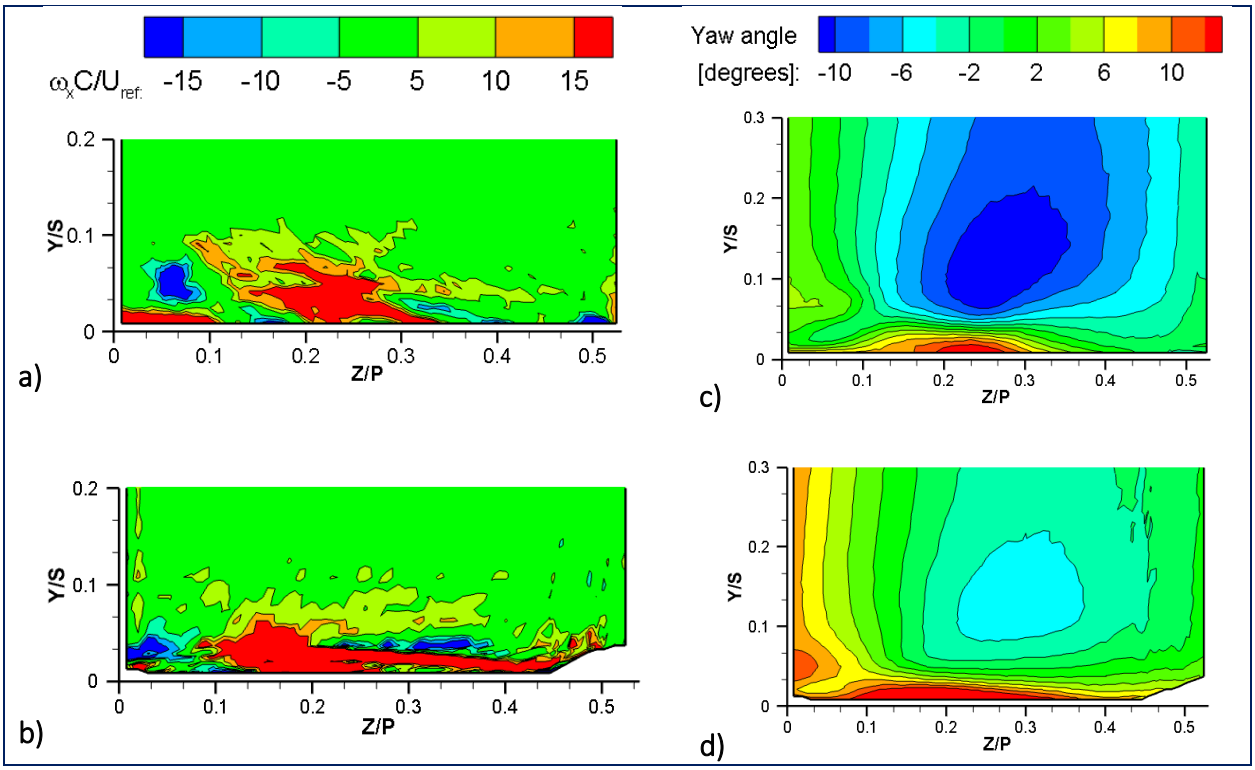

FIGURE 5.11 CONTOURS OF NORMALISED AXIAL VORTICITY ($\omega_X C/U_{REF}$) (LEFT) AND YAW ANGLE (TURNING ABOUT Z-AXIS) (RIGHT) AT PLANE-2 (X_G/C_{AX} = 0.58) FOR (A, C) BASELINE AND (B, D) FILLET.

Furthermore, the $\omega_X C/U_{Ref}$ distributions are compared in Figure 5.11 at plane-2 for the baseline (top) and fillet (bottom) with the yaw angle contours shown on the right in the same figure. The contours of pitch angle for the same test cases and axial location are provided in Figure E.17 for completeness. The axial vorticity in the secondary flow region is expected to be high because of the flow rotations in the passage vortex. In Figure 5.11(a), the high positive values of $\omega_X C/U_{Ref}$ indicate clockwise rotation in the pressure-side leg vortex and high negative values of $\omega_X C/U_{Ref}$ indicate counter-clockwise rotation in the suction-side leg vortex. The influence of the fillet is evident in Figure 5.11(b) which is compared with the baseline case in Figure 5.11(a) due to the $\omega_X C/U_{Ref}$ size of the large contour values (both positive and negative) near the endwall in Figure 5.11(b), where the positive $\omega_X C/U_{Ref}$ is suppressed towards the endwall surface and appears to be pushed closer towards the suction side. This may be the result of the pressure-side fillet geometry, which ultimately affects the pitchwise velocity gradients and reduces the effects of the passage cross-flow leading to weakened axial vorticity along the endwall. Positive axial vorticity seems to be enhanced near the pressure side in Figure 5.11(b) and is most likely the cause of boundary layer re-attachment at this location. Therefore, the working effects of the fillets are visible but do not completely eliminate the secondary flow structures because the passage vortex size still remains dominant on the endwall. The improved orientation is implied by the flow yaw angle, which is reduced near the endwall and more oriented towards the axial direction with the fillet, as shown in Figure 5.11 (d) compared with the baseline data in Figure 5.11(c).

The total pressure loss contours for baseline and fillet at the exit of the passage, plane-3, are given in Figure 5.12 on the left. The exit flow field is measured just aft of the trailing edge (TE) located at Z/P = 0.0 in the figures. A strong passage vortex represented by high $C_{Pt,Loss}$ values occurs at -0.1 < Z/P < 0.2 and 0.1 < Y/S < 0.2 in the baseline contour plot. With the suction-side horseshoe vortex absorbed in this larger vortex system, high value contours are seen near the trailing edge (Wang et al., 1997) at Z/P = 0.0 on the endwall, which represent corner vortices. The column region of high pressure loss coefficient values just about the trailing edge (Z/P < -0.05) are due to the passage wake, a region not well resolved by the five-hole probe.

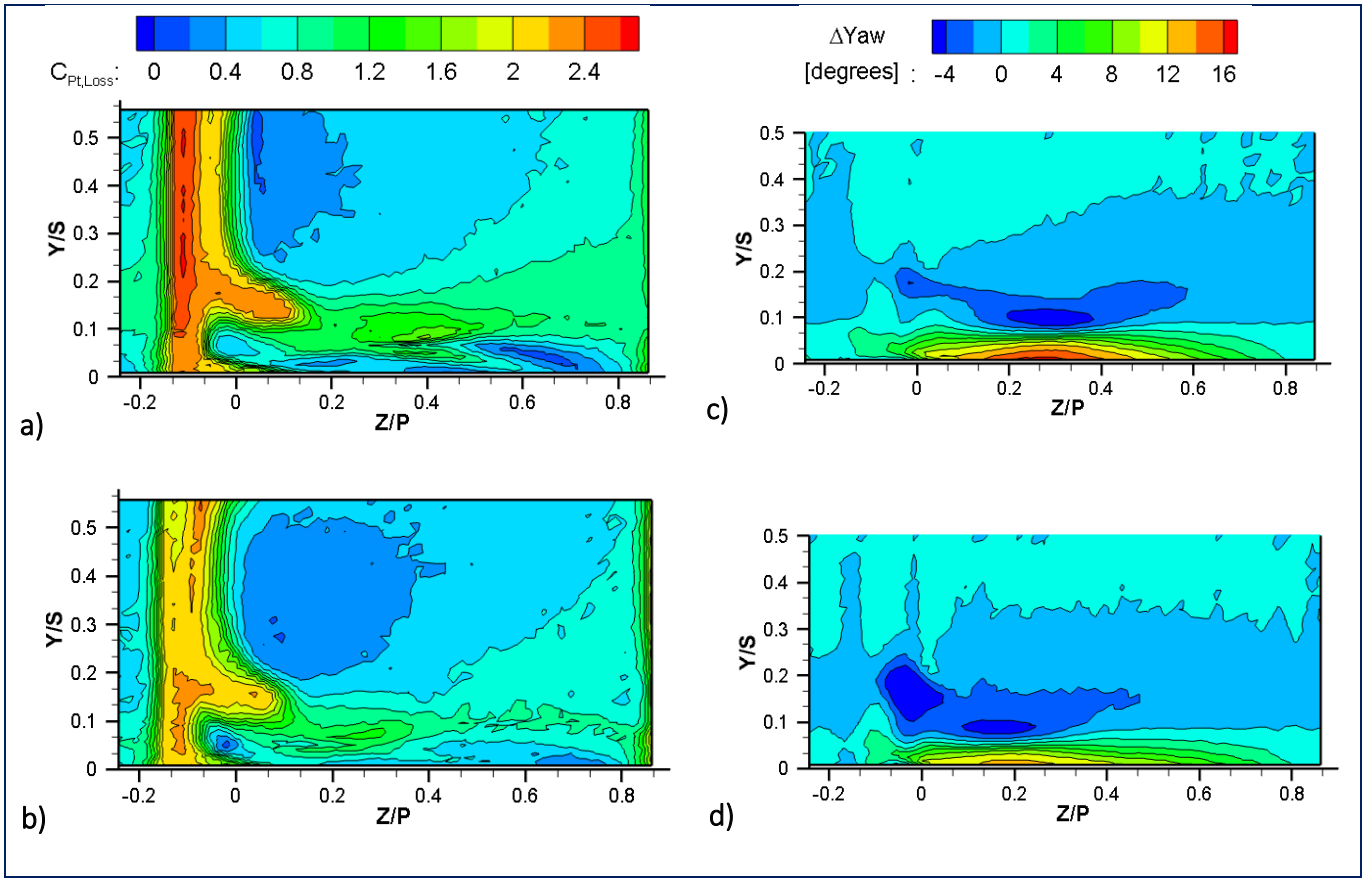

FIGURE 5.12 CONTOURS OF $C_{PT,LOSS}$ (LEFT) AND YAW ANGLE DEVIATION (ΔYAW) (RIGHT) AT PLANE-3 (X_G/C_{AX} = 1.042) FOR (A, C) BASELINE AND (B, D) FILLET.

The fillet case, shown in Figure 5.12 b), indicates a weakened passage vortex with lower $C_{Pt,Loss}$ values at the vortex core, and with slightly smaller region of high $C_{Pt,Loss}$. The yaw angle deviation contours are provided next to the total pressure loss coefficient distributions in Figure 5.12(c) and (d) at plane-3. The yaw angle deviation is computed from the difference between the yaw angles at the midspan (Y/S = 0.5) and local values in the same place. This provides an indication of the flow deviations from the inviscid flow direction leaving the passage. Lower values of ΔYaw are expected at the exit plane for the flow uniformity as the flow enters the next row of blades in the gas turbine passages. The baseline case in Figure 5.12(c) shows large deviations of the flow turning

in the near-wall region (Y/S < 0.1). This region is largely due to the cross-flow in the passage and its effects are minimised when the fillet is introduced. The magnitude of flow angle deviation is reduced slightly in the fillet case along the endwall.

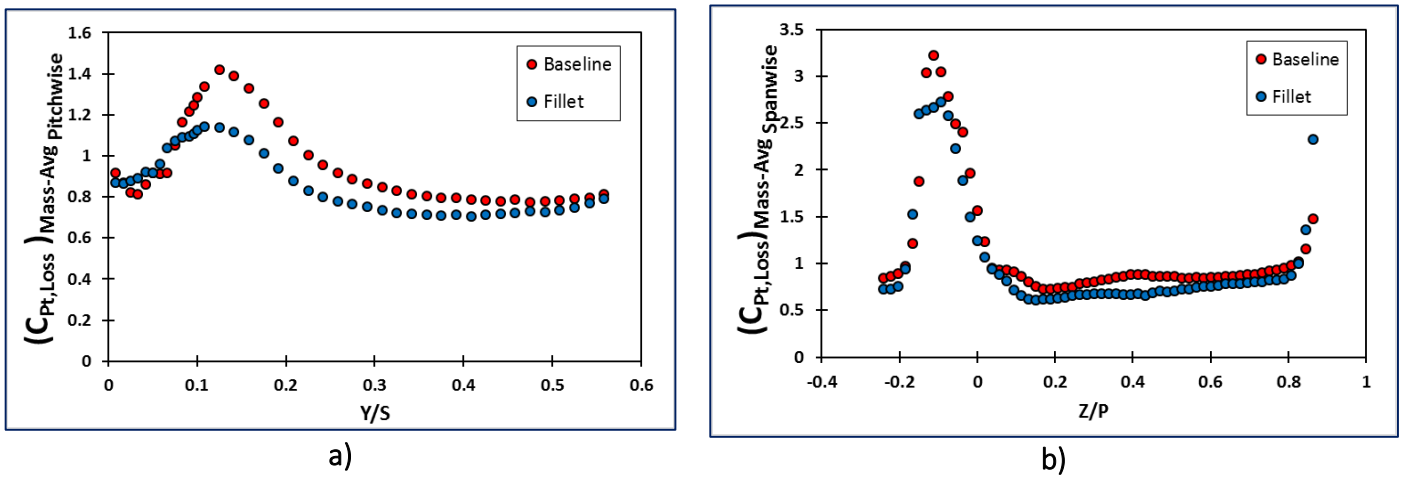

FIGURE 5.13 (A) PITCHWISE- AND (B) SPANWISE MASS -AVERAGED $C_{PT,LOSS}$ AT PLANE-3.

The effects of the fillet are seen at the exit of the passage in the pitchwise (a) and spanwise (b) mass-averaged plots of $C_{Pt,loss}$ at plane-3 in Figure 5.13. The $(C_{Pt,Loss})_{Mass\text{-}Avg}$ values in Figure 5.13 are computed from the local data distributions in Figure 5.12(a & b) at constant Y/S (pitchwise) and Z/P (spanwise) locations in Eq.(5.1) with Simpson's trapezoidal rule for numerical integration. The limit A on the integral is the line area at a given Y-location (pitchwise) or Z-location (spanwise) .The pitchwise mass-averaged $C_{Pt,loss}$ values in Figure 5.13(a) indicate much lower magnitudes across the span of the passage when the fillet is employed, where the most visible results are seen at 0.1 < Y/S < 0.2 where the passage vortex is located, although its influence does not reduce the secondary flow structures completely but rather weakens them downstream of the passage throat. The spanwise mass-averaged $C_{Pt,loss}$ values in Figure 5.13(b) show the same trends as those of the weakened passage vortex, which shows lower magnitudes about the trailing edge (Z/P < 0.0) when the fillet is compared with the baseline result.

$(C_{Pt,Loss})_{Mass\text{-}Avg}$:
$$\left(C_{Pt,Loss}\right)_{Mass-Avg} = \int \rho U \left(\frac{P_{t,ref} - P_{t,local}}{P_{t,ref} - P_{s,ref}}\right) dA \qquad (5.1)$$

Hence the main effects of the fillet are seen upstream of the throat region where the pressure gradient between the pressure side and suction side and the flow angles are reduced, thereby affecting the development and size of the passage vortex system adversely. Additionally, the flow deviations are improved at the passage exit near the endwall surface. The fillet affects the passage cross-flow on the endwall but this reduction in the pitchwise pressure gradients does not reduce

the passage vortex development enough to eliminate its presence at the exit. At this point, there is still potential for further flow field improvements. The effects of upstream slot film-cooling will be discussed next.

5.4 Film-cooling case

The flow field results with the introduction of upstream slot film-cooling are evaluated for the cases of baseline (no fillet) and fillet with four continuous slots. Figure 5.3 shows that the influence of the slot film injection on the blade static pressure at the midspan location is negligible for high inlet blowing ratios and causes almost no change from the baseline measurements. The flow field measurements when the film-cooling flow and fillet are employed, then extend slightly beyond the midspan location. However, the flow field results are presented only in the region above the endwall where the influences of the film-cooling and fillet are present. Therefore, the flow field results will provide further details in the near-wall region where the slot film flow is expected to interact with the boundary layer flow separation and secondary flows in the vane passage. The slot film-cooling blowing ratios and mass flow ratios (MFR) which will be investigated are provided in Table 5.2. The definition of inlet blowing ratio, M_{in} and mass flux ratio (MFR) are provided by Eq. (3.14) and Eq. (3.16) in Chapter 3.

TABLE 5.2 SLOT FILM-COOLING PARAMETERS.

M_{in}	MFR %	
	Case-1 : Baseline	Case-2 : Fillet
1.1	0.8	0.72
1.4	2.53	1.6
1.8	5.12	2.4
2.3	8	3.71

Since film-cooling case-1 employs all four slots injecting coolant into the blade passage, the mass flux ratio is high and increases with M_{in}. The same inlet blowing ratios are applied for case-2 but the film flow rate differs in comparison with that of case-1, being much smaller at the higher M_{in}. This occurs because the case-2 configuration is used as the baseline for the comparison when the fillet is employed along with the film-cooling slots. The fillet covers two of the coolant supply slots just upstream of the blade leading edge. Then case-2 employs only two central slots of which the total cross-sectional area of the film flow ejection plane is less for coolant to be supplied at the same pressure as in the baseline case of 1. This results in higher coolant momentum flow per slot in case-2. The effects of coolant flow rate and momentum can then be evaluated along with slot location for each film-cooling case. The geometry and configuration of the slots are given in Figure 3.15. The flow field results will be compared with the baseline case without the film flow and fillet.

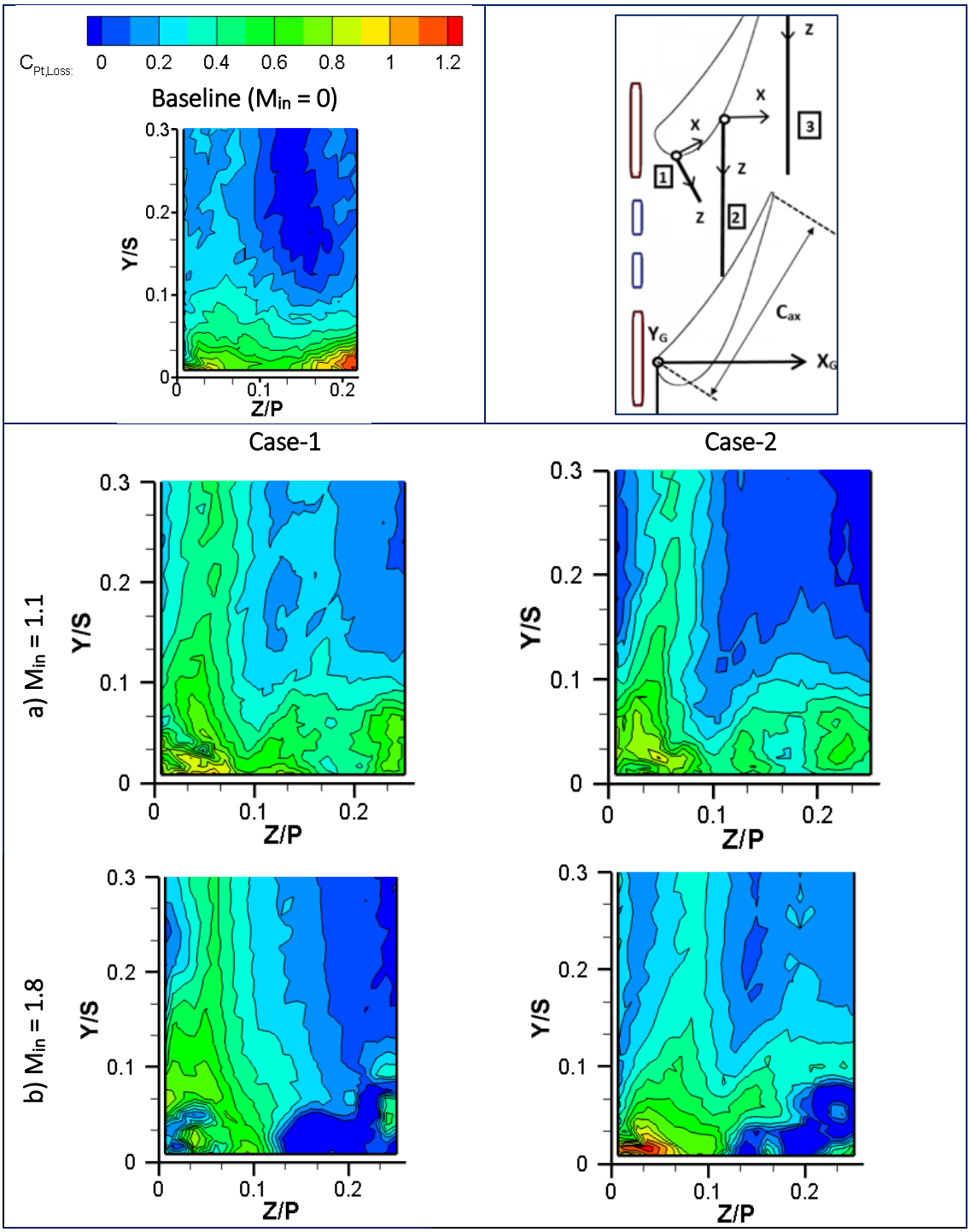

FIGURE 5.14 CONTOURS OF $C_{PT,LOSS}$ AT PLANE-1 (X_G/C_{AX} = 0.251) FOR BASELINE (M_{IN} = 0) AND WITH FILM-COOLING FOR (A) M_{IN} = 1.1 AND (B) M_{IN} = 1.8.

The contours of $C_{Pt,Loss}$ at plane-1 in are given for the two film-cooling cases at M_{in} = 1.1 and 1.8 in Figure 5.14. For completeness M_{in} = 1.4 and 2.3 results for this plane are shown in Figure E.1. As indicated, the case-1 in the figure refers to the configuration of four open slots, while the case-2 configuration refers to the two open slots for the film-cooling. The range of the contour values is

kept the same as in the baseline case given in Figure 5.7, shown again here for comparison. The coolant flow regions are more visible for the higher M_{in}, which are represented by the dark blue regions (zero values) in (b) for both case-1 and case-2. The slots introduce negative total pressure flow in relation to the free stream, which is maintained under suction by the axial fans located downstream of the cascade. Therefore, the actual pressure loss coefficients in these contours are below zero due to the pressure difference between coolant supply and free-stream supply. Nonetheless, they provide clear indication of the film flow effects inside the passage. In Figure 5.14(a), there is very little improvement in the $C_{Pt,Loss}$ distribution for both film-cooling cases.

Comparing the two M_{in} cases in Figure 5.14, it is evident that the higher M_{in} has more favourable effects on the pressure losses. As indicated earlier, the higher the $C_{Pt,Loss}$, the higher the pressure losses. The suction-side blade-endwall junction (Z/P = 0.0) shows lower $C_{Pt,Loss}$ contour values and lower pressure losses when the inlet blowing ratio is increased. At the same location near the suction side, the $C_{Pt,Loss}$ increases slightly as M_{in} increases for case-2. Film-cooling case-1 has better influence at this region because the slots located near the leading edge impact on both the pressure side-leg and suction-side horseshoe vortex formation. However, the higher inlet blowing ratio shows large reductions in pressure losses associated with the pressure-side vortex due to the slot injection (Z/P > 0.1). The effects of case-2, with no slot injection at the leading edge, are then seen with less influence on the suction-side blade corner where the pressure losses remain high. The location of the slots at the leading edge has proven to be effective as the slots impact on the secondary flows at the inlet of the cascade. Friedrichs et al. (1999) emphasised the influence of the three-dimensional separation lines on the film-cooling effectiveness of coolant injected downstream of this region. Therefore, with the slots located about $0.08C_{ax}$ upstream from the leading edge, the interaction between the slot film flow and these separation lines is inevitable.

The vertical wake structures seen in Figure 5.14 for all cases and not seen for the baseline case of Figure 5.7 at 0 < Z/P < 0.15, near the SS surface, are most likely due to the inconsistency of the probe location during measurements as it was difficult to obtain the exact same coordinates for the probe traverse which is manually adjusted for each measurement plane. However, these regions of $C_{Pt,Loss}$ occur due to the proximity of probe resulting in some blockage as well as the boundary layer effect present on the SS blade surface, but appear to be moderately low.

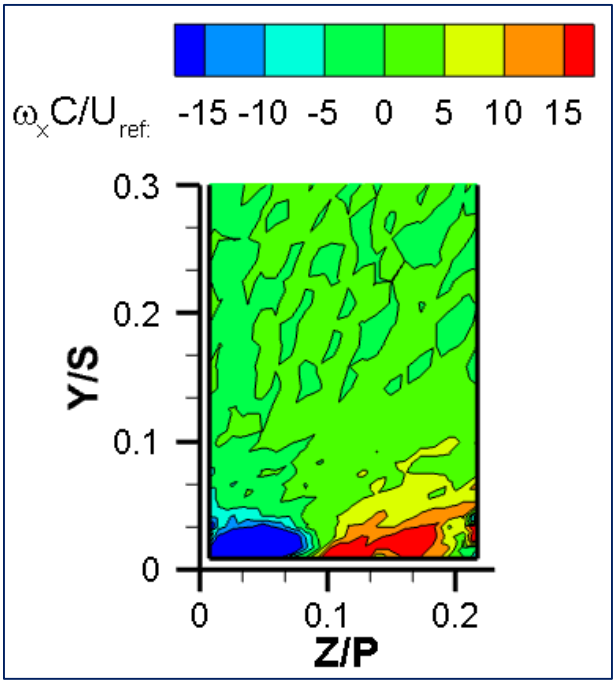

FIGURE 5.15 CONTOUR OF NORMALISED AXIAL VORTICITY AT PLANE-1 (X_G/C_{AX} = 0.251) FOR BASELINE CASE (M_{IN} = 0).

Figure 5.15 provides the normalised axial vorticity distribution at plane-1 for the baseline without film flow. The suction-side corner (Z/P = 0.0) shows negative vorticity, which represents the CCW-rotating suction-side leg horseshoe vortex. Further along the endwall towards the pressure side, a larger region of positive axial vorticity is seen to represent the pressure-side leg horseshoe vortex, with CW-rotation (Mahmood et al., 2008).

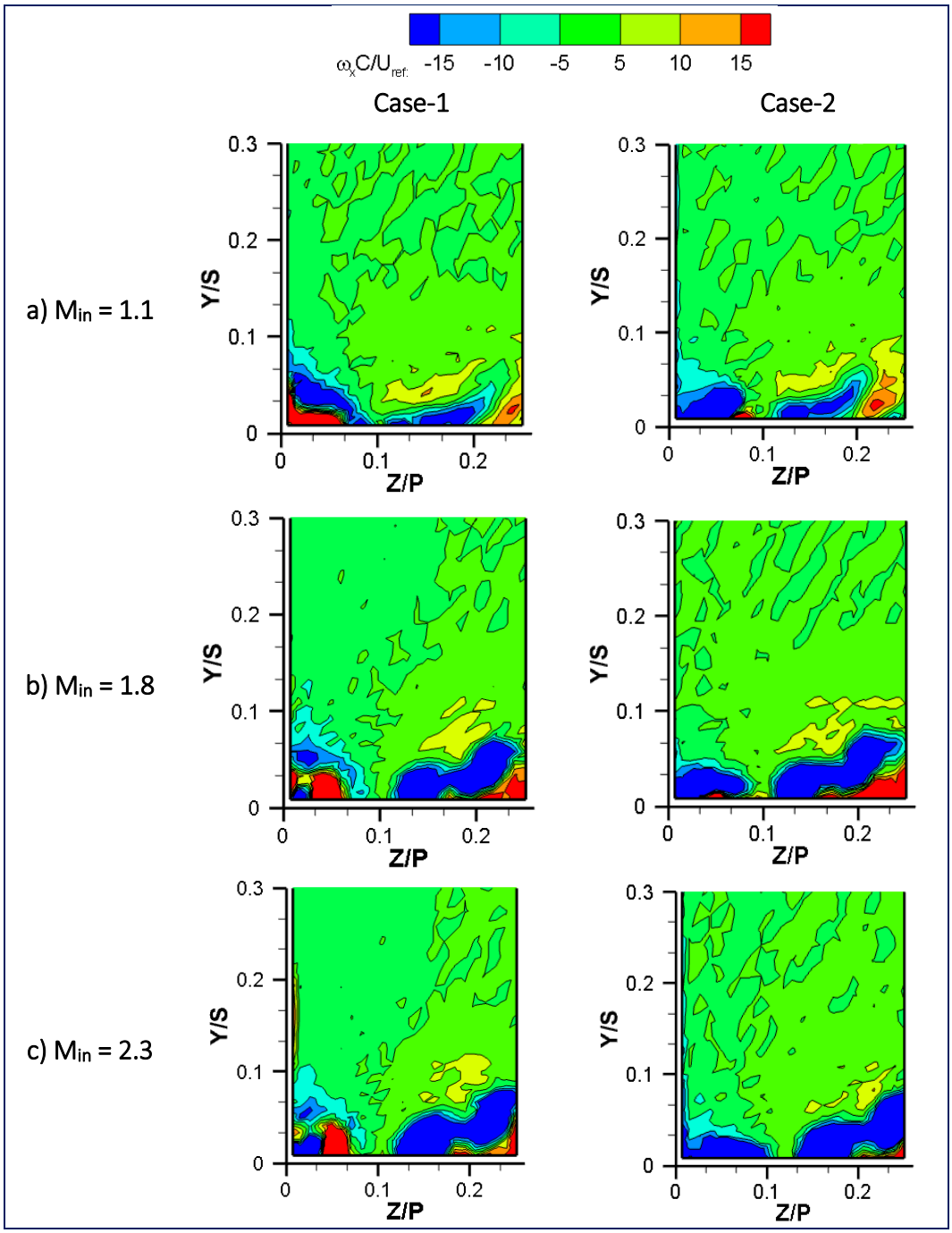

FIGURE 5.16 CONTOURS OF NORMALISED AXIAL VORTICITY AT PLANE-1 (X_G/C_{AX} = 0.251) WITH FILM-COOLING FOR (A) M_{IN} = 1.1; (B) M_{IN} = 1.8 AND (C) M_{IN} = 2.3.

The influences of slot film-cooling are shown in Figure 5.16 for the normalised axial vorticity distributions ($\omega_x C/U_{ref}$) at plane-1 and are compared at different inlet blowing ratios for both film-cooling cases. For M_{in} = 1.4 $\omega_x C/U_{ref}$ contours are shown in Figure E.2, The effects of the leading-edge slots in case-1 and the effects of the central slots in case-2 can be deduced from the contours of $\omega_x C/U_{ref}$ near the endwall surface (Y/S < 0.1), $\omega_x C/U_{ref}$ just above the endwall in Figure 5.16 is

evidence of the film-cooling flow and is caused by the interaction between the film-cooling flow and the boundary layer separation. Comparing the axial vorticity contours for all M_{in} in case-1 indicates that positive axial vorticity is introduced from the leading-edge slots. The leading-edge slot injection then pushes the suction-side vortex (negative) away from the endwall in some cases. The central slots are seen to contribute negative axial vorticity, which seems to move laterally towards the pressure side. The slot injection also travels further into the passage as the inlet blowing ratio increases. In case-1, there are interactions between the film flow from the slots and between the film flow and boundary layer near the suction side. In case-2, there are interactions between the film flow and boundary layer separation near the suction side only. These interactions cause the differences in $\omega_x C/U_{ref}$ contours near the suction side in Figure 5.16. Overall, both film-cooling cases show improvement in the flow field with counteracting axial vorticity. This will further correct the large turning of flow near the endwall-blade junction.

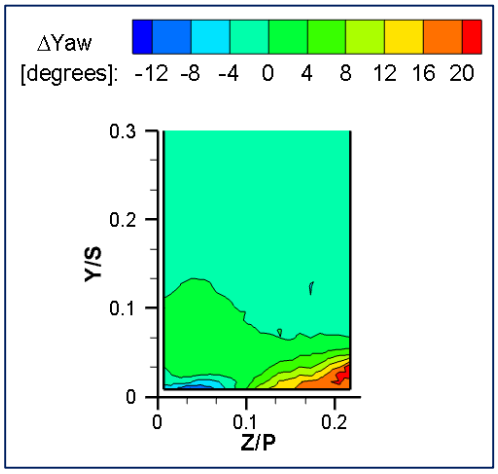

FIGURE 5.17 CONTOUR OF YAW ANGLE DEVIATION (ΔYAW) AT PLANE-1 (X_G/C_{AX} = 0.251) FOR BASELINE CASE (M_{IN} = 0).

The yaw angle deviation for the baseline case (M_{in} = 0) at plane-1 in Figure 5.17 gives an indication of turning of flow near the endwall due to the secondary flows. The positive and negative angles are taken about the z-axis and described in Figure 3.8. The yaw angle deviation is defined by the difference in yaw angle at the midspan to those measured in the same pitch location. Comparing the baseline contour in Figure 5.17 with the film-cooling cases in Figure 5.18 shows a major reduction in the yaw angle deviation along the endwall. The contours for M_{in} = 1.1 and 1.8 are provided in Figure E.3 for completeness. In the contours where the inlet blowing ratio is high, the film-injection region becomes visible by the dark blue values (negative ΔYaw) near the endwall (Y/S < 0.1). The region covered by the slot injection further validates the directional influence shown in the axial vorticity distributions, where the film flow enhances lateral movement towards the pressure side at Z/P > 0.1 and Y/S < 0.1. The effects of each film-cooling case and inlet blowing ratio downstream will provide further details as the passage throat region is evaluated in plane-2.

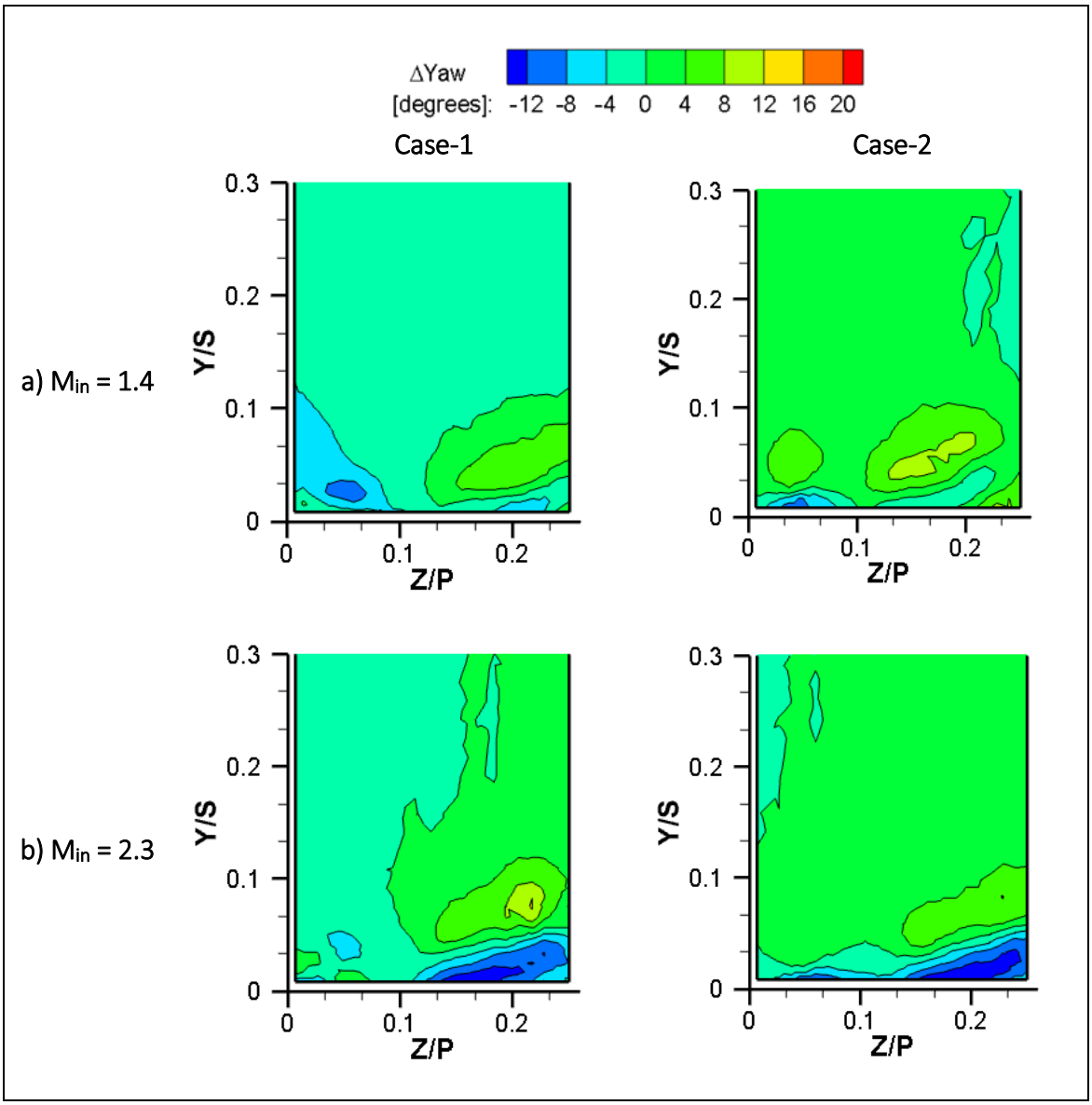

FIGURE 5.18 CONTOURS OF YAW ANGLE DEVIATION AT PLANE-1 (X_G/C_{AX} = 0.251) WITH FILM-COOLING (A) M_{IN} = 1.4 AND (B) M_{IN} = 2.3.

The flow field results at plane-2 are summarised in Figure 5.19 and Figure 5.20 for the film-cooling cases at the lower inlet blowing ratios of 1.1 and 1.4 where the pitchwise-averaged values of yaw angle deviation are provided along with contour plots of $C_{Pt,Loss}$. Refer to Figure E.4 and E.5 for the complete set of results for the film-cooling cases at M_{in} = 1.1 and 1.4 for $C_{Pt,Loss}$ and ΔYaw contours, respectively. The pitchwise-averaged ΔYaw is computed by taking the average of the local yaw angle deviation values at each span location Y/S along the pitch direction. These inlet blowing ratios are fairly low in terms of coolant flow rate and injection momentum and as such show minimal influence on the aerodynamic losses. The presence of film-cooling flow for both case-1 and case-2 does not show any improvement in Figure 5.19(a, b) in the near-wall region (Y/S < 0.05) when compared with the baseline case in Figure 5.10(a), also shown again here for comparison.

Burd and Simon (1999) show that the pressure losses increase in the boundary layer region when film-cooling is introduced at low blowing ratio due to the mixing of coolant and mainstream flows but these losses reduce at an optimum coolant supply rate. The yaw angle deviation in Figure 5.20(a, b) shows a slight improvement at the endwall (Y/S < 0.1) due to the slot injection. Overall, both results in Figure 5.19 and Figure 5.20, follow the same trend as the baseline case and display small influences in lowering the $C_{Pt,Loss}$ and flow yaw-angle deviations because the film-cooling flow at low M_{in} is employed. The decrease in ΔYaw near the endwall inside the passage is desirable with any film-cooling flow because: (i) the pitchwise flow is then reduced, adversely affecting the passage vortex formation and (ii) the coolant flow then also spreads uniformly in the pitchwise direction, positively affecting the film coverage on the endwall.

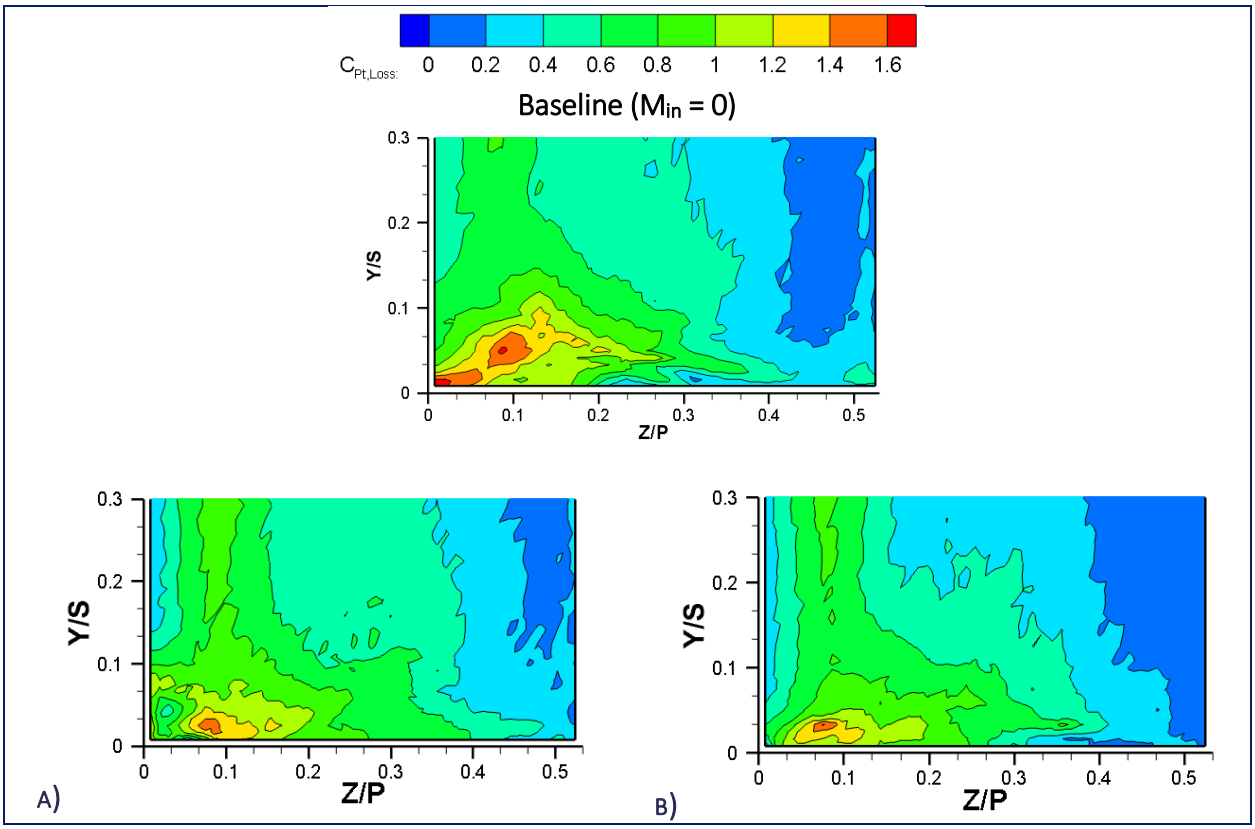

FIGURE 5.19 CONTOUR PLOT OF $C_{PT,LOSS}$ AT PLANE-2 (X_G/C_{AX} = 0.58) FOR BASELINE (M_{IN} = 0) FILM-COOLING (A) CASE-1 M_{IN} = 1.4 AND (B) CASE-2 M_{IN} = 1.1.

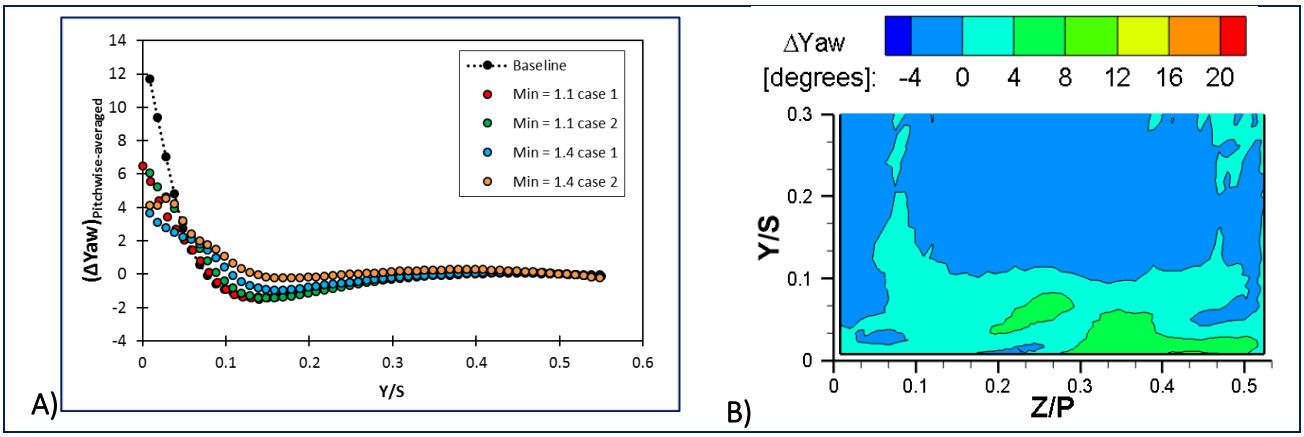

FIGURE 5.20 A) LINE PLOT OF PITCHWISE-AVERAGED YAW ANGLE DEVIATION (ΔYAW) AT PLANE-2 (X_G/C_{AX} = 0.58) FOR FILM-COOLING CASES AT M_{IN} = 1.1 AND 1.4 AND B) CONTOUR OF YAW ANGLE DEVIATION (ΔYAW) AT PLANE-2 (X_G/C_{AX} = 0.58) FOR FILM-COOLING CASE-1 AT M_{IN} = 1.4.

Plane-2 is located just upstream of the throat region near the vane-4 suction side and at this location, the baseline case shows the presence of a combined suction-side leg and pressure-side leg vortex system known as the passage vortex. and Figure 5.22 compare the contours of $C_{Pt,Loss}$ at plane-2 for the two film-cooling cases at M_{in} = 1.8 and 2.3 respectively. The baseline contour of $C_{Pt,Loss}$ in the same plane is also included in for the convenience of comparisons.

The effects of the slot injection on the passage vortex are more pronounced in case-1 than in case-2 near the suction-side blade surface (Z/P < 0.05) for both inlet blowing ratios in and Figure 5.22. Additionally, the strong presence of coolant flow from the slot injection is more pronounced at M_{in} = 2.3 for both cases (0.2 < Z/P < 0.4) where $C_{Pt,Loss}$ contours have negative values just above the endwall. By observing the contour magnitudes, it is evident that case-1 is more successful in reducing the intensity of the secondary flows with suppressed structures near the suction-side blade-endwall region at this location. Case-2 tends to enhance the pressure losses along the blade span, which suggests that the increased film flow rates at the leading edge have adverse effects in this region. Case-1 in general reduces the strength of the vortex structures in the blade-endwall corner on the suction side where $C_{Pt,Loss}$ values are lower compared with the baseline and Case-2. Near the pressure-side region at Z/P > 0.4, the $C_{Pt,Loss}$ < 0 values just above the endwall show a large region of the film flow from the slot located at the leading edge of vane-3, at M_{in} = 2.3. Knost and Thole (2005) indicate that the film-cooling distribution is highly dependent on the near-wall pressure field and streamlines along the passage endwall.

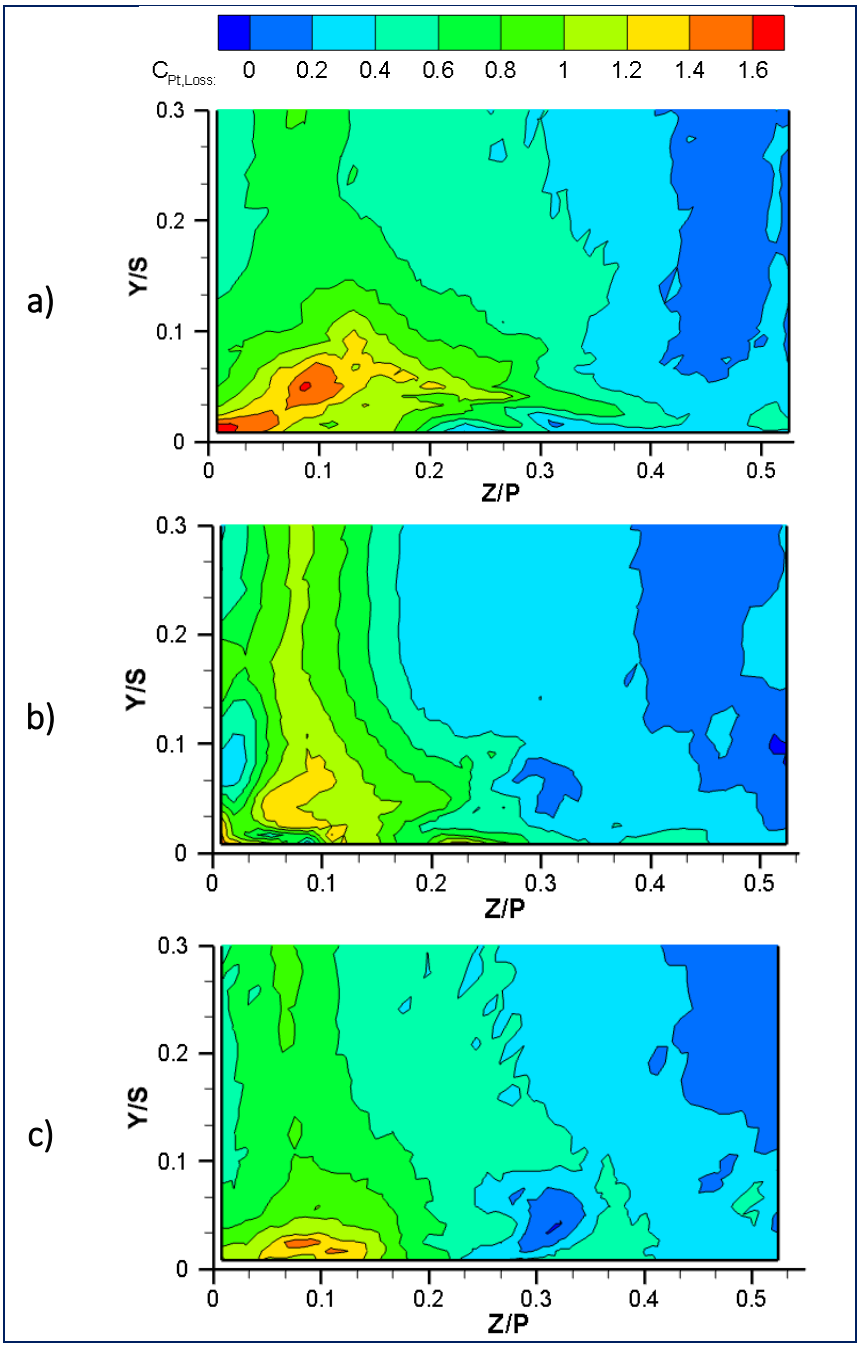

FIGURE 5.21 CONTOURS OF $C_{PT,LOSS}$ AT PLANE-2 (X_G/C_{AX} = 0.58) FOR (A) BASELINE (M_{IN} = 0) AND WITH FILM-COOLING M_{IN} = 1.8 FOR (B) CASE-1 AND (C) CASE-2.

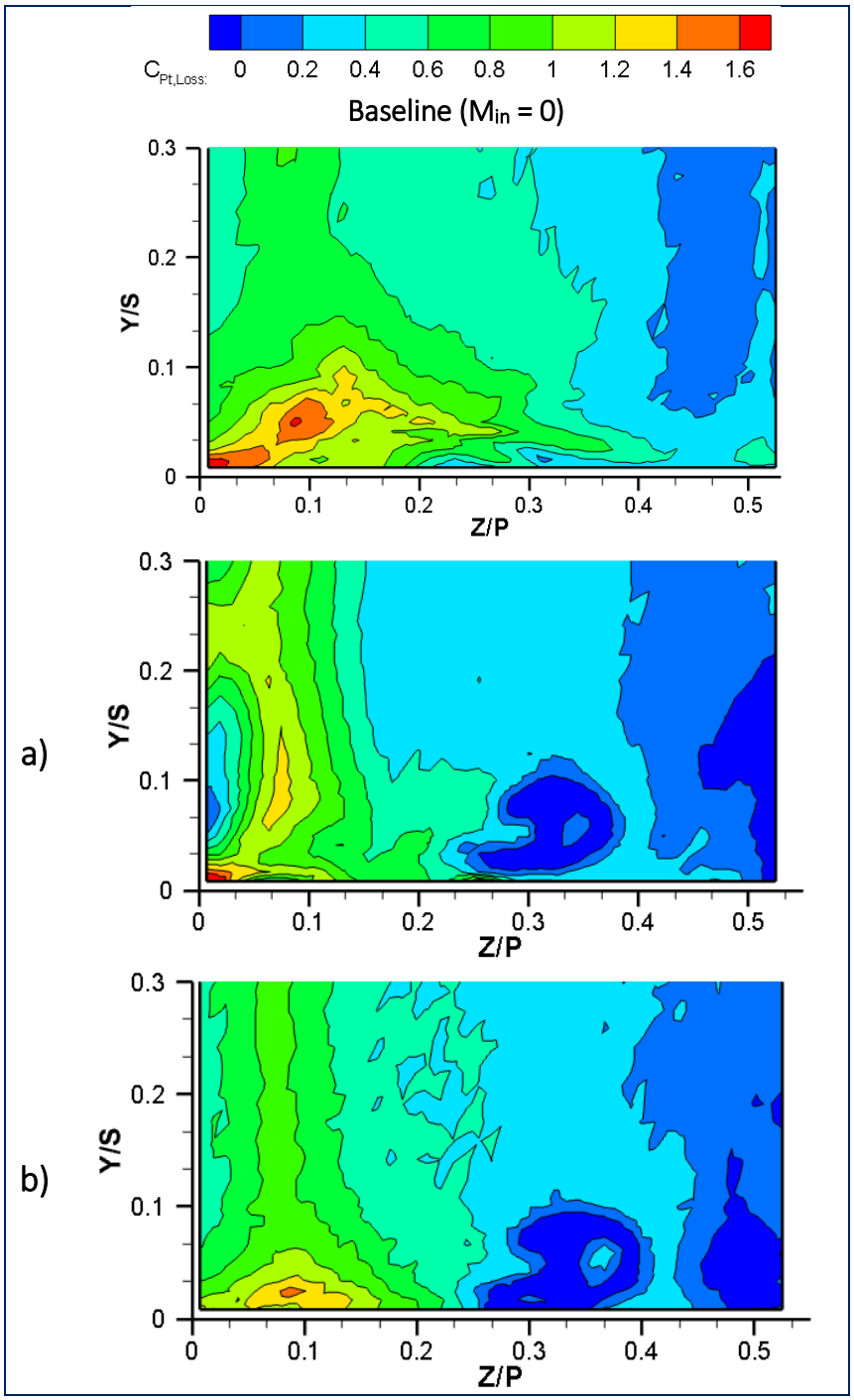

FIGURE 5.22 CONTOURS OF $C_{PT,LOSS}$ AT PLANE-2 (X_G/C_{AX} = 0.58) FOR BASELINE (M_{IN} = 0) AND WITH FILM-COOLING M_{IN} = 2.3 FOR (A) CASE-1 AND (B) CASE-2.

Evidently, case-2 shows better reductions in the pressure losses near the suction-side endwall. Thus, comparison of the yaw angle deviation in this plane for case-2 at the higher inlet blowing ratios is given in Figure 5.23. The baseline case in Figure 5.23 a) shows large flow angle deviation in the near-wall region (Y/S < 0.1) where the effects of the passage cross-flow are seen. Because the yaw angle notation given in Figure 3.8 describes the change in the flow direction along the

blade pitch, the ΔYaw contours in Figure 5.23 then describe the pitchwise velocity gradients in the passage (z-direction).

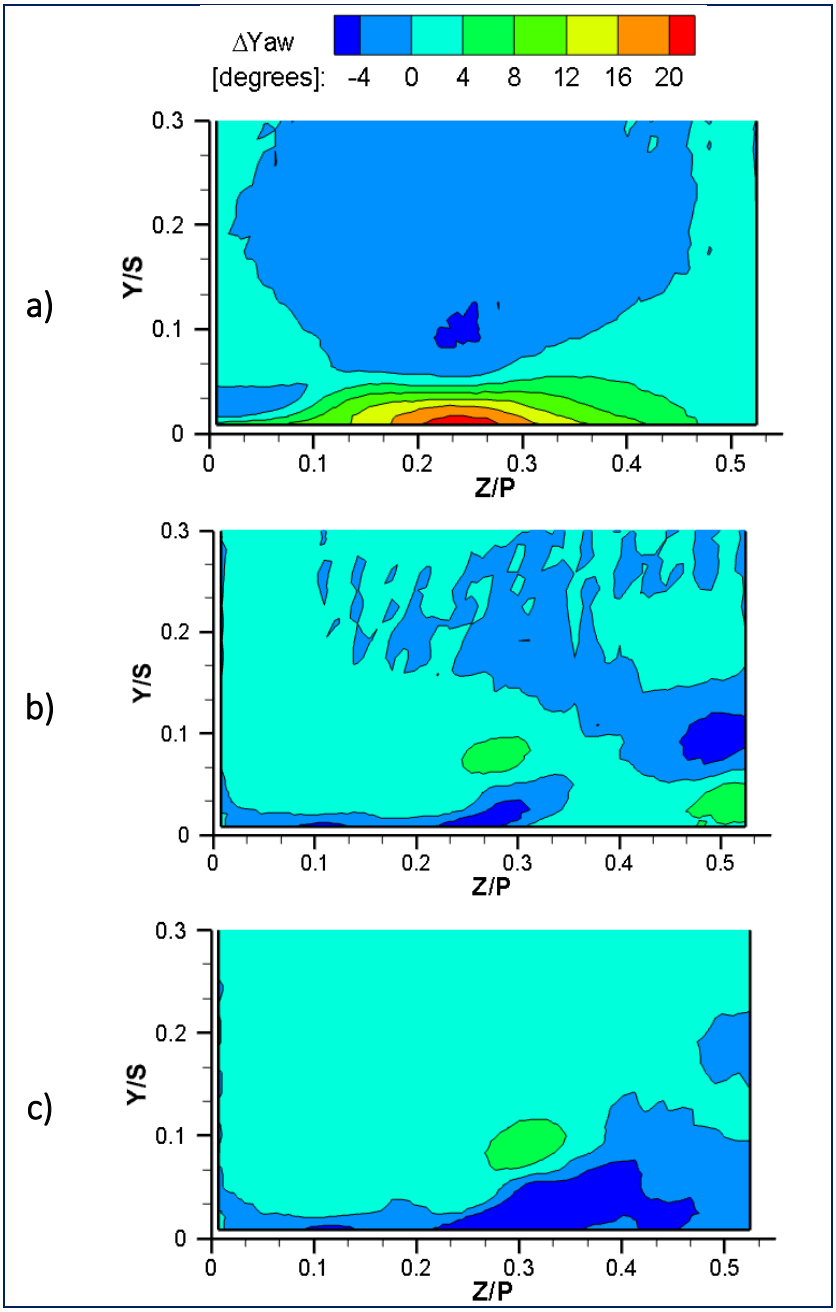

FIGURE 5.23 CONTOURS OF YAW ANGLE DEVIATION AT PLANE-2 (X_G/C_{AX} = 0.58) FOR (A) BASELINE (M_{IN} = 0) AND FILM-COOLING CASE-2 (B) M_{IN} = 1.8 AND (C) M_{IN} = 2.3.

Comparing the yaw angle deviation contours when film-cooling is introduced at high MFR in Figure 5.23 b) and c) shows ΔYaw < 0 implicating a complete reversal in the flow angles near the endwall surface. For the same M_{in} and film-cooling case 1, refer to Figure E.6.

The effects of the high momentum slot flow are further evaluated by comparing the normalised axial vorticity distribution at plane-2 for both film-cooling cases in Figure 5.24. For the inlet blowing ratio M_{in} = 1.4, the contour plots of normalised axial vorticity are provided in Figure E.7 at plane-2. As noted before, the axial vorticity describes the rotation and size of the vortex structures present, with negative values indicating counter-clockwise rotation. The baseline case provided in Figure 5.11 a), and shown here again for comparison, indicates that the larger positive pressure-side vortex is enhanced by the strong cross-flow in the passage along the endwall. A smaller region of negative axial vorticity then represents the suction-side vortex structure in the passage vortex system. However, the high values of the vorticity contours just above the endwall shown in Figure 5.24 for film-cooling flows do not indicate the pressure side-leg and suction side-leg vortex distinctively because of the strong interactions between the film flow and boundary layer, and interactions between the film flow and secondary flows. Figure 5.24a) presents the normalised axial vorticity contours at M_{in} = 1.1 and shows less pronounced vortex structures. The high values of positive and negative $\omega_x C/U_{ref}$ just above the endwall become more prominent as the M_{in} increases in Figure 5.24 and indicate the stronger and wider presence of the coolant flow across the pitch as M_{in} increases. This occurs as the high momentum jet of the film flow at high M_{in} travels further into the passage before being lifted by the secondary flows. In addition, the influence of the film on the secondary flows, boundary layer, and on each other from the different slots grow stronger as M_{in} increases to cause high $\omega_x C/U_{ref}$ distributions in Figure 5.24.

As seen in plane-1, the slot injection induces large regions of negative axial vorticity due to the interaction with the passage flow field. The large blue regions grow in size with increasing M_{in} and for case-1, the effects are attenuated along the pressure-side blade region ($Z/P > 0.4$). Furthermore, the negative vorticity regions of the slot injection indicate lateral movement towards the pressure-side blade for all cases at the higher inlet blowing ratios. This movement is seen to be opposite to the cross-flow direction of the passage and can be attributed to the reduction in the pitchwise pressure gradient and the improvement in the flow angles seen previously. From Figure 5.24, the leading-edge slot injection in case-1 interacts with the blade-endwall junction and the figure shows positive induced axial vorticity in those regions $Z/P < 0{,}1$ and $Z/P > 0.4$, which conveniently counteracts the suction-side vorticity with increasing M_{in}. The pressure-side region, $Z/P > 0.3$, however, results in enhanced positive axial vorticity and for case-2, these effects are not dealt with because only the central slots are employed. Therefore, case-1 has favourable effects near the suction-side endwall junction and case-2 has more influence on the passage cross-flow, which drives the passage vortex, seen in Figure 5.24(c) for case-2, where there is a smaller region of positive $\omega_x C/U_{ref}$ values between $0.2 < Z/P < 0.4$ near the endwall ($Y/S < 0.1$). Increasing M_{in}, however, reduces the adverse effects of the pressure-side $\omega_x C/U_{ref}$ values to some degree.

The effects of the induced vorticity patterns created by the slot injection have deterministic effects on the passage flow field and influence the total pressure losses. These effects are summarised in

the pitchwise-averaged line plots of $C_{Pt,Loss}$ and yaw angle deviation (ΔYaw) at plane-2 for M_{in} = 1.8 and 2.3 in Figure 5.26 and Figure 5.25 respectively. The pitchwise-averaged data is computed by taking the arithmetic average of the local values at each span location Y/S along the pitch direction.

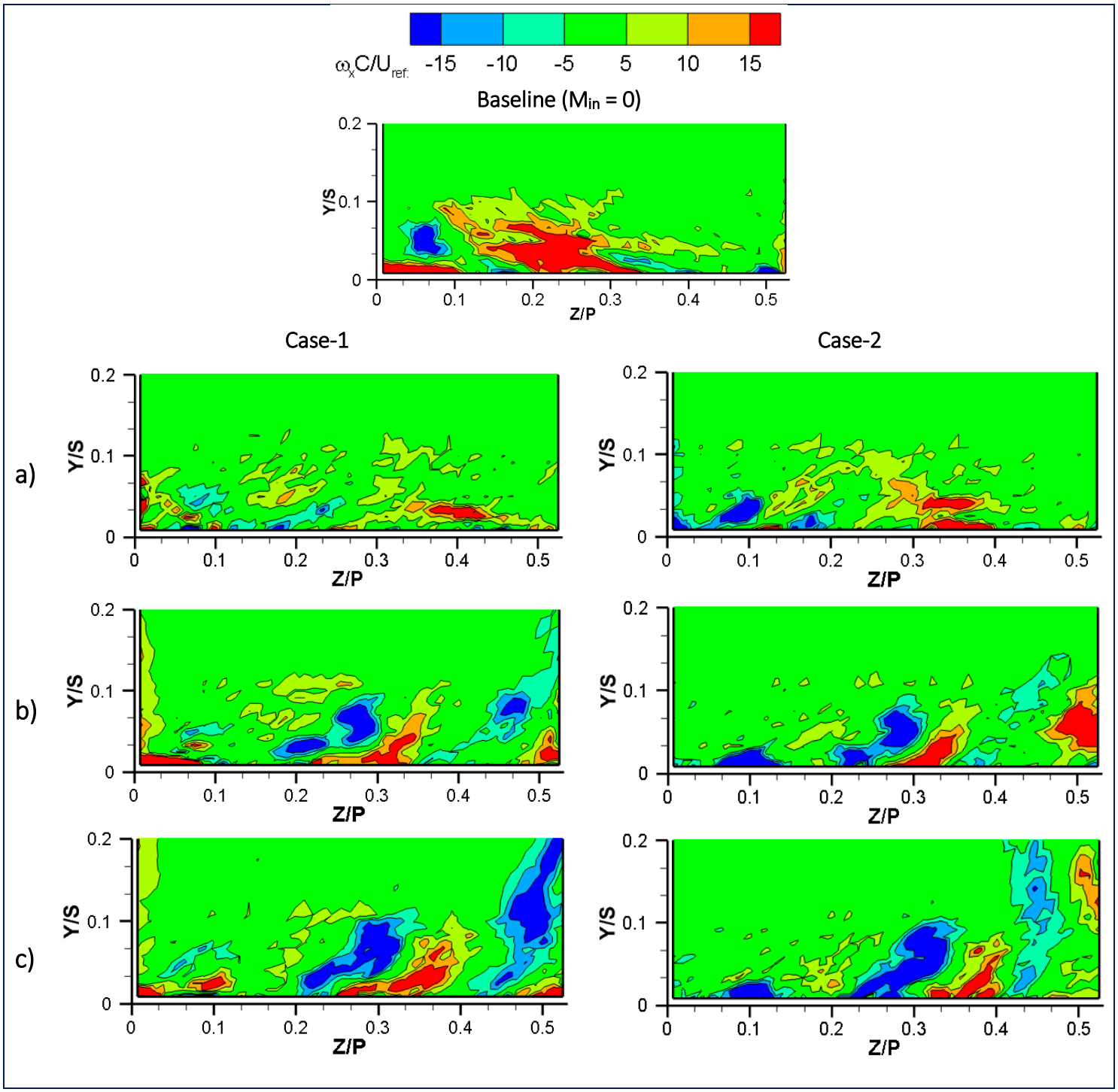

FIGURE 5.24 CONTOURS OF NORMALISED AXIAL VORTICITY AT PLANE-2 (X_G/C_{AX} = 0.58) FOR BASELINE (M_{IN} = 0) AND WITH FILM-COOLING (A) M_{IN} = 1.1, (B) M_{IN} = 1.8 AND (C) M_{IN} = 2.3.

At high MFR (M_{in}), it can be seen that the averaged yaw angle deviation in Figure 5.25 is reversed in magnitude at the near-wall region from baseline data, i.e. ΔYaw for the film flow is negative where ΔYaw for the baseline is positive and vice versa. These correspond to the lowest averaged $C_{Pt,Loss}$ near the endwall for the same film-cooling M_{in} in Figure 5.26. The highly reversed flow direction near the endwall therefore has significant implications on the pressure loss and provides some form of counteraction in the secondary flows. The highest M_{in} proves to be most effective in reducing the aerodynamic losses at plane-2. Measurements in plane-3 will be evaluated next to determine the effects of upstream slot film-cooling at the passage exit.

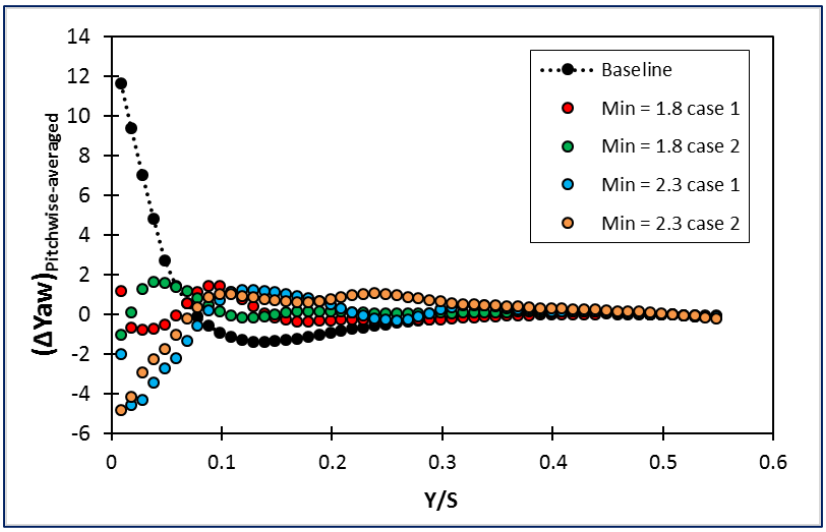

FIGURE 5.25 LINE PLOT OF PITCHWISE-AVERAGED YAW ANGLE DEVIATION (ΔYAW) AT PLANE-2 (X_G/C_{AX} = 0.58) FOR FILM-COOLING CASES AT M_{IN} = 1.8 AND 2.3.

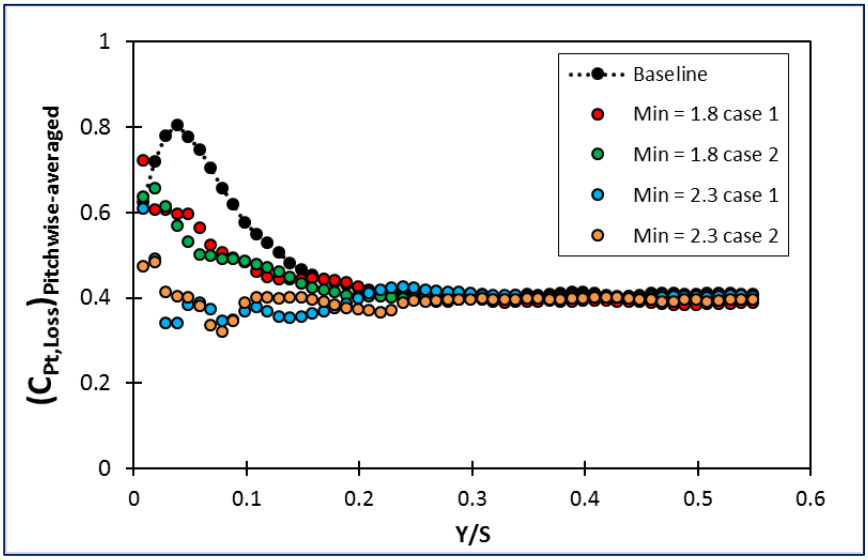

FIGURE 5.26 LINE PLOT OF PITCHWISE-AVERAGED $C_{PT,LOSS}$ AT PLANE-2 (X_G/C_{AX} = 0.58) FOR FILM-COOLING CASES AT M_{IN} = 1.8 AND 2.3.

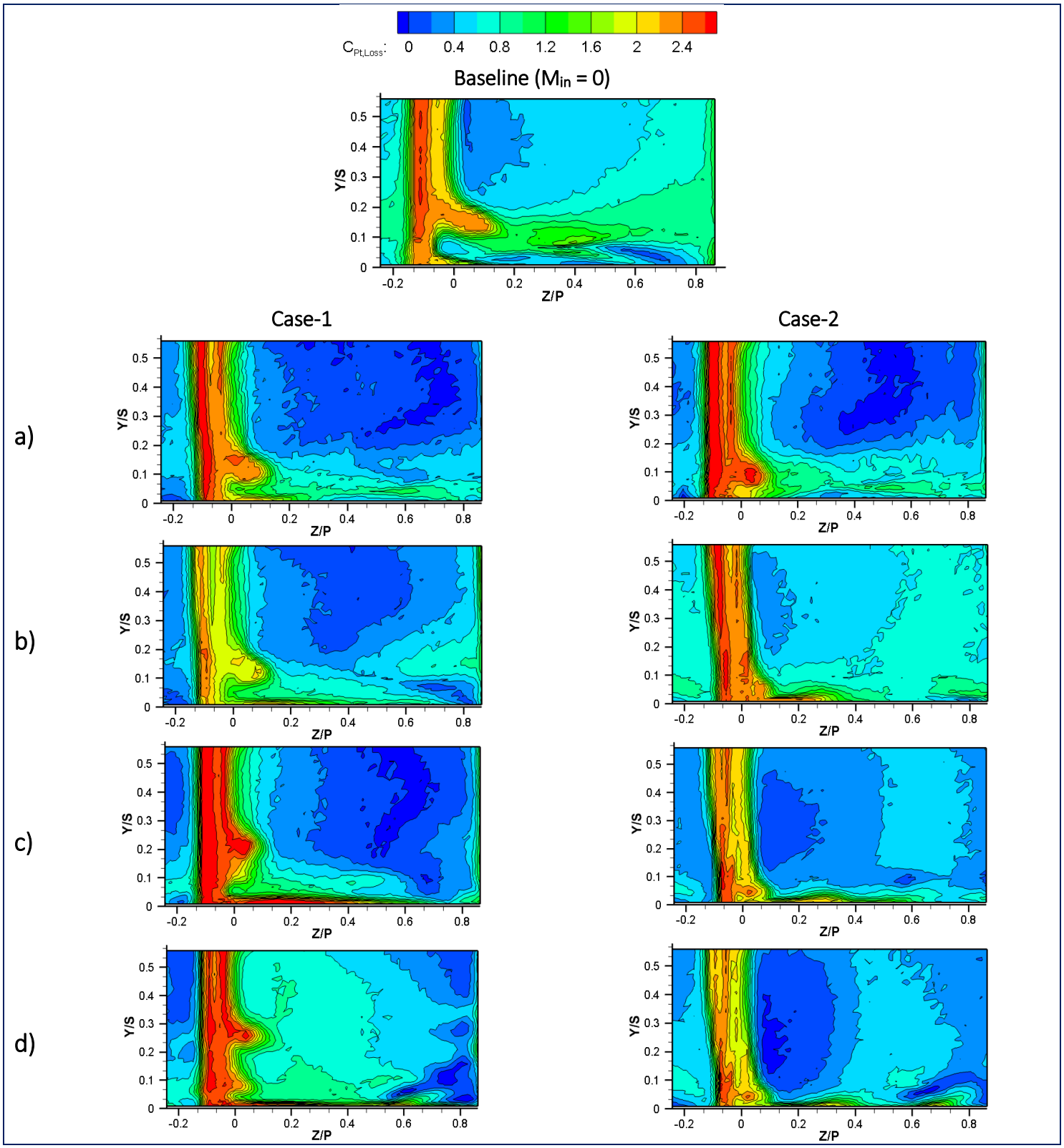

FIGURE 5.27 CONTOURS OF $C_{PT,LOSS}$ AT PLANE-3 (X_G/C_{AX} = 1.042) FOR BASELINE (M_{IN} = 0) AND FILM-COOLING CASES AT (A) M_{IN} = 1.1, (B) M_{IN} = 1.4, (C) M_{IN} = 1.8 AND (D) M_{IN} = 2.3.

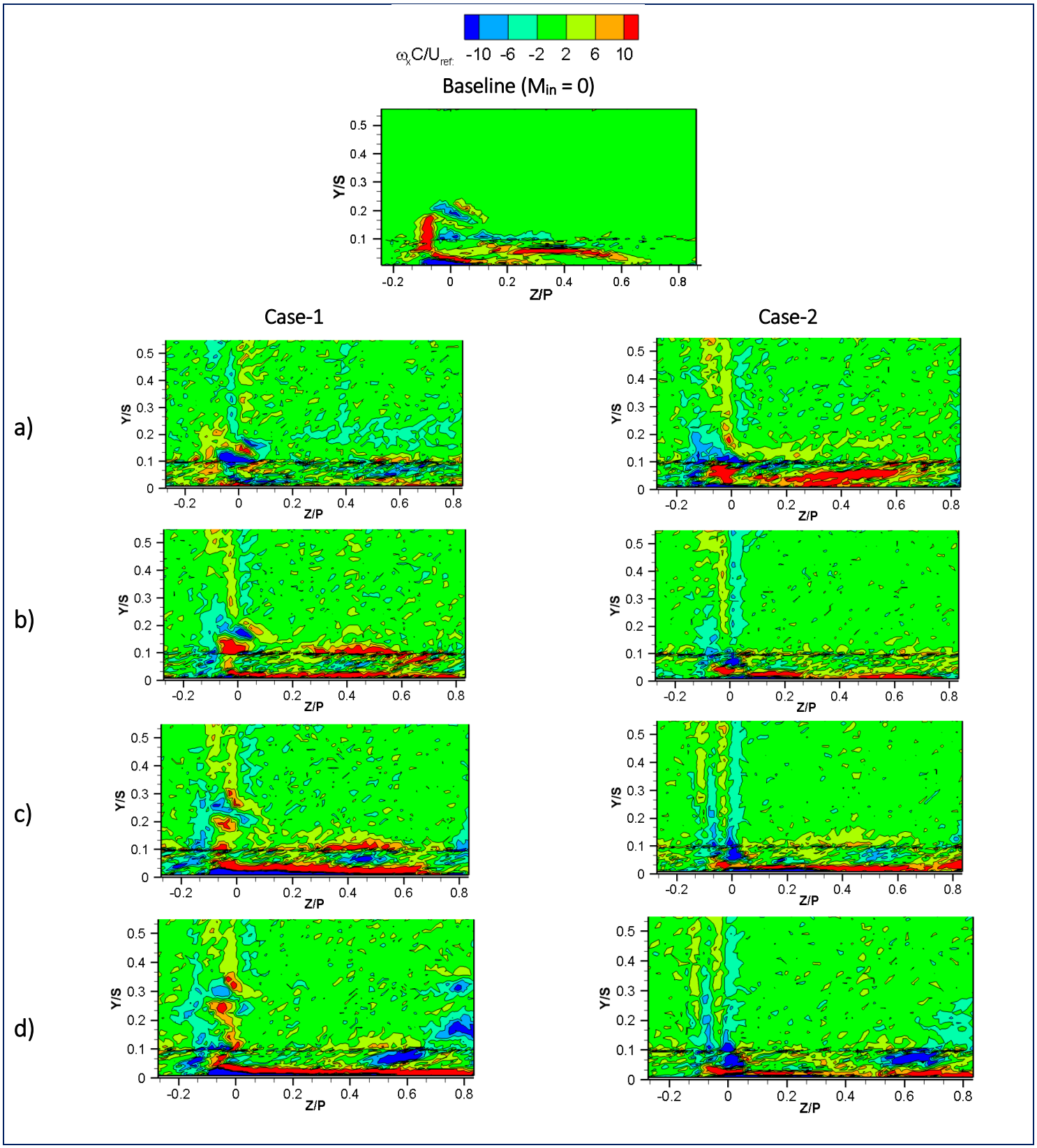

FIGURE 5.28 CONTOURS OF $\omega_X C/U_{REF}$ AT PLANE-3 (X_G/C_{AX} = 1.042) FOR BASELINE (M_{IN} = 0) AND FILM-COOLING CASES AT (A) M_{IN} = 1.1, (B) M_{IN} = 1.4, (C) M_{IN} = 1.8 AND (D) M_{IN} = 2.3.

Figure 5.27 compares contours of $C_{Pt,Loss}$ at plane-3 and Figure 5.28 provides the contours of $\omega_x C/U_{ref}$ for all inlet blowing ratios and both film-cooling cases. The baseline contour of $C_{Pt,Loss}$ at this plane is shown in Figure 5.12(a), provided again here for comparison. The contour levels are kept the same in both Figure 5.12(a) and Figure 5.27 for convenience. At the exit of the passage, the passage vortex is now fully developed and migrates towards the suction-side blade surface where the suction-side vortex is now entrained in this larger vortex system. The passage wake is seen in the columnar region of high $C_{Pt,Loss}$ located near the trailing edge of vane-4 at about -0.14 <Z/P< -0.07. The high $C_{Pt,Loss}$ region beyond the trailing-edge wake region then indicates the passage vortex region in Figure 5.12(a) (baseline) and Figure 5.27 (Case-1). However, the complete structure and size of the passage vortex are difficult to distinguish in Figure 5.27 and Figure 5.12 (a) because the passage vortex interacts with the trailing-edge wake. Consequently, a distinctive $C_{Pt,Loss}$ region in the passage vortex of Case-2 is not seen clearly in Figure 5.27. The $\omega_x C/U_{ref}$ contours shown in Figure 5.28 exhibit similar instances where the passage vortex is not clearly distinguished but it can be seen that the slot injection results in some changes along the endwall surface with both positive and negative values of $\omega_x C/U_{ref}$ for Y/S < 0.1. Case-2 also shows a larger reduction in the passage vortex region near the wake at -0.2 < Z/P < 0.0 when M_{in} increases, when compared with those of case-1 and the baseline case (M_{in} = 0).

All film-cooling cases and M_{in} in Figure 5.27 indicate a reduction in the $C_{Pt,Loss}$ values in the passage vortex region implicating the weaker passage vortex system compared with the baseline result. At the lower M_{in} = 1.1 and 1.4 in Figure 5.27(a & b), the main effects are seen in the reduction of the passage vortex size. However, the passage vortex strength at M_{in}=1.1 for case-2 seems to be slightly higher than for case-1 due to enhanced $C_{Pt,Loss}$ at the vortex core (0 < Z/P < 0.1). The passage vortex core with higher $C_{Pt,Loss}$ for the case-2 at all M_{in} seems to be located nearer the endwall. This may be the result of the weaker passage vortex system for case-2. The passage vortex migrates further away from the endwall as it gains energy from the cross-flow (Mahmood et al., 2005). Case-1 shows an opposing effect as the increased film flow rates with M_{in} tend to push the vortex system further away from the endwall with increased strength. Aunapu et al. (2000) describes the same results as in case-1 and suggests that the mainstream flow would carry away the vortex system and improve the endwall boundary layer considerably. At M_{in} = 2.3 for case-1, however, the slot injection results in a distinctive second high $C_{Pt,Loss}$ region near the endwall, which fairs worse than in case-2. This may be the adverse effects of positive axial vorticity induced by the film flow as can be seen at the plane-2 upstream slots. Thus, the most effective film-cooling supply is seen to be for M_{in} = 2.3 with case-2 providing the highest reduction in the total pressure loss at the exit of the passage. Additionally, the higher M_{in} results in a relocation of the boundary layer reattachment line in the passage causing the boundary layer to be thicker due to the film flow from the slots in both cases. Thus, the endwall boundary layer is re-energised with the introduction of slot film flow, similarly shown by Knost and Thole (2005) and Gustafson et al.

(2007), which has favourable effects on the passage flow field. Kang et al. (1999) further indicates that more intense secondary flows arise when the endwall boundary layer becomes thinner.

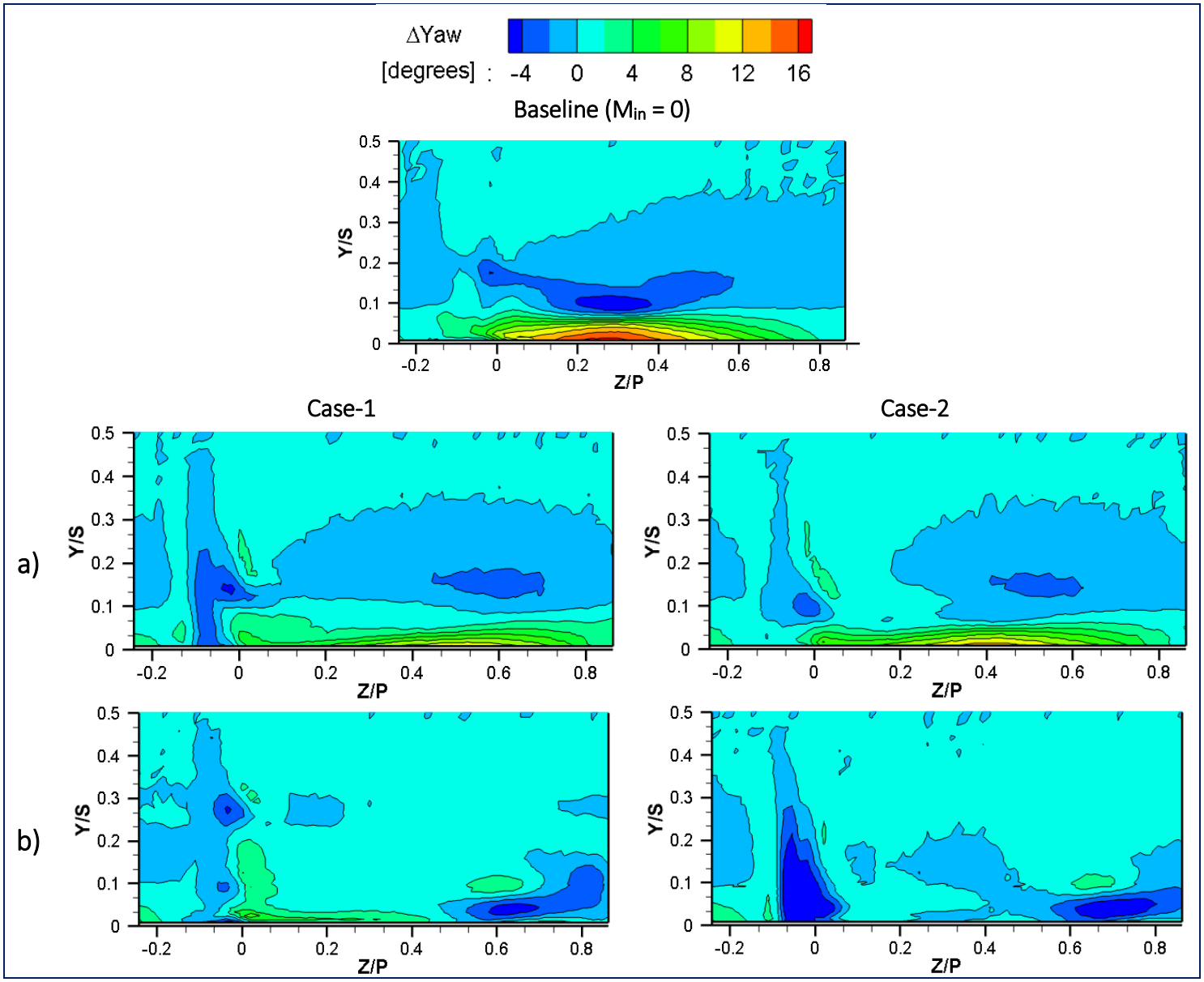

FIGURE 5.29 CONTOURS OF YAW ANGLE DEVIATION (ΔYAW) AT PLANE-3 (X_G/C_{AX} = 1.042) FOR BASELINE (M_{IN} = 0) AND FILM-COOLING AT (A) M_{IN} = 1.1 AND (B) M_{IN} = 2.3.

The flow angles at the passage exit are compared in with contours of the yaw angle deviation at plane-3 for both film-cooling cases at M_{in} = 1.1 and 2.3. The lower M_{in} shows minor reductions in the yaw angle deviation because there is still a large region along the endwall with high yaw turning of the flow as in the baseline contour in Figure 5.12, shown again here for comparison. The ΔYaw contours at M_{in} = 1.4 and 1.8 are provided in Figure E.8 for completeness. The contours of pitch angle are then presented for both film-cooling cases and all M_{in} at plane-3 in Figure E.16 for full

display of the flow angle behaviour at this location in the passage. The large region of turning is attributed to the passage cross-flow and is thus too strong to be influenced by the low film flow injection. At M_{in} = 2.3, both film-cooling cases show significant reduction of ΔYaw compared with those in the baseline flow near the endwall. The film flow is indicated in both cases at the endwall regions of negative ΔYaw.

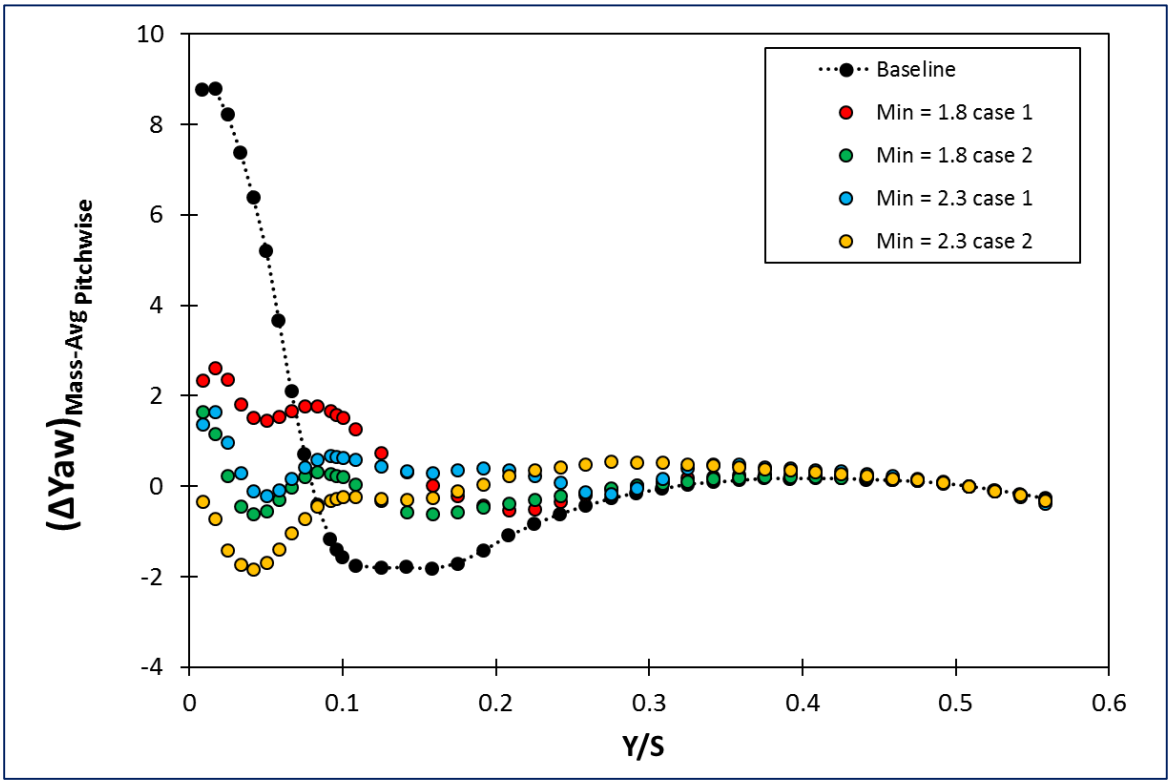

FIGURE 5.30 LINE PLOT OF PITCHWISE MASS-AVERAGED YAW ANGLE DEVIATION (ΔYAW) AT PLANE-3 (X_G/C_{AX} = 1.042) FOR FILM-COOLING CASES AT M_{IN} = 1.8 AND 2.3.

The pitchwise mass-averaged yaw angle deviation ΔYaw at plane-3 is shown in Figure 5.30 and summarises the performance of the film-cooling cases at high M_{in}. The pitchwise mass-averaged ΔYaw is computed similarly as in the $C_{Pt,Loss}$ by numerical integration at constant Y-locations using the data distributions such as those in . It can be seen that case-2 induces yaw angle deviation closer to 0° near the endwall, which ties in with the vorticity strength seen earlier at plane-2 and plane-3 in Figure 5.24 and Figure 5.27. These flow field effects then result in the reduction of the passage cross-flow at the exit, which is achieved at high slot injection rates. The outcome of this reduction in the passage cross-flow is then seen by the reduction in total pressure loss of the passage vortex system. The lower film flow rates therefore do not encourage this flow turnaround further into the passage as with the higher M_{in}.

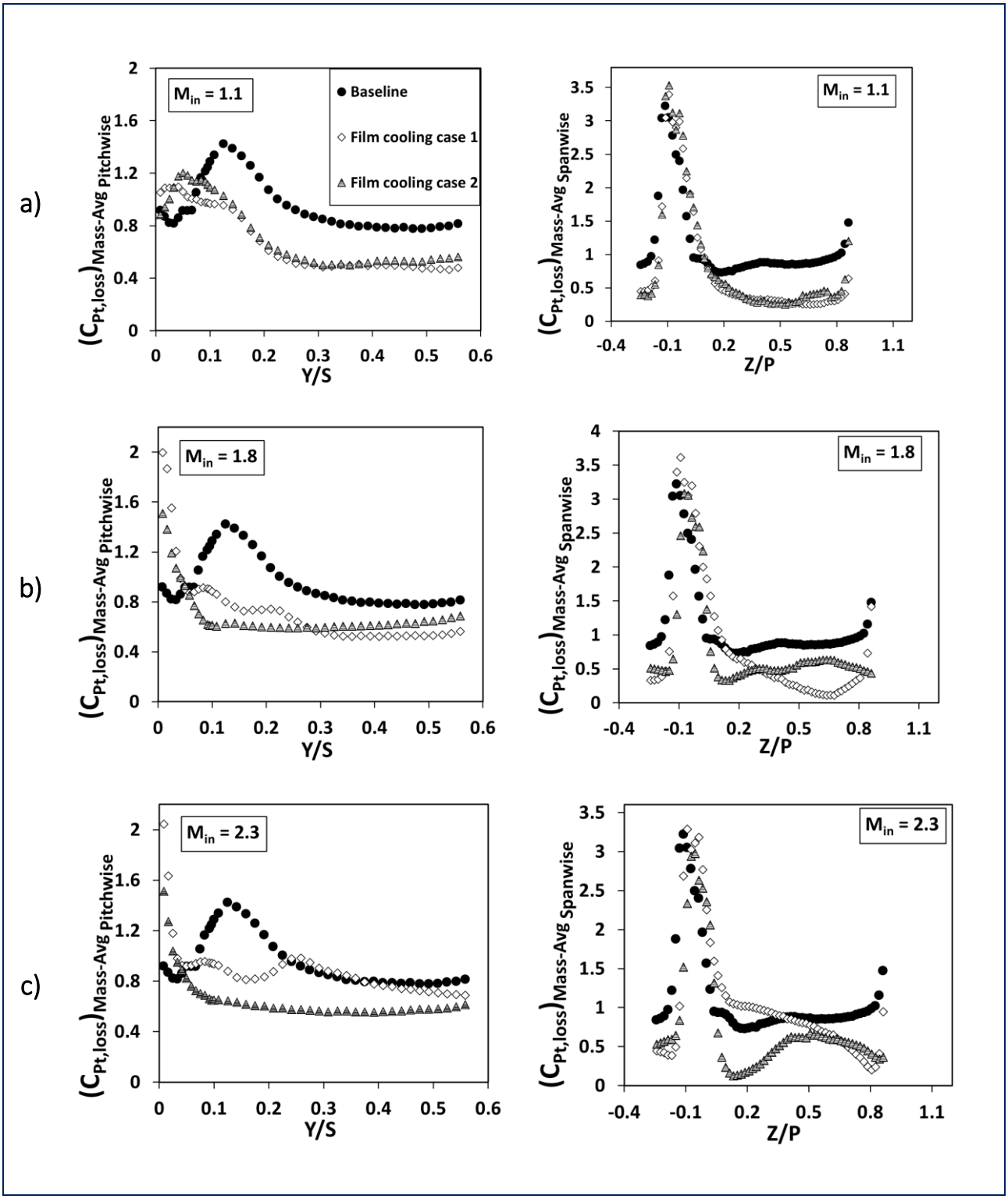

FIGURE 5.31 LINE PLOTS OF PITCHWISE (LEFT) AND SPANWISE MASS-AVERAGED $C_{PT,LOSS}$ AT PLANE-3 (X_G/C_{AX} = 1.042) FOR FILM-COOLING (A) M_{IN} = 1.1, (B) M_{IN} = 1.8 AND (C) M_{IN} = 2.3.

To further evaluate the effects of the film-cooling cases, line plots of the pitchwise and spanwise mass-averaged total pressure loss coefficient at plane-3 are computed in Figure 5.31. The pitchwise mass-averaged $C_{Pt,Loss}$ is computed by numerical integration along the pitch-line area at each span location (Y/S) while the spanwise mass-averaged values are obtained with numerical integration along the span-line area at each pitch location (Z/P), as in Eq.(5.1). Comparisons are provided between inlet blowing ratios of 1.1, 1.8 and 2.3 to indicate the effects of the higher inlet blowing ratios near the endwall regions of the mass-averaged $C_{Pt,Loss}$ (Y/S < 0.1) . It can be seen that the higher inlet blowing ratios of the plots to the left side of Figure 5.31 (b & c) result in higher pitchwise mass-averaged $C_{Pt,Loss}$ near the endwall due to the location of the vortex structures there with the slot film flows. Hence the pitchwise mass-averaged $C_{Pt,Loss}$ is higher for case-1 than for case-2 all along the span as the leading-edge slots are shown to induce larger positive axial vorticity, which enhances the passage vortex system or introduces some additional vortex flows along the endwall. The higher inlet blowing ratios (M_{in} = 2.3) indicate major reductions in the pitchwise mass-averaged $C_{Pt,Loss}$ everywhere with film-cooling case-2. The spanwise mass-averaged $C_{Pt,Loss}$ plots on the right side of Figure 5.31 (a – c) describe the pressure loss effects experienced inside the passage. The high mass-averaged $C_{Pt,Loss}$ values seen at -0.14 < Z/P < -0.07 are due to the passage wake, which is located near the trailing edge. The differences in the spanwise mass-averaged $C_{Pt,Loss}$ between baseline and film flow cases in the wake region are insignificant. The slight increase in the mass-averaged $C_{Pt,Loss}$ in the wake is apparent for the film-cooling cases and is expected because induced turbulent kinetic energy (Radomsky and Thole, 1999) and entropy generation are inevitable when high momentum flow interacts with the blade-surface boundary layer in the passages (Burd and Simon, 1999, Friedrichs et al., 1997, Friedrichs et al., 1999). Away from the trailing edge (Z/P > 0), the averaged losses are much lower for all M_{in} for case-2, suggesting that the passage flow field at the exit has improved as with the yaw angle deviation (ΔYaw) shown in this region. The same is true for the case-1 for M_{in} <= 1.8. Overall, the flow field shows best improvement in terms of the reductions of the total pressure losses and flow angle deviations for the film-cooling case-2 at the highest M_{in} at the passage exit. The next section investigates the effects of upstream slot film-cooling with the leading-edge fillet employed in the flow field measurements.

5.5 Film-cooling with fillet

The introduction of the leading-edge fillet with film-cooling is investigated for all M_{in} as in section 5.4. The fillet geometry at the leading-edge region occupies almost the full length of the upstream slot located near the blade stagnation edge, therefore only film-cooling case-2 is used as the baseline film-cooling case to show the effects of the fillet on the film-cooling flow aerodynamics inside the passage. Therefore, the leading-edge slots are masked by tape before employing the fillets in the passage. The passage then consists of only the central two slots for the film-cooling flow when the fillets are employed. Case-2 of the film-cooling also employs the central two slots

upstream of the test passage. The slot flow rates are provided in Table 5.2 for film-cooling case-2 and are identical for the fillet test cases. Thus the employment of film-cooling with the fillet will be investigated from the first measurement plane through to the exit of the passage as before. Contours of $C_{Pt,Loss}$ and normalised pitchwise velocity w/U_{ref} are compared at plane-1 at M_{in} = 1.1 and 2.3 in Figure 5.32, and contours for M_{in} = 1.4 and 1.8 provided in Figure E.9 for completeness. The contour range of $C_{Pt,Loss}$ in the figures is set to the baseline results for comparisons. The influences of film-cooling with the fillets on $C_{Pt,Loss}$ are clearly seen when comparisons are made with case-2 of the film-cooling in plane-1 in section 5.4.

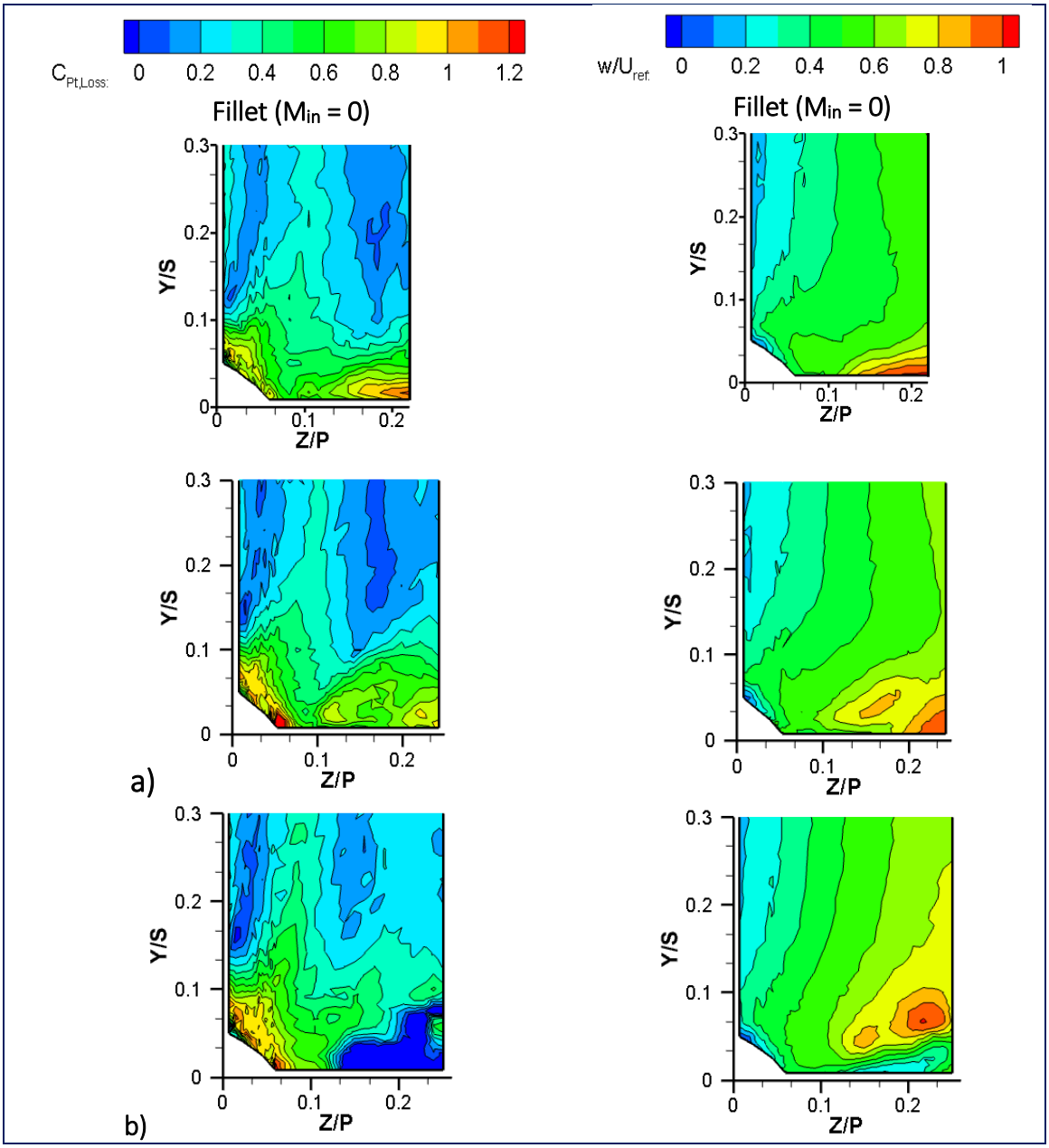

FIGURE 5.32 CONTOURS OF $C_{PT,LOSS}$ (LEFT) AND NORMALISED PITCHWISE VELOCITY (RIGHT) AT PLANE-1 (X_G/C_{AX} = 0.251) FOR FILLET (M_{IN} = 0) AND FILM-COOLING WITH FILLET AT (A) M_{IN} = 1.1 AND (B) M_{IN} = 2.3.

The slot injection at high M_{in} clearly impacts on the pressure-side leg vortex structure in Figure 5.32(b) where there is a large region of $C_{Pt,Loss} < 0$ at $Z/P > 0.1$ representing the film flow. In the baseline contour shown in Figure 5.7 for baseline and fillet without film-cooling ($M_{in} = 0$) (shown again here for comparison), the pressure-side leg vortex is migrating towards the suction side due to the passage cross-flow along the endwall. The fillet without film-cooling was seen to reduce the strength of the $C_{Pt,Loss}$ for both the suction- and pressure-side leg vortices. At low inlet blowing ratio of $M_{in} = 1.1$, the pressure-side leg vortex is still present but with reduced strength when the fillet is employed (as compared with the data in Figure 5.7) while a large region of pressure loss along the endwall at $Z/P > 0.1$ and $Y/S < 0.1$ remains. The $C_{Pt,Loss}$ near the suction-side corner at $Z/P < 0.1$ increases with M_{in} with the fillet. The $C_{Pt,Loss}$ increases at $M_{in} = 2.3$ with the decrease in Pt at $Z/P < 0.1$ because of mixing losses between the high mass flux of slot jet and suction-side leg vortex.

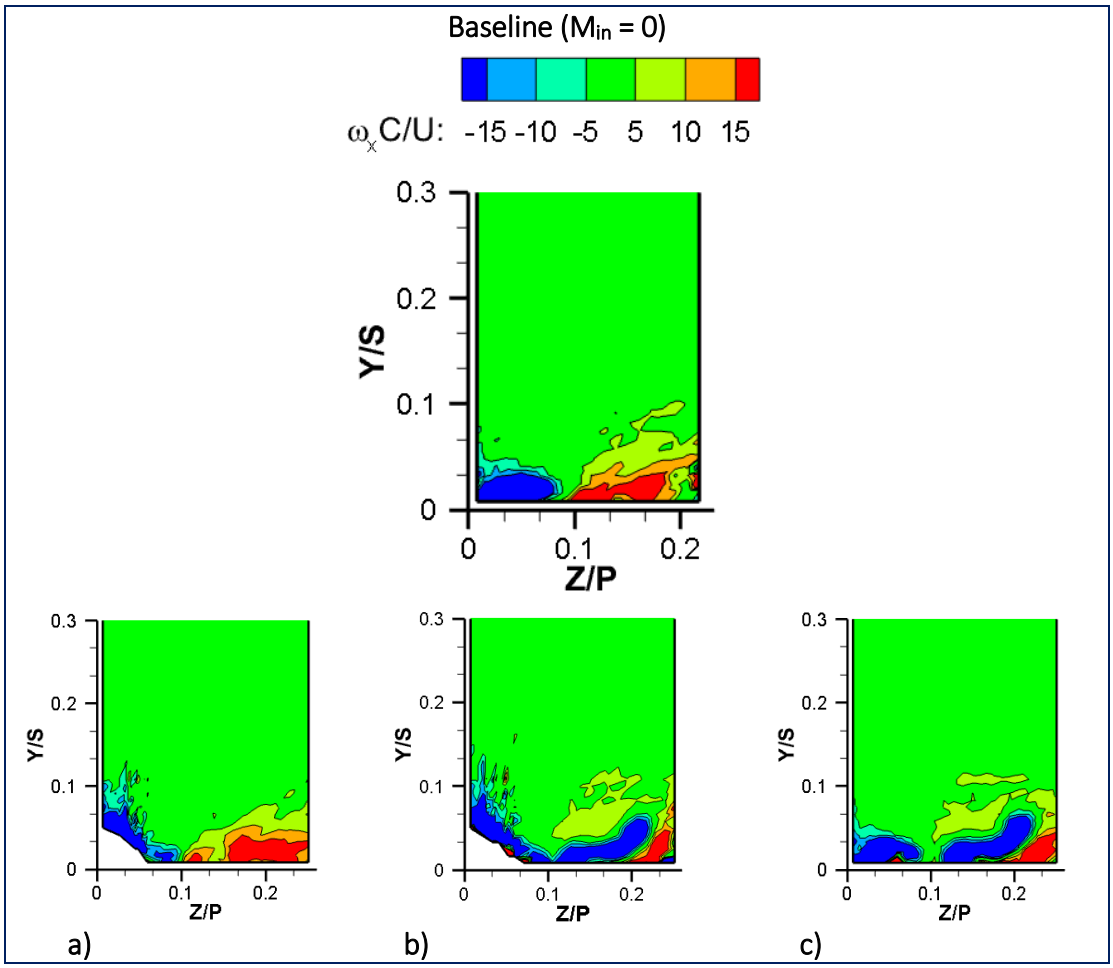

FIGURE 5.33 CONTOURS OF NORMALISED AXIAL VORTICITY AT PLANE-1 ($X_G/C_{AX} = 0.251$) FOR BASELINE ($M_{IN} = 0$), (A) FILLET ($M_{IN} = 0$), (B) FILLET $M_{IN} = 1.4$ AND (C) $M_{IN} = 1.4$ NO FILLET (CASE-2).

The fillet has no influence on the film flow region at this location as similar patterns are seen in the w/U_{ref} contours at Z/P > 0.1 in Figure 5.32 where the slot coverage is located. However, the influence of the slot film flow is seen in the w/U_{ref} contours towards the pressure side Z/P > 0.1 even at the lowest M_{in} where the pressure-side leg vortex is slightly reduced in strength. The higher M_{in} results in opposing w/U_{ref} components on the endwall surface (Y/S < 0.05) at Z/P > 0.1 and is seen to push the pressure-side leg vortex away from the endwall. Therefore, the fillet geometry has more influence on the suction-side corner at this stage in the passage where the suction-side leg vortex is impacted by the fillet profile seen for all cases with and without film-cooling. The normalised axial vorticity contours in confirm the presence of the slot injection flow at plane-2 where the large blue regions are located along the endwall (Y/S < 0.1) at Z/P > 0.1. The fillet case without film-cooling in (a) shows a larger region of positive axial vorticity along the endwall due to the pressure-side leg vortex. When film-cooling is introduced, the slot injection induces counter negative axial vorticity at Z/P > 0.1 in (b, c) along the endwall Y/S < 0.1. For the fillet film-cooling cases of M_{in} not shown in , refer to Figure E.13 for completeness.

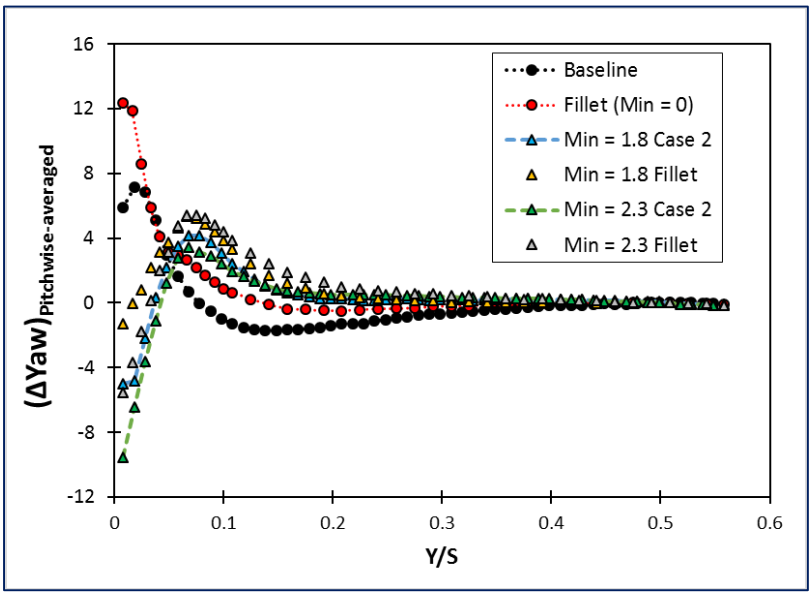

FIGURE 5.34 LINE PLOT OF PITCHWISE-AVERAGED YAW ANGLE DEVIATION ΔYAW AT PLANE-1 (X_G/C_{AX} = 0.251) FOR FILM-COOLING WITH AND WITHOUT FILLET (CASE-2).

The flow angles at plane-1 are compared in Figure 5.34, which presents the pitchwise-averaged yaw angle deviation for film-cooling case-2 with and without fillets at M_{in} = 1.8 and 2.3. The ΔYaw contours for the film-cooling cases are provided in Figure E.10 for completeness. The data from the baseline and fillet cases without the coolant flow (M_{in}=0) are also included in the figure for comparisons. The pitchwise-averaged ΔYaw is computed by taking the average of the local yaw angle deviation values at each span location (Y/S) along the pitch direction. The baseline case shows large averaged positive yaw angle deviations near the endwall (Y/S < 0.07). When film-cooling is introduced, there is a large decrease in the averaged yaw angle deviation, which

supports the change in pitchwise velocity and axial vorticity along the endwall. The fillet then increases the deviation from the film-cooling case as seen with the baseline and fillet (M_{in} = 0) results at this axial location plane. This is due to the fillet profile, which influence the flow angles near the fillet surface. Thus the local ΔYaw at the wall region (Y/S < 0.1) is higher with fillet film-cooling but the opposite is seen at regions further from the wall (Y/S > 0.1).

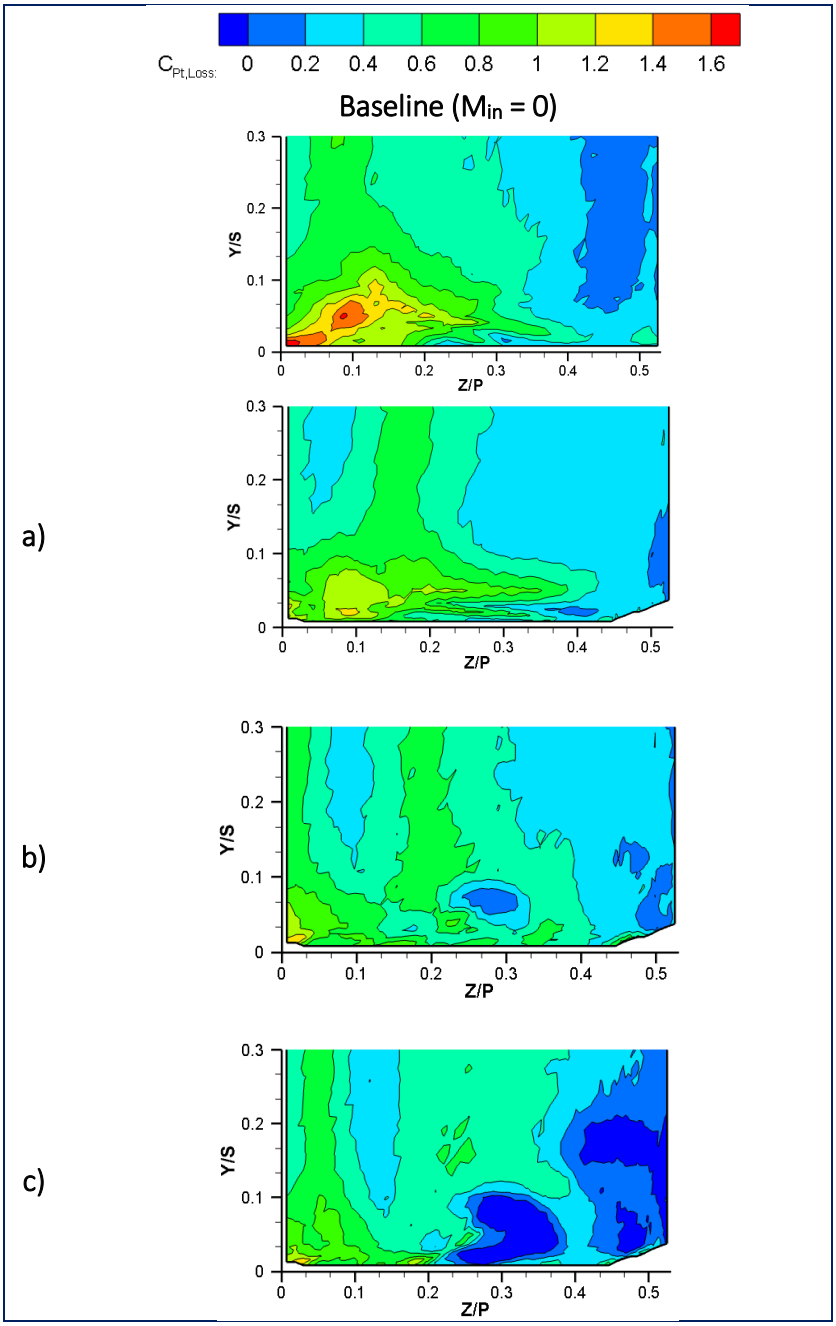

FIGURE 5.35 CONTOURS OF $C_{PT,LOSS}$ AT PLANE-2 (X_G/C_{AX} = 0.58) FOR BASELINE (M_{IN} = 0), (A) FILLET (M_{IN} = 0), (B) FILLET M_{IN} = 1.8 AND (C) FILLET M_{IN} = 2.3.

The flow field effects of the fillet film-cooling cases are further analysed downstream at plane-2 located just aft of the passage throat. The fillet case without film-cooling is able to reduce the passage vortex strength at this location in the passage and is attributed to the reduction in the passage cross-flow measured through the endwall static pressure measurements. Figure 5.35 compares contours of $C_{Pt,Loss}$ at plane-2 for the baseline-fillet case M_{in} = 0 and fillet with film-cooling at the higher inlet blowing ratios of 1.8 and 2.3. Contours of $C_{Pt,Loss}$ at plane-2 for inlet blowing ratios of 1.1 and 1.4 are provided in Figure E.11 for completeness. There is a large reduction in the higher $C_{Pt,Loss}$ both in magnitude and area at the passage vortex region (Z/P < 0.2) in Figure 5.35(b, c) with increasing M_{in} in comparison with the baseline fillet case in Figure 5.35(a). Both film-cooling supply rates therefore reduce the passage vortex strength and size near the suction side on the left side of the plots. The low $C_{Pt,Loss}$ regions are larger and more visible at Z/P > 0.25 just above the endwall when the film-cooling flow is employed. The low $C_{Pt,Loss}$ region above the endwall becomes the largest for M_{in} = 2.3, which suggests that more film flow is directed there and the film coverage on the endwall is wider and better as M_{in} increases.

These occurrences are amplified with the introduction of the fillet when compared with the film-cooling cases without the fillet in . The lower total pressure losses with M_{in} is the consequence of: (i) the jet momentum of slot flow penetrating through the boundary layer separation region of the passage vortex and (ii) the reduction in the pitchwise pressure gradient along the passage just above the endwall. Both of these consequences then factor in the formation of the passage vortex, which is evidently weaker and smaller with the film-cooling flow at plane-2, as indicated. Thus the fillet further contributes to the reduction in the pitchwise pressure gradients to counteract the passage vortex formation. These results are confirmed by the summarised details of the total pressure loss coefficient at plane-2 in .

The pitchwise-averaged $C_{Pt,Loss}$ at plane-2 shown in for the film-cooling cases with and without the fillet at the higher coolant supply rates shows definite improvement near the endwall (Y/S < 0.05) with lower values of $C_{Pt,Loss}$ as well as further into the passage (Y/S < 0.25). The fillet film-cooling cases also show $C_{Pt,Loss}$ reduction from earlier results without the fillet employed and the baseline fillet case indicating the desired passage flow field with less total pressure losses at the highest M_{in}. The passage flow field uniformity (in terms of deviations from the midspan region away from boundary layer) also benefits when the fillet is combined with slot film-cooling as indicated in Figure 5.37. Yaw angle deviation contours for the fillet film-cooling case at M_{in} = 1.1 and 1.8 are provided in Figure E.12 for completeness. As mentioned earlier, low values of ΔYaw near the endwall are the desired outcomes of any modifications at the endwall to reduce the pitchwise pressure gradient and maintain uniformity in the streamline direction spanwise. Such uniform streamline distributions provide better film coverage on the endwall.

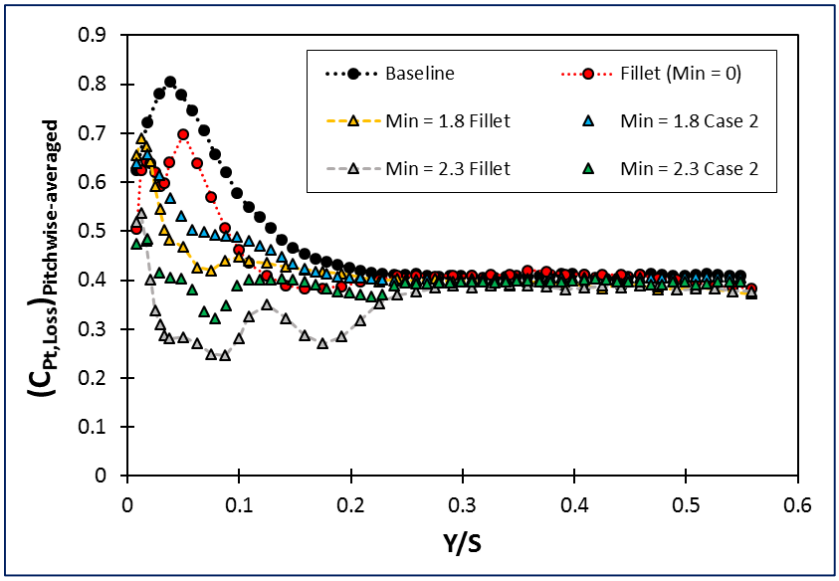

FIGURE 5.36 LINE PLOT OF PITCHWISE-AVERAGED $C_{PT,LOSS}$ AT PLANE-2 (X_G/C_{AX} = 0.58) FOR FILM-COOLING WITH AND WITHOUT FILLET (CASE-2).

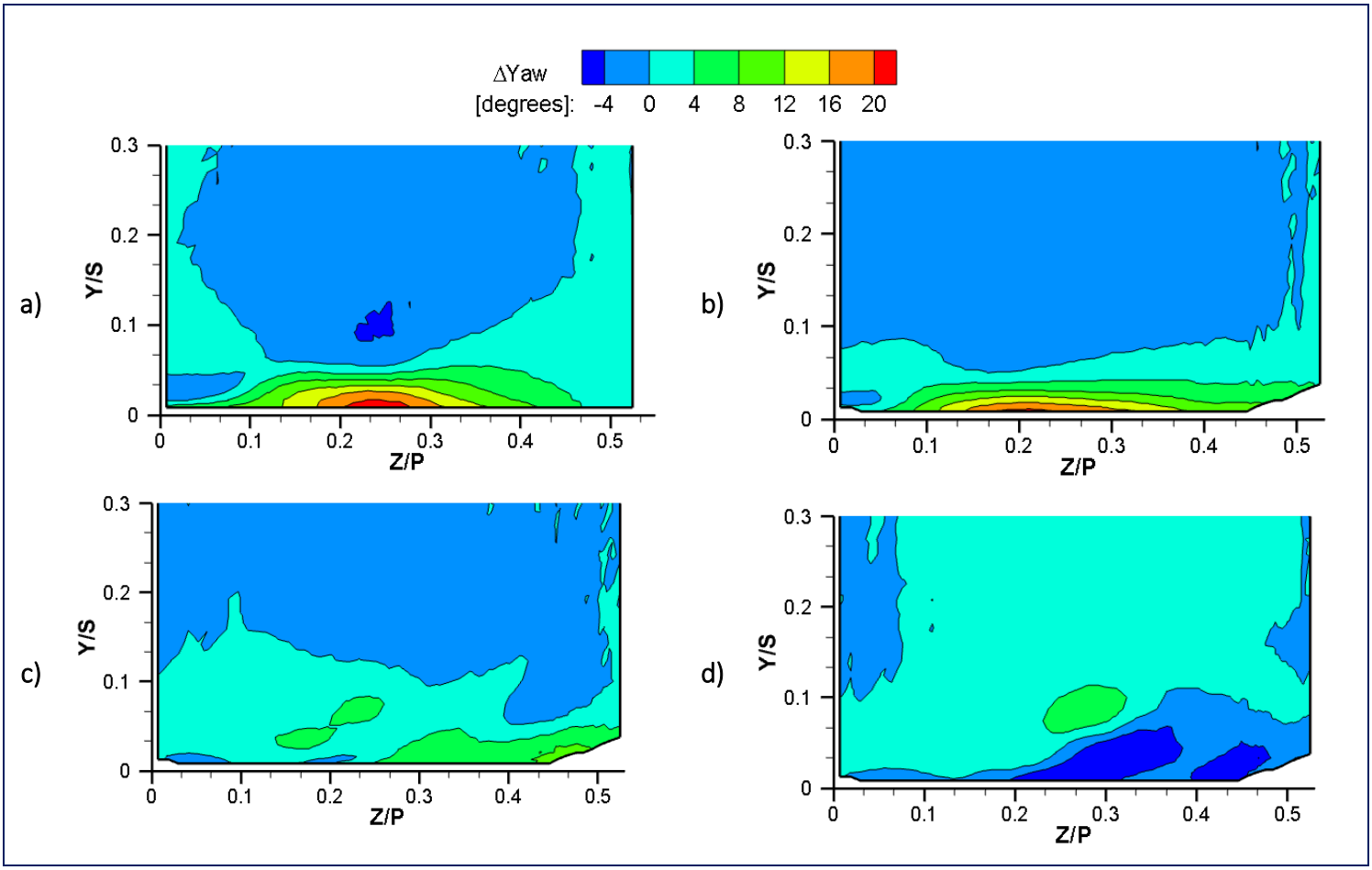

FIGURE 5.37 CONTOURS OF YAW ANGLE DEVIATION AT PLANE-2 (X_G/C_{AX} = 0.58) FOR (A) BASELINE (M_{IN} = 0), (B) FILLET (M_{IN} = 0), (C) FILLET M_{IN} = 1.4 AND (D) FILLET M_{IN} = 2.3.

The baseline fillet case (M_{in} = 0) shown in Figure 5.37(b) shows only marginal ΔYaw decrease near the endwall surface (Y/S < 0.05), whereas the film-cooling cases with the fillet are significantly more effective at reducing the flow field distortion at the passage inlet. The film-cooling slots of case-2 therefore are located in a critical position at the passage inlet and contribute to the reductions in the yaw angle deviations adjacent to the endwall, as seen by the large negative regions of ΔYaw in Figure 5.37(c, d). The same trends are present prior to introducing the fillet with film-cooling case-2. The effect of high momentum coolant injection is thus beneficial in influencing the flow field further downstream of the injection locations, particularly affecting the passage cross-flow.

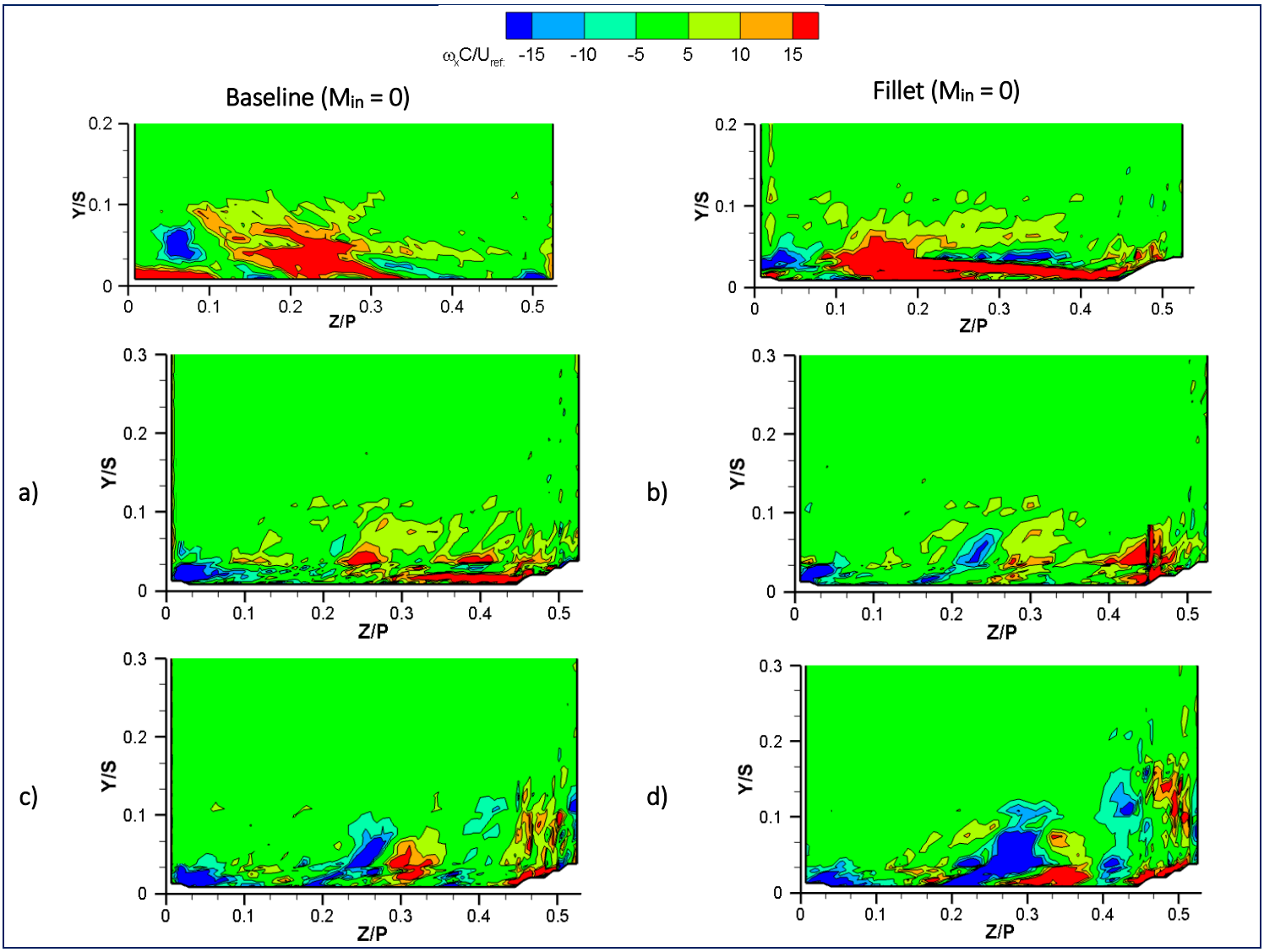

FIGURE 5.38 CONTOURS OF NORMALISED AXIAL VORTICITY AT PLANE-2 (X_G/C_{AX} = 0.58) FOR BASELINE (M_{IN} = 0), FILLET (M_{IN} = 0) AND FILM-COOLING WITH FILLET AT (A) M_{IN} = 1.1, (B) M_{IN} = 1.4, (C) M_{IN} = 1.8 AND (D) M_{IN} = 2.3.

The normalised axial vorticity contours $\omega_x C/U_{ref}$ are compared at all inlet blowing ratios for the filleted film-cooling case at plane-2 in Figure 5.38. At $M_{in} = 1.1$, the axial vorticity distribution shows slight improvement from the baseline fillet case in Figure 5.11 b) due to the slot injection even at this low coolant supply. However, a large presence of positive axial vorticity is still attributed to the interaction between the film flow and passage cross-flow and in all cases, the suction-side vorticity remains fairly unchanged in that blade-endwall corner ($Z/P < 0.05$). This again notes the directional influence of the film-cooling case-2 from the slots, mainly targeting the passage cross-flow region along the endwall, while the fillet alone affects the suction-side vorticity.

As the coolant supply increases, the effects of the slot injection become more prominent with larger regions of negative $\omega_x C/U_{ref}$ extending along pitchwise by the film flow. From the middle of the endwall ($0.1 < Z/P < 0.4$), the positive $\omega_x C/U_{ref}$ region moves further towards the pressure side (right side of the plots) as the inlet blowing ratio increases to 2.3. This result illustrates the large increase of negative axial vorticity with M_{in} and coolant momentum, which is able to counteract the positive pitchwise flow in the passage

The implications of high coolant momentum coupled with the flow field modification imposed by the leading-edge fillet at plane-2 are examined in Figure 5.39 where the pitchwise-averaged yaw angle deviation for film-cooling case-2 with and without the fillets are compared with that of the baseline cases ($M_{in} = 0$). The pitchwise-averaged ΔYaw is calculated by taking the average of the local values at each span location (Y/S) along the pitch direction (Z/P). Inlet blowing ratios of 1.1 and 1.8 are presented for comparative reasons. In this case, the flow angles are fairly similar at each M_{in} to each other with or without the fillet, but do not clearly indicate that the fillet changes the deviation in flow angles when coupled with film-cooling case-2. Overall though, the averaged yaw angle deviation is reduced near the endwall region ($Y/S < 0.05$) when increasing the coolant supply, which is attributed to the reduction in the pitchwise pressure and velocity gradients.

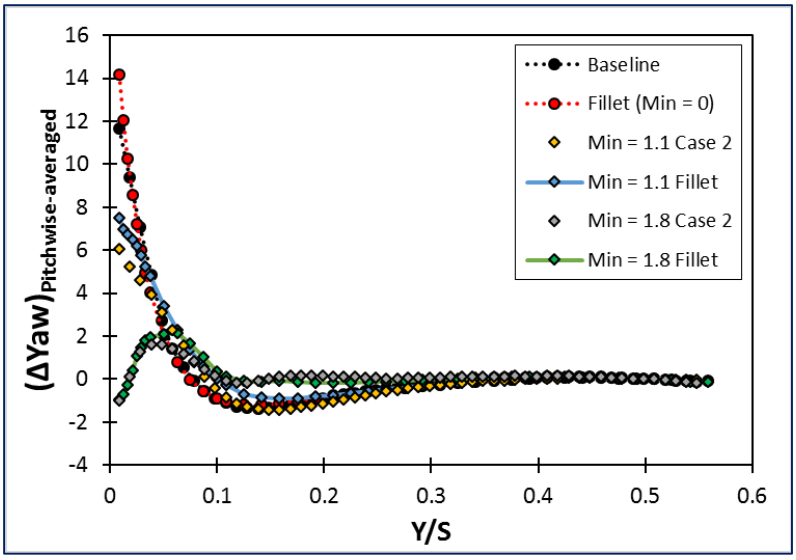

FIGURE 5.39 LINE PLOT OF PITCHWISE-AVERAGED YAW ANGLE DEVIATION ΔYAW AT PLANE-2 (X_G/C_{AX} = 0.58) FOR FILM-COOLING WITH AND WITHOUT FILLET (CASE-2).

To provide a complete analysis of the fillet film-cooling performance, the passage exit is evaluated in plane-3 just aft of the trailing edge. In the baseline case (M_{in} = 0, no fillet), the contours of $C_{Pt,Loss}$ indicate a large elliptical region of significant total pressure loss, which represents the passage vortex structure leaving the passage near the wake region. Additionally, there are also moderately high total pressure losses (i.e. $C_{Pt,Loss}$ region) along the endwall at plane-3 due to the boundary layer present there. The wake region is also seen to experience high total pressure losses and is largely attributed to the mixing and increase of turbulence between the interactions of strong passage vortex and trailing-edge wake. Figure 5.40 presents contours of $C_{Pt,Loss}$ at plane-3 for the fillet film-cooling case at all inlet blowing ratios investigated (M_{in} = 1.1 to 2.3). The contour magnitudes are set to the film-cooled baseline range (M_{in} > 0 cases without fillet) for comparisons where it is evident that for all inlet blowing ratios (no fillet cases), there are escalations in the total pressure losses due to the mixing of film flow and passage vortex. Further comparisons are provided with contours of normalized axial vorticity at plane-3 for all M_{in} in Figure E.15 when the fillet is combined with film-cooling case-2.

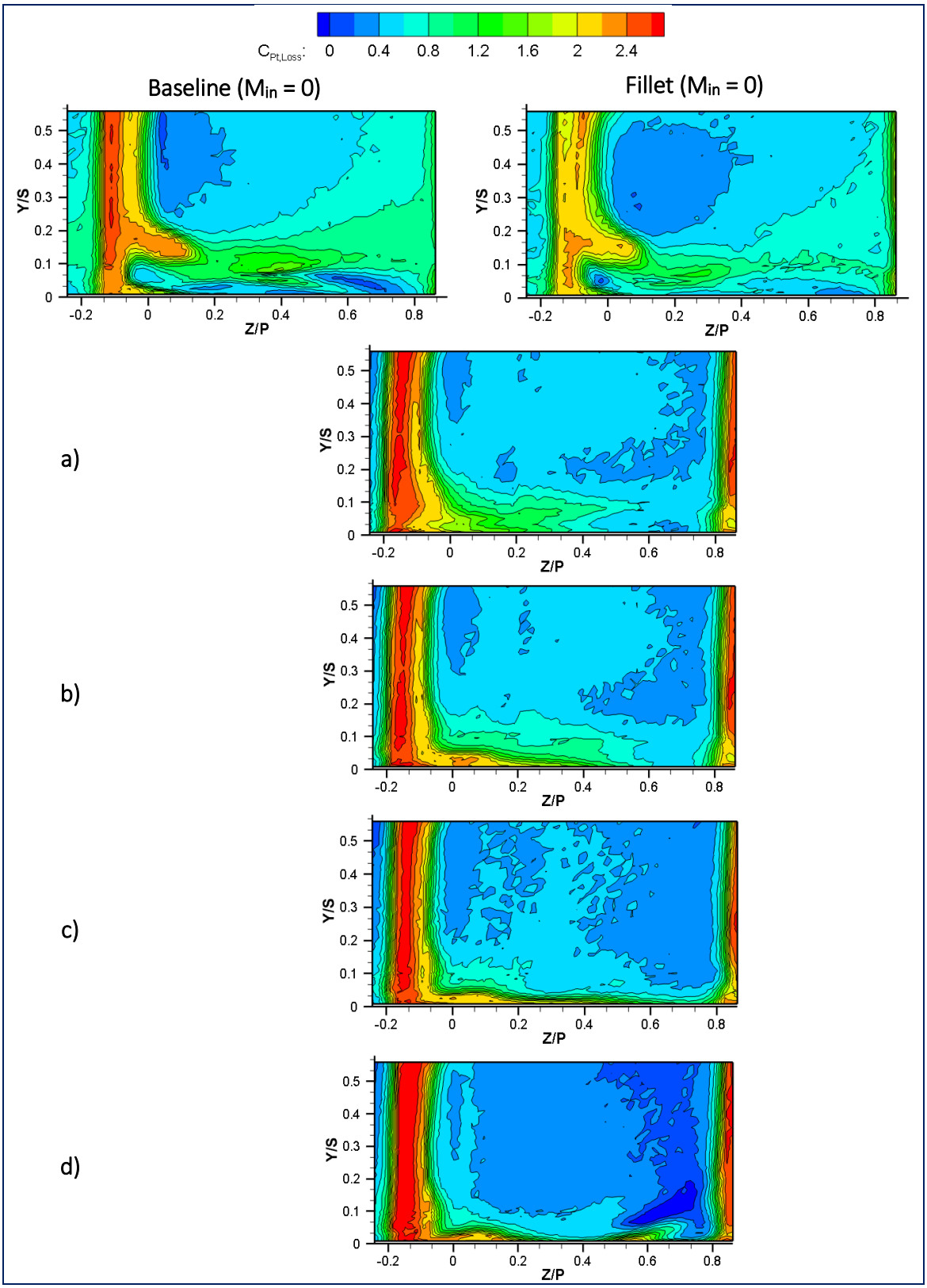

FIGURE 5.40 CONTOURS OF $C_{PT,LOSS}$ AT PLANE-3 (X_G/C_{AX} = 1.042) FOR BASELINE (M_{IN} =0), FILLET (M_{IN} = 0) AND FILM-COOLING WITH FILLET AT (A) M_{IN} = 1.1, (B) M_{IN} = 1.4, (C) M_{IN} = 1.8 AND (D) M_{IN} = 2.3.

In Figure 5.40(a), there is a distinct passage vortex system represented by high $C_{Pt,Loss}$ values near Y/S < 0.2 and -0.2 < Z/P < 0.0. Comparing this region in Figure 5.40(b, c, d) as M_{in} increases and in the baseline case and fillet (without film-cooling) Figure 5.12(a, b), there is visible reduction in $C_{Pt,Loss}$ magnitudes and size. Furthermore, the reduction of $C_{Pt,Loss}$ values in the passage vortex region is much more in than that in Figure 5.40 (a) as compared with the reduction in $C_{Pt,Loss}$ for the film-cooling case-2 without the fillet for M_{in} = 1.1 in the left plot in Figure 5.27(a). At high M_{in} (1.8 and 2.3) in Figure 5.40(c, d), a narrow region above the endwall (Y/S < 0.05) is represented as the boundary layer region, which is strengthened and grown thicker by the jet momentum of slot flow. Thus the $C_{Pt,Loss}$ increases in this region. Also seen is a small region of $C_{Pt,Loss}$ < 0 at 0.6 < Z/P < 0.8 and Y/S < 0.2 in Figure 5.40(d) at the highest M_{in}, which is caused by the presence of some film jet at this location, which has high momentum and total pressure. This is also an indication that slot jet covers almost the entire pitch length at the exit, a very desirable result for the effective film-cooling coverage of the endwall. The influence of slot film-cooling cases at the exit was seen previously to increase the pressure losses in the trailing-edge wake as well. Previously, the effects of film-cooling case-2 were seen to weaken the passage vortex system nearer to the endwall, with the most effective results coming with the highest M_{in}. In this case, Figure 5.40, the endwall boundary layer is also seen to be restored with the passage vortex being absorbed into the deeper wake region to greater effect as M_{in} increases. At the highest M_{in}, it is also not clear where the passage vortex is now located within the wake region.

Viewing the results in Figure 5.40 in conjunction with the contours of yaw angle deviation and pitch angles at plane-3 for the fillet film-cooling case in Figure 5.41, it is evident that the upstream slot film-cooling reduces the deviations of the endwall region streamlines from the free-stream region. Refer to Figure E.14 for contours of M_{in} not shown in Figure 5.41 for completeness. Figure 5.41(a) shows the ΔYaw < 0 and high pitch angle contours for the fillet case without film-cooling, where a strong passage vortex structure is seen by the high turning of flow in the circular region. The introduction of film-cooling in Figure 5.41(b, c) shows significant reductions for both yaw angle deviation and pitch angle variation as there are no visible regions of high turning. The yaw angle deviation adjacent to the endwall for the baseline fillet case on the left of Figure 5.41(a) indicates the presence of strong cross-flow along the pitch direction. These effects are clearly eliminated by the slot injection, more so with increased M_{in}.

The influence of high momentum coolant flow is further emphasised in Figure 5.42 as the pitchwise mass-averaged yaw angle deviations at plane-3 are compared for M_{in} = 1.1 and 2.3 with and without fillets. The pitchwise-averaged ΔYaw is computed by numerical integration of local ΔYaw values in the pitch-line area (Z/P) for each span location (Y/S). As indicated in Figure 5.42, the increase in coolant supply has favourable effects on the near-wall (Y/S < 0.08) yaw angle deviation, which is reduced to greater effect at the highest M_{in}. The reduction is seen to be within -2° of the yaw angle deviation, which is highly improved compared with that of the baseline case

(M_{in} = 0) of 8° near the endwall. These effects also extend further away from the endwall as the yaw angle deviations fair closer to 0° at the higher M_{in}.

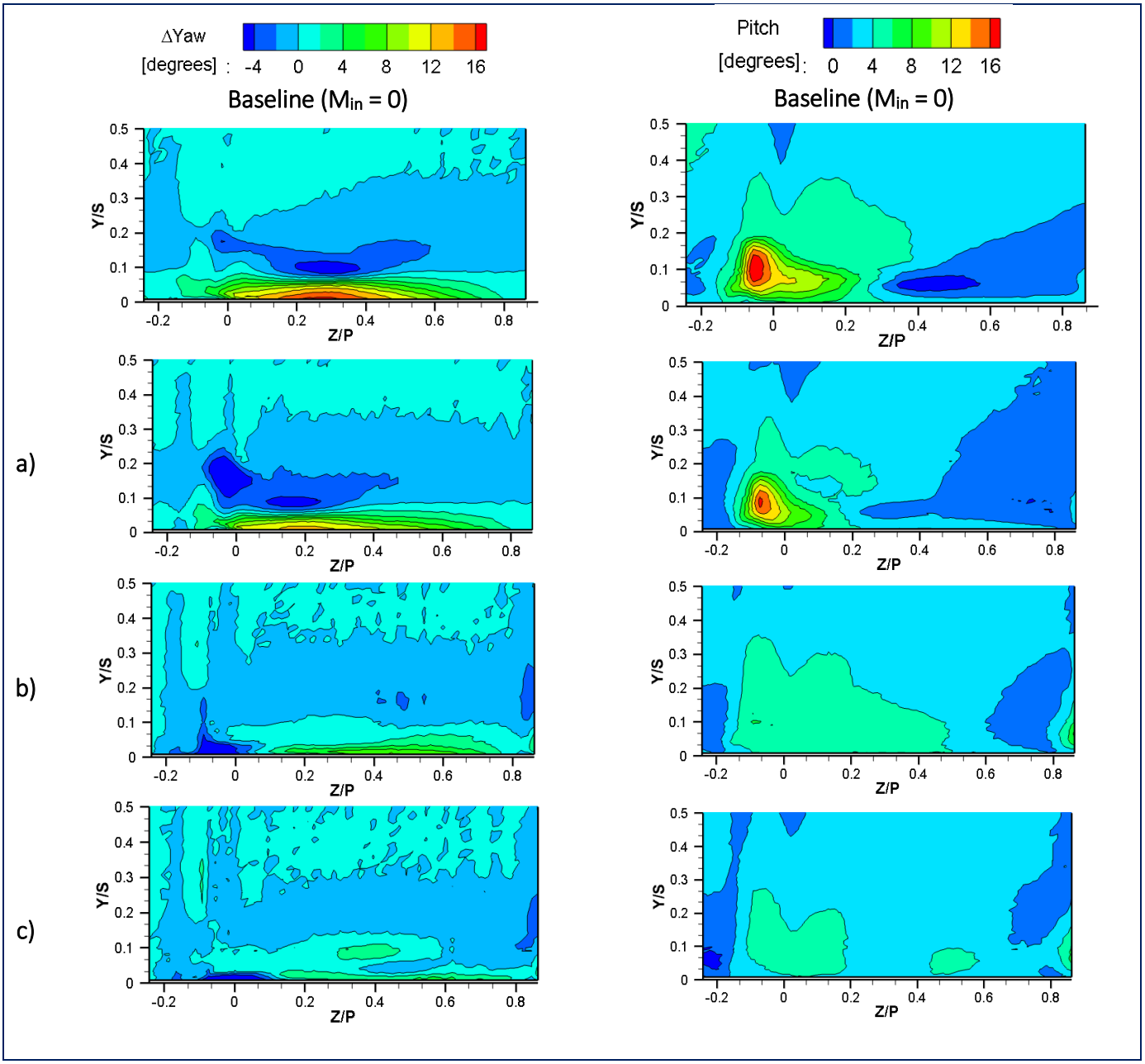

FIGURE 5.41 CONTOURS OF YAW ANGLE DEVIATION (LEFT) AND PITCH ANGLE (RIGHT) AT PLANE-3 (X_G/C_{AX} = 1.042) FOR BASELINE (M_{IN} = 0), (A) FILLET (M_{IN} = 0), FILM-COOLING (B) M_{IN} = 1.4 FILLET AND (C) M_{IN} = 1.8 FILLET.

Figure 5.43 provides a summary of the performance at the passage exit in plane-3 with pitchwise mass-averaged (left) and spanwise mass-averaged (right) $C_{Pt,Loss}$ for the fillet and film-cooling cases at M_{in} = 1.1, 1.8 and 2.3 with the same slot configuration for the coolant flow injection. The pitchwise mass-averaged $C_{Pt,Loss}$ is computed by numerical integration over the pitch-line area at

each span location (Y/S) while the spanwise mass-averaged values are obtained by numerical integration over the span-line area at each pitch location (Z/P). At M_{in} = 1.1, the influence of fillet film-cooling results in higher mass-averaged $C_{Pt,Loss}$ across most of the span of the passage (in Y/S > 0.15) in the left of Figure 5.43 a) in comparison with film-cooling case-2 without the fillets employed. Increasing the inlet blowing ratio to 1.8 shows a reduction in the pitchwise mass-averaged $C_{Pt,Loss}$ in the near wall region (Y/S > 0.1) but high mass-averaged losses are seen on the endwall surface (Y/S < 0.1) when comparing film-cooling cases with and without fillet. This occurs because the passage vortex system is located closer to the endwall and is weaker and smaller in size when the fillet is employed with film-cooling. The same is seen for M_{in} = 2.3.

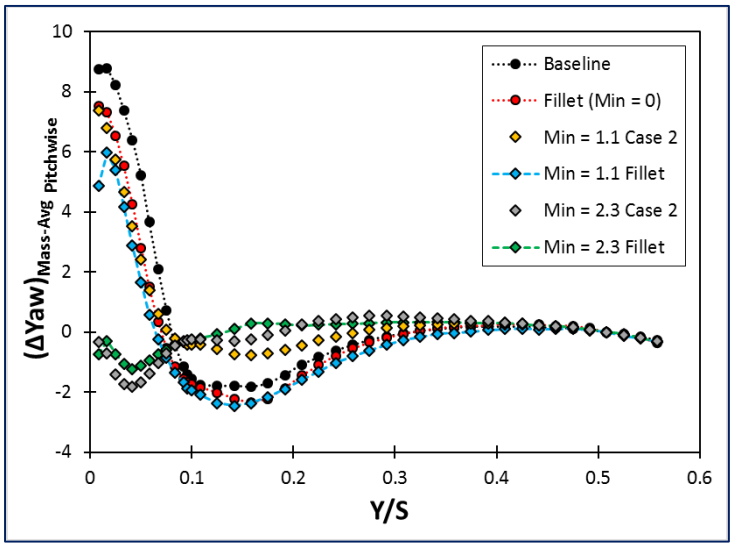

FIGURE 5.42 LINE PLOT OF PITCHWISE MASS-AVERAGED YAW ANGLE DEVIATION AT PLANE-3 (X_G/C_{AX} = 1.042) FOR FILM-COOLING WITH AND WITHOUT FILLET (CASE-2).

The spanwise mass-averaged $C_{Pt,Loss}$ along the pitch (Z/P) on the right of Figure 5.43 b) shows the effects of the wake on the pressure losses in the passage, with the filleted film-cooling case having the highest losses associated with the wake location. The increase in M_{in} further, to 2.3, shows even higher losses associated with the wake and therefore contributes to the overall pressure losses in the passage. The pitchwise mass-averaged total pressure loss at the highest inlet blowing ratio shows better results for the fillet film-cooling case. Again the mass-averaged losses are higher for the fillet film-cooling case at the near-wall region due to the weakening of the passage vortex onto the endwall but in this case, the peak value is lower than M_{in} = 1.8 due to the presence of film flow at the exit. The endwall boundary layer is also thicker when film flow rate increases and the fillet is employed. Also, the high momentum of film jet causes the near-endwall streamlines to be aligned towards the free-stream streamlines, and hence the streamline orientations are more uniform with the slot film flow. At M_{in} = 2.3, the spanwise mass-averaged total pressure losses appear to be less within the blade passage.

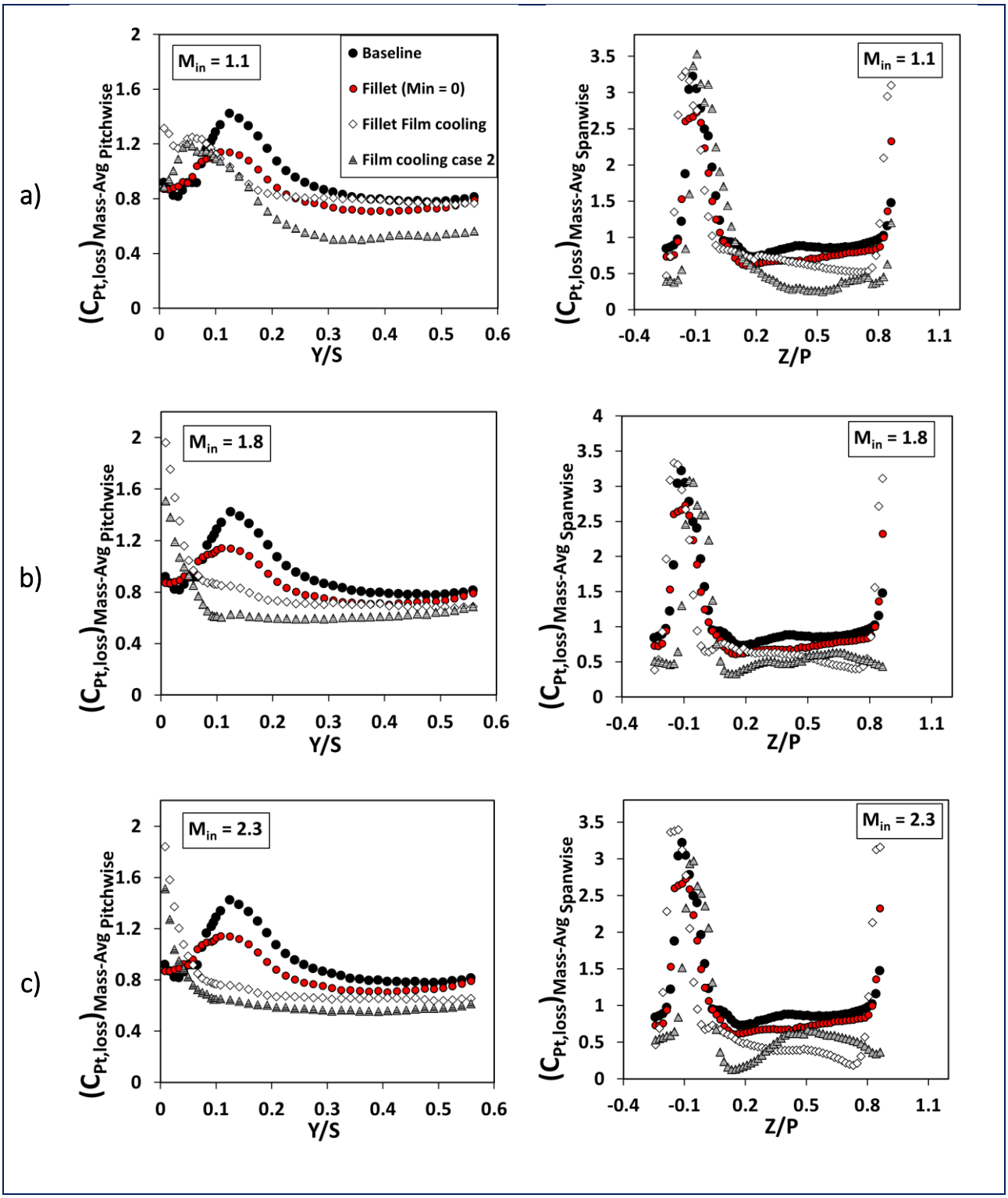

FIGURE 5.43 LINE PLOTS OF PITCHWISE (LEFT) AND SPANWISE (RIGHT) MASS-AVERAGED $C_{PT,LOSS}$ AT PLANE-3 (X_G/C_{AX} = 1.042) FOR FILM-COOLING WITH AND WITHOUT FILLET AT (A) M_{IN} = 1.1, (B) M_{IN} = 1.8 AND (C) M_{IN} = 2.3.

Comparing the mass-averaged total pressure loss coefficients for the filleted film-cooling results at the passage exit indicates a much weaker and smaller passage vortex system, which effectively contributes to the reduction in yaw angle deviation leaving the blade passage.

The endwall static pressure coefficient ($C_{Ps,endwall}$) distribution on the bottom endwall where film-cooling is employed is presented for film-cooling case-2 with and without fillets at M_{in} = 2.3 in Figure 5.44. The $C_{Ps,endwall}$ distribution for both cases appears to be similar qualitatively and thus difficult to compare in this form. Therefore, the maximum pressure difference between pressure and suction sides is computed for all film-cooling and baseline cases compared in Figure 5.45 and Figure 5.46. The measured static pressure at the closest position of the pressure side of vane 3 and suction side of vane 4 is used to compute the maximum pressure difference at each axial location in the passage.

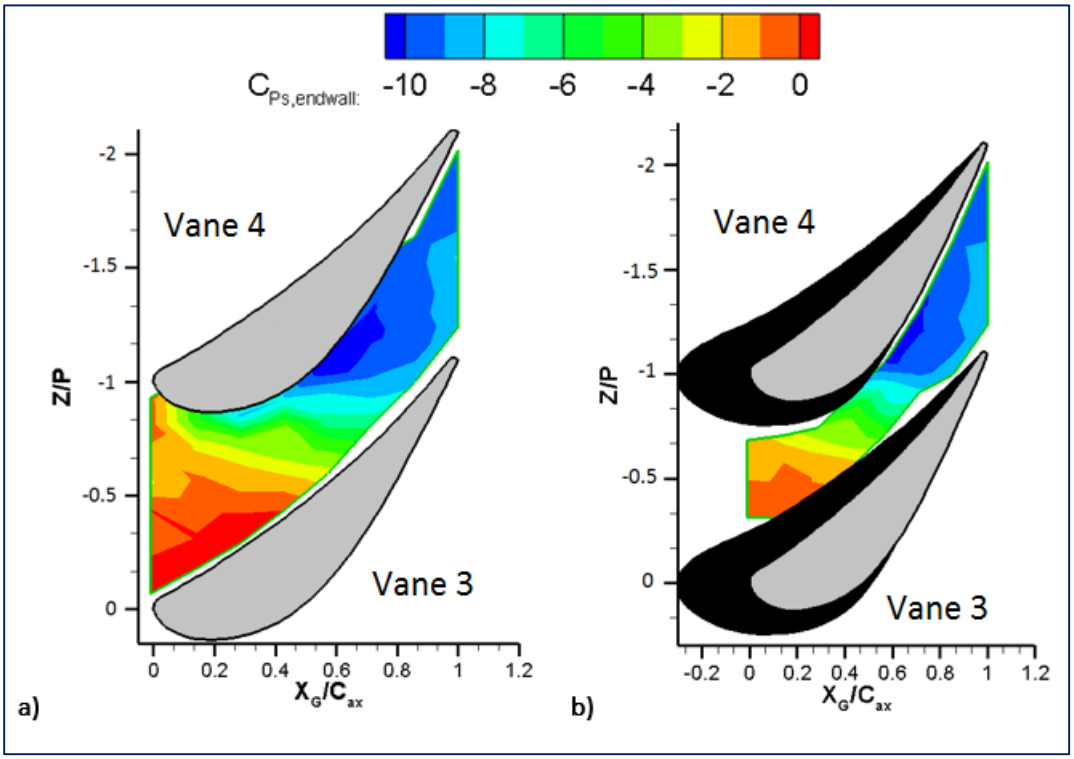

FIGURE 5.44 CONTOURS OF ENDWALL STATIC PRESSURE COEFFICIENT FOR FILM-COOLING (A) M_{IN} = 2.3 CASE-2 AND (B) M_{IN} = 2.3 FILLET.

In Figure 5.45, the influence of film-cooling on the endwall pressure gradients (in pitchwise direction) are clearly evident from the inlet of the cascade ($X_G/C_{ax} > 0$) as the ($P_{PS} - P_{SS}$) increases with M_{in} for all film-cooling cases. The pressure differences are highest near the throat entrance ($X_G/C_{ax} = 0.5$). ($P_{PS} - P_{SS}$) for the film-cooling flow is higher because the jets do not reach the suction side in $X_G/C_{ax} < 0.5$. The jets near the pressure side increase P_{PS} on the endwall, causing ($P_{PS} - P_{SS}$)

to be higher. As the jet reaches the suction side and covers the entire pitch length, (P_{PS} – P_{SS}) becomes the same as for the baseline and fillet cases.

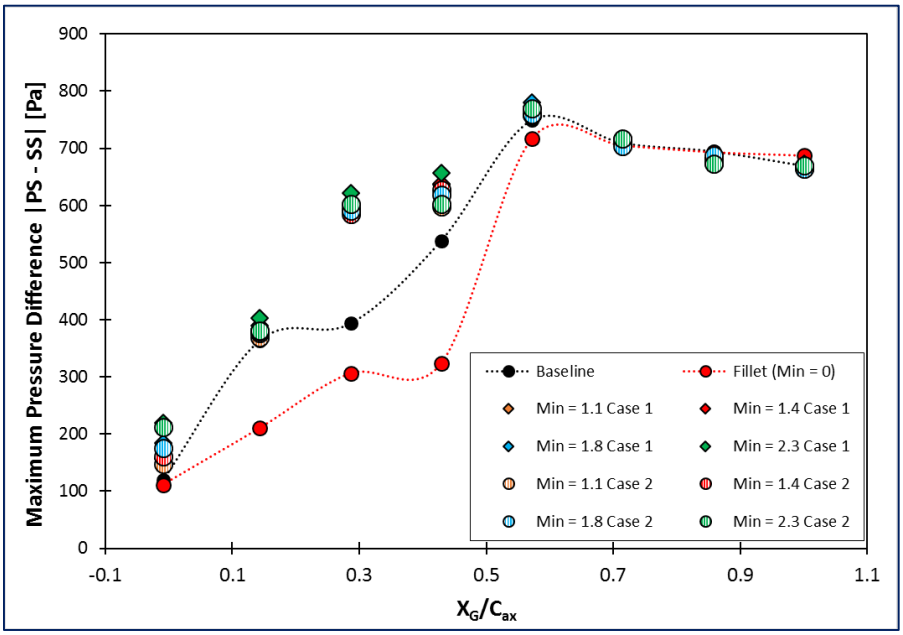

FIGURE 5.45 ENDWALL STATIC PRESSURE DIFFERENCE (MAXIMUM) BETWEEN PRESSURE AND SUCTION SIDES FOR FILM-COOLING CASES.

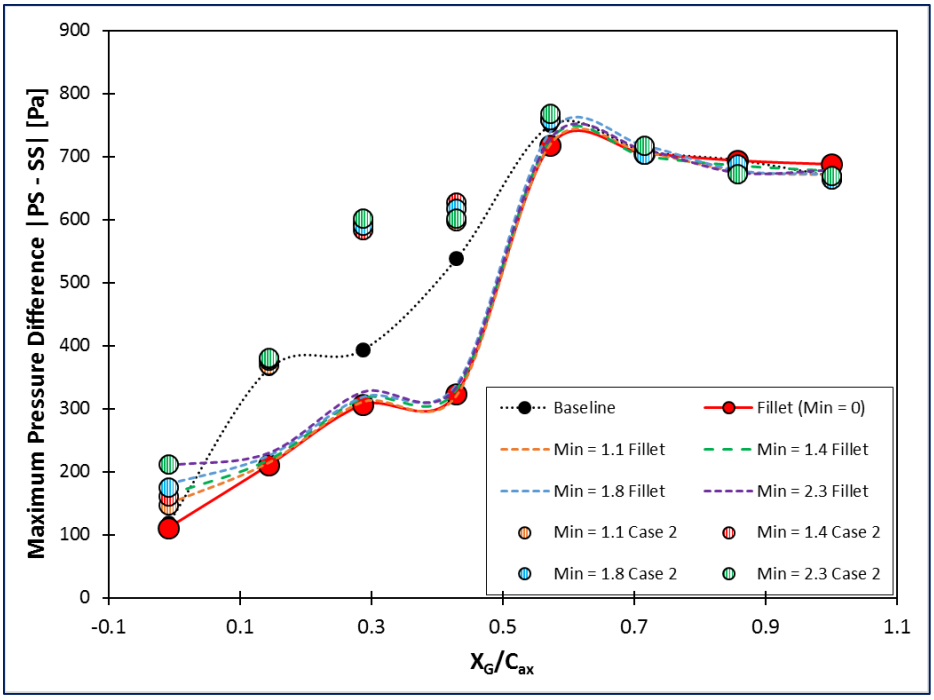

FIGURE 5.46 ENDWALL STATIC PRESSURE DIFFERENCE (MAXIMUM) BETWEEN PRESSURE AND SUCTION SIDES FOR FILM-COOLING WITH AND WITHOUT FILLET (CASE-2).

In Figure 5.46, when the fillet is introduced with film-cooling case-2, the pressure differences are minimised as the fillet reduces the pitchwise pressure gradient along the endwall, shown in Figure 5.5 similarly.

5.6 Summary

Experimental investigations of the endwall, blade static pressure distribution and passage flow field are presented for the evaluation of aerodynamic performance inside a linear vane cascade with upstream slot film-cooling and leading-edge fillets employed on the blade-endwall junction. The blade loading conditions are considered at the midspan location and show no interruption with both the leading-edge fillet and upstream slot film-cooling at high inlet blowing ratios. Also, the total pressure loss, yaw and pitch angle, and vorticity distributions show that at the free-stream region, these quantities change little as the fillet and endwall film-cooling flow are employed. Thus the passage flow field is largely influenced in the near-wall region as desired. To determine the overall performance of these modifications inside the blade passages, the globally mass-averaged $C_{Pt,Loss}$ at plane-3 is computed and provided in Figure 5.47 for all test cases considered in this study.

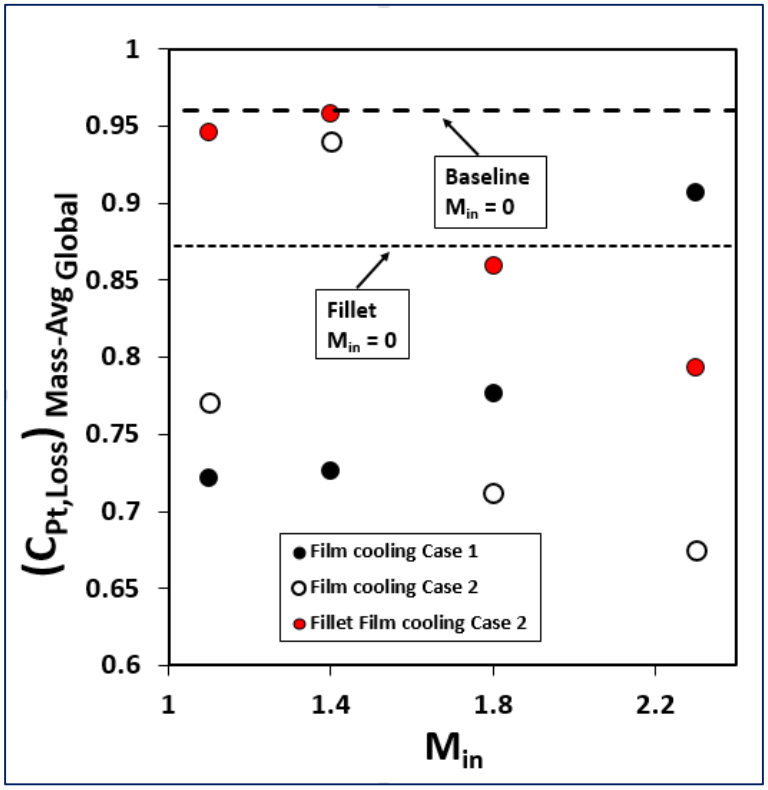

FIGURE 5.47 GLOBALLY MASS-AVERAGED $C_{PT,LOSS}$ AT PLANE-3 (X_G/C_{AX} = 1.042) FOR ALL TEST CASES.

The globally mass-averaged $C_{Pt,Loss}$ in Figure 5.47 is computed by considering all measured locations and therefore provides a summary of the aerodynamic loss performance across the

blade passage by considering the exit flow field. The baseline cases with and without the leading-edge fillet employed are also presented by constant dashed lines for comparison. It can be seen that the fillet (M_{in} = 0) case is effective in reducing the overall total pressure loss in the passage. These improvements are attributed to the reduction in the passage cross-flow by the fillet profile, which weakens the passage vortex formation and thereby improves the passage flow field considerably.

The effects of upstream slot film-cooling are investigated for two film-cooling cases related to the use of four flush slots just upstream of the leading edge of the cascade. The first test case makes use of all four slots injecting coolant into the passage while only the second case employs two central slots to provide film flow. As a result in the change in slot injection area, the coolant flow rates differ and provide a measure of the influence of film flow rate and film jet location on the aerodynamic performance.

The overall performance of the film-cooling cases are compared in Figure 5.47 at the passage exit, plane-3. The cases without the fillet show improvements against the baseline value, with film-cooling case-2 providing the most significant reductions in overall mass-average $C_{Pt,Loss}$ at the higher M_{in} (1.8 & 2.3), while the opposite is seen for case-1, as can be seen in Figure 5.27 where high coolant momentum results in two distinct regions of high $C_{Pt,Loss}$ values forming the passage vortex region. This verifies that the second case counteracts the secondary flow structures by reducing size and weakening strength of the passage vortex considerably near the endwall. At the M_{in} <= 1.8, case-1 shows lower average $C_{Pt,Loss}$ than baseline case without film-cooling. At higher M_{in} = 2.3 in case-1, the interaction and mixing of slot injection, boundary layer and secondary flows are attributed to the increased pressure losses. The leading-edge slots of case-1 are also seen to enhance the passage vortex system at the higher M_{in} as they induce larger positive axial vorticity in these regions.

The effects of film-cooling case-2 combined with leading-edge fillet modifications are compared with the effects of the previous film-cooling cases as well in Figure 5.47. The results for this experimental case show unfavourable effects in a global sense as the mass-averaged total pressure loss coefficients are similar to the baseline results at the lower inlet blowing ratio. At higher coolant supply rates, the performance increases with higher reduction in $C_{Pt,Loss}$ but is still less effective than for case-2 without the fillet. These effects are best compared with the flow field contours of total pressure loss (Figure 5.40) where it is seen that the higher induced averaged losses are mainly due to the higher total pressure losses of the endwall boundary layer as well as the increased pressure losses present in the wake region due to the film flow.

From a design viewpoint, the aerodynamic loss evaluation is highly dependent on the coolant supply, which is sourced from the compressor and thereby requires consideration to maintain turbine performance. Figure 5.48 compares the globally mass-averaged $C_{Pt,Loss}$ per mass fraction

ratio of coolant with main flow (MFR) at plane-3 to determine the effects of coolant supply for all cases.

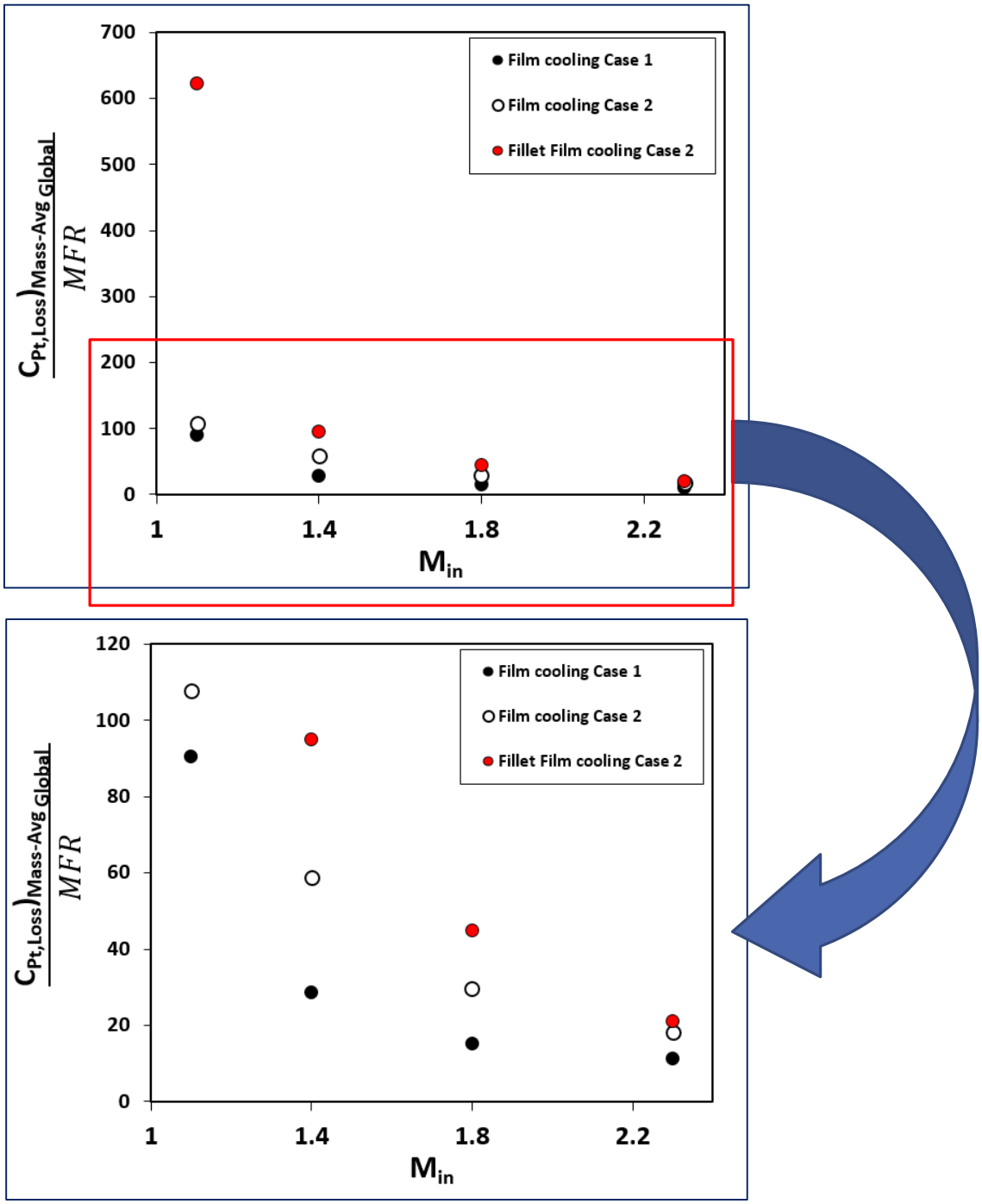

FIGURE 5.48 GLOBALLY MASS-AVERAGED $C_{PT,LOSS}$ PER MASS FRACTION RATIO (MFR) AT PLANE-3 (X_G/C_{AX} = 1.042) FOR FILM-COOLING CASES.

Film-cooling case-2 has fewer slots and thus creates a smaller cross-sectional injection area resulting in lower coolant flow rate but increased coolant momentum. The effects are evident as the globally mass-averaged $C_{Pt,Loss}$ per MFR decreases with increasing M_{in} for all three cases in Figure 5.48. However, the differences become smaller with higher M_{in}. Friedrichs et al. (1997) found that an optimum coolant supply pressure was reached when the streamwise velocity components of the coolant and mainstream were similar. Furthermore, they attributed the reduction in the passage vortex system with high coolant injection into the inlet endwall boundary layer as seen in this study. This result is both favourable for design and performance because less energy is then extracted from the compressor stage and this will contribute to improved aerodynamic performance in the turbine stages. Li et al. (2015) and Li et al. (2016) also found that higher momentum coolant flow had greater impact on the secondary flow losses in the passage.

Film-cooling case-2 results in lower coolant supply rates but ineffectively amounts to higher total pressure losses per MFR. Thus film-cooling case-1 is seen to be most successful, and at the highest inlet blow ratio results in the lowest total pressure losses even though the coolant supply suffers. The effect of the filleted film-cooling case has further implications as the total pressure losses increase; however, these losses are largely attributed to the primary flow conditions (wake region and endwall boundary layer). The difference in performance with and without the fillet for film-cooling case-2 is then dependent on the resultant secondary flow structures as the flow field uniformity faired the same in each case.

CHAPTER 6: SUMMARY, CONCLUSIONS AND RECOMMENDATIONS

The time-averaged flow field properties were measured to investigate the effects of upstream slot film-cooling with and without leading-edge fillets in a linear vane cascade for different slot-film injection rates. The vane geometry is based on the hub-side airfoil of GE-E^3 first-stage vane blade and was scaled to six times to form the two-dimensional cascade passage for the experiments. The other cascade geometric parameters are also six times of the actual hub-side geometry of the first-stage vane of GE-E^3. The cascade consists of seven two-dimensional vane blades to form six passages and is housed in an atmospheric wind tunnel. The primary objectives of the investigations were to quantify the reductions in the secondary flow losses across the vane cascade. The slot configuration consists of four flush slots placed parallel to the cascade inlet plane upstream of the vane stagnation in close proximity to the leading edge. Two of the slots are located directly upstream of the leading edges of two vanes comprising the test passage of the cascade. Two film-cooling cases are compared by employing all four slots and then considering the effects of coolant injection from only two central slots, blocking the two slots upstream of the leading edges. Further experiments are conducted with the leading-edge fillets and film-cooling with the central slots. The inlet velocity to the cascade is 9.6 m/s at 0° incidence and provides a Reynolds number of 233 000 based on the true vane-airfoil chord at the laboratory atmospheric conditions. A turbulence grid in the wind tunnel upstream of the cascade test section increased the free-stream turbulence to 3% at the inlet flow. The fillet was employed at the vane-endwall junction along the vane profile. The fillet profile extends from the leading edge to trailing edge on the pressure side and to throat region on the suction side such that the throat of the vane cascade was not affected. Also, the fillet height varied linearly from the vane wall to endwall and blended smoothly into the vane and endwall simultaneously inside the passage. For all experimental test cases, the blade static pressure was measured at the midspan location to ensure equal mass flow in the passage and periodicity within the cascade. The experimental results were presented in terms of the static pressure distributions on endwall and vane airfoil, and passage flow properties such as the axial vorticity, flow angle variation and total pressure losses. The flow properties were measured and analysed at three axial location planes along the cascade passage. The top and bottom endwall static pressure distributions were measured to provide further details of the influences of the fillet employed at the vane-endwall junction. The effects of these modifications were evaluated and summarised below. The experimental set-up without any fillet and film-cooling flow is referred to as the baseline case.

(i) The pressure distribution along the blade midspan remained the same as for the baseline cascade when both the fillet and the film-cooling cases were employed irrespective of the coolant flow rate or inlet blowing ratio employed. The flow field properties (total pressure, flow angles, axial vorticity) also showed minor changes along most of the blade span beyond the boundary layer (0.10S) when the fillet and film-cooling flows were employed. These endwall modifications were mainly influential in the near-wall flow field. Vane loading was assumed to be unaffected to design standards with the fillet and leading-edge film-cooling flows. This is a favourable objective for any design modification in the blade passage by the gas turbine designers because no further design considerations (such as turbine/compressor size requirements) are needed with the addition of these endwall modifications.

(ii) The introduction of the fillet profile resulted in lower total pressure losses throughout the passage and in particular at the exit plane. The total pressure losses experienced at the passage exit were further reduced with upstream slot injection for film-cooling case-2 with and without fillet, particularly at high blowing rates. Film-cooling case-2 resulted in the weakening of the passage vortex system at the exit plane. Alternatively, film-cooling case-1 showed that high coolant momentum flows tend to push the vortex structures away from the endwall towards the inviscid region, and pulled in by the trailing-edge wake at the passage exit. Both cases invoked favourable endwall boundary layer conditions along the passage by reducing the pitchwise velocity components and reducing the aerodynamic losses immensely. Further improvements were seen when film-cooling case-2 and the fillet were combined as the passage vortex system was weakened and reduced in size even more on the endwall surface, especially at the higher coolant supply rate. The endwall boundary layer was thickened downstream of the throat region at the exit of the passage with the increased slot injection rates. These results were then expected to decrease the endwall heat transfer as well.

(iii) The flow field uniformity, which is the streamline turning relative to the free-stream streamlines, was greatly improved from the baseline case as the fillet (without the film-cooling flow) was significant as the fillet profile reduced the large turning of endwall region flow induced by the secondary flows. Thereafter, the film-cooling cases (with and without fillet) showed that the yaw angle deviations relative to the free-stream were reduced further near the endwall region when higher inlet blowing ratios were employed. These effects were seen throughout the passage and contributed to greater endwall film coverage in the passage. In the actual turbine passage, the streamline deviations from the free-stream orientation also aid in the upstream film-cooling of the next stage. However, the combined influences of film-cooling and fillet did not show any further improvement from film-cooling case-2 because the yaw angle deviations were fairly similar throughout the passage for both test cases.

(iv) The introduction of upstream slot film-cooling at higher inlet blowing ratio M_{in} contributed to reducing the axial vorticity extensively throughout the passage compared to the baseline cascade. The effects of the passage cross-flow in the pitchwise direction also were reduced with high coolant momentum flow for both cases of film-cooling configuration. These occurred as the film flows from the central slots created laterally weakening momentum to counteract the pitchwise pressure gradient and velocity component, and thus reduced the size and magnitudes of axial vorticity. Similarly, the suction-side horseshoe vortex was reduced significantly in size and strength with high slot injection rates at the leading edge in case-1. However, at high inlet blowing ratios, case-1 was seen to enhance the total pressure losses as the slot injection at the leading edges contributed to increased levels of positive axial vorticity, which then strengthened the passage vortex structure. In case-2, the pitchwise cross-flow in the passage was reduced and the secondary flow structures were less pronounced at the exit of the cascade. When the fillet was employed, it was able to reduce the pitchwise cross-flow in the passage further when compared with the fillet case without film-cooling. The endwall flow region near the suction side of the cascade passage in particular benefited greatly with the fillet presence because the fillet profile was able to counteract the secondary flow formation in this region. However, the fillet case alone without film-cooling was not as effective in reducing the passage vortex formation, particularly at the exit plane.

(v) The effects of coolant blowing were considered on the overall mass-averaged total pressure losses experienced at the passage exit and it was found that the highest M_{in} for case-2 contributed to the largest reduction in total pressure losses. When considering film-cooling with the fillet, it was seen that the total pressure losses were slightly higher than for this configuration of film-cooling case-2. However, the additional losses with the fillet employed were associated mostly with the enhanced mixing between the passage vortex and trailing-edge wake as well as a thickened endwall boundary layer at the passage exit. Furthermore, comparisons of the passage vortex structures between the filleted (with film-cooling) and baseline film-cooling cases (without fillet) showed that there was a superior reduction in both size and strength in the secondary flow structures when the fillet was employed with film-cooling. Thus, the filleted film-cooling case contributed to further reduction of secondary flow development within the passage.

The overall results are beneficial for turbine design considerations with upstream slot film-cooling geometry and leading-edge fillets. The upstream slots represent a modified design (interrupted slots) of the clearance gap between the discs of the stationary vane stage and rotating rotor stage. This upstream slot film-cooling approach thereby has great potential to reduce the aerodynamic losses experienced in the turbine blade passages because it is able to re-energise the endwall boundary layer and counteract the pitchwise cross-flow inside the blade passages. The success in the flow field improvements can then aid in reducing the endwall heat transfer, which is usually enhanced due to the secondary flows. The addition of fillet geometry at the blade-endwall junction

reduces the aerodynamic loss even further and is largely attributed to the chosen fillet design and shape at the leading-edge region. The leading-edge slots of film-cooling case-1 can therefore be replaced by the fillet geometry, which will complement film flow from the central slots of case-2 to better improve the passage flow field.

Recommendations to improve the results of the current study would be to investigate the effects of additional fillet profiles. The present fillet profile is not optimised in terms of reducing the passage vortex structure and endwall region flow deviations. Additionally, turbulence measurements within the blade passages will provide more information on the flow field behaviour when film-cooling is introduced. Lastly, flow visualisation studies and endwall temperature distributions can aid in tracking the film-cooling flow along the endwall to assess film coverage of the endwall. Another potential study can be the employment of discrete holes instead of the slots upstream. The orientation of the hole blowing and hole ejection angle relative to the flow incidence angle can influence the endwall region flow when the fillet is present.

REFERENCES

Ackert, S. 2011. Engine Maintenance Concepts for Financiers: Elements of Turbofan shop maintenance costs. *Aircraft Monitor.* Second ed.

Aunapu, N. V., Volino, R. J., Flack, K. A. & Stoddard, R. M. 2000. Secondary Flow Measurements in a Turbine Passage With Endwall Flow Modification. *Journal of Turbomachinery,* 122**,** 651-658.

Burd, S. W. & Simon, T. W. 1999. Measurements of Discharge Coefficients in Film Cooling. *Journal of Turbomachinery,* 121**,** 243-248.

Dunn, P. F. 2014. *Measurement and data analysis for engineering and science*, CRC press.

Eckerle, W. A. & Langston, L. 1987. Horseshoe vortex formation around a cylinder. *Journal of Turbomachinery,* 109**,** 278-285.

Friedrichs, S., Hodson, H. & Dawes, W. Distribution of film-cooling effectiveness on a turbine endwall measured using the ammonia and diazo technique. ASME 1995 International Gas Turbine and Aeroengine Congress and Exposition, 1995. American Society of Mechanical Engineers, V004T09A001-V004T09A001.

Friedrichs, S., Hodson, H. P. & Dawes, W. N. 1997. Aerodynamic Aspects of Endwall Film-Cooling. *Journal of Turbomachinery,* 119**,** 786-793.

Friedrichs, S., Hodson, H. P. & Dawes, W. N. 1999. The Design of an Improved Endwall Film-Cooling Configuration. *Journal of Turbomachinery,* 121**,** 772-780.

Goldstein, R. J., Wang, H. P. & Jabbari, M. Y. 1995. Darryl E. Metzger Memorial Session Paper: The Influence of Secondary Flows Near the Endwall and Boundary Layer Disturbance on Convective Transport From a Turbine Blade. *Journal of Turbomachinery,* 117**,** 657-665.

Gregory-Smith, D. & Biesinger, T. Turbulence Evaluation within the Secondary Flow Region of a Turbine Cascade. ASME 1992 International Gas Turbine and Aeroengine Congress and Exposition, 1992. American Society of Mechanical Engineers, V001T01A027-V001T01A027.

Gritsch, M., Schulz, A. & Wittig, S. 2001. Effect of Crossflows on the Discharge Coefficient of Film Cooling Holes With Varying Angles of Inclination and Orientation. *Journal of Turbomachinery,* 123**,** 781-787.

Gustafson, R., Mahmood, G. I. & Acharya, S. Flowfield in a Film-Cooled Three-Dimensional Contoured Endwall Passage: Aerodynamic Measurements. ASME Turbo Expo 2007: Power for Land, Sea, and Air, 2007. American Society of Mechanical Engineers, 871-887.

Hermanson, K. S. & Thole, K. A. 2000. Effect of inlet conditions on endwall secondary flows. *Journal of Propulsion and Power,* 16**,** 286-296.

Jorgensen, F. E. 2004. How to measure turbulence with Hot-wire anemometers. Dantec Dynamics A/S.

Kang, M. B., Kohli, A. & Thole, K. 1999. Heat transfer and flowfield measurements in the leading edge region of a stator vane endwall. *Journal of Turbomachinery,* 121**,** 558-568.

Kaszeta, R. W., Simon, T. W., Oke, R. A. & Burd, S. W. Flow Measurements in Film Cooling Flows With Lateral Injection. ASME 1998 International Gas Turbine and Aeroengine Congress and Exhibition, 1998. American Society of Mechanical Engineers, V004T09A005-V004T09A005.

Knost, D. G. & Thole, K. A. 2005. Adiabatic Effectiveness Measurements of Endwall Film-Cooling for a First-Stage Vane. *Journal of Turbomachinery,* 127**,** 297-305.

Kubendran, L., Bar-Sever, A. & Harvey, W. 1988. Flow control in a wing/fuselage-type juncture.

Lethander, A. T., Thole, K. A., Zess, G. & Wagner, J. Optimizing the vane-endwall junction to reduce adiabatic wall temperatures in a turbine vane passage. ASME Turbo Expo 2003, collocated with the 2003 International Joint Power Generation Conference, 2003. American Society of Mechanical Engineers, 711-721.

Li, X., Ren, J. & Jiang, H. 2015. Film cooling effectiveness distribution of cylindrical hole injections at different locations on a vane endwall. *International Journal of Heat and Mass Transfer,* 90**,** 1-14.

Li, X., Ren, J. & Jiang, H. 2016. Multi-row film cooling characteristics on a vane endwall. *International Journal of Heat and Mass Transfer,* 92**,** 23-33.

Ligrani, P., Singer, B. & Baun, L. 1989a. Miniature five-hole pressure probe for measurement of three mean velocity components in low-speed flows. *Journal of Physics E: Scientific Instruments,* 22**,** 868.

Ligrani, P., Singer, B. & Baun, L. 1989b. Spatial resolution and downwash velocity corrections for multiple-hole pressure probes in complex flows. *Experiments in Fluids,* 7**,** 424-426.

Lynch, S. P. & Thole, K. A. 2011. The Effect of the Combustor-Turbine Slot and Midpassage Gap on Vane Endwall Heat Transfer. *Journal of Turbomachinery,* 133**,** 041002.

Lynch, S. P., Thole, K. A., Kohli, A. & Lehane, C. 2011. Computational predictions of heat transfer and film-cooling for a turbine blade with nonaxisymmetric endwall contouring. *Journal of Turbomachinery,* 133**,** 041003.

Mahmood, G. & Acharya, S. 2007. Experimental investigation of secondary flow structure in a blade passage with and without leading edge fillets. *Journal of Fluids Engineering,* 129**,** 253-262.

Mahmood, G., Gustafson, R. & Acharya, S. 2005. Experimental investigation of flow structure and Nusselt number in a low-speed linear blade passage with and without leading-edge fillets. *Journal of heat transfer,* 127**,** 499-512.

Mahmood, G. I., Saha, A. K. & Acharya, S. 2008. Secondary flow and upstream film cooling in a linear NGV cascade in compressible flows: computations and experiments. *HEFAT 2008*.

Moffat, R. J. 1988. Describing the uncertainties in experimental results. *Experimental thermal and fluid science,* 1**,** 3-17.

Pierce, F. & Shin, J. 1992. The development of a turbulent junction vortex system (data bank contribution). *Journal of fluids engineering,* 114**,** 559-565.

Praisner, T., Seal, C., Takmaz, L. & Smith, C. 1997. Spatial-temporal turbulent flow-field and heat transfer behavior in end-wall junctions. *International Journal of Heat and Fluid Flow,* 18**,** 142-151.

Radomsky, R. & Thole, K. 2000. High freestream turbulence effects in the endwall leading edge region. *ASME J. Turbomach,* 122**,** 699-708.

Radomsky, R. W. & Thole, K. A. 1999. Flowfield Measurements for a Highly Turbulent Flow in a Stator Vane Passage. *Journal of Turbomachinery,* 122**,** 255-262.

S. L. Dixon, C. a. H. 2010. *Fluid Mechanics and Thermodynamics of Turbomachinery,* Oxford, Butterworth-Heinemann.

Sauer, H., Muller, R. & Vogeler, K. 2001. Reduction of secondary flow losses in turbine cascades by leading edge modifications at the endwall. *Journal of turbomachinery,* 123**,** 207-213.

Schneider, C. M., Schrack, D., Kuerner, M., Rose, M. G., Staudacher, S., Guendogdu, Y. & Freygang, U. 2013. On the Unsteady Formation of Secondary Flow Inside a Rotating Turbine Blade Passage. *Journal of Turbomachinery,* 136**,** 061004-061004.

Shih, T. I. P. & Lin, Y. L. 2003. Controlling Secondary-Flow Structure by Leading-Edge Airfoil Fillet and Inlet Swirl to Reduce Aerodynamic Loss and Surface Heat Transfer. *Journal of Turbomachinery,* 125**,** 48-56.

Standard, A. 1984. Measurement of fluid flow in pipes using orifice, nozzle and venturi. *ASME MFC-3M.* United Engineering Center 345 East 47th Street, New York.

Sung, C. & Lin, C. 1988. Numerical Investigation on the Effect of Fairing on the Vortex Flows Around Airfoil/Flat-Plate Junctures, AIAA Paper 88-0615, Jan. 1988.

Thole, K. A. & Knost, D. G. 2005. Heat transfer and film-cooling for the endwall of a first stage turbine vane. *International Journal of Heat and Mass Transfer,* 48**,** 5255-5269.

Timko, L. P. 1990. Energy Efficient Engine High Pressure Turbine Component Test Performance Report. Contract Report for NASA. Report No. NASA CR-168289

Wang, H.-P., Olson, S. J., Goldstein, R. J. & Eckert, E. R. Flow visualization in a linear turbine cascade of high performance turbine blades. ASME 1995 International Gas Turbine and Aeroengine Congress and Exposition, 1995. American Society of Mechanical Engineers, V004T09A007-V004T09A007.

Wang, H. P., Olson, S. J., Goldstein, R. J. & Eckert, E. R. G. 1997. Flow Visualization in a Linear Turbine Cascade of High Performance Turbine Blades. *Journal of Turbomachinery,* 119**,** 1-8.

Zess, G. A. & Thole, K. A. 2002. Computational Design and Experimental Evaluation of Using a Leading Edge Fillet on a Gas Turbine Vane. *Journal of Turbomachinery,* 124**,** 167-175.

APPENDIX A: PRESSURE TRANSDUCER CALIBRATION

Differential pressure transducers were used to measure reference pressures, five-hole probe pressures and endwall static pressures inside the test section. Hence, to determine accurate pressure readings, each transducer was calibrated according to its specified range to determine calibration curves and analytical equations for simple conversions. A total of nine differential pressure transducers were used for pressure measurements relating to reference pressure for the pitot-static probe (total and static pressure measured individually), five-hole probe ports (five individual pressure ports measured), pressure drop across the orifice plate used for estimating film-cooling flow rate (pressure drop measured with single transducer) and total pressure inside the plenum to determine the film-cooling inlet blow ratio. The pressure transducers were calibrated using a Setra Micro-Cal Automated low pressure air calibrator, which has a pressure range of 0 - 3500 Pa and an accuracy of 1.42 Pa.

TABLE A.1 PRESSURE TRANSDUCER LIST AND SPECIFICATIONS.

Pressure Transducer	Manufacturer	Pressure Range [Pa]	Measurement
1	Siemens SITRANS P	0 – 496	Five-hole probe Port 1
2	Omega PX653	0 – 1242	Five-hole probe Port 2
3	Omega PX653	0 – 1242	Five-hole probe Port 3
4	Omega PX653	0 – 1242	Five-hole probe Port 4
5	Omega PX653	0 – 1242	Five-hole probe Port 5
6	Omega PX2650	0 – 124	Pitot-static probe Total Pressure
7	Omega PX2650	0 – 496	Pitot-static probe Static Pressure
8	Omega PX2650	0 – 1242	Plenum Total Pressure
9	Omega PX164	0 – 1242	Orifice Pressure Drop

Before each transducer was connected to the calibrator, the calibrator system was zeroed to remove any air inside. The data acquisition system used to collect offset values before experiments were conducted was used to record the calibration procedure, created in Labview™. The calibrator air tubes provided both positive and negative terminals to connect the corresponding

channels on the transducers. Thereafter, depending on the specified range of each transducer, the pressure values were increased incrementally from 0 Pa to a nominal maximum and repeated for the decrease in similar increments as a check for hysteresis in the transducer. However, all of the pressure transducers showed good agreement when the calibration pressure was lowered back to 0 Pa indicating no hysteresis. Details of each pressure transducer are given in Table A.1.

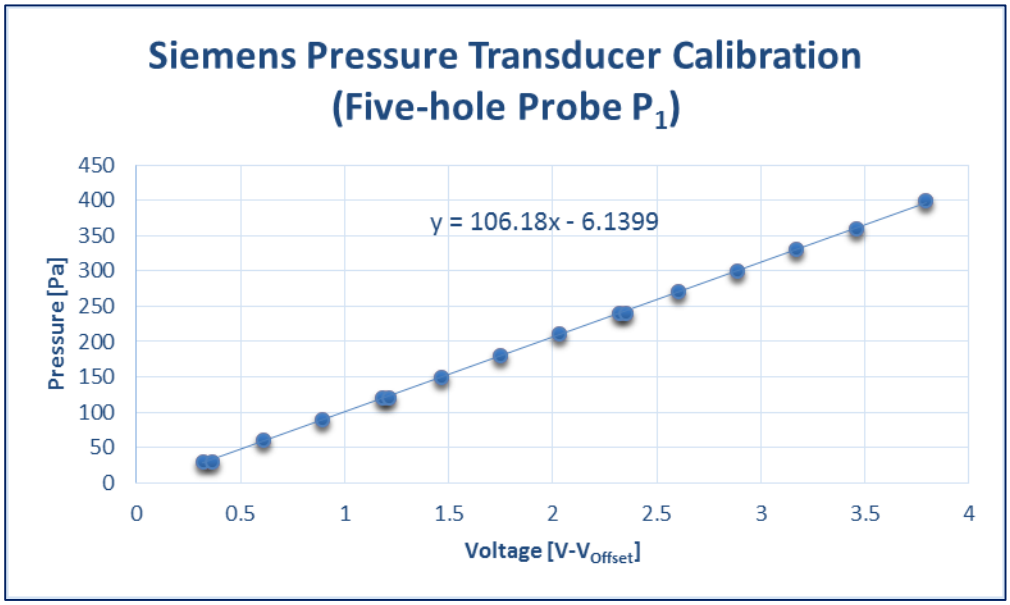

FIGURE A.1 SIEMENS PRESSURE TRANSDUCER CALIBRATION CURVE – FIVE-HOLE PROBE PORT 1.

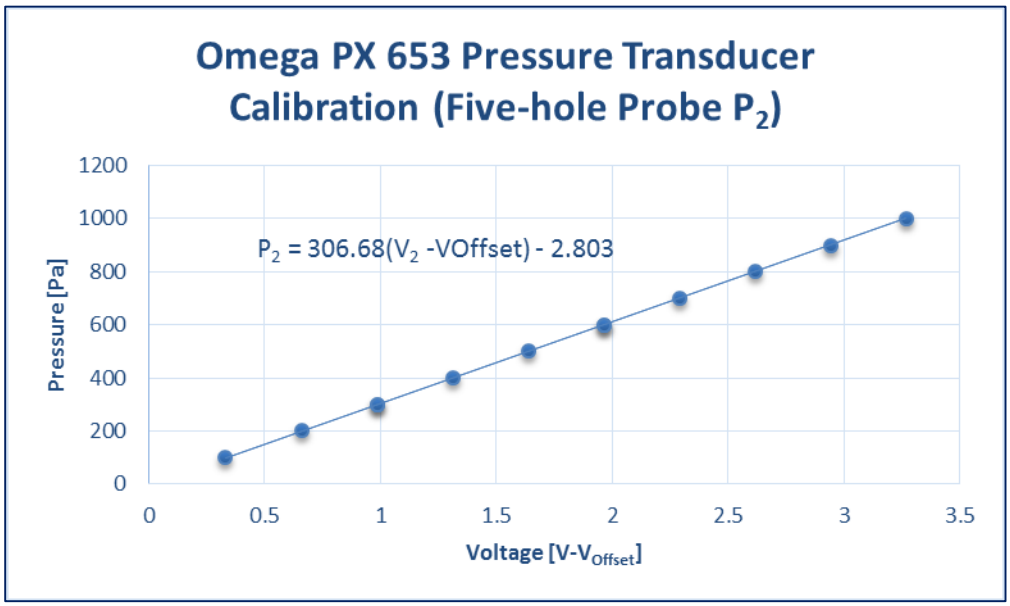

FIGURE A.2 OMEGA PX 653 PRESSURE TRANSDUCER CALIBRATION CURVE – FIVE-HOLE PROBE PORT 2.

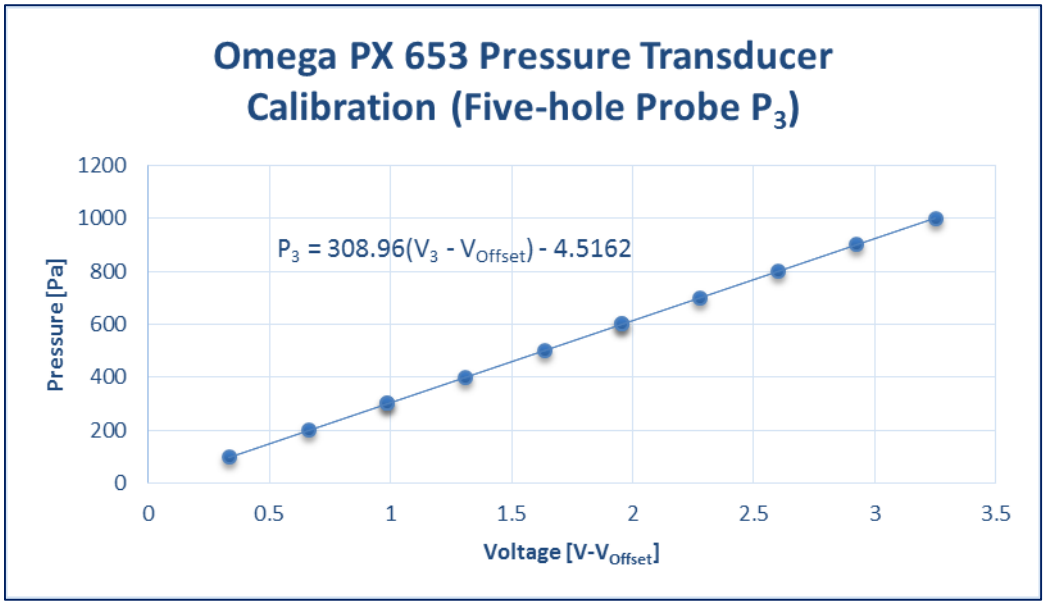

FIGURE A.3 OMEGA PX 653 PRESSURE TRANSDUCER CALIBRATION CURVE – FIVE-HOLE PROBE PORT 3.

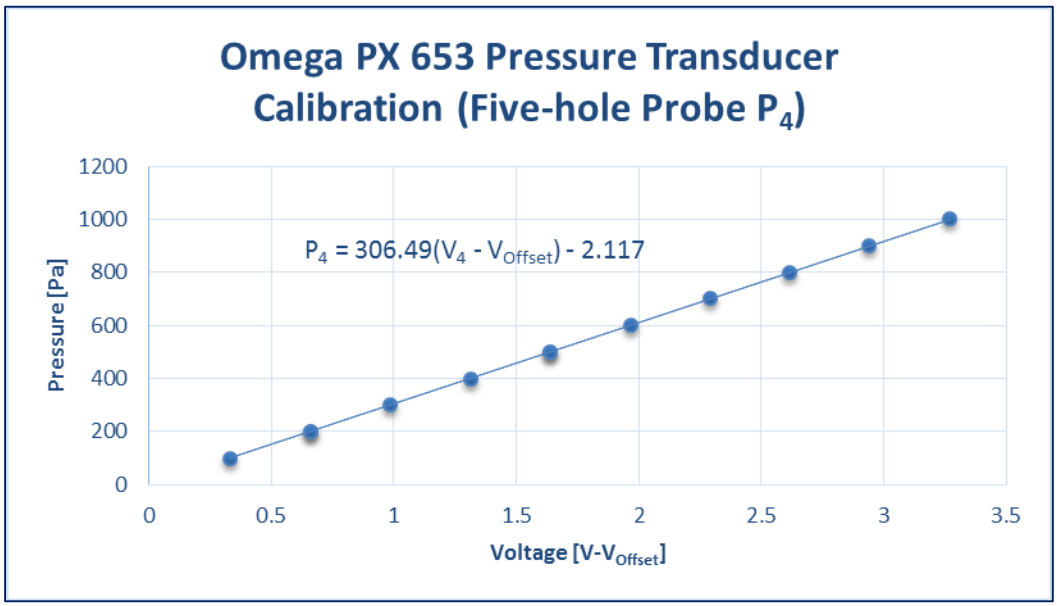

FIGURE A.4 OMEGA PX 653 PRESSURE TRANSDUCER CALIBRATION CURVE – FIVE-HOLE PROBE PORT 4.

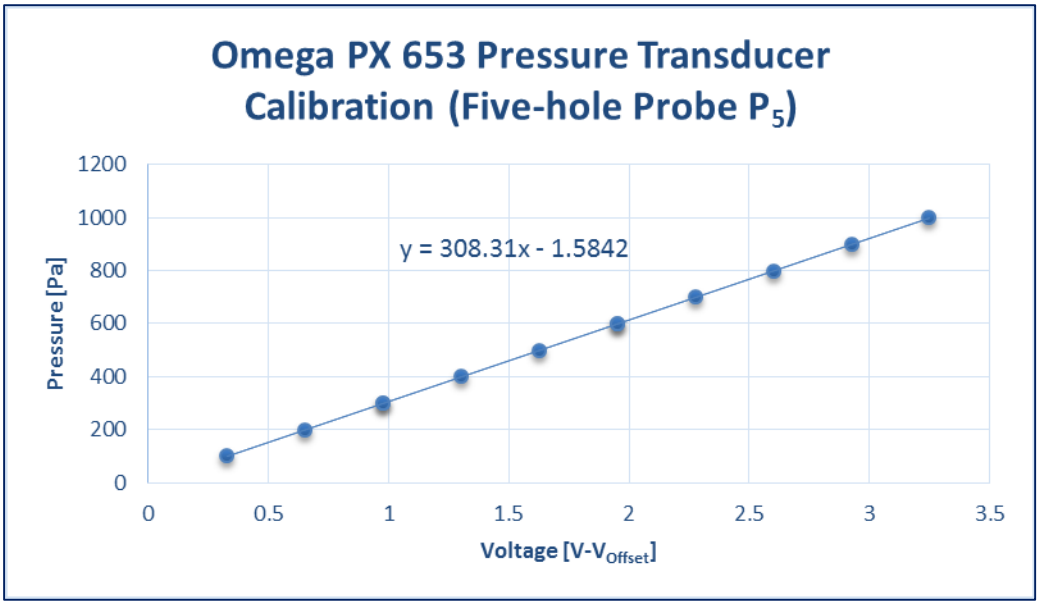

FIGURE A.5 OMEGA PX 653 PRESSURE TRANSDUCER CALIBRATION CURVE – FIVE-HOLE PROBE PORT 5.

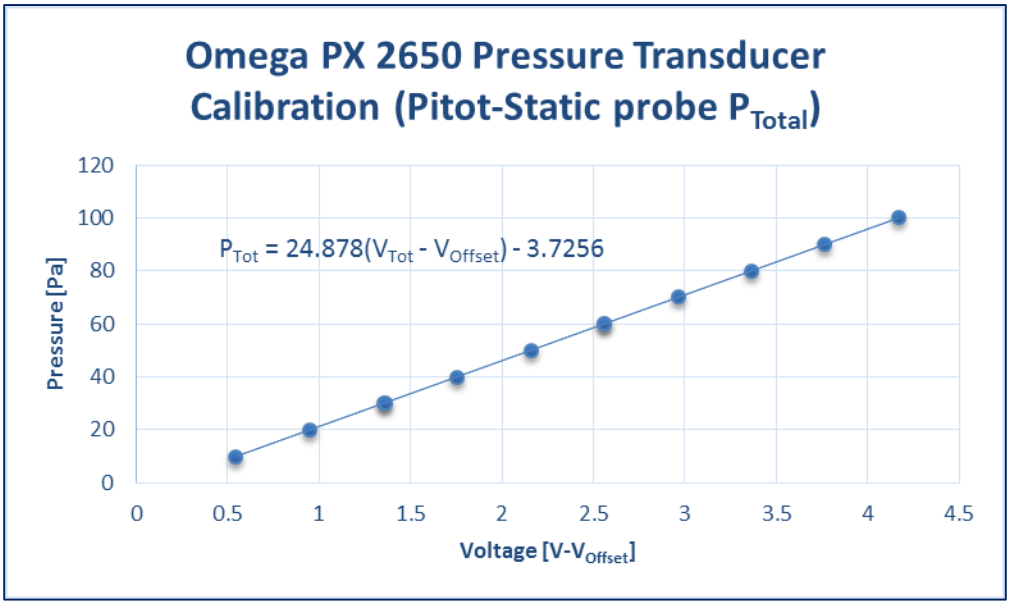

FIGURE A.6 OMEGA PX 2650 PRESSURE TRANSDUCER CALIBRATION CURVE – PITOT-STATIC PROBE TOTAL PRESSURE.

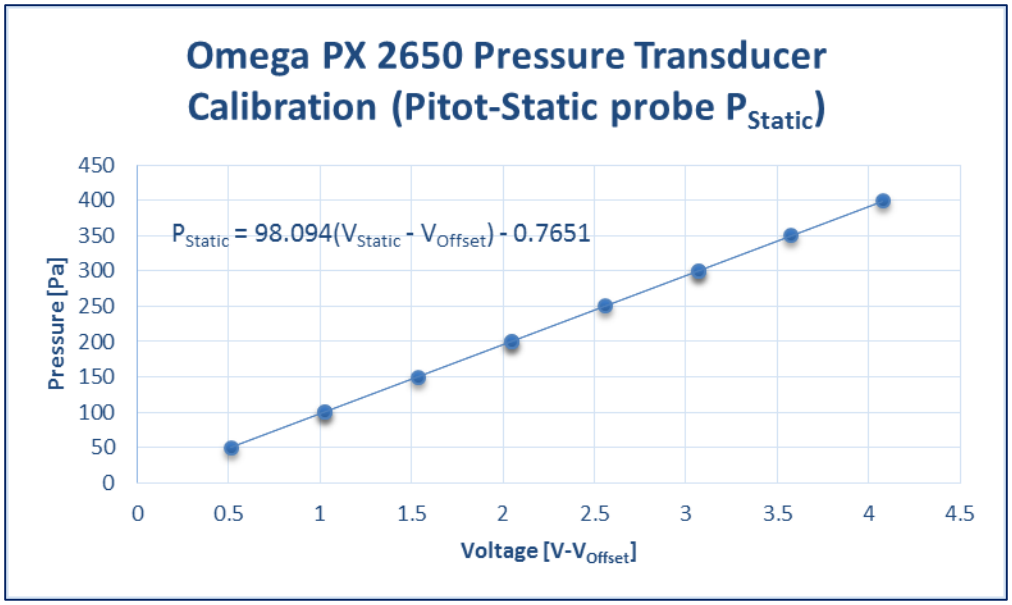

FIGURE A.7 OMEGA PX 2650 PRESSURE TRANSDUCER CALIBRATION CURVE – PITOT-STATIC PROBE STATIC PRESSURE.

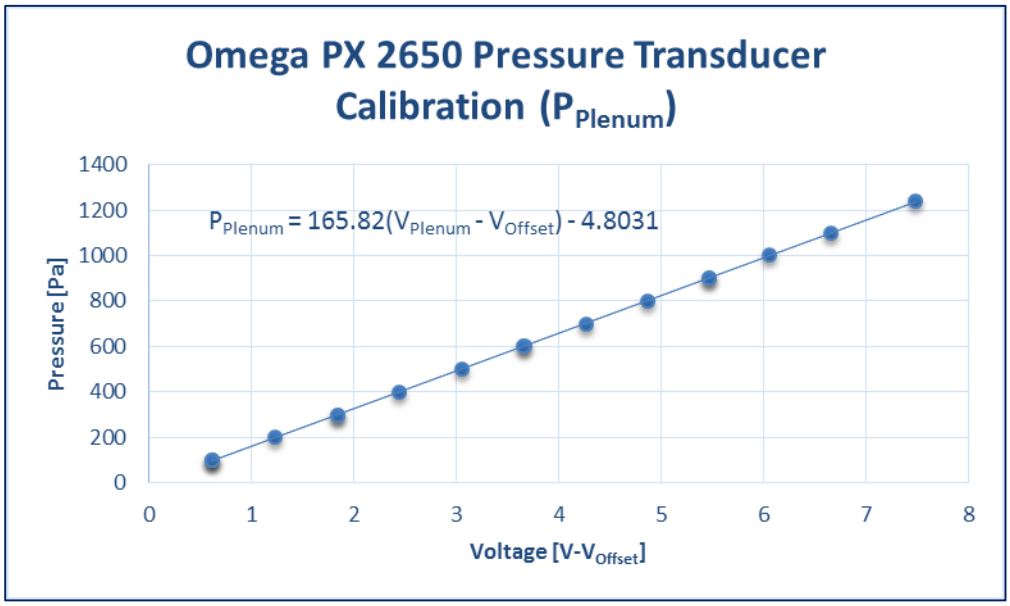

FIGURE A.8 OMEGA PX 2650 PRESSURE TRANSDUCER CALIBRATION CURVE – PLENUM PRESSURE.

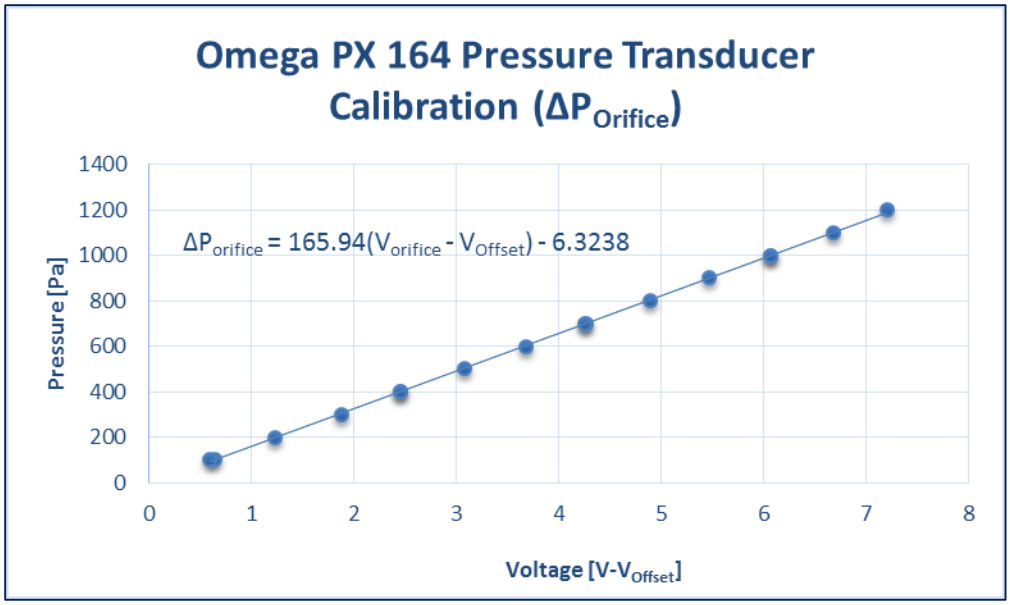

FIGURE A.9 OMEGA PX 164 PRESSURE TRANSDUCER CALIBRATION CURVE – ORIFICE PRESSURE DROP.

Figures A-1 to A-9 show the calibration curves for each of the pressure transducers specified in Table A.1 as well as the derived analytical conversion equations based on a linear curve fitted to the data set to determine the relationship between the resultant pressure and voltage across the transducer. It is important to note that prior to conducting any experiments, offset voltages with no-flow conditions are recorded to provide input for data conversion with completed experimental data measured with each transducer. These equations are then used for data conversion and processing of all experimental investigations using these pressure transducers.

APPENDIX B: FIVE-HOLE PROBE CALIBRATION

The five-hole probe calibration was conducted in the upstream section of the turbulence grid where the free-stream velocity was 8.7m/s. The procedure involved manually fixing the probe at a known yaw angle and then rotating the tip over the range of pitch angles. The calibration range was taken between -25° to +25° for both the pitch and yaw angle. The calibration coefficients were presented next and showed good agreement with Ligrani et al. (1989a).

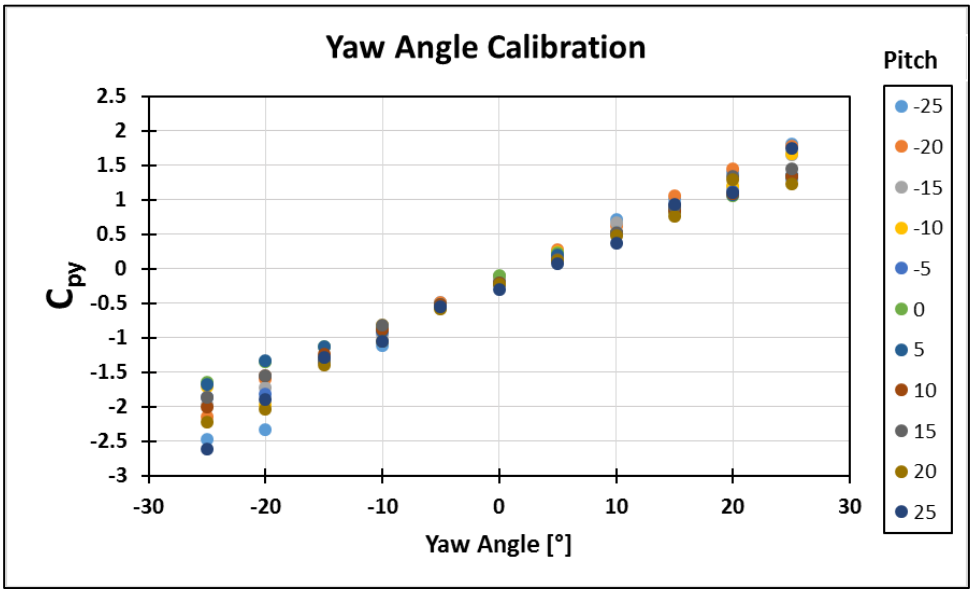

FIGURE B.1 VARIATION OF C_{PY} WITH YAW ANGLE AND PITCH ANGLE.

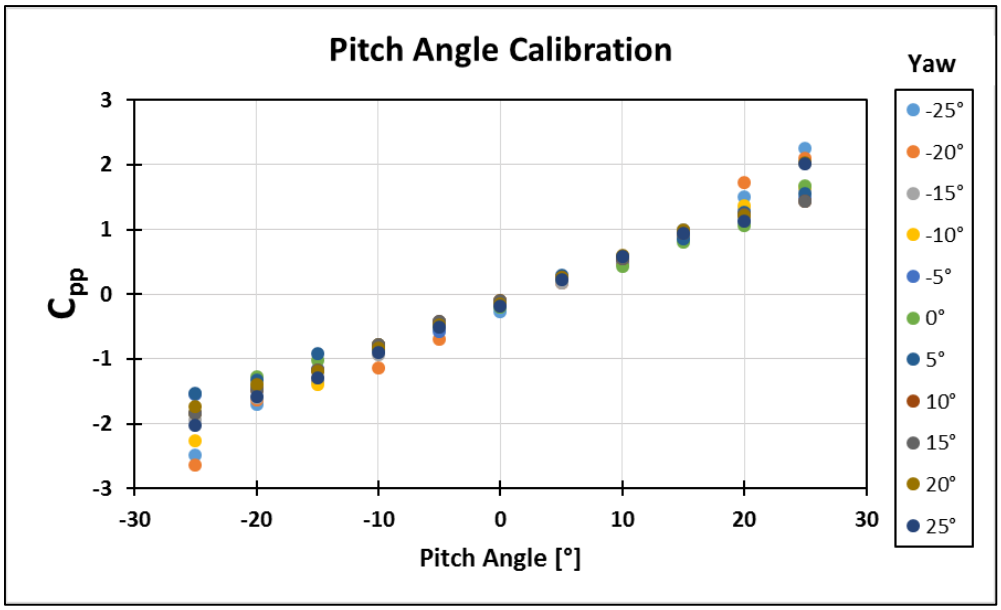

FIGURE B.2 VARIATION OF C_{PP} WITH PITCH ANGLE AND YAW ANGLE.

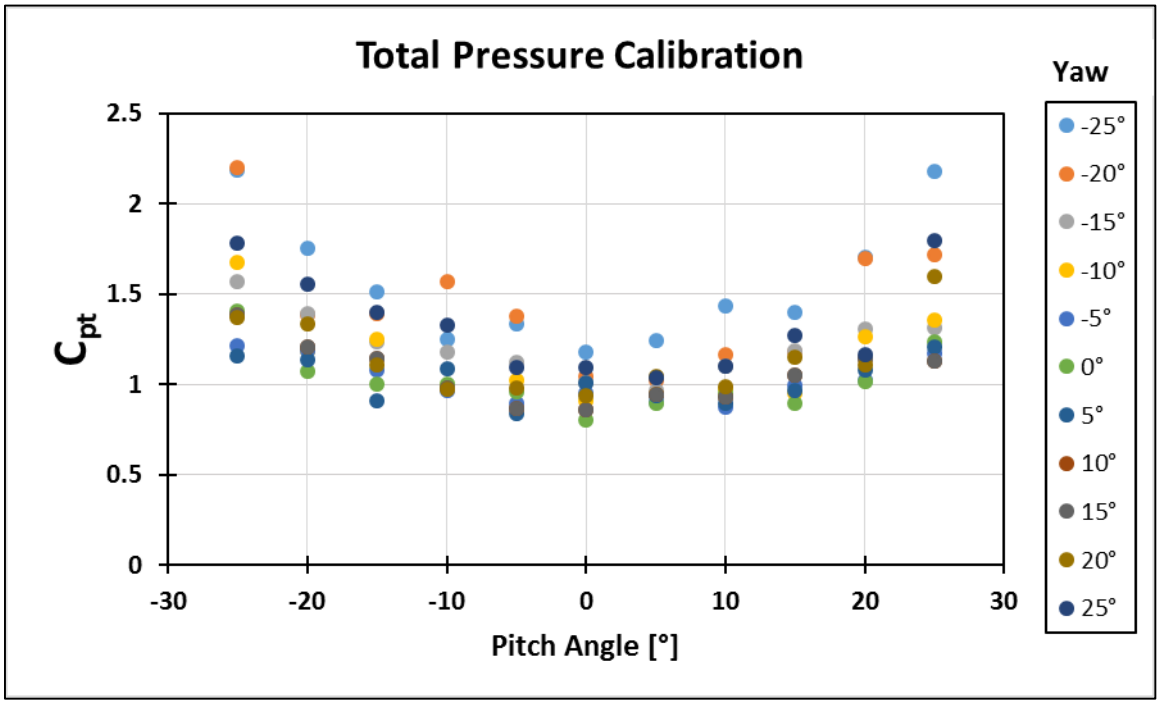

FIGURE B.3 VARIATION OF C_{PT} WITH PITCH ANGLE AND YAW ANGLE.

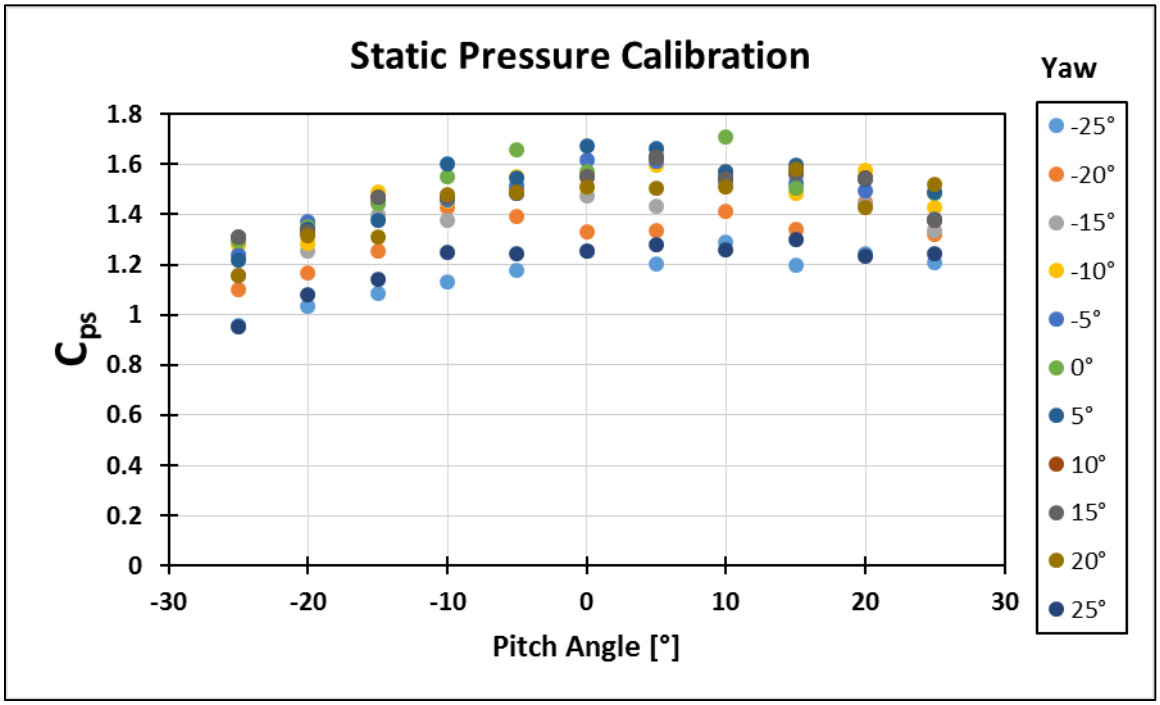

FIGURE B.4 VARIATION OF C_{PS} WITH PITCH ANGLE AND YAW ANGLE.

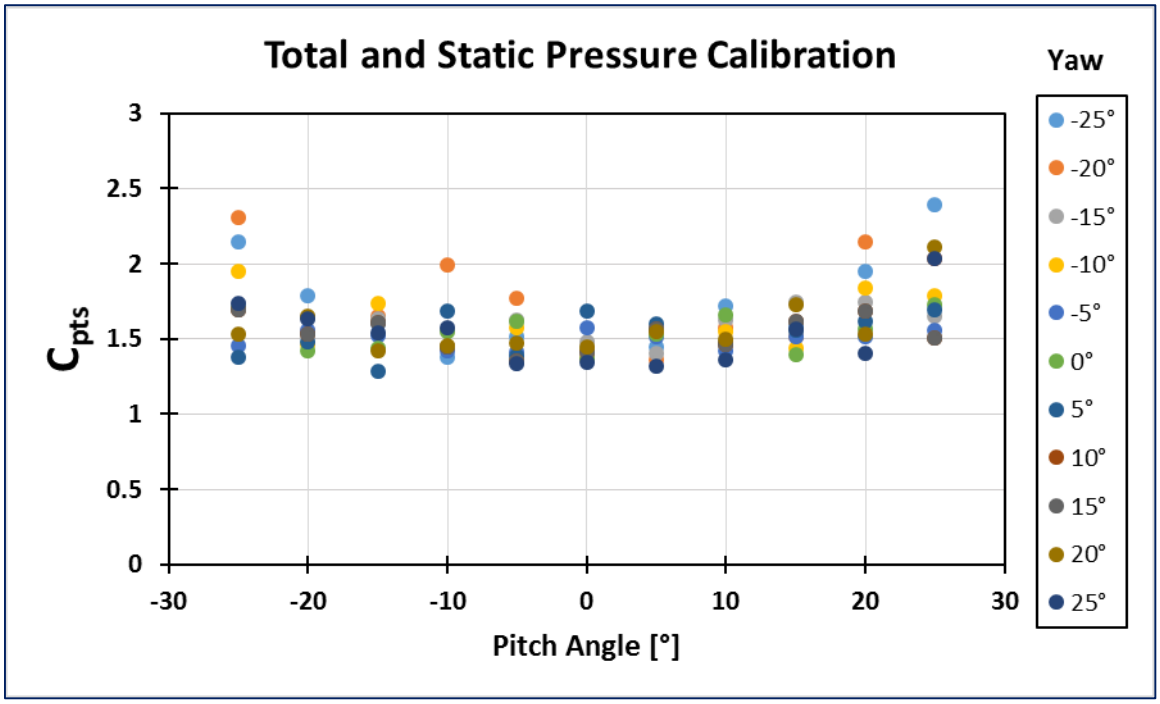

FIGURE B.5 VARIATION OF C_{PTS} WITH PITCH ANGLE AND YAW ANGLE.

APPENDIX C: UNCERTAINTY ANALYSIS

C.1 Introduction

An uncertainty analysis provides a method of establishing the degree of accuracy in experimental data as well as the degree of accuracy in experimental equipment and instrumentation. The uncertainty estimation of measured values is further used to determine the uncertainty of calculated results. The methodology used to determine uncertainties in measured and calculated values is described for this study in the sections to follow.

C.2 Theory and methodology

Two types of errors arise during experimental measurement, bias and precision errors. The bias error refers to the accuracy of the measurement, which is generally specified by the manufacturer of the related instrument. The bias errors arise due to calibration as well as manufacturing errors and imperfections which exist in the measuring equipment. Precision errors refer to the variation in measured data, which can be attributed to factors such as external interference in electrical signals as well as changes in ambient atmospheric conditions during experiments. The total uncertainty is taken as the magnitude of the bias and precision errors of which a 95% confidence level is assumed for the probability that the actual error does not exceed the estimate. The uncertainty in a single measurement is described as follows (Moffat, 1988):

Overall uncertainty: $$\delta x_i = (b_i{}^2 + p_i{}^2)^{1/2} \quad \text{(C.1)}$$

x_i represents the observation in a single sample of experimental data while δx_i is defined as the standard deviation multiplied by the Student's t-variable. The result of a measurement may be the function of several independent variables that are measured:

Result: $$R = R(x_1, x_2, x_3, \dots, x_n) \quad \text{(C.2)}$$

By determining the uncertainties of x_i, the uncertainty of R can be deduced through a sensitivity analysis of the calculated result with respect to each independent variable:

Uncertainty in Result: $$\delta R_{x_i} = \frac{\partial R}{\partial x_i}\delta x_i \quad \text{(C.3)}$$

The sensitivity coefficient, δR_{x_i}, of each variable contributes to the overall uncertainty in the result R. These terms are combined in a root-sum-square method to estimate the overall uncertainty:

Root-sum-square $$\delta R = \left\{ \sum_{i=1}^{n} \left(\frac{\delta R}{\delta x_i} \delta x_i \right)^2 \right\}^{1/2} \quad \text{(C.4)}$$

The precision error for the pressure transducers is determined from the calibration data using linear regression. Linear regression analysis provides a suitable method to determine a mathematical relationship between two or more variables (Dunn, 2014). Because the x-variable is known, the y-variable is obtained from the measurement and therefore the uncertainty lies in the y-variable. The uncertainty in the dependent variable can be determined by equations C.5 – C.12 derived from Dunn (2014):

$$\delta y = \pm t S_{yx} \sqrt{\frac{1}{N} + \frac{1}{M} + \frac{(x_i - \bar{x_i})^2}{S_{xx}}} \quad \text{(C.5)}$$

where:

t	: Student's t-variable
S_{yx}	: Standard error of best fit
N	: Number of data points
M	: Number of measured points (sample)
$\bar{x_i}$	: Average of x data
S_{xx}	: Sum of the squares of x data
S_{xy}	: Sum of the squares of x and y data
$\bar{y_i}$	: Average of y data (measured)
y_{ci}	: Calculated y data
a	: Best-fit intercept
b	: Best-fit slope
n	: Degree of freedom of linear fit

$$S_{xx} = \sum_{i=1}^{n} (x_i - \bar{x_i})^2 \quad \text{(C.6)}$$

$$S_{xy} = \sum_{i=1}^{n} (x_i - \bar{x_i})(y_i - \bar{y_i}) \quad \text{(C.7)}$$

$$b = \frac{S_{xy}}{S_{xx}} \tag{C.8}$$

$$a = \bar{y}_l - b\bar{x}_l \tag{C.9}$$

$$y_{ci} = bx_i + a \tag{C.10}$$

$$S_{yx} = \sqrt{\frac{\sum_{i=1}^{n}(y_i - y_{ci})^2}{n-2}} \tag{C.11}$$

The uncertainty in the x-variable can be determined by the slope of the regression line when the uncertainty in y is known:

$$\delta x = \frac{\delta y}{b} \tag{C.12}$$

C.3 Pressure transducers

The method described in section C.2 is used to determine the precision error for each of the pressure transducers. A sample calculation is shown for one of the pressure transducers. The pressure transducer used to measure five-hole probe port 5 is used in the sample calculation to follow. Here, the x-variable relates to pressure and the y-variable to output voltage.

$$S_{xx} = \sum_{i=1}^{n}(x_i - \bar{x}_l)^2$$

$$\begin{aligned} S_{xx} = {} & (0 - 457.14)^2 + (100 - 457.14)^2 + (200 - 457.14)^2 + (300 - 457.14)^2 \\ & + (400 - 457.14)^2 + (500 - 457.14)^2 + (600 - 457.14)^2 \\ & + (700 - 457.14)^2 + (800 - 457.14)^2 + (900 - 457.14)^2 \\ & + (1000 - 457.14)^2 + (600 - 457.14)^2 + (300 - 457.14)^2 \\ & + (0 - 457.14)^2 \end{aligned}$$

$$\therefore S_{xx} = 1374285.714\ Pa^2$$

$$S_{xy} = \sum_{i=1}^{n}(x_i - \bar{x}_l)(y_i - \bar{y}_l)$$

$$S_{xy} = (0 - 457.14)(1.038875 - 2.526) + (100 - 457.14)(1.36612 - 2.526) + (200 - 457.14)(1.69254 - 2.526) + (300 - 457.14)(2.01798 - 2.526) + (400 - 457.14)(2.34298 - 2.526) + (500 - 457.14)(2.666995 - 2.526) + (600 - 457.14)(2.990725 - 2.526) + (700 - 457.14)(3.314525 - 2.526) + (800 - 457.14)(3.638725 - 2.526) + (900 - 457.14)(3.962665 - 2.526) + (1000 - 457.14)(4.28629 - 2.526) + (600 - 457.14)(2.990395 - 2.526) + (300 - 457.14)(2.01654 - 2.526) + (0 - 457.14)(1.03888 - 2.526)$$

$$\therefore S_{xy} = 4462.166\ PaV$$

$$b = \frac{S_{xy}}{S_{xx}}$$

$$b = \frac{4462.166}{1391597.633}$$

$$b = 0.003247\frac{V}{Pa}$$

$$a = \bar{y_i} - b\bar{x_i}$$

$$a = 2.526 - 0.003247 * 457.14$$

$$a = 1.04172\ V$$

$$S_{yx} = \sqrt{\frac{\sum_{i=1}^{n}(y_i - y_{ci})^2}{n-2}}$$

At $x_i = 100\ Pa, y_i = 1.36612\ V$ the y_{ci} is found by:

$$y_{ci} = bx_i + a$$

$$y_{ci} = (0.003247 * 100) + 1.04172$$

$$y_{ci} = 1.36642\ V$$

$$\sum_{i=1}^{n}(y_i - y_{ci})^2 = (1.038875 - 1.04172)^2 + (1.36612 - 1.36641)^2 + (1.69254 - 1.6911)^2$$
$$+ (2.01798 - 2.01579)^2 + (2.34298 - 2.34048)^2 + (2.666995 - 2.66517)^2$$
$$+ (2.990725 - 2.989859)^2 + (3.314525 - 3.314549)^2$$
$$+ (3.638725 - 3.639239)^2 + (3.962665 - 3.963929)^2$$
$$+ (4.28629 - 4.288619)^2 + (2.990395 - 2.989859)^2$$
$$+ (2.01654 - 2.01579)^2 + (1.03888 - 1.04172)^2$$

$$\sum_{i=1}^{n}(y_i - y_{ci})^2 = 4.1586\,E-05\,V^2$$

$$S_{yx} = \sqrt{\frac{4.1586\,E-05}{14-2}}$$

$$\therefore S_{yx} = 1.86158\,E-03\,V$$

Therefore, the precision component at 1 000 Pa can be determined by combining Eq. C.5 and C.12:

$$p_{P_5} = \pm 2.145 * \frac{1.86158\,E-03}{0.003247}\sqrt{\frac{1}{200}+\frac{1}{14}+\frac{(1000-492.307)^2}{1374285.714}}$$

$$\therefore p_{P_5} = \pm\, 0.66323\ Pa$$

The accuracy of the calibrator unit indicated as $\pm\, 0.04\%$ Full-scale (3550 Pa), which provides the bias component for the calibrator pressure uncertainty, is determined to be 1.42 Pa. Therefore the pressure transducers are calibrated accordingly to account for the operating conditions. The total uncertainty of this pressure transducer for the average of the calibrated pressures is then calculated by taking the manufacturer's quoted accuracy (as % of full scale):

$$\delta P_5 = ({b_{P_5}}^2 + {p_{P_5}}^2 + {b_{cal}}^2)^{1/2}$$

$$\delta P_5 = (3.105^2 + 0.66323^2 + 1.42^2)^{1/2}$$

$$\therefore \delta P_5 = \pm 3.47\ Pa$$

$$\overline{P_5} = 457.14\ Pa$$

The percentage uncertainty is then defined by dividing by the average calibrated pressure:

$$\delta P_5\% = \frac{3.47}{457.14} \times 100 = 0.76\ \%$$

This is the overall uncertainty for nominal pressure of 1 000 Pa.

The overall uncertainties for all pressure transducers are given in Table C.1.

TABLE C.1 UNCERTAINTIES OF PRESSURE TRANSDUCERS FOR AVERAGE CALIBRATED PRESSURES

Pressure Transducer	Manufacturer	Measurement	Bias Component (manufacturer Accuracy) [Pa]	Max. Precision Component [Pa]	Max. Overall Uncertainty [Pa]	Max. Overall Uncertainty %
1	Siemens SITRANS P	Five-hole probe Port 1	1.0	2.67	3.18	1.83
2	Omega PX653	Five-hole probe Port 2	3.105	1.08	3.58	0.78
3	Omega PX653	Five-hole probe Port 3	3.105	1.69	3.812	0.83
4	Omega PX653	Five-hole probe Port 4	3.105	0.867	3.523	0.79
5	Omega PX653	Five-hole probe Port 5	3.105	0.66	3.47	0.76
6	Omega PX2650	Pitot-static probe Total Pressure	0.31	1.279	1.936	4.23
7	Omega PX2650	Pitot-static probe Static Pressure	1.24	0.506	1.953	1.05
8	Omega PX2650	Plenum Total Pressure	3.1	2.57	3.93	0.75
9	Omega PX164	Orifice Pressure Drop	3.0	4.77	5.81	1.04

C.4 Uncertainty of calculated results

The uncertainty of calculated results is determined by a sensitivity analysis of the independent variables, which define the calculated results. For this study, calculated results refer to the coefficient of total pressure loss ($C_{Pt,Loss}$), coefficient of static pressure (C_{Ps}), film-cooling inlet blow ratio (M_{in}), film-cooling flow rate based on orifice plate correlation ($\dot{m}_{Film}$) and free-stream velocity (U_{ref}). The calculated results for the five-hole probe is determined numerically based on a computerised uncertainty analysis described by Moffat (1988) using the five-hole probe analysis program. This is chosen for the current study as a numerical approach is taken for data reduction

of five-hole probe measurements. Thus the analytical approach to calculating uncertainty in the results of five-hole probe measurements becomes difficult as numerical techniques such as interpolation and iteration with spline fits are used in the reduction process.

C.4.1 Free-stream velocity

$$U_{ref} = \sqrt{\frac{2P_{Dyn,ref}}{\rho}} \tag{C.13}$$

$$U_{ref} = \sqrt{\frac{2(P_{t,ref} - P_{s,ref})}{\rho}} \tag{C.14}$$

$$\delta U_{ref} = \left[\left(\frac{\partial U_{ref}}{\partial P_{t,ref}}\delta P_{t,ref}\right)^2 + \left(\frac{\partial U_{ref}}{\partial P_{s,ref}}\delta P_{s,ref}\right)^2\right]^{1/2}$$

$$\delta U_{ref} = \left[\left(\frac{\sqrt{2}}{2}\sqrt{\frac{1}{\rho(P_{t,ref} - P_{s,ref})}}\delta P_{t,ref}\right)^2 + \left(\frac{-\sqrt{2}}{2}\sqrt{\frac{1}{\rho(P_{t,ref} - P_{s,ref})}}\delta P_{s,ref}\right)^2\right]^{1/2}$$

As an example, for the endwall static pressure experiment with film-cooling Case-2 M_{in} = 1.4 with a sample of 69 recorded reference pressures from the Pitot - static tube:

$$\overline{P_{t,ref}} = -22.253\ Pa$$

$$\overline{P_{s,ref}} = -84.284\ Pa$$

$$(Negative\ due\ to\ suction - type\ wind\ tunnel)$$

Air density:
$$\rho = \frac{(P_{atm} + \overline{P_{s,ref}})}{(RT_{atm})} \tag{C.15}$$

$$P_{atm} = 655\ mmHg = P_{mmHg} * \rho_{Hg} * g * \rho_{H_2O} * \frac{1m}{1000mm} \tag{C.16}$$

$$P_{atm} = 655 * 13.6 * 9.81 * 998 * \frac{1m}{1000mm}$$

$$\therefore P_{atm} = 87123.8\ Pa$$

$$\therefore \rho = \frac{(87123.8 - 84.284)}{287.04 * (20 + 273.15)K}$$

$$\therefore \rho = 1.03438\ kg/m^3$$

The air density is assumed to be constant throughout experiments and its sensitivity coefficient is shown to be very small (1E-07) and therefore its influence on the overall uncertainty is insignificant when combined in the root-sum-square method. The overall uncertainty of each independent variable is determined as previously shown by Eq. C.17 derived from Moffat (1988):

$$p_{i_{P_{t,ref}}} = \frac{t * \sigma_{P_{t,ref}}}{\sqrt{n-1}} \qquad \text{(C.17)}$$

Where:

σ	:Standard deviation
t	:Student's t-variable
n	:Number of degrees of freedom (data points) – (n-1) if n < 20

$$p_{i_{P_{t,ref}}} = \frac{2 * 0.230500373}{\sqrt{69}}$$

$$p_{i_{P_{t,ref}}} = 0.055497968\ Pa$$

$$\delta P_{t,ref} = \left(b_{i_{P_{t,ref}}}{}^2 + p_{i_{P_{t,ref}}}{}^2\right)^{1/2}$$

$$\delta P_{t,ref} = (1.936^2 + 0.055497968\ ^2)^{1/2}$$

$$\therefore \delta P_{t,ref} = \pm 1.936\ Pa$$

$$\delta P_{t,ref}\ \% = 8.7\ \%$$

This is the uncertainty for 22.2 Pa of negative gauge total pressure.

Similarly, the overall uncertainty in the reference static pressure can be found:

$$\delta P_{s,ref} = \pm 1.963\ Pa$$

$$\therefore \delta P_{s,ref} = 2.33\%$$

This is the uncertainty % for 84.3 Pa of negative gauge static pressure.

$$\delta U_{ref} = \left[\left(\frac{\sqrt{2}}{2}\sqrt{\frac{1}{\rho(-22.253+84.284\ )}}(1.963\ )\right)^2 + \left(\frac{-\sqrt{2}}{2}\sqrt{\frac{1}{\rho(-22.253+84.284\ )}}(1.936)\right)^2\right]^{1/2}$$

$$\therefore \delta U_{ref} = \pm 0.2435\ m/s$$

This is the uncertainty for 10.95 m/s of nominal upstream velocity.

The calculated average free-stream velocity:

$$\overline{U_{ref}} = \sqrt{\frac{2(\overline{P_{t,ref}} - \overline{P_{s,ref}})}{\rho}}$$

$$\overline{U_{ref}} = \sqrt{\frac{2(-22.253+84.284\ )}{1.03438}}$$

$$\overline{U_{ref}} = 10.95\ m/s$$

Hence the total uncertainty in the free-stream velocity is:

$$\delta U_{ref}\% = \frac{\delta U_{ref}}{\overline{U_{ref}}} \times 100\%$$

$$\delta U_{ref}\% = \frac{0.2435}{10.95} \times 100\%$$

$$\delta U_{ref}\% = 2.22\ \%$$

This is the uncertainty for 10.95 m/s of nominal upstream velocity.

C.4.2 Coefficient of static pressure

$$C_{Ps} = \frac{P_{Local} - P_{s,ref}}{P_{t,ref} - P_{s,ref}} = \frac{P_{s,ref} - P_{Local}}{P_{s,ref} - P_{t,ref}}\ (Negative\ due\ to\ suction)$$

$$\delta C_{Ps} = \left[\left(\frac{\partial C_{Ps}}{\partial P_{s,ref}}\delta P_{s,ref}\right)^2 + \left(\frac{\partial C_{Ps}}{\partial P_{t,ref}}\delta P_{t,ref}\right)^2 + \left(\frac{\partial C_{Ps}}{\partial P_{Local}}\delta P_{Local}\right)^2\right]^{1/2}$$

$$\frac{\partial C_{Ps}}{\partial P_{s,ref}} = \frac{P_{Local} - P_{s,ref}}{\left(P_{s,ref} - P_{t,ref}\right)^2} + \frac{1}{\left(P_{s,ref} - P_{t,ref}\right)}$$

$$\frac{\partial C_{Ps}}{\partial P_{t,ref}} = -\frac{P_{Local} - P_{s,ref}}{\left(P_{s,ref} - P_{t,ref}\right)^2}$$

$$\frac{\partial C_{Ps}}{\partial P_{Local}} = -\frac{1}{\left(P_{s,ref} - P_{t,ref}\right)}$$

As an example, for the endwall static pressure experiment with film-cooling case-2 M_{in} = 1.4 with a sample of six recorded local pressures at nine locations on the endwall:

Endwall static port 33 (Coordinates can be found in Appendix E):

$$\overline{P_{Endwall\ 33}} = -648.9\ Pa \qquad \delta P_{Endwall\ 33} = \pm 12.22\ Pa \qquad \delta P_{Endwall\ 33}\% = 1.88\%$$

The sensitivity coefficients can be calculated based on the reference pressures given in the previous section:

$$\frac{\partial C_{Ps,Endwall\ 8}}{\partial P_{s,ref}} = \frac{648.9\ \ -84.284}{(84.284 - 22.253)^2} + \frac{1}{(84.284 - 22.253)} = 0.161082$$

$$\frac{\partial C_{Ps,Endwall\ 8}}{\partial P_{t,ref}} = -\frac{648.9\ \ -84.284}{(84.284 - 22.253)^2} = -0.14505$$

$$\frac{\partial C_{Ps,Endwall\ 8}}{\partial P_{Endwall\ 8}} = -\frac{1}{(84.284 - 22.253)} = -0.01603$$

Therefore, the total uncertainty in C_{Ps} at Port 8 on the endwall is:

$$\delta C_{Ps,Endwall\ 8} = [(0.161082 * 2.47)^2 + (-0.14505 * 1.967\ )^2 + \ (-0.01603 * 12.22\ )^2]^{1/2}$$

$$\delta C_{Ps,Endwall\ 8} = \pm 0.527$$

$$\overline{C_{Ps,Endwall\ 8}} = \frac{\overline{P_{s,ref}} - \overline{P_{Endwall\ 8}}}{\overline{P_{s,ref}} - \overline{P_{t,ref}}}$$

$$\overline{C_{Ps,Endwall\ 8}} = \frac{84.284 - 648.9}{84.284 - 22.253} = -9.102$$

$$\therefore \delta C_{Ps}\ \% = 5.79\%$$

This equals to the uncertainty % for C_{Ps} = -9.102 nominal value.

C.4.3 Film-cooling inlet blowing ratio

$$M_{in} = \sqrt{\frac{P_{0,Plenum} - P_{s,ref}}{P_{t,ref} - P_{s,ref}}} = \sqrt{\frac{P_{0,Plenum} + P_{s,ref}}{P_{s,ref} - P_{t,ref}}} \; (Negative\ due\ to\ suction)$$

$$\delta M_{in} = \left[\left(\frac{\partial M_{in}}{\partial P_{s,ref}}\delta P_{s,ref}\right)^2 + \left(\frac{\partial M_{in}}{\partial P_{t,ref}}\delta P_{t,ref}\right)^2 + \left(\frac{\partial M_{in}}{\partial P_{0,Plenum}}\delta P_{0,Plenum}\right)^2\right]^{1/2}$$

$$\frac{\partial M_{in}}{\partial P_{s,ref}} = \frac{-\left(\frac{P_{0,Plenum} + P_{s,ref}}{(P_{s,ref} - P_{t,ref})^2} - \frac{1}{(P_{s,ref} - P_{t,ref})}\right)}{\left(2\left(\frac{P_{0,Plenum} + P_{s,ref}}{P_{s,ref} - P_{t,ref}}\right)\right)^{1/2}}$$

$$\frac{\partial M_{in}}{\partial P_{t,ref}} = \frac{(P_{0,Plenum} + P_{s,ref})}{\left(2\left(\frac{P_{0,Plenum} + P_{s,ref}}{P_{s,ref} - P_{t,ref}}\right)^{1/2}(P_{s,ref} - P_{t,ref})^2\right)}$$

$$\frac{\partial M_{in}}{\partial P_{0,Plenum}} = \frac{1}{2[(P_{s,ref} - P_{t,ref})(P_{0,Plenum} + P_{s,ref})]^{1/2}}$$

As an example, for a five-hole measurement with film-cooling case-2 M_{in} = 1.4:

$\overline{P_{0,Plenum}} = 31.16\ Pa$ $\quad$ $\overline{P_{t,ref}} = -14.25\ Pa$ $\quad$ $\overline{P_{s,ref}} = -59.38\ Pa$

$\delta P_{0,Plenum} = \pm 3.93\ Pa$ $\quad$ $\delta\ P_{t,ref} = \pm 1.936\ Pa$ $\quad$ $\delta\ P_{s,ref} = \pm 1.953\ Pa$

$\delta P_{0,Plenum}\% = 12.61\%$ $\quad$ $\delta\ P_{t,ref}\% = 13.58\%$ $\quad$ $\delta\ P_{s,ref}\% = 3.29\%$

The sensitivity coefficients can be computed to determine the overall uncertainty in the inlet blowing ratio:

$$\frac{\partial M_{in}}{\partial P_{s,ref}} = \frac{-\left(\frac{31.16 + 59.38}{(59.38 - 14.25)^2} - \frac{1}{(59.38 - 14.25)}\right)}{\left(2\left(\frac{31.16 + 59.38}{59.38 - 14.25}\right)\right)^{1/2}} = -0.0111$$

$$\frac{\partial M_{in}}{\partial P_{t,ref}} = \frac{(31.16 + 59.38)}{\left(2\left(\frac{31.16 + 59.38}{59.38 - 14.25}\right)^{1/2}(59.38 - 14.25)^2\right)} = 0.0156$$

$$\frac{\partial M_{in}}{\partial P_{0,Plenum}} = \frac{1}{2[(59.38 - 14.25)(31.16 + 59.38)]^{1/2}} = 0.0078$$

The overall uncertainty in the film-cooling inlet blowing ratio is then:

$$\delta M_{in} = [(-0.0111 * 1.953\ )^2 + (0.0156 * 1.936)^2 + (0.0078 * 3.93\ )^2]^{1/2}$$

$$\therefore \delta M_{in} = \pm 0.048$$

$$\overline{M_{in}} = \sqrt{\frac{31.16 + 59.38}{59.38 - 14.25}} = 1.42$$

$$\therefore \delta M_{in}\% = \ 3.38\%$$

This equals to the uncertainty % for M_{in} = 1.42 nominal value.

C.4.4 Film-cooling flow rate (Orifice flow rate correlation)

$$\dot{m}_{Film} = \rho C_D \left(\frac{\pi}{4} {D_{Orifice}}^2\right) \sqrt{\frac{2\Delta P_{Orifice}}{\rho(1-\beta)}}$$

$$\delta \dot{m}_{Film} = \left[\left(\frac{\partial \dot{m_{Film}}}{\partial \Delta P_{Orifice}} \delta \Delta P_{Orifice}\right)^2\right]^{1/2}$$

$$\frac{\partial \dot{m}_{Film}}{\partial \Delta P_{Orifice}} = \frac{1}{2} \rho C_D \left(\frac{\pi}{4} {D_{Orifice}}^2\right) \sqrt{\frac{2}{\rho(1-\beta)}} \left(\Delta P_{Orifice}\right)^{-1/2}$$

As an example, for a five-hole measurement with film-cooling case-2 M_{in} = 1.4:

$$\overline{\Delta P_{Orifice}} = 61.21\ Pa$$

$$\delta \Delta P_{Orifice} = \pm 5.81\ Pa$$

$$\delta \Delta P_{Orifice}\% = 9.49\%$$

The sensitivity coefficients can be computed to determine the overall uncertainty in the film-cooling flow rate:

$$\frac{\partial \dot{m}_{Film}}{\partial \Delta P_{Orifice}} = \frac{1}{2}(1.03438) * 0.6 * \left(\frac{\pi}{4}(0.036)^2\right) \sqrt{\frac{2}{1.03438 * (1 - 0.7)}} (61.21\ )^{-\frac{1}{2}}$$
$$= 1.0249E - 04$$

The overall uncertainty in the film-cooling flow rate is then:

$$\delta\dot{m}_{Film} = \left[\left((1.0152E-04)*4.97\right)^2\right]^{1/2} = \pm 5.093E-04\ kg/s$$

$$\overline{\dot{m}_{Film}} = (1.03438)*0.6*\left(\frac{\pi}{4}(0.036)^2\right)\sqrt{\frac{2*62.392}{1.03438*(1-0.7)}} = 0.0126679\ kg/s$$

$$\therefore \delta\dot{m}_{Film}\% = 4.02\ \%$$

This equals to the uncertainty % for $\dot{m}_{Film} = 0.0126679\ kg/s$ nominal value.

C.4.5 Coefficient of total pressure loss

$$C_{Pt,Loss} = \frac{P_{t,ref} - P_{Fivehole\_Total}}{P_{t,ref} - P_{s,ref}} = \frac{P_{Fivehole\_Total} - P_{t,ref}}{P_{s,ref} - P_{t,ref}}\ (Negative\ due\ to\ suction)$$

$$\delta C_{Pt,Loss} = \left[\left(\frac{\partial C_{Pt,Loss}}{\partial P_{s,ref}}\delta P_{s,ref}\right)^2 + \left(\frac{\partial C_{Pt,Loss}}{\partial P_{t,ref}}\delta P_{t,ref}\right)^2 + \left(\frac{\partial C_{Pt,Loss}}{\partial P_{Fivehole\_Total}}\delta P_{Fivehole\_Total}\right)^2\right]^{1/2}$$

$$\frac{\partial C_{Pt,Loss}}{\partial P_{Static}} = \frac{P_{t,ref} - P_{Fivehole\_Total}}{\left(P_{s,ref} - P_{t,ref}\right)^2}$$

$$\frac{\partial C_{Pt,Loss}}{\partial P_{t,ref}} = -\frac{P_{t,ref} - P_{Fivehole\_Total}}{\left(P_{s,ref} - P_{t,ref}\right)^2} - \frac{1}{P_{s,ref} - P_{t,ref}}$$

$$\frac{\partial C_{Pt,Loss}}{\partial P_{Fivehole\_Total}} = \frac{1}{P_{s,ref} - P_{t,ref}}$$

Because the value of $P_{Fivehole\_Total}$ is determined by methods described by Ligrani et al. (1989a), Ligrani et al. (1989b), the uncertainty in this value is determined by the method of sequential perturbation described by Moffat (1988) for uncertainties in calculated results, which involve operations that are difficult to differentiate analytically such as table look-ups and numerical integration. Hence the five-hole probe analysis programs that are used to process raw data obtained with the relevant pressure transducers are utilised to conduct an uncertainty analysis in five-hole probe results. The method of sequential perturbation involves perturbing the input values and accumulating the individual uncertainty contributions. The input values used and measured independently for the five-hole probe analysis program are the five pressure ports of the probe and the reference static and total pressures. Therefore, each independent variable is increased and decreased by its uncertainty interval and the results obtained and combined in a root-sum-square to determine the overall uncertainty in the calculated result. Because the five-hole probe measures pressure in spatial regions, a sample scan is taken for four observations in three areas within the measurement plane-2: a region near the pressure-side endwall, suction-

side endwall and the inviscid region at midpitch in the passage. For the sample calculation, a selected pressure measurement near the suction-side endwall region is used to determine the uncertainty in the coefficient of total pressure loss.

$$\overline{P_{Fivehole\_Total}} = -107.39\ Pa \qquad \overline{P_{t,ref}} = -13.11\ Pa \qquad \overline{P_{s,ref}} = -54.27\ Pa$$

$$\delta\ P_{Fivehole\_Total} = \pm 1.24\ Pa \qquad \delta\ P_{t,ref} = \pm 1.936\ Pa \qquad \delta\ P_{s,ref} = \pm 1.955\ Pa$$

$$\delta\ P_{Fivehole\_Total}\% = 1.15\% \qquad \delta\ P_{t,ref}\% = 14.76\% \qquad \delta\ P_{s,ref}\% = 3.6\%$$

$$(Negative\ due\ to\ suction - type\ wind\ tunnel)$$

The sensitivity coefficients can be computed to determine the overall uncertainty in the coefficient of total pressure loss:

$$\frac{\partial C_{Pt,Loss}}{\partial P_{s,ref}} = \frac{13.11\ - 107.39}{(54.27 - 13.11\ )^2} = -0.0556$$

$$\frac{\partial C_{Pt,Loss}}{\partial P_{t,ref}} = -\frac{13.11\ - 107.39}{(54.27 - 13.11\ )^2} - \frac{1}{54.27 - 13.11} = 0.03135$$

$$\frac{\partial C_{Pt,Loss}}{\partial P_{Fivehole\_Total}} = \frac{1}{54.27 - 13.11} = 0.02429$$

The overall uncertainty in the coefficient of total pressure loss is then:

$$\delta C_{Pt,Loss} = [(-0.0556 * 1.955)^2 + (0.03135 * 1.936)^2 + (0.024529 * 1.24)^2]^{1/2} = \pm 0.128$$

$$\overline{C_{Pt,Loss}} = \frac{107.39\ - 13.11}{54.27 - 13.11} = 2.29$$

$$\therefore \delta C_{Pt,Loss}\% = 5.58\%$$

This equals to the uncertainty % for $C_{Pt,Loss} = 2.26$ nominal value.

C.4.6 Turbulence intensity

$$TI\ \% = \frac{U_{rms}}{\overline{U_{ref}}} \times 100\%$$

Therefore, the uncertainty in TI % is:

$$\delta TI\ = \left[\left(\frac{\partial TI}{\partial U_{rms}}\delta U_{rms}\right)^2 + \left(\frac{\partial TI}{\partial \overline{U_{ref}}}\delta \overline{U_{ref}}\right)^2\right]^{1/2}$$

$$\frac{\partial TI}{\partial U_{rms}} = \frac{1}{\overline{U_{ref}}}$$

$$\frac{\partial TI}{\partial \overline{U_{ref}}} = -\frac{U_{rms}}{\overline{U_{ref}}^2}$$

The uncertainties in velocity variance and average are:

$$U_{rms} = 0.2984\ m/s \qquad \overline{U_{ref}} = 8.97\ m/s$$

$$\delta U_{rms} = \pm 0.014\ m/s \qquad \delta\overline{U_{ref}} = \pm\ 0.0735\ m/s$$

$$\delta U_{rms}\ \% = 4.69\ \% \qquad \delta\overline{U_{ref}}\ \% = 0.8194\ \%$$

The overall uncertainty in TI % is:

$$\delta TI\ = \left[\left(\frac{1}{8.97} * 0.014\right)^2 + \left(-\frac{0.2984}{8.97^2} * 0.0735\right)^2\right]^{1/2}$$

$$\delta TI\ = \pm 0.0016$$

$$\overline{TI}\ = \frac{U_{rms}}{\overline{U_{ref}}} = \frac{0.2984}{8.97} = 0.033$$

$$\therefore \delta TI\ \%\ = 4.74\ \%$$

This equals to the uncertainty % for $\overline{TI} = 0.033$ nominal value.

C.5 Conclusion

The method and procedure to determine the uncertainty in measured pressures and calculated results are presented in this appendix. Sample calculations for the uncertainty estimates of pressure transducers using linear regression analysis as well as the uncertainty in calculated results such as the free-stream velocity, coefficient of static pressure, coefficient of total pressure loss, film-cooling inlet blow ratio and film-cooling flow rate are provided. The bias error of the pressure transducers is taken as the accuracy of the calibration unit and transducer's quoted manufacturer accuracy while the precision error is determined through linear regression analysis. The uncertainty in calculated results is computed numerically for the five-hole probe quantities based on the method of sequential perturbation and root-sum-square approximation. Other quantities which could be determined analytically are based on a sensitivity analysis using partial derivatives of relevant equations and variables, combined in a root-sum-square approximation.

APPENDIX D: STATIC PRESSURE ENDWALL COORDINATES

D.1 Top wall (Baseline and fillet)

Origin is taken at leading-edge stagnation point of Blade 3.

Location	A.1			A.2			A.3			A.4	
Port	x(mm)	z(mm)	Port	x(mm)	z(mm)	Port	x(mm)	z(mm)	Port	x(mm)	z(mm)
A1	-9.42	-49.07	A1	-9.42	-155.07	A1	-9.42	-261.07	A1	-9.42	-367.07
A2	-9.42	-59.07	A2	-9.42	-165.07	A2	-9.42	-271.07	A2	-9.42	-377.07
A3	-9.42	-69.07	A3	-9.42	-175.07	A3	-9.42	-281.07	A3	-9.42	-387.07
A4	-9.42	-79.07	A4	-9.42	-185.07	A4	-9.42	-291.07	A4	-9.42	-397.07
A5	-9.42	-89.07	A5	-9.42	-195.07	A5	-9.42	-301.07	A5	-9.42	-407.07
A6	-9.42	-99.07	A6	-9.42	-205.07	A6	-9.42	-311.07	A6	-9.42	-417.07
A7	-9.42	-109.07	A7	-9.42	-215.07	A7	-9.42	-321.07	A7	-9.42	-427.07
A8	-9.42	-119.07	A8	-9.42	-225.07	A8	-9.42	-331.07	A8	-9.42	-437.07
A9	-9.42	-129.07	A9	-9.42	-235.07	A9	-9.42	-341.07	A9	-9.42	-447.07
A10	-9.42	-139.07	A10	-9.42	-245.07	A10	-9.42	-351.07	A10	-9.42	-457.07
A11	0.58	-49.07	A11	0.58	-155.07	A11	0.58	-261.07	A11	0.58	-367.07
A12	0.58	-59.07	A12	0.58	-165.07	A12	0.58	-271.07	A12	0.58	-377.07
A13	0.58	-69.07	A13	0.58	-175.07	A13	0.58	-281.07	A13	0.58	-387.07
A14	0.58	-79.07	A14	0.58	-185.07	A14	0.58	-291.07	A14	0.58	-397.07
A15	0.58	-89.07	A15	0.58	-195.07	A15	0.58	-301.07	A15	0.58	-407.07
A16	0.58	-99.07	A16	0.58	-205.07	A16	0.58	-311.07	A16	0.58	-417.07
A17	0.58	-109.07	A17	0.58	-215.07	A17	0.58	-321.07	A17	0.58	-427.07
A18	0.58	-119.07	A18	0.58	-225.07	A18	0.58	-331.07	A18	0.58	-437.07
A19	0.58	-129.07	A19	0.58	-235.07	A19	0.58	-341.07	A19	0.58	-447.07
A20	0.58	-139.07	A20	0.58	-245.07	A20	0.58	-351.07	A20	0.58	-457.07
A21	10.58	-49.07	A21	10.58	-155.07	A21	10.58	-261.07	A21	10.58	-367.07
A22	10.58	-59.07	A22	10.58	-165.07	A22	10.58	-271.07	A22	10.58	-377.07
A23	10.58	-69.07	A23	10.58	-175.07	A23	10.58	-281.07	A23	10.58	-387.07
A24	10.58	-79.07	A24	10.58	-185.07	A24	10.58	-291.07	A24	10.58	-397.07
A25	10.58	-89.07	A25	10.58	-195.07	A25	10.58	-301.07	A25	10.58	-407.07
A26	10.58	-99.07	A26	10.58	-205.07	A26	10.58	-311.07	A26	10.58	-417.07
A27	10.58	-109.07	A27	10.58	-215.07	A27	10.58	-321.07	A27	10.58	-427.07
A28	10.58	-119.07	A28	10.58	-225.07	A28	10.58	-331.07	A28	10.58	-437.07
A29	10.58	-129.07	A29	10.58	-235.07	A29	10.58	-341.07	A29	10.58	-447.07
A30	10.58	-139.07	A30	10.58	-245.07	A30	10.58	-351.07	A30	10.58	-457.07
A31	20.58	-49.07	A31	20.58	-155.07	A31	20.58	-261.07	A31	20.58	-367.07
A32	20.58	-59.07	A32	20.58	-165.07	A32	20.58	-271.07	A32	20.58	-377.07
A33	20.58	-69.07	A33	20.58	-175.07	A33	20.58	-281.07	A33	20.58	-387.07
A34	20.58	-79.07	A34	20.58	-185.07	A34	20.58	-291.07	A34	20.58	-397.07
A35	20.58	-89.07	A35	20.58	-195.07	A35	20.58	-301.07	A35	20.58	-407.07
A36	20.58	-99.07	A36	20.58	-205.07	A36	20.58	-311.07	A36	20.58	-417.07
A37	20.58	-109.07	A37	20.58	-215.07	A37	20.58	-321.07	A37	20.58	-427.07
A38	20.58	-119.07	A38	20.58	-225.07	A38	20.58	-331.07	A38	20.58	-437.07
A39	20.58	-129.07	A39	20.58	-235.07	A39	20.58	-341.07	A39	20.58	-447.07
A40	20.58	-139.07	A40	20.58	-245.07	A40	20.58	-351.07	A40	20.58	-457.07
A41	30.58	-49.07	A41	30.58	-155.07	A41	30.58	-261.07	A41	30.58	-367.07
A42	30.58	-59.07	A42	30.58	-165.07	A42	30.58	-271.07	A42	30.58	-377.07
A43	30.58	-69.07	A43	30.58	-175.07	A43	30.58	-281.07	A43	30.58	-387.07
A44	30.58	-79.07	A44	30.58	-185.07	A44	30.58	-291.07	A44	30.58	-397.07
A45	30.58	-89.07	A45	30.58	-195.07	A45	30.58	-301.07	A45	30.58	-407.07
A46	30.58	-99.07	A46	30.58	-205.07	A46	30.58	-311.07	A46	30.58	-417.07
A47	30.58	-109.07	A47	30.58	-215.07	A47	30.58	-321.07	A47	30.58	-427.07
A48	30.58	-119.07	A48	30.58	-225.07	A48	30.58	-331.07	A48	30.58	-437.07
A49	30.58	-129.07	A49	30.58	-235.07	A49	30.58	-341.07	A49	30.58	-447.07
A50	30.58	-139.07	A50	30.58	-245.07	A50	30.58	-351.07	A50	30.58	-457.07

Location	C.1			C.2			C.3			C.4			C.5	
Port	x(mm)	z(mm)	Port	x(mm)	z(mm)	Port	x(mm)	z(mm)	Port	x(mm)	z(mm)	Port	x(mm)	z(mm)
C1	47.48	-53.35	C1	109.98	-161.6	C1	172.48	-269.85	C1	53.35	-323.35	C1	109.98	-421.6
C2	47.48	-63.35	C2	109.98	-171.6	C2	172.48	-279.85	C2	63.35	-333.35	C2	109.98	-431.6
C3	47.48	-73.35	C3	109.98	-181.6	C3	172.48	-289.85	C3	73.35	-343.35	C3	109.98	-441.6
C4	47.48	-83.35	C4	109.98	-191.6	C4	172.48	-299.85	C4	83.35	-353.35	C4	109.98	-451.6
C5	47.48	-93.35	C5	109.98	-201.6	C5	172.48	-309.85	C5	93.35	-363.35	C5	109.98	-461.6
C6	47.48	-103.35	C6	109.98	-211.6	C6	172.48	-319.85	C6	103.35	-373.35	C6	109.98	-471.6
C7	47.48	-113.35	C7	109.98	-221.6	C7	172.48	-329.85	C7	113.35	-383.35	C7	109.98	-481.6
C8	47.48	-123.35	C8	109.98	-231.6	C8	172.48	-339.85	C8	123.35	-393.35	C8	109.98	-491.6
C9	47.48	-133.35	C9	109.98	-241.6	C9	172.48	-349.85	C9	133.35	-403.35	C9	109.98	-501.6
C10	47.48	-143.35	C10	109.98	-251.6	C10	172.48	-359.85	C10	143.35	-413.35	C10	109.98	-511.6
C11	47.48	-153.35	C11	109.98	-261.6	C11	172.48	-369.85	C11	153.35	-423.35	C11	109.98	-521.6
C12	47.48	-163.35	C12	109.98	-271.6	C12	172.48	-379.85	C12	163.35	-433.35	C12	109.98	-531.6
C13	47.48	-173.35	C13	109.98	-281.6	C13	172.48	-389.85	C13	173.35	-443.35	C13	109.98	-541.6
C14	47.48	-183.35	C14	109.98	-291.6	C14	172.48	-399.85	C14	183.35	-453.35	C14	109.98	-551.6
C15	47.48	-193.35	C15	109.98	-301.6	C15	172.48	-409.85	C15	193.35	-463.35	C15	109.98	-561.6
C16	47.48	-203.35	C16	109.98	-311.6	C16	172.48	-419.85	C16	203.35	-473.35	C16	109.98	-571.6
C17	57.48	-63.35	C17	119.98	-171.6	C17	182.48	-279.85	C17	63.35	-333.35	C17	119.98	-431.6
C18	57.48	-73.35	C18	119.98	-181.6	C18	182.48	-289.85	C18	73.35	-343.35	C18	119.98	-441.6
C19	57.48	-83.35	C19	119.98	-191.6	C19	182.48	-299.85	C19	83.35	-353.35	C19	119.98	-451.6
C20	57.48	-93.35	C20	119.98	-201.6	C20	182.48	-309.85	C20	93.35	-363.35	C20	119.98	-461.6
C21	57.48	-103.35	C21	119.98	-211.6	C21	182.48	-319.85	C21	103.35	-373.35	C21	119.98	-471.6
C22	57.48	-113.35	C22	119.98	-221.6	C22	182.48	-329.85	C22	113.35	-383.35	C22	119.98	-481.6
C23	57.48	-123.35	C23	119.98	-231.6	C23	182.48	-339.85	C23	123.35	-393.35	C23	119.98	-491.6
C24	57.48	-133.35	C24	119.98	-241.6	C24	182.48	-349.85	C24	133.35	-403.35	C24	119.98	-501.6
C25	57.48	-143.35	C25	119.98	-251.6	C25	182.48	-359.85	C25	143.35	-413.35	C25	119.98	-511.6
C26	57.48	-153.35	C26	119.98	-261.6	C26	182.48	-369.85	C26	153.35	-423.35	C26	119.98	-521.6
C27	57.48	-163.35	C27	119.98	-271.6	C27	182.48	-379.85	C27	163.35	-433.35	C27	119.98	-531.6
C28	57.48	-173.35	C28	119.98	-281.6	C28	182.48	-389.85	C28	173.35	-443.35	C28	119.98	-541.6
C29	57.48	-183.35	C29	119.98	-291.6	C29	182.48	-399.85	C29	183.35	-453.35	C29	119.98	-551.6
C30	57.48	-193.35	C30	119.98	-301.6	C30	182.48	-409.85	C30	193.35	-463.35	C30	119.98	-561.6
C31	57.48	-203.35	C31	119.98	-311.6	C31	182.48	-419.85	C31	203.35	-473.35	C31	119.98	-571.6
C32	57.48	-213.35	C32	119.98	-321.6	C32	182.48	-429.85	C32	213.35	-483.35	C32	119.98	-581.6
C33	67.48	-83.35	C33	129.98	-191.6	C33	192.48	-299.85	C33	83.35	-353.35	C33	129.98	-451.6
C34	67.48	-93.35	C34	129.98	-201.6	C34	192.48	-309.85	C34	93.35	-363.35	C34	129.98	-461.6
C35	67.48	-103.35	C35	129.98	-211.6	C35	192.48	-319.85	C35	103.35	-373.35	C35	129.98	-471.6
C36	67.48	-113.35	C36	129.98	-221.6	C36	192.48	-329.85	C36	113.35	-383.35	C36	129.98	-481.6
C37	67.48	-123.35	C37	129.98	-231.6	C37	192.48	-339.85	C37	123.35	-393.35	C37	129.98	-491.6
C38	67.48	-133.35	C38	129.98	-241.6	C38	192.48	-349.85	C38	133.35	-403.35	C38	129.98	-501.6
C39	67.48	-143.35	C39	129.98	-251.6	C39	192.48	-359.85	C39	143.35	-413.35	C39	129.98	-511.6
C40	67.48	-153.35	C40	129.98	-261.6	C40	192.48	-369.85	C40	153.35	-423.35	C40	129.98	-521.6
C41	67.48	-163.35	C41	129.98	-271.6	C41	192.48	-379.85	C41	163.35	-433.35	C41	129.98	-531.6
C42	67.48	-173.35	C42	129.98	-281.6	C42	192.48	-389.85	C42	173.35	-443.35	C42	129.98	-541.6
C43	67.48	-183.35	C43	129.98	-291.6	C43	192.48	-399.85	C43	183.35	-453.35	C43	129.98	-551.6
C44	67.48	-193.35	C44	129.98	-301.6	C44	192.48	-409.85	C44	193.35	-463.35	C44	129.98	-561.6
C45	67.48	-203.35	C45	129.98	-311.6	C45	192.48	-419.85	C45	203.35	-473.35	C45	129.98	-571.6
C46	67.48	-213.35	C46	129.98	-321.6	C46	192.48	-429.85	C46	213.35	-483.35	C46	129.98	-581.6
C47	67.48	-223.35	C47	129.98	-331.6	C47	192.48	-439.85	C47	223.35	-493.35	C47	129.98	-591.6
C48	67.48	-233.35	C48	129.98	-341.6	C48	192.48	-449.85	C48	233.35	-503.35	C48	129.98	-601.6
C49	77.48	-93.35	C49	139.98	-201.6	C49	202.48	-309.85	C49	93.35	-363.35	C49	139.98	-461.6
C50	77.48	-103.35	C50	139.98	-211.6	C50	202.48	-319.85	C50	103.35	-373.35	C50	139.98	-471.6
C51	77.48	-113.35	C51	139.98	-221.6	C51	202.48	-329.85	C51	113.35	-383.35	C51	139.98	-481.6
C52	77.48	-123.35	C52	139.98	-231.6	C52	202.48	-339.85	C52	123.35	-393.35	C52	139.98	-491.6
C53	77.48	-133.35	C53	139.98	-241.6	C53	202.48	-349.85	C53	133.35	-403.35	C53	139.98	-501.6
C54	77.48	-143.35	C54	139.98	-251.6	C54	202.48	-359.85	C54	143.35	-413.35	C54	139.98	-511.6
C55	77.48	-153.35	C55	139.98	-261.6	C55	202.48	-369.85	C55	153.35	-423.35	C55	139.98	-521.6
C56	77.48	-163.35	C56	139.98	-271.6	C56	202.48	-379.85	C56	163.35	-433.35	C56	139.98	-531.6
C57	77.48	-173.35	C57	139.98	-281.6	C57	202.48	-389.85	C57	173.35	-443.35	C57	139.98	-541.6
C58	77.48	-183.35	C58	139.98	-291.6	C58	202.48	-399.85	C58	183.35	-453.35	C58	139.98	-551.6
C59	77.48	-193.35	C59	139.98	-301.6	C59	202.48	-409.85	C59	193.35	-463.35	C59	139.98	-561.6
C60	77.48	-203.35	C60	139.98	-311.6	C60	202.48	-419.85	C60	203.35	-473.35	C60	139.98	-571.6
C61	77.48	-213.35	C61	139.98	-321.6	C61	202.48	-429.85	C61	213.35	-483.35	C61	139.98	-581.6
C62	77.48	-223.35	C62	139.98	-331.6	C62	202.48	-439.85	C62	223.35	-493.35	C62	139.98	-591.6
C63	77.48	-233.35	C63	139.98	-341.6	C63	202.48	-449.85	C63	233.35	-503.35	C63	139.98	-601.6
C64	77.48	-243.35	C64	139.98	-351.6	C64	202.48	-459.85	C64	243.35	-513.35	C64	139.98	-611.6
C65	77.48	-253.35	C65	139.98	-361.6	C65	202.48	-469.85	C65	253.35	-523.35	C65	139.98	-621.6
C66	87.48	-113.35	C66	149.98	-221.6	C66	212.48	-329.85	C66	113.35	-383.35	C66	149.98	-481.6
C67	87.48	-123.35	C67	149.98	-231.6	C67	212.48	-339.85	C67	123.35	-393.35	C67	149.98	-491.6
C68	87.48	-133.35	C68	149.98	-241.6	C68	212.48	-349.85	C68	133.35	-403.35	C68	149.98	-501.6
C69	87.48	-143.35	C69	149.98	-251.6	C69	212.48	-359.85	C69	143.35	-413.35	C69	149.98	-511.6
C70	87.48	-153.35	C70	149.98	-261.6	C70	212.48	-369.85	C70	153.35	-423.35	C70	149.98	-521.6

C71	87.48	-163.35	C71	149.98	-271.6	C71	212.48	-379.85	C71	163.35	-433.35	C71	149.98	-531.6
C72	87.48	-173.35	C72	149.98	-281.6	C72	212.48	-389.85	C72	173.35	-443.35	C72	149.98	-541.6
C73	87.48	-183.35	C73	149.98	-291.6	C73	212.48	-399.85	C73	183.35	-453.35	C73	149.98	-551.6
C74	87.48	-193.35	C74	149.98	-301.6	C74	212.48	-409.85	C74	193.35	-463.35	C74	149.98	-561.6
C75	87.48	-203.35	C75	149.98	-311.6	C75	212.48	-419.85	C75	203.35	-473.35	C75	149.98	-571.6
C76	87.48	-213.35	C76	149.98	-321.6	C76	212.48	-429.85	C76	213.35	-483.35	C76	149.98	-581.6
C77	87.48	-223.35	C77	149.98	-331.6	C77	212.48	-439.85	C77	223.35	-493.35	C77	149.98	-591.6
C78	87.48	-233.35	C78	149.98	-341.6	C78	212.48	-449.85	C78	233.35	-503.35	C78	149.98	-601.6
C79	87.48	-243.35	C79	149.98	-351.6	C79	212.48	-459.85	C79	243.35	-513.35	C79	149.98	-611.6
C80	87.48	-253.35	C80	149.98	-361.6	C80	212.48	-469.85	C80	253.35	-523.35	C80	149.98	-621.6
C81	87.48	-263.35	C81	149.98	-371.6	C81	212.48	-479.85	C81	263.35	-533.35	C81	149.98	-631.6
C82	87.48	-273.35	C82	149.98	-381.6	C82	212.48	-489.85	C82	273.35	-543.35	C82	149.98	-641.6
C83	97.48	-133.35	C83	159.98	-241.6	C83	222.48	-349.85	C83	133.35	-403.35	C83	159.98	-501.6
C84	97.48	-143.35	C84	159.98	-251.6	C84	222.48	-359.85	C84	143.35	-413.35	C84	159.98	-511.6
C85	97.48	-153.35	C85	159.98	-261.6	C85	222.48	-369.85	C85	153.35	-423.35	C85	159.98	-521.6
C86	97.48	-163.35	C86	159.98	-271.6	C86	222.48	-379.85	C86	163.35	-433.35	C86	159.98	-531.6
C87	97.48	-173.35	C87	159.98	-281.6	C87	222.48	-389.85	C87	173.35	-443.35	C87	159.98	-541.6
C88	97.48	-183.35	C88	159.98	-291.6	C88	222.48	-399.85	C88	183.35	-453.35	C88	159.98	-551.6
C89	97.48	-193.35	C89	159.98	-301.6	C89	222.48	-409.85	C89	193.35	-463.35	C89	159.98	-561.6
C90	97.48	-203.35	C90	159.98	-311.6	C90	222.48	-419.85	C90	203.35	-473.35	C90	159.98	-571.6
C91	97.48	-213.35	C91	159.98	-321.6	C91	222.48	-429.85	C91	213.35	-483.35	C91	159.98	-581.6
C92	97.48	-223.35	C92	159.98	-331.6	C92	222.48	-439.85	C92	223.35	-493.35	C92	159.98	-591.6
C93	97.48	-233.35	C93	159.98	-341.6	C93	222.48	-449.85	C93	233.35	-503.35	C93	159.98	-601.6
C94	97.48	-243.35	C94	159.98	-351.6	C94	222.48	-459.85	C94	243.35	-513.35	C94	159.98	-611.6
C95	97.48	-253.35	C95	159.98	-361.6	C95	222.48	-469.85	C95	253.35	-523.35	C95	159.98	-621.6
C96	97.48	-263.35	C96	159.98	-371.6	C96	222.48	-479.85	C96	263.35	-533.35	C96	159.98	-631.6
C97	97.48	-273.35	C97	159.98	-381.6	C97	222.48	-489.85	C97	273.35	-543.35	C97	159.98	-641.6

Location	B.1		Location	B.1		Location	B.1		Location	B.1	
Port	x(mm)	z(mm)	Port	x(mm)	z(mm)	Port	x(mm)	z(mm)	Port	x(mm)	z(mm)
B1	179.58	-464.66	B21	189.58	-494.66	B41	199.58	-534.66	B61	209.58	-594.66
B2	179.58	-474.66	B22	189.58	-504.66	B42	199.58	-544.66	B62	209.58	-604.66
B3	179.58	-484.66	B23	189.58	-514.66	B43	199.58	-554.66	B63	209.58	-614.66
B4	179.58	-494.66	B24	189.58	-524.66	B44	199.58	-564.66	B64	209.58	-624.66
B5	179.58	-504.66	B25	189.58	-534.66	B45	199.58	-574.66	B65	209.58	-634.66
B6	179.58	-514.66	B26	189.58	-544.66	B46	199.58	-584.66	B66	219.58	-534.66
B7	179.58	-524.66	B27	189.58	-554.66	B47	199.58	-594.66	B67	219.58	-544.66
B8	179.58	-534.66	B28	189.58	-564.66	B48	199.58	-604.66	B68	219.58	-554.66
B9	179.58	-544.66	B29	189.58	-574.66	B49	199.58	-614.66	B69	219.58	-564.66
B10	179.58	-554.66	B30	189.58	-584.66	B50	199.58	-624.66	B70	219.58	-574.66
B11	179.58	-564.66	B31	189.58	-594.66	B51	199.58	-634.66	B71	219.58	-584.66
B12	179.58	-574.66	B32	189.58	-604.66	B52	199.58	-644.66	B72	219.58	-594.66
B13	179.58	-584.66	B33	189.58	-614.66	B53	209.58	-514.66	B73	219.58	-604.66
B14	179.58	-594.66	B34	189.58	-624.66	B54	209.58	-524.66	B74	219.58	-614.66
B15	179.58	-604.66	B35	189.58	-634.66	B55	209.58	-534.66	B75	219.58	-624.66
B16	179.58	-614.66	B36	189.58	-644.66	B56	209.58	-544.66	B76	219.58	-634.66
B17	179.58	-624.66	B37	199.58	-494.66	B57	209.58	-554.66			
B18	179.58	-634.66	B38	199.58	-504.66	B58	209.58	-564.66			
B19	179.58	-644.66	B39	199.58	-514.66	B59	209.58	-574.66			
B20	189.58	-484.66	B40	199.58	-524.66	B60	209.58	-584.66			

D.2 Bottom wall (Baseline, film-cooling and fillet)

Origin is taken at leading-edge stagnation point of Blade 4.

Port	Xmm	Zmm	Port	Xmm	Zmm
1	-1.89	249.08	25	86.92	19.58
2	-1.89	216.28	26	115.86	108.08
3	-1.89	183.48	27	115.86	76.58
4	-1.89	150.68	28	115.86	45.08
5	-1.89	117.88	29	115.86	13.58
6	-1.89	85.08	30	115.86	-17.92
7	-1.89	52.28	31	144.8	50.68
8	-1.89	19.48	32	144.8	23.68
9	29.04	219.08	33	144.8	-3.32
10	29.04	184.08	34	144.8	-30.32
11	29.04	149.08	35	144.8	-57.32
12	29.04	114.08	36	144.8	-84.32
13	29.04	79.08	37	173.74	0.68
14	29.04	44.08	38	173.74	-33.52
15	57.98	189.08	39	173.74	-67.72
16	57.98	159.08	40	173.74	-101.92
17	57.98	129.08	41	173.74	-136.12
18	57.98	99.08	42	173.74	-170.32
19	57.98	69.08	43	202.68	-63.32
20	57.98	39.08	44	202.68	-104.92
21	86.92	151.58	45	202.68	-146.52
22	86.92	118.58	46	202.68	-188.12
23	86.92	85.58	47	202.68	-229.72
24	86.92	52.58	48	202.68	-271.32

APPENDIX E: COMPLETE EXPERIMENTAL RESULTS

This section serves as an additional representation of the experimental results which are not discussed in Chapter 5. Hence, these results are not discussed but are presented here for completeness to the reader.

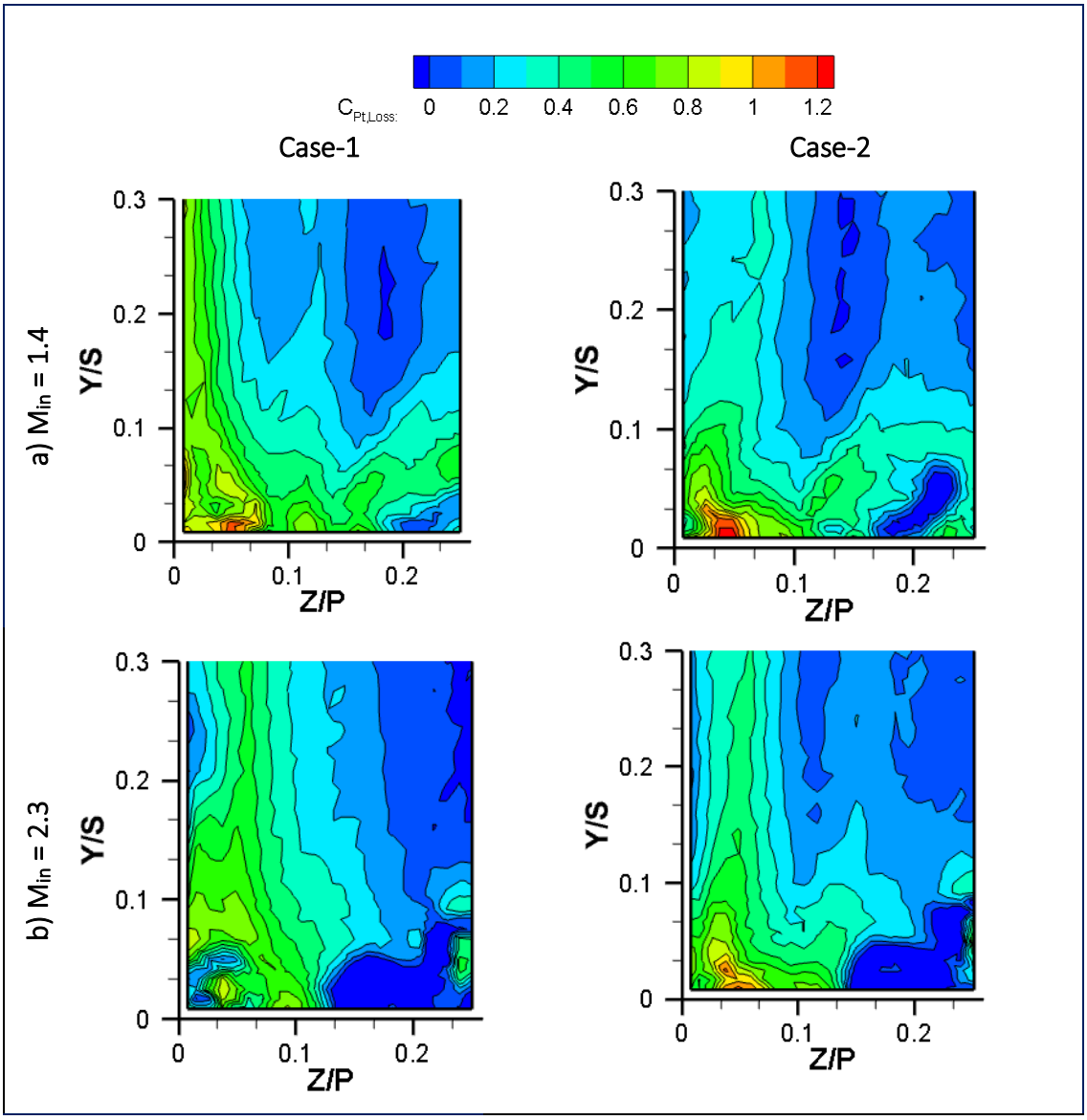

FIGURE E.1 CONTOURS OF $C_{PT,LOSS}$ AT PLANE-1 (X_G/C_{AX} = 0.251) WITH FILM-COOLING FOR (A) M_{IN} = 1.4 AND (B) M_{IN} = 2.3.

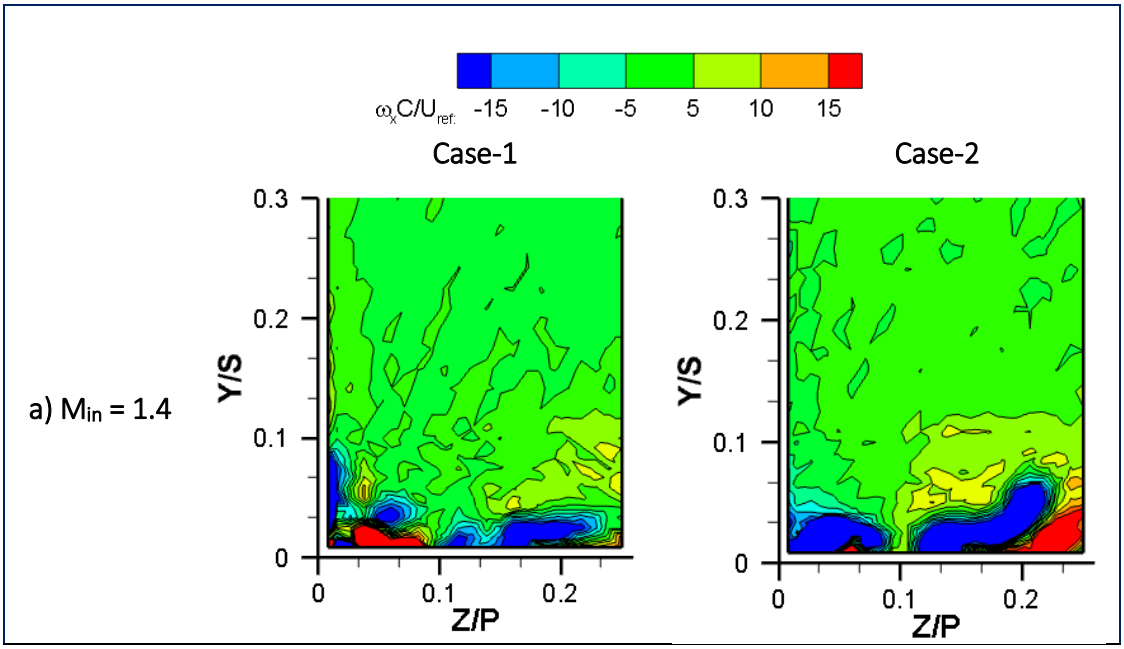

FIGURE E.2 CONTOURS OF NORMALISED AXIAL VORTICITY AT PLANE-1 (X_G/C_{AX} = 0.251) WITH FILM-COOLING FOR (A) M_{IN} = 1.4.

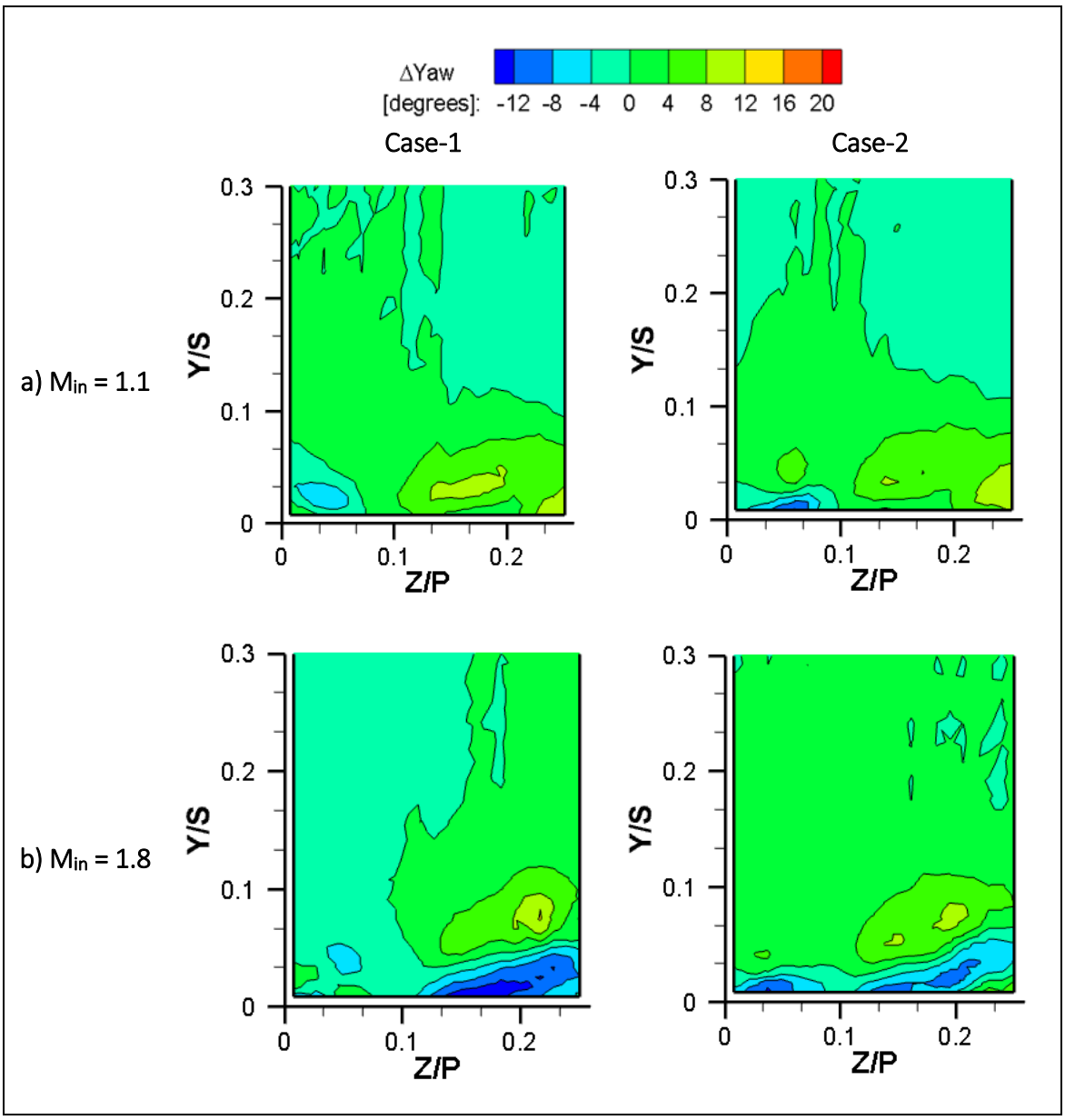

FIGURE E.3 CONTOURS OF YAW ANGLE DEVIATION AT PLANE-1 (X_G/C_{AX} = 0.251) WITH FILM-COOLING (A) M_{IN} = 1.1 AND (B) M_{IN} = 1.8.

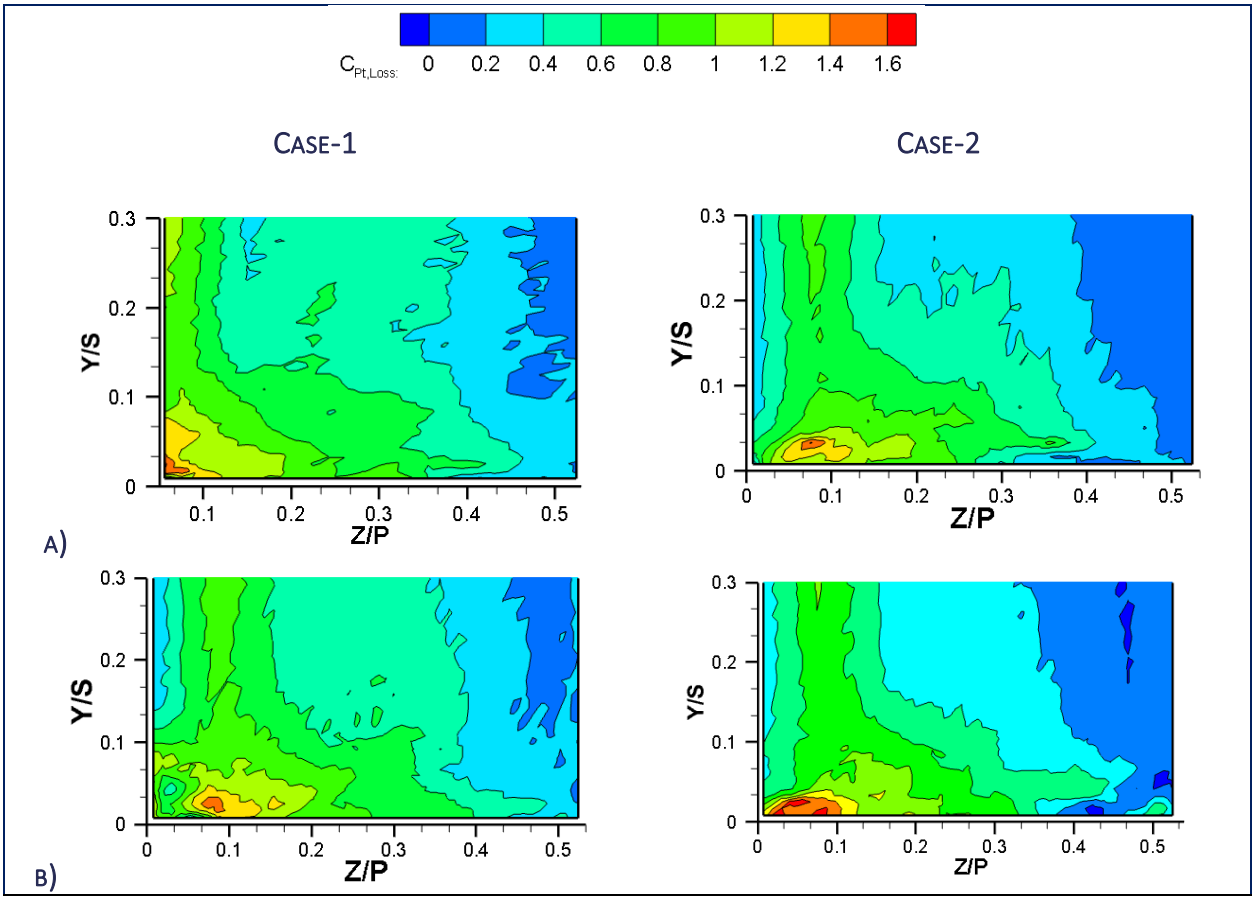

FIGURE E.4 CONTOUR PLOT OF $C_{PT,LOSS}$ AT PLANE-2 (X_G/C_{AX} = 0.58) FOR BOTH FILM-COOLING CASES AT (A) M_{IN} = 1.1 (B) M_{IN} = 1.4.

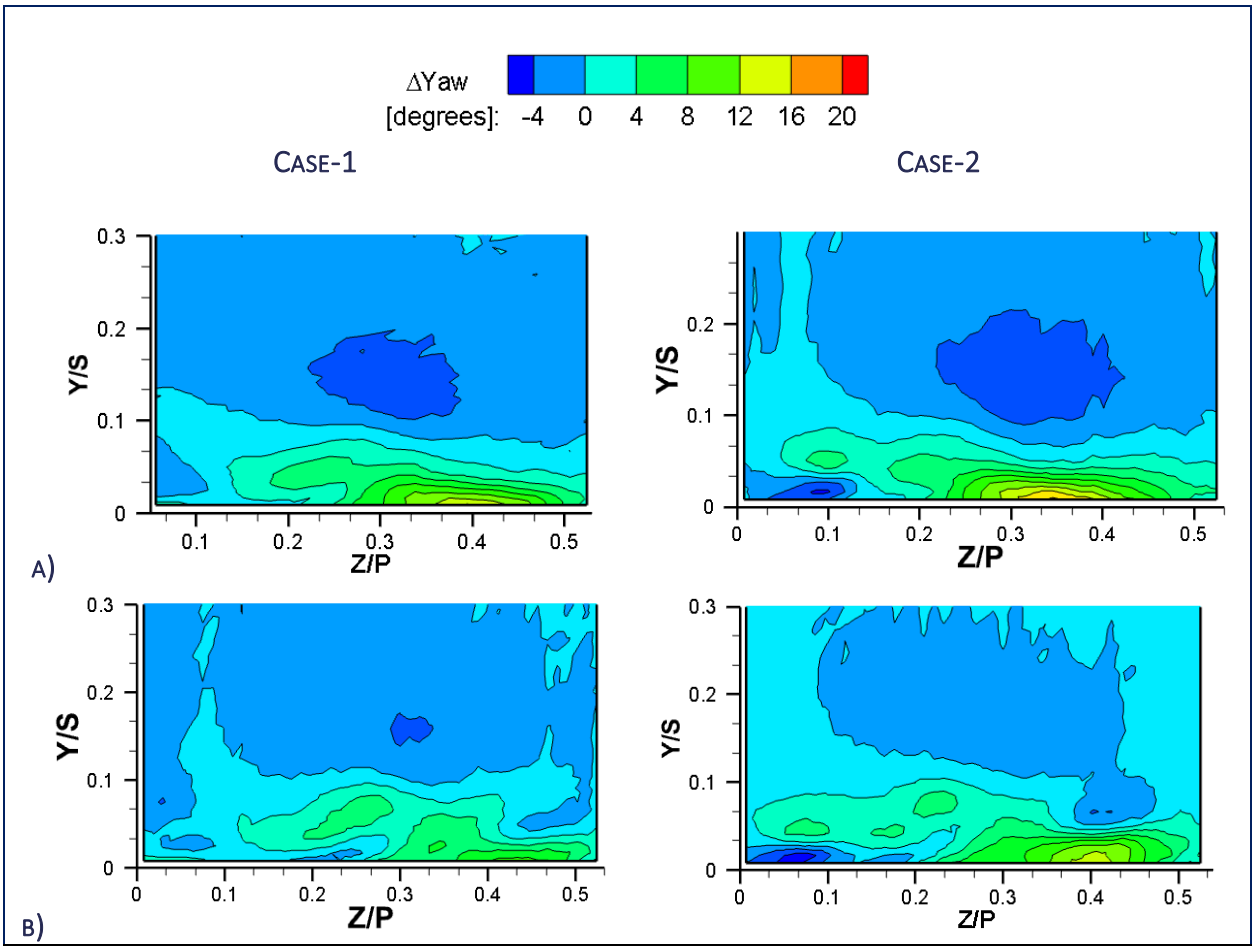

FIGURE E.5 CONTOUR PLOTS OF ΔYAW AT PLANE-2 (X_G/C_{AX} = 0.58) FOR BOTH FILM-COOLING CASES AT (A) M_{IN} = 1.1 (B) M_{IN} = 1.4.

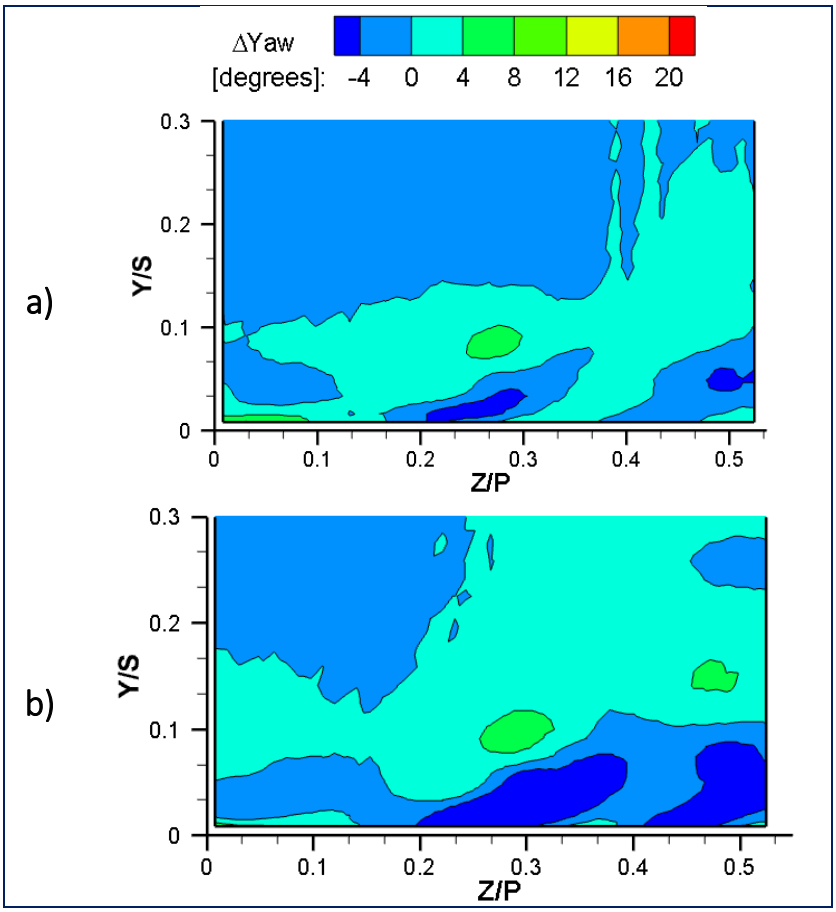

FIGURE E.6 CONTOURS OF YAW ANGLE DEVIATION AT PLANE-2 (X_G/C_{AX} = 0.58) FOR FILM-COOLING CASE-1 (A) M_{IN} = 1.8 AND (B) M_{IN} = 2.3.

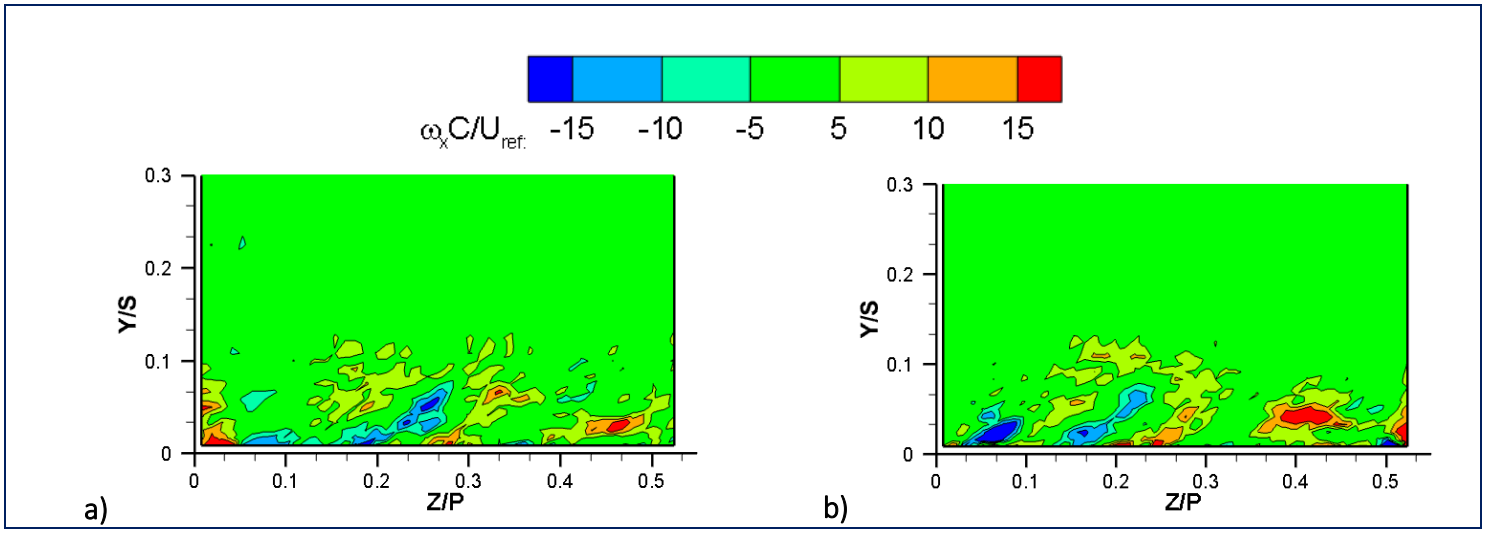

FIGURE E.7 CONTOURS OF NORMALISED AXIAL VORTICITY AT PLANE-2 (X_G/C_{AX} = 0.58) WITH FILM-COOLING M_{IN} = 1.4 FOR (A) CASE-1 AND (B) CASE-2.

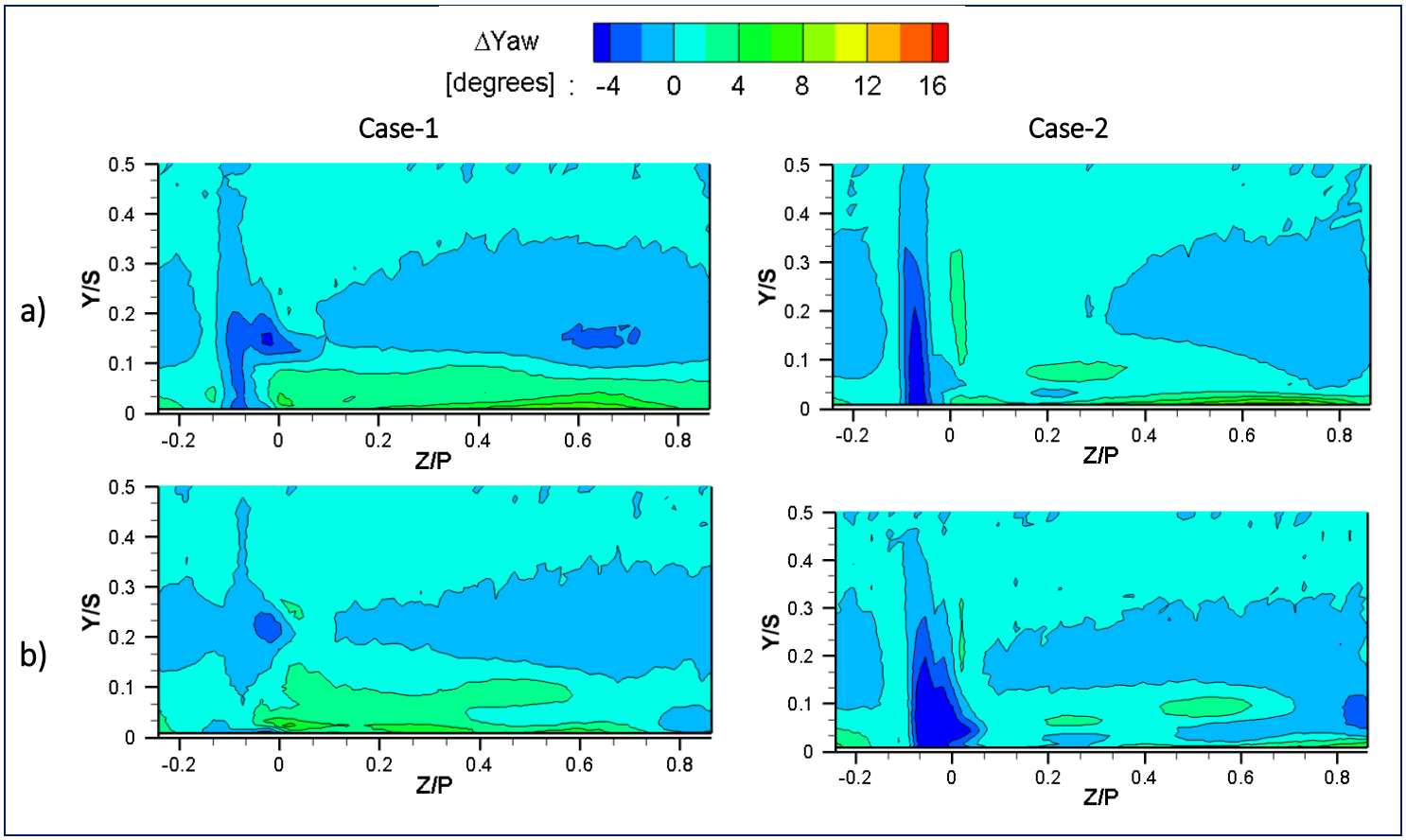

FIGURE E.8 CONTOURS OF YAW ANGLE DEVIATION (ΔYAW) AT PLANE-3 (X_G/C_{AX} = 1.042) FOR FILM-COOLING AT (A) M_{IN} = 1.4 AND (B) M_{IN} = 1.8.

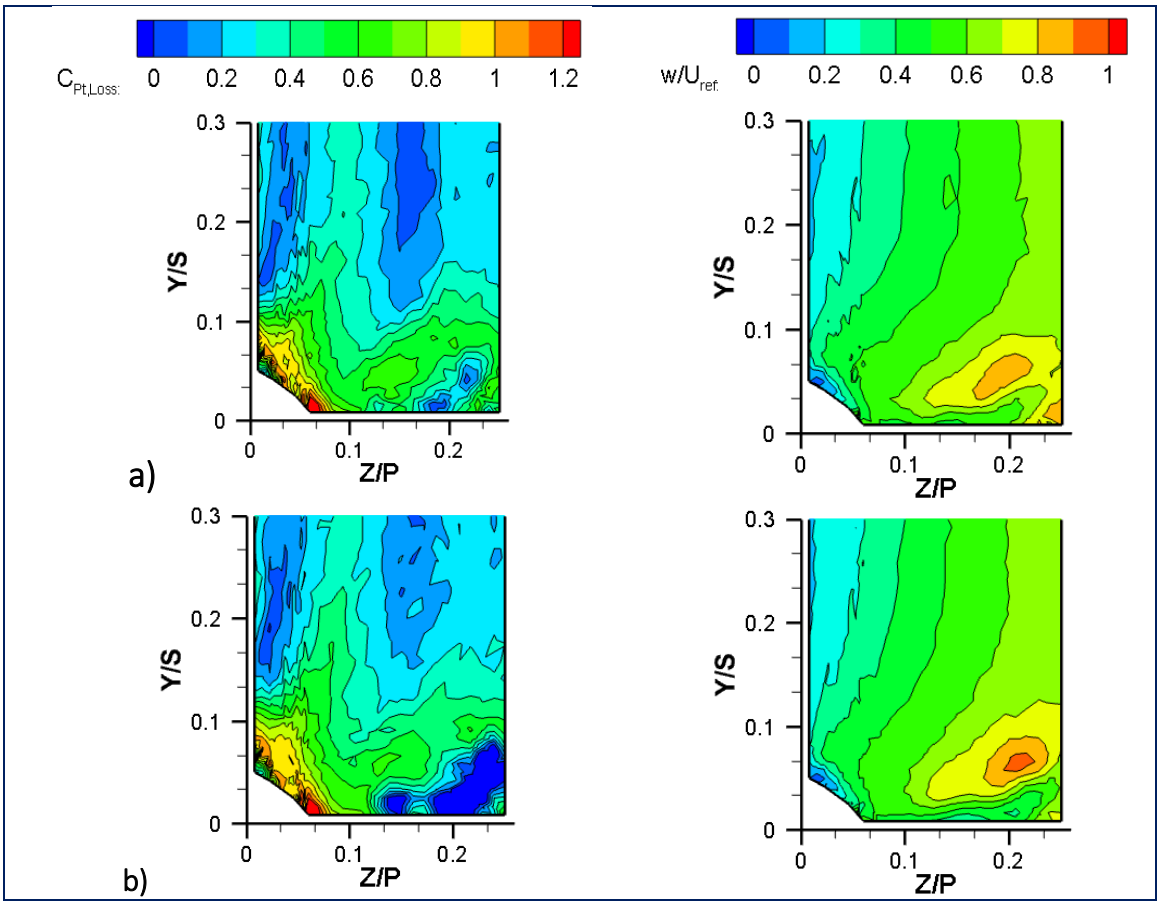

FIGURE E.9 CONTOURS OF $C_{PT,LOSS}$ (LEFT) AND NORMALISED PITCHWISE VELOCITY (RIGHT) AT PLANE-1 (X_G/C_{AX} = 0.251) FOR FILM-COOLING WITH FILLET AT (A) M_{IN} = 1.4 AND (B) M_{IN} = 1.8.

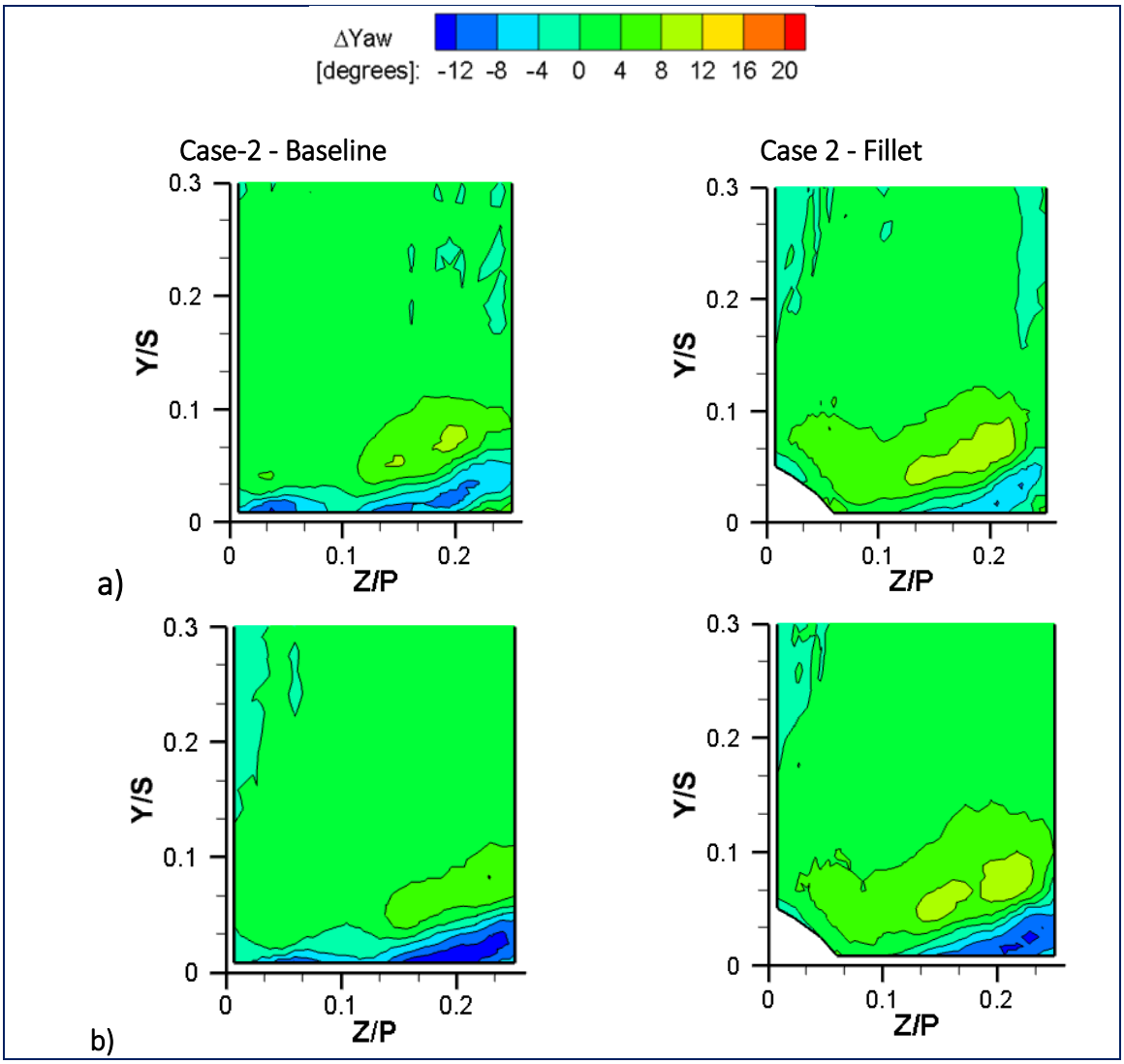

FIGURE E.10 CONTOURS OF YAW ANGLE DEVIATION (ΔYAW) AT PLANE-1 (X_G/C_{AX} = 1.042) FOR FILM-COOLING CASE-2 WITH AND WITHOUT FILLET AT (A) M_{IN} = 1.8 AND (B) M_{IN} = 2.3.

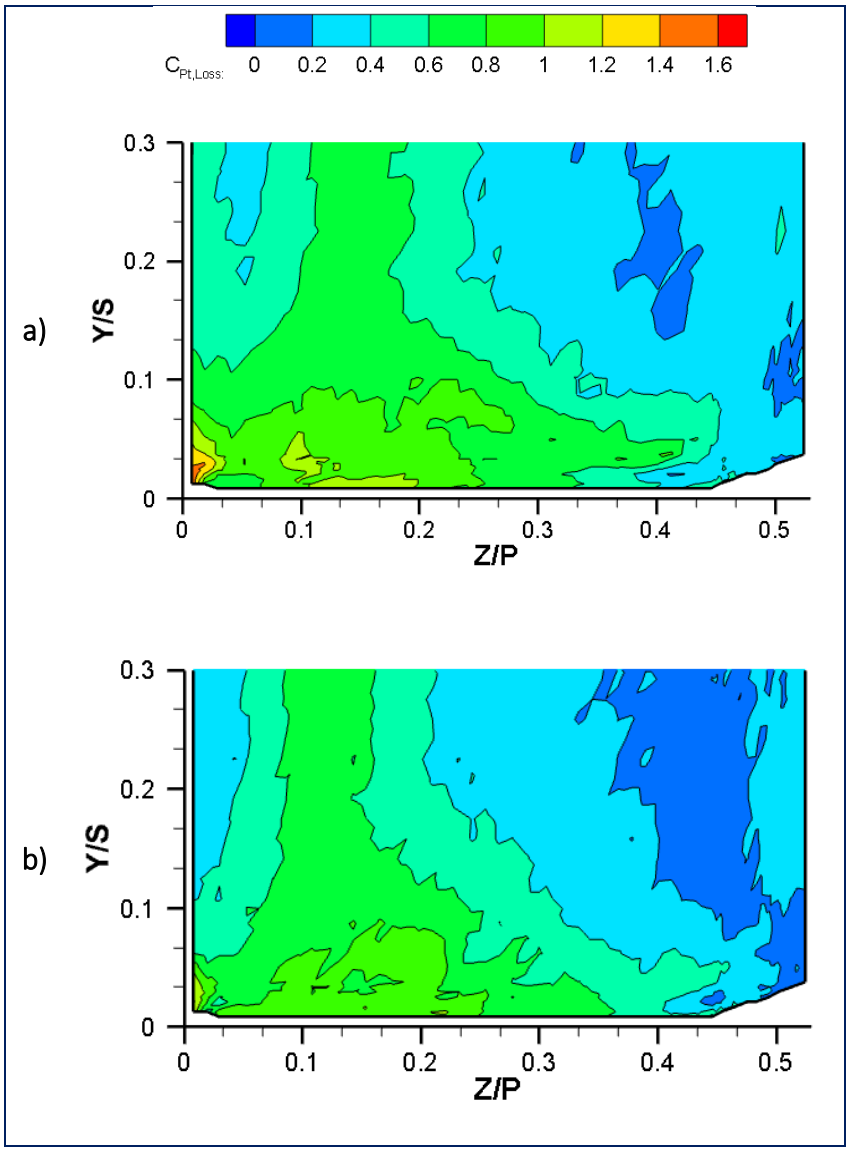

FIGURE E.11 CONTOURS OF $C_{PT,LOSS}$ AT PLANE-2 (X_G/C_{AX} = 0.58) FOR (A) FILLET M_{IN} = 1.1 AND (C) FILLET M_{IN} = 1.4.

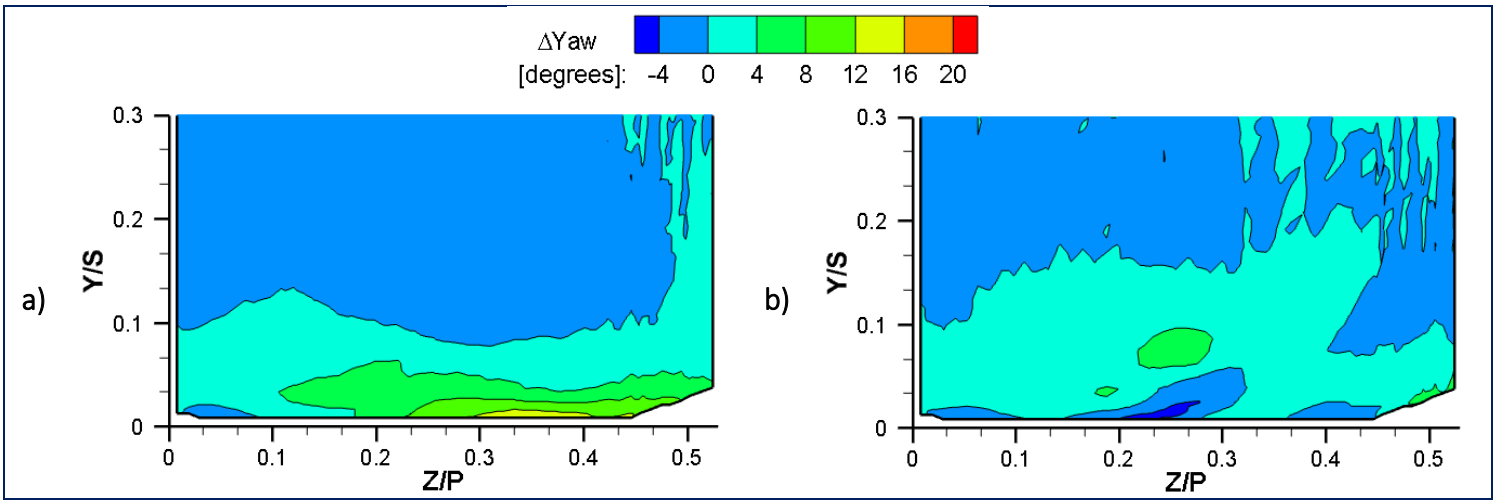

FIGURE E.12 CONTOURS OF YAW ANGLE DEVIATION AT PLANE-2 (X_G/C_{AX} = 0.58) FOR (A) FILLET M_{IN} = 1.1 AND (B) FILLET M_{IN} = 1.8.

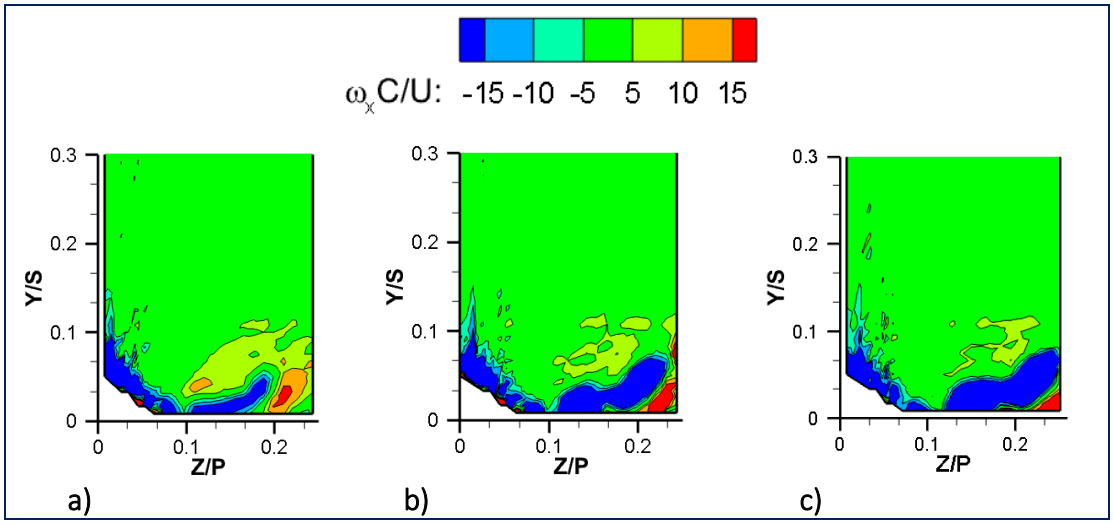

FIGURE E.13 CONTOURS OF NORMALISED AXIAL VORTICITY AT PLANE-1 (X_G/C_{AX} = 0.251) FOR FILM-COOLING WITH FILLET AT (A) M_{IN} = 1.1, (B) M_{IN} = 1.8 AND (C) M_{IN} = 2.3

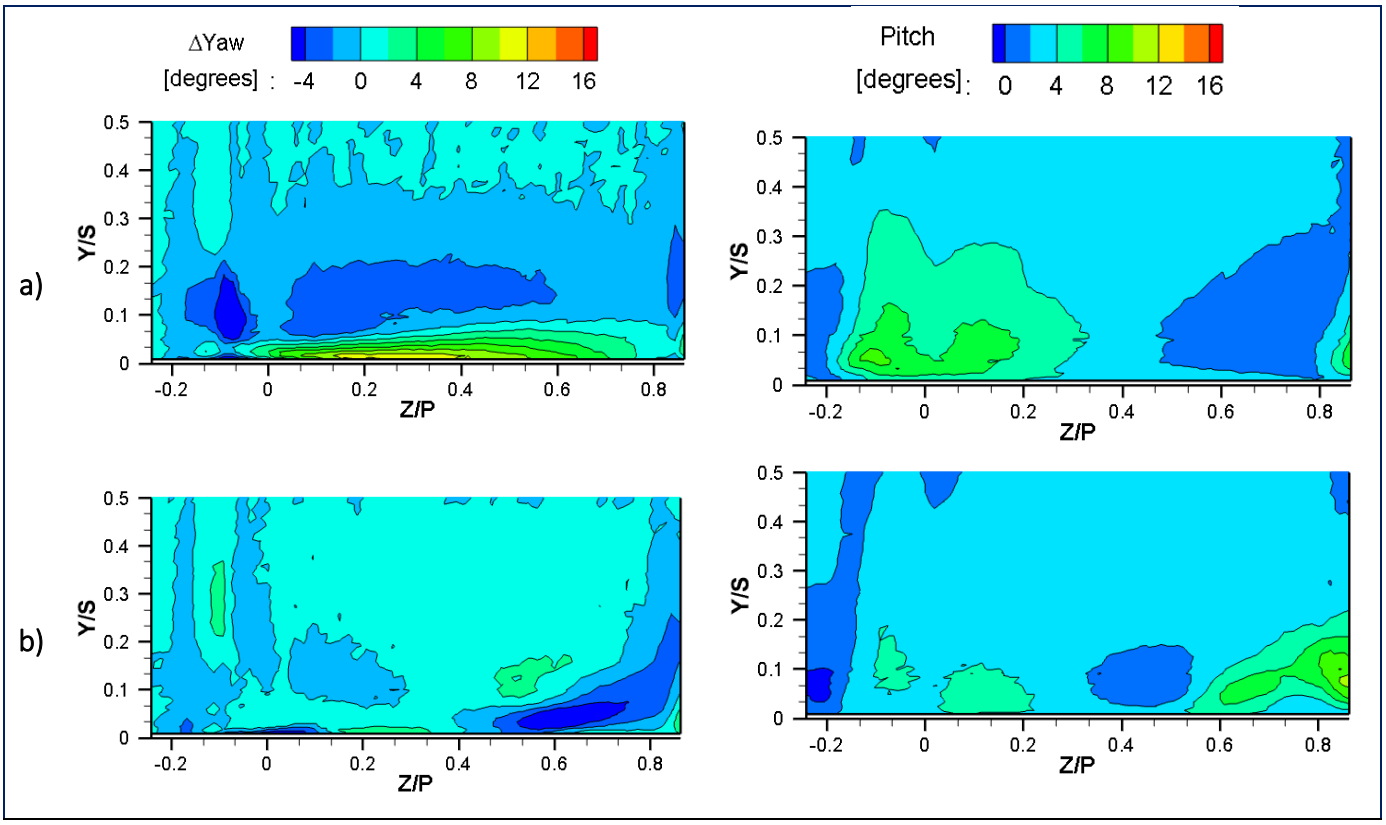

FIGURE E.14 CONTOURS OF YAW ANGLE DEVIATION (LEFT) AND PITCH ANGLE (RIGHT) AT PLANE-3 (X_G/C_{AX} = 1.042) FOR (A) M_{IN} = 1.1 FILLET AND (B) M_{IN} = 2.3 FILLET.

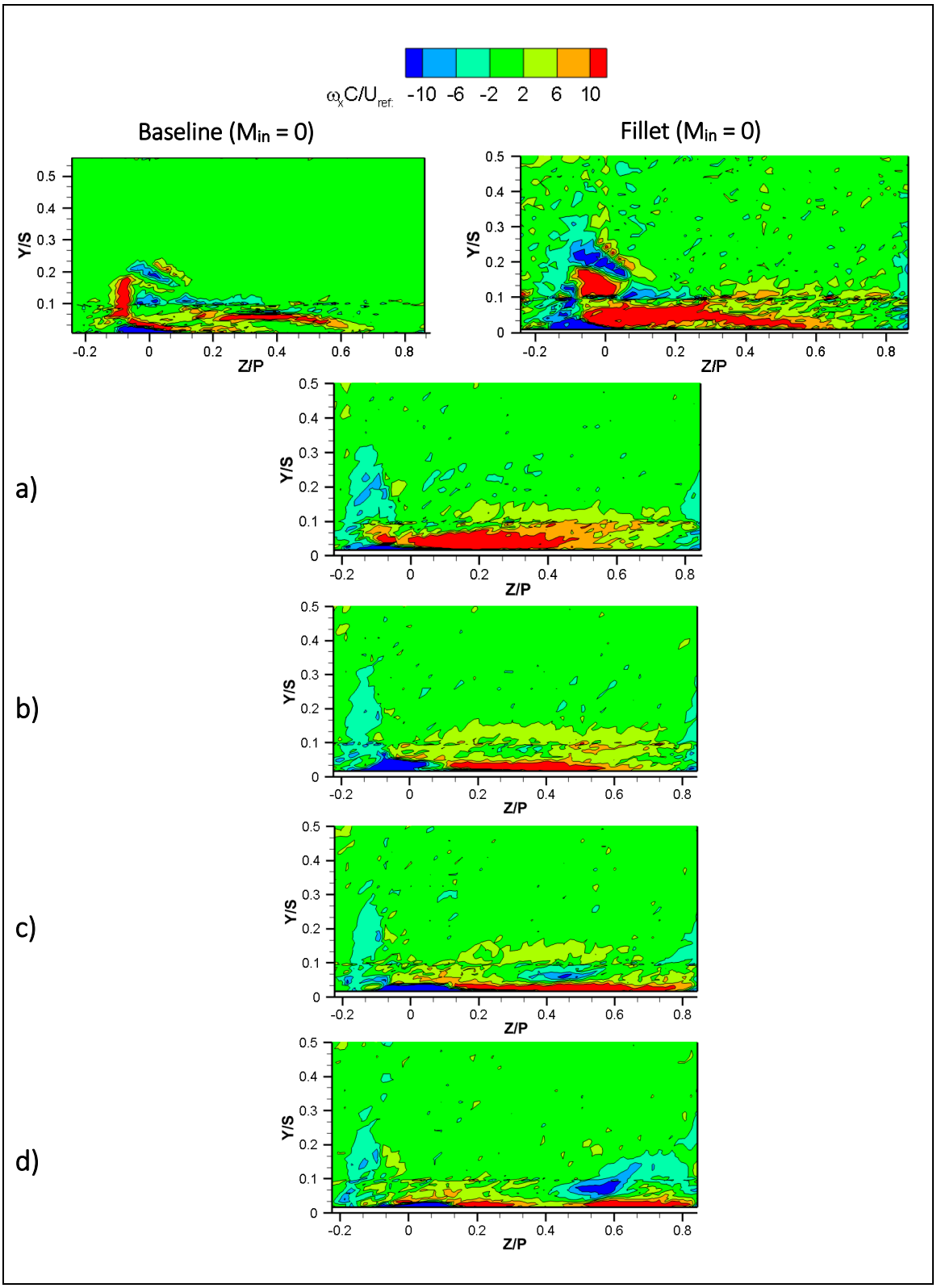

FIGURE E.15 CONTOURS OF $\omega_X C/U_{REF}$ AT PLANE-3 (X_G/C_{AX} = 1.042) FOR FILM-COOLING CASE WITH FILLET AT (A) M_{IN} = 1.1, (B) M_{IN} = 1.4, (C) M_{IN} = 1.8 AND (D) M_{IN} = 2.3.

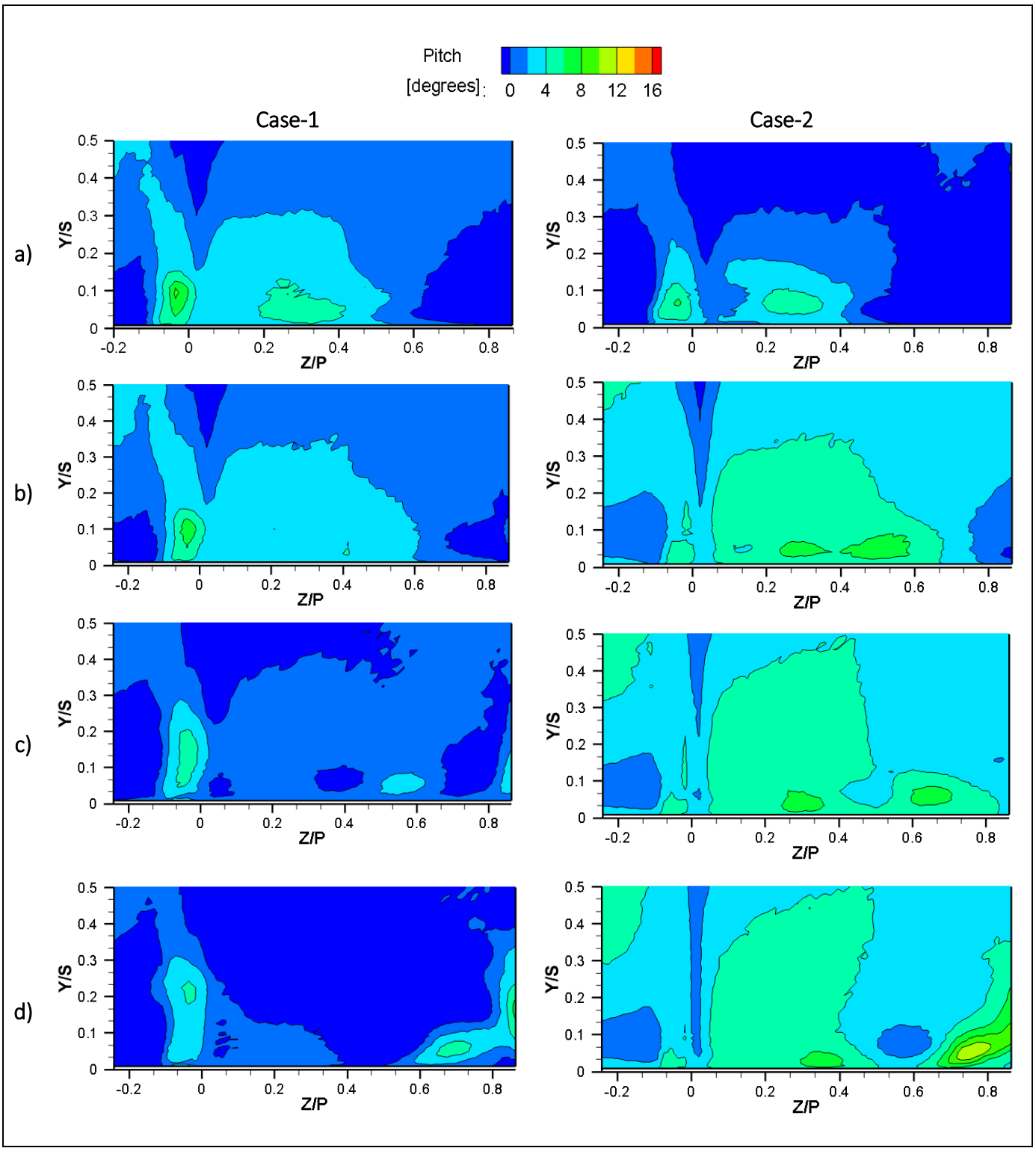

FIGURE E.16 CONTOURS OF PITCH ANGLE AT PLANE-3 (X_G/C_{AX} = 1.042) FOR FILM-COOLING CASES (WITHOUT FILLET) AT (A) M_{IN} = 1.1, (B) M_{IN} = 1.4, (C) M_{IN} = 1.8 AND (D) M_{IN} = 2.3.

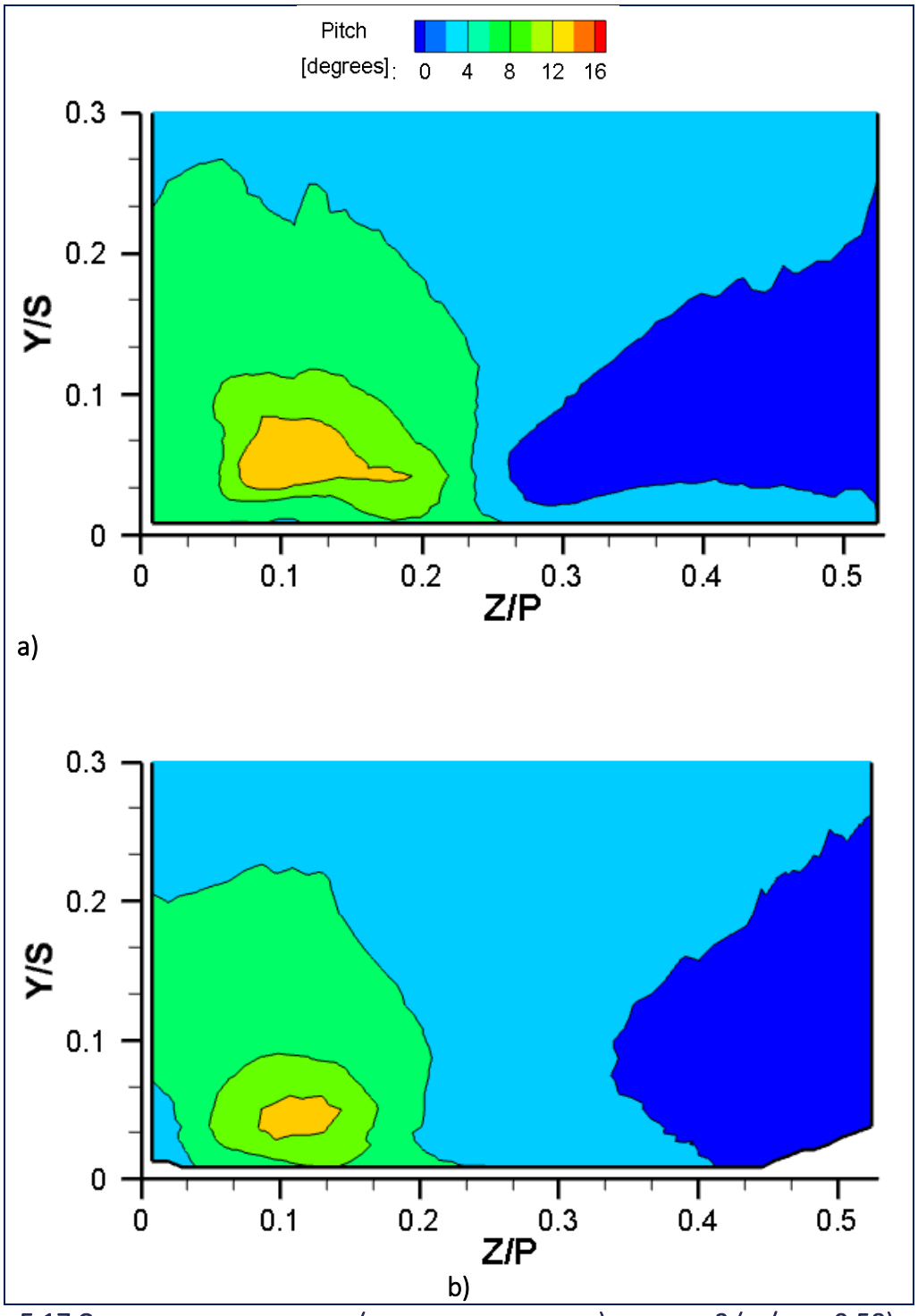

FIGURE E.17 CONTOURS OF PITCH ANGLE (TURNING ABOUT Y-AXIS) AT PLANE-2 (X_G/C_{AX} = 0.58) FOR (A) BASELINE AND (B) FILLET.

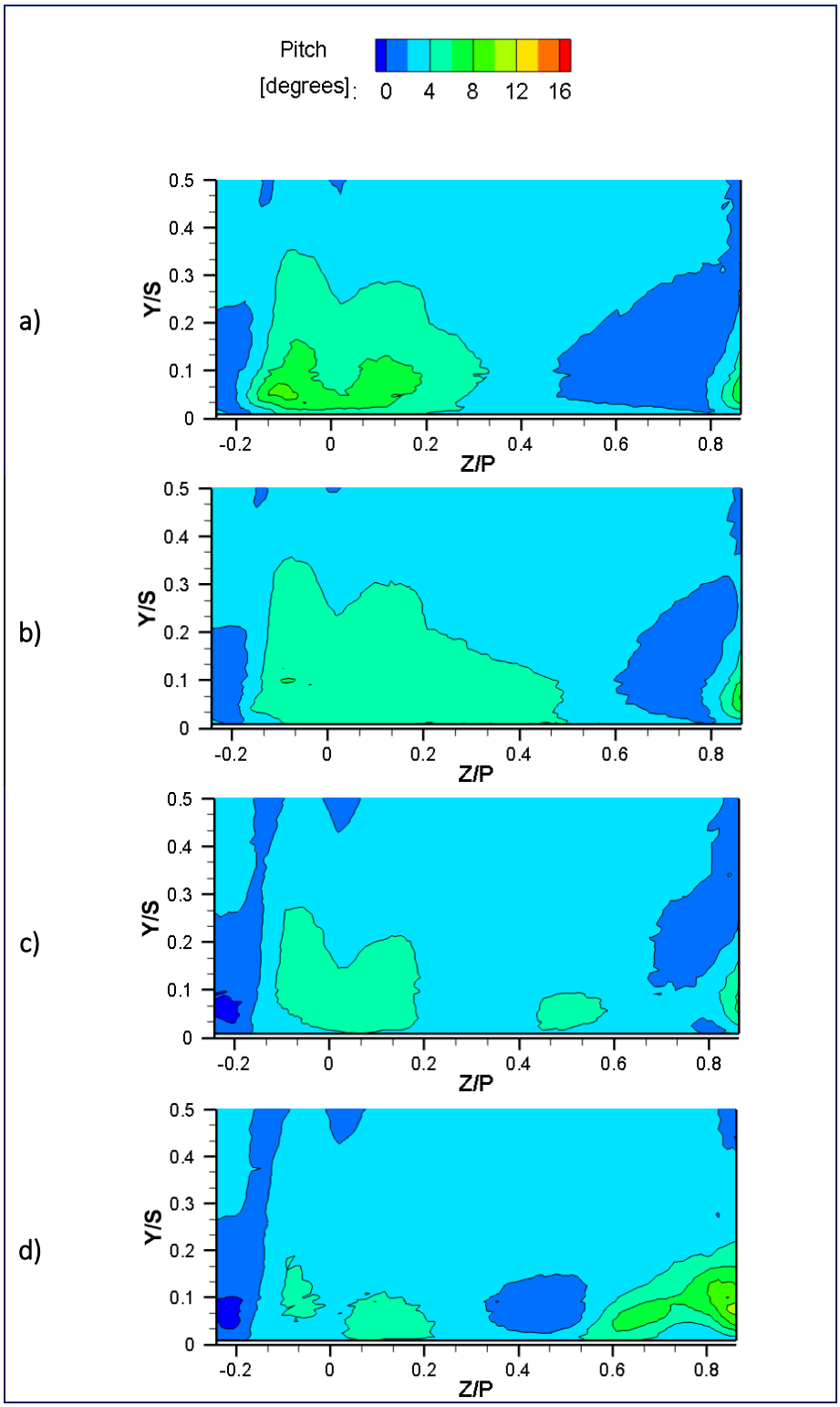

FIGURE E.18 CONTOURS OF PITCH ANGLE AT PLANE-3 (X_G/C_{AX} = 1.042) FOR FILM-COOLING CASE WITH FILLET AT (A) M_{IN} = 1.1, (B) M_{IN} = 1.4, (C) M_{IN} = 1.8 AND (D) M_{IN} = 2.3.

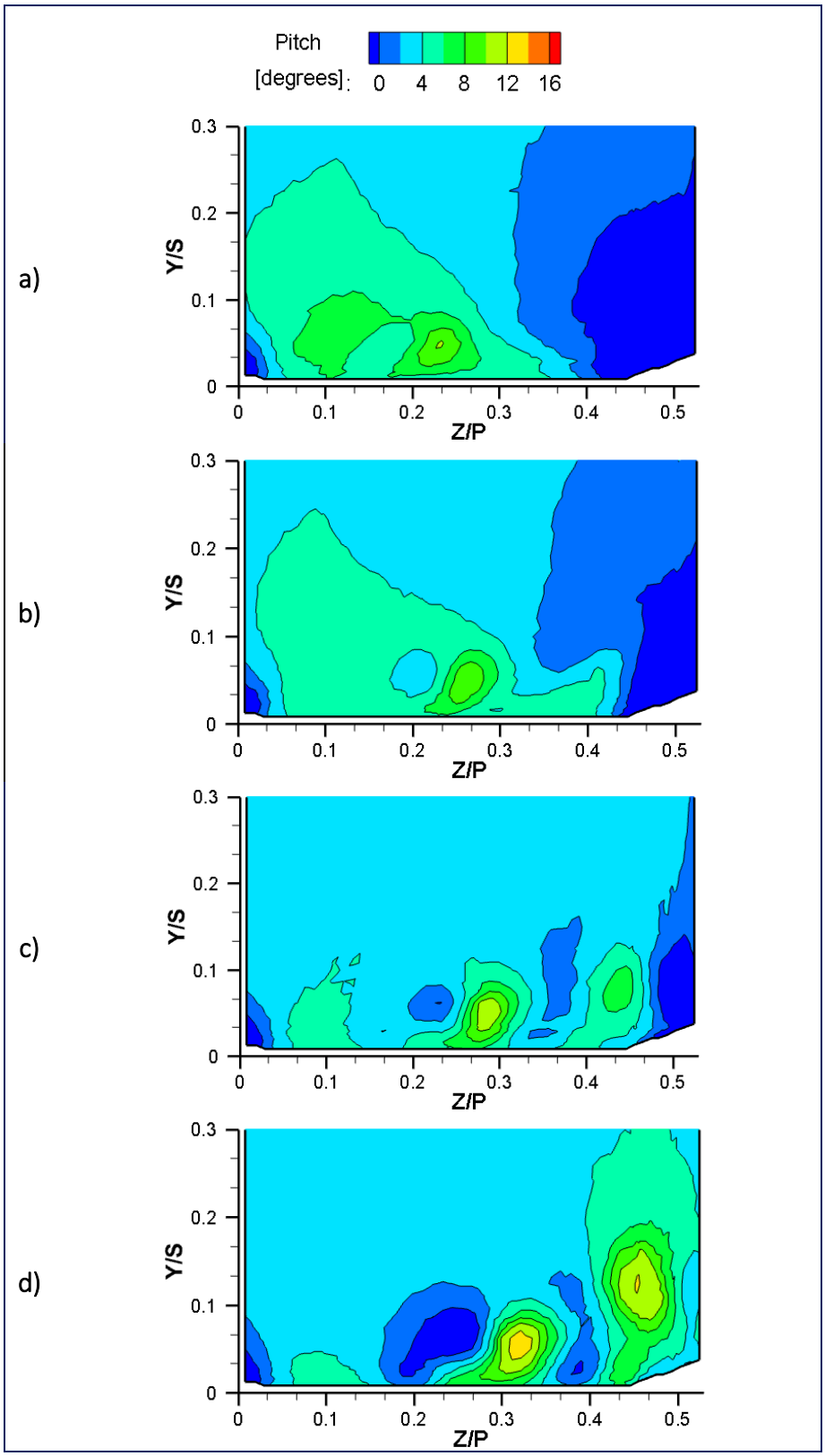

FIGURE E.19 CONTOURS OF PITCH ANGLE AT PLANE-2 (X_G/C_{AX} = 0.58) FOR FILM-COOLING CASE WITH FILLET AT (A) M_{IN} = 1.1, (B) M_{IN} = 1.4, (C) M_{IN} = 1.8 AND (D) M_{IN} = 2.3.

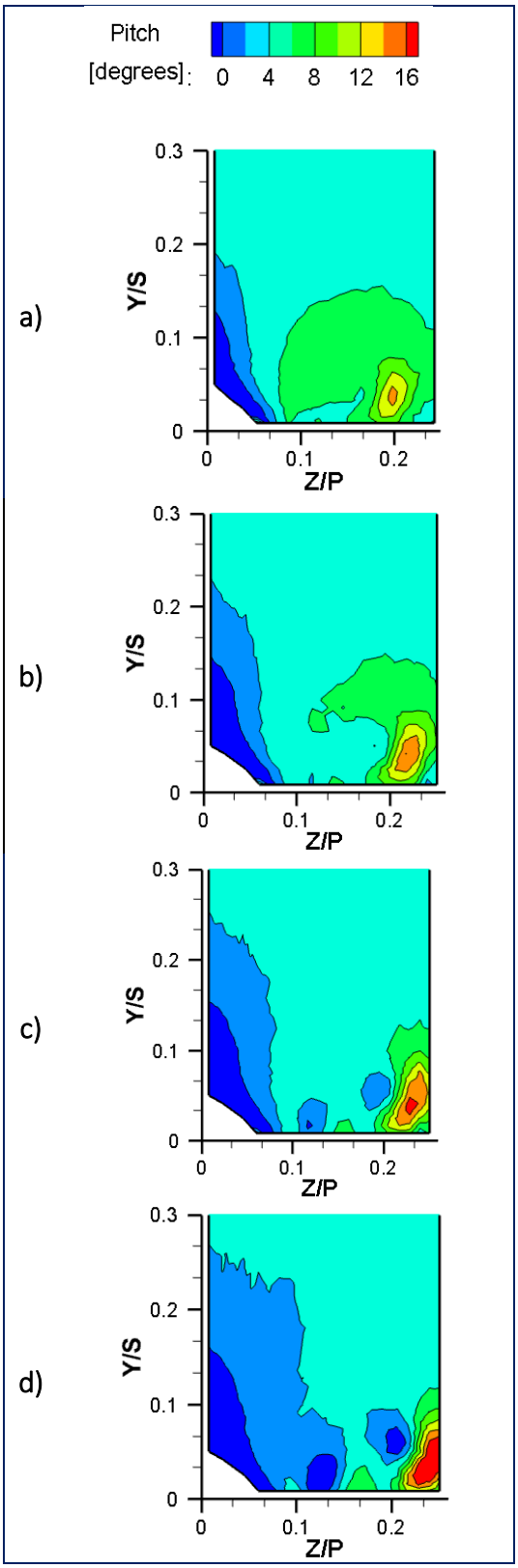

FIGURE E.20 CONTOURS OF PITCH ANGLE AT PLANE-1 (X_G/C_{AX} = 0.251) FOR FILM-COOLING CASE WITH FILLET AT (A) M_{IN} = 1.1, (B) M_{IN} = 1.4, (C) M_{IN} = 1.8 AND (D) M_{IN} = 2.3.

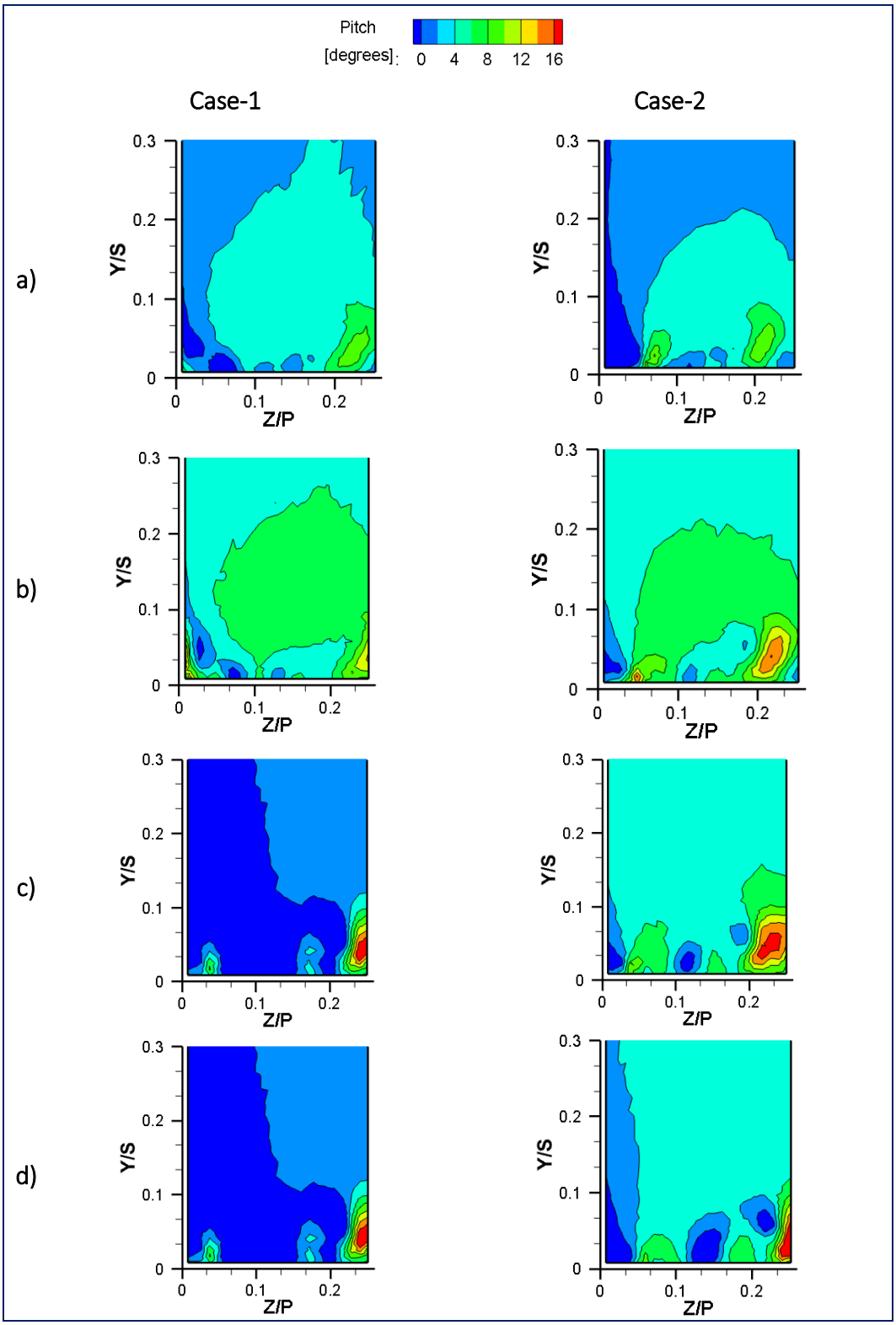

FIGURE E.21 CONTOURS OF PITCH ANGLE AT PLANE-1 (X_G/C_{AX} = 0.251) FOR BOTH FILM-COOLING CASES (WITHOUT FILLET) AT (A) M_{IN} = 1.1, (B) M_{IN} = 1.4, (C) M_{IN} = 1.8 AND (D) M_{IN} = 2.3.

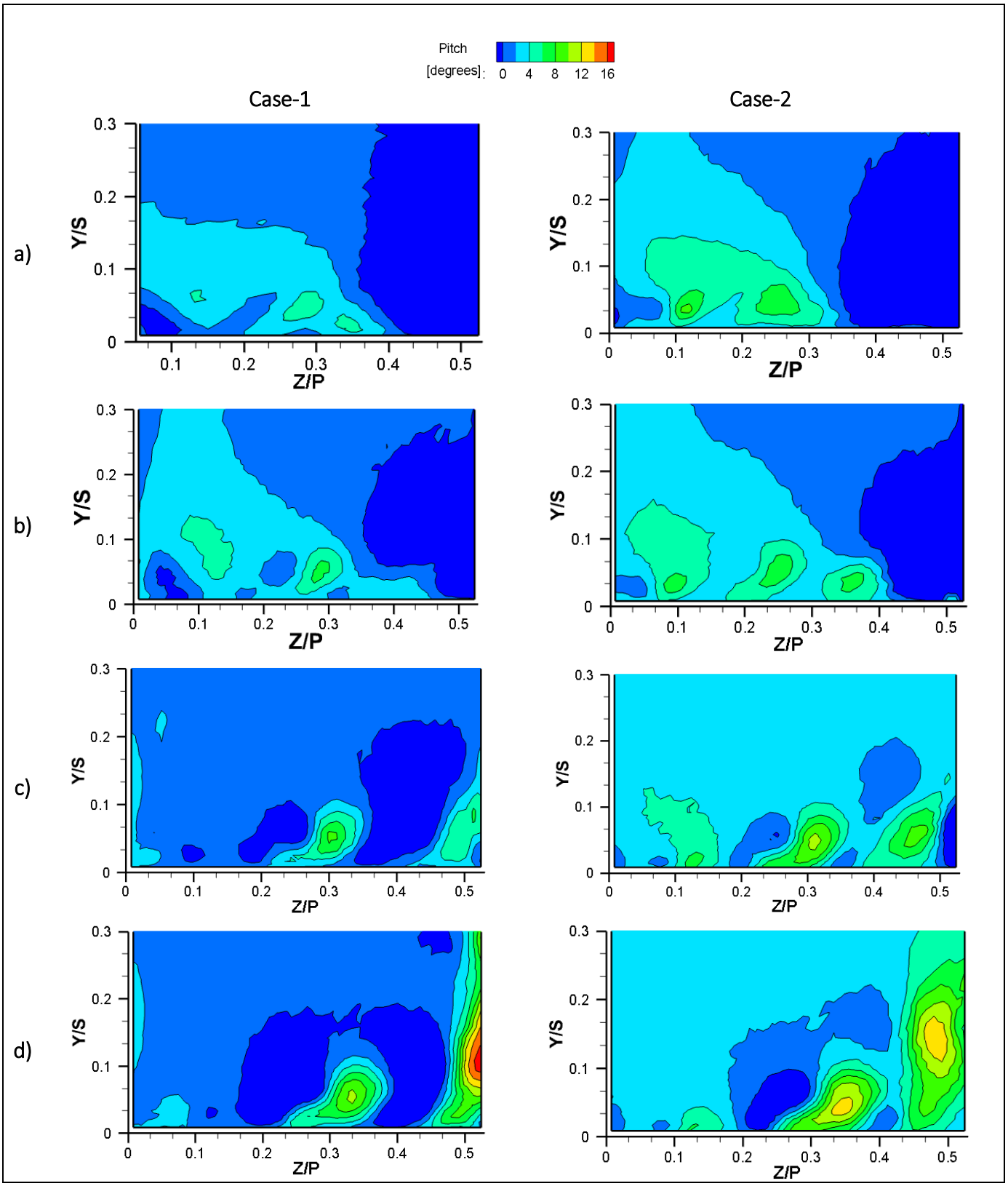

FIGURE E.22 CONTOURS OF PITCH ANGLE AT PLANE-2 (X_G/C_{AX} = 0.58) FOR BOTH FILM-COOLING CASES (WITHOUT FILLET) AT (A) M_{IN} = 1.1, (B) M_{IN} = 1.4, (C) M_{IN} = 1.8 AND (D) M_{IN} = 2.3.